2024

The development and validation of a novel patient-derived 3D meningioma cell culture model

van de Weijer, Laurien Lisette

https://pearl.plymouth.ac.uk/handle/10026.1/22057

http://dx.doi.org/10.24382/5148
University of Plymouth

Copyright Statement

UNIVERSITY OF
PLYMOUTH

The development and validation of a novel patient-derived 3D meningioma cell culture model

By

LAURIEN LISETTE VAN DE WEIJER

A thesis submitted to the University of Plymouth
in partial fulfilment of the degree of

DOCTOR OF PHILOSOPHY

Peninsular Medical School
August 2023

Acknowledgements

Firstly, I would like to extend my sincere thanks to my Director of Studies Professor Oliver Hanemann for giving me the opportunity to undertake a PhD and develop myself into an independent researcher. I much appreciate your guidance and trust in me during this project.

I would also like to extensively thank Emanuela Ercolano. Without you my PhD would have gone very differently. Thank you for always being there along the way and believing in me. You really taught me to be confident in my work and it has been a pleasure to learn from you. I will forever be grateful for all your guidance and for motivating me throughout this project. I will dearly miss your infectious enthusiasm and our daily discussions. I truly believe this thesis was a team effort.

Of my supervisory team I would like to thank Dr. Jon Gil-Ranedo and Dr. David Hilton. Jon thanks for always keeping your door open and for providing a fresh view on my ideas. Your encouragements pushed me to make the most of it. David, I am grateful for your assistance with all my histology and for taking the time to go over endless stained slides. Your expertise and advice enabled me to succeed. Related to this, I would also like to express my gratitude to the other members of the Derriford neuropathology department for all their support.

There are several academics outside of my supervisory team I would also like to extend my thanks to for their assistance with my project. Dr Claire Adams, thank you for all your efforts with the brain tumour bank which has been invaluable to my project and for always being there to answer my questions. Dr. Juri Na, thank you for being a friend in the lab and helping me to get my project back on the rails when it was almost derailing. Thank you for your positivity and cheerfulness in the lab and your encouraging words towards me. I am grateful to Dr. Matthew Banton and Maryam Shah and for helping me with the DNA genomics analysis and to Ting Zhang for her help with collecting the transcriptomic samples.

My thanks also go to the many members of the Hanemann group, past and present. I am certain that my time as a PhD student would not have been as enjoyable or productive without your input. Jemma, Foram, Yeasmin and Liyam thanks for welcoming me to Plymouth and showing me the ropes. To Foram and Leandro, thank you for being the best car sharers I could’ve wished for and making the commute from Exeter much more fun. Kevin and Nsikan, thanks for all the Friday afternoon conversations/discussions we had, regardless of what day of the week it was. These conversations were often the highlight of my day, whether it was nonsense or science. Art and Sarah, thank you for making sure we all kept a positive mindset and for getting me over my fear of entering running competitions. You are all amazing.

Finally, I would like to express my thanks to my family for their support. Opa, now you can finally brag about having a grandchild with a PhD. And lastly, to Ino, for being there during all the highs and lows, for inspiring me, believing in me and your continued support. Thank you for making this adventure to England one to never forget.

Author’s declaration

At no time during the registration for the degree of Doctor of Philosophy has the author been registered for any other University award without prior agreement of the Doctoral College Quality Sub-Committee.

Work submitted for this research degree at the University of Plymouth has not formed part of any other degree either at the University of Plymouth or at another establishment.

This study was financed with the aid of a studentship from the Peninsula Medical Foundation and Brain Tumour Research.

Publications

Van de Weijer L.L., Ercolano E., Zhang T., Shah M., Banton M.L., Na J., Adams C.L., Hilton D., Kurian K.M., Hanemann C.O. A novel patient-derived meningioma spheroid model as a tool to study and treat epithelial-to-mesenchymal transition (EMT) in meningiomas. Acta Neuropathol Commun. 2023. DOI: 10.1186/s40478-023-01677-9

Presentations at Conferences:

- The 11th Brain Tumour Meeting 2022 – Berlin, May 2022 – Poster Presentation
- The 2023 CTF NF Conference – Phoenix, – June 2023, Invited speaker for oral presentation.

Word count of main body of thesis: 40146

Signed: Laurien van de Weijer

Date: 18 August 2023

Laurien Lisette van de Weijer

The development and validation of a novel patient-derived 3D meningioma cell culture model

Abstract

Meningiomas are the most frequent intracranial brain tumours. Current treatment options of surgery and radiotherapy are sometimes insufficient and effective systemic therapies remain unestablished. The development of accurate *in vitro* systems to model the complexity of meningioma pathology is essential for predicting drug response and developing novel therapeutics. Therefore, in this study, I established an easy-to-use *in vitro* patient-derived meningioma spheroid model that maintained the morphological and molecular features of the parental tumours, including tissue histology, the tumour microenvironment, and the mutational profile. Comprehensive characterisation of the global transcriptomes of the novel patient-derived spheroids with traditional meningioma monolayer cultures and parental tissues revealed an enhanced Notch1-mediated mesenchymal gene expression signature in the spheroids compared to traditional 2D monolayer cultures. These features were confirmed by the presence of other mesenchymal traits such as invasion capacity, demonstrating this spheroid model as the first meningioma 3D culture method capable of studying functional invasion, and indicating its relevance for studying the molecular mechanisms associated with invasion and the related oncogenic process of epithelial-to-mesenchymal transition (EMT). The suitability of this model for use as a tool for research questions, including pre-clinical drug testing, was demonstrated by studying the effect of Notch1 shRNA targeting, and by treatment using several inhibitors. Concomitantly, this proof-of-concept study allowed for the development of a novel effective combination therapy of MER tyrosine kinase (MERTK) and histone deacetylase (HDAC) inhibition, which in addition to having a synergistic inhibitory effect on spheroid viability, also decreased spheroid proliferation, expression of EMT-associated proteins and spheroid invasion capacity. Hence, I propose this meningioma spheroid model as novel preclinical drug screening tool to assess the efficacy of drug compounds targeting EMT and brain invasion of meningiomas and the combination of HDAC and MERTK inhibitors as a promising therapeutic strategy.

Table of Contents

List of Figures

List of Tables

Abbreviations

ADAM	A Disintegrin and metalloproteinase domain-containing protein
ASC	adult stem cell
AKT1	V-akt murine thymoma viral oncogene homolog 1
APOC2	Apolipoprotein C2
BAP1	BRCA1 associated protein 1
BSA	Bovine Serum Albumin
CDH1	E-cadherin
CSC	cancer stem-like cells
CDKN2A/B	cyclin-dependent kinase inhibitor 2A
CD68	cluster of differentiation 68
CD163	cluster of differentiation 163
CNS	central nervous system
CSF	cerebrospinal fluid
CT	computed tomography
DEG	differentially expressed genes
DIPG	diffuse intrinsic pontine glioma
DLL	Delta-like molecules
DMEM	Dulbecco's Modified Eagle Medium
DMSO	dimethyl sulphoxide
EANO	European Association of Neuro-Oncology
ECM	Extracellular matrix
EGF	epithelial growth factor
EMT	Epithelial-to-Mesenchymal Transition
FBS	fetal bovine serum
FDA	U.S. Food and Drugs administration
FDR	False discovery rate
FFPE	Formalin Fixed Paraffin Embedded
FGF	fibroblastic growth factor
Flt3	Fms Related Receptor Tyrosine Kinase 3)
FPKM	Fragments Per Kilobase of transcript per Million mapped reads
GAPDH	Glyceraldehyde 3-phosphate dehydrogenase
GBOM	Glioblastoma organoid medium
GFP	green fluorescent protein
GFS	Growth Factor Supplemented medium
GO	Gene ontology
GSEA	Gene Set Enrichment Analysis
GTR	gross total resection
HAT	histone acetyltransferases
HDAC	Histone deacetylase
Hes1	Hairy and enhancer of split-1
Hey1	Hes related family bHLH transcription factor with YRPW motif 1
bHLH	basic helix-loop-helix
HPF	high power fields
HRP	horseradish peroxidase
HU	hydroxyurea
H_2O	water
H3	histone 3
H&E	Haematoxylin & Eosin
ICC	immunocytochemistry
IHC	immunohistochemistry

IR	ionising radiation
iPSC	induced pluripotent stem cell
KEGG	Kyoto Encyclopaedia of Genes and Genomes
KLF4	Krüppel-like factor 4
MC	methylation classes
MEK	Mitogen-activated protein kinase kinase
MERTK	Mer receptor tyrosine kinase
MET	Mesenchymal-to-Epithelial Transition
MgO	Meningioma Organoid
MN1	Meningioma grade 1 growth medium
MN2	Meningioma grade 2 growth medium
MRI	magnetic resonance imaging
mTORC1	mammalian target of rapamycin complex 1
NICD	Notch1 intracellular domain
NF2	Neurofibromatosis 2
NFκB	Nuclear factor kappa B
NGS	Next-generation sequencing
NMT	normal meningeal tissue
oHSV	oncolytic herpes simplex virus
OS	overall survival
PBS	phosphate buffered saline
PCA	principal component analysis
PFA	paraformaldehyde
PFS	progression free survival
PGDS	prostaglandin D2 synthase
PgR	progesterone receptor
PIK3CA	phosphatidylinositol-4,5-biphosphate 3-kinase catalytic subunit α
RIPA	Radioimmunoprecipitation assay
qPCR	quantitative polymerase chain reaction
PI3K	phosphoinositide-3-kinase
PTEN	Phosphatase and TENsin homolog deleted on chromosome 10
POLR2A	RNA polymerase II
PROS1	vitamin K-dependent protein S
RBC	red blood cell
RIN	RNA Integrity Number
RPL37A	60S ribosomal protein L37a
RTK	receptor tyrosine kinase
PVDF	polyvinylidene fluoride
Scr	Scramble
SDS-PAGE	Sodium dodecyl sulphate polyacrylamide gel
SHH	sonic hedgehog
SMARCB1	switch/sucrose nonfermentable-related matrix-associated actin-dependent regulator of chromatin subfamily B member 1
SMARCE1	switch/sucrose nonfermentable-related matrix-associated actin-dependent regulator of chromatin subfamily E member 1
SMO	smoothened
SSTR2	somatostatin receptor 2
STR	subtotal resection
SWI/SNF	Switch/sucrose non-fermentable
SWGLH	Southwest Genomic Laboratory Hub
TA	tumour associated
TAM	Tyro3, Axl, MERTK

TBS	Tris buffered saline
TERT	Telomerase reverse transcriptase
TGF-β	Transforming growth factor-β
TLE	Groucho/transducing-like enhancer of split family co-repressor
TME	tumour microenvironment
TNF	tumour necrosis factor receptor associated factor 7
TRAF7	TNF receptor associated
TSA	Trichostatin A
ULA	ultra low adherend
VEGF	vascular endothelial growth factor
WHO	World Health Organisation
Wnt	Wingless/integrated
ZEB1/2	zinc-finger E-box-binding homeobox ½
ZO-1	Zonula Occludens-1
2D	Two-dimensional
3D	Three-dimensional

1 Introduction

1.1 Background of the study

Meningiomas are the most common primary intracranial brain tumours and account for approximately 36% of all primary tumours of the central nervous system (CNS) (1). The World Health Organisation (WHO) classifies meningiomas into WHO grade I (benign), WHO grade II (atypical), and WHO grade III (anaplastic) (2). WHO grade I meningiomas (80%) have a good prognosis with an estimated 10-year overall survival of 80-90%, while WHO grade 2 (15-18%) and grade 3 (2-4%) are more aggressive and have a high risk of recurrency (3,4). Indeed, 10-year overall survival for high grade meningiomas (grade 2/3) is estimated as 14-34% (4). There are currently no effective chemotherapeutics that are routinely offered to patients, and existing treatment options of surgery and radiotherapy can leave patients with post-operative morbidity, radiation neurotoxicity and tumour recurrence (1,5,6). Recent comprehensive studies have identified the genetic background of meningiomas and revealed several disease causing mutations (NF2, TRAF7, AKT1, KLF4, SMO, POLR2A, PIK3CA, SMARCE1, SMARCB1) (7–11). However, progress in the development of therapeutic approaches directly targeting genetically stratified tumours remains limited.

One of the factors limiting the therapeutic advances of meningiomas is the long-standing translational gap that exists between preclinical *in vitro* study results and clinical trials (12). This is a consequence of the narrow selection of *in vitro* models available to accurately model the complexity of meningioma pathogenesis (13) . The few meningioma immortalized cell lines available , do not maintain the three-dimensional (3D) structure, cellular heterogeneity, and microenvironment of a tumour, which fundamentally limits their translational power (13). While some of these disadvantages can be overcome using xenograft mice models, animal studies are costly and resource-intensive, which limits their potential for high throughput studies (14). In addition, xenograft models use immunodeficient mice which impedes immune modelling (15). Fortunately, 3D cell culture technology has emerged as relevant *in vitro* experimental tool for tumour modelling. The advantage of 3D culture models is that they can accurately resemble tissue-specific architecture including cell-cell, cell-extracellular matrix (ECM) and cell-microenvironment interactions, and tissue-specific physiological conditions, such as oxygen, nutrient and metabolic waste gradients (16). Thus, 3D cultures are superior to monolayers for use in preclinical studies selecting effective drug targets and therapies. Adopting such models in meningioma research has the potential to diminish the number of candidate therapeutic compounds that are inappropriately selected for further investigation. At the start of this study, a 3D cell culture model for meningiomas hadn’t been established yet. Since then, few 3D cell culture models for meningiomas have been established, but these haven’t yet been widely adopted by other research groups (17–20). Moreover, the established methods are complex and require high expertise. Having an easy-to-use 3D meningioma *in vitro* model could provide a valuable study platform for basic and translational meningioma research. Therefore, this PhD thesis describes how I developed a novel *in vitro* 3D meningioma spheroid model and validated it for use as tool in drug development. Additionally, I show that meningioma spheroid cultures demonstrate the oncogenic process of epithelial-to-mesenchymal transition (EMT), which was chosen as process of interest in proof-of-concept experiments validating the use of this model as tool in *in vitro* experimental setups.

The following introduction is a comprehensive literature review of meningioma biology, current treatment strategies and recent advances in 3D cell culture. In addition, I discuss the relevance of the EMT process in meningioma biology and the prospective to target this process.

1.2 Overview of meningiomas

1.2.1 Grading and Origin

Meningiomas are the most common intracranial brain tumours of the CNS, of which the majority are slow-growing benign lesions. They are stratified by the WHO into three grades based on histological and molecular characteristics: CNS WHO grade 1 benign meningiomas, accounting for approximately 80% of cases, CNS WHO Grade 2 atypical meningiomas, accounting for approximately 18% and CNS WHO grade 3 anaplastic meningioma, accounting for approximately 1-3% (21,22).

Meningiomas are formed from the meninges (fig. 1.1A). The meninges consist of three membranes, the dura mater, the arachnoid mater, and the pia mater, which cover the brain and spinal cord. Besides providing a physical barrier protecting the neuronal tissue against physical damage, they are involved in the regulation of immunological processes and homeostasis maintenance in the cerebrospinal fluid (CSF) (21). Specifically, meningioma is thought to arise from the web-like arachnoid layer of the meninges. This layer is enclosed between the dura mater, situated closest to the skull and vertebrae, and the pia mater, the thinnest and most apical layer (21). Together, the arachnoid and the pia mater form the leptomeninges. The arachnoid layer contains arachnoid villi, which are microscopic villi that protrude through the dura into the sinuses and are essential for the absorption of CSF (23). The arachnoid villi are structured from several components, including an endothelial layer, fibrous capsule, arachnoid layer, arachnoid cap cells and a central core (fig. 1.1B) (24). Arachnoid cap cells are suggested as the meningioma cell of origin. This is based on their cytological similarities with meningioma cells; arachnoid cap cells form calcified aggregates also known as psammoma bodies, which are also observed in meningiomas (25). Additionally, Kalamarides *et al.* showed evidence for prostaglandin D2 synthase (PGDS)-expressing arachnoid cells on arachnoid villi as the meningioma cell of origin in mice by demonstrating the generation of meningiomas following inactivation of the common meningioma driver gene *Neurofibromatosis 2* (NF2) (26). Interestingly, features of different meningioma subtypes, ranging from meningothelial to fibroblastic histology, correspond with the histology of the various non-neoplastic cells found in arachnoid villi. Albayrak & Black (24) contradicted the arachnoid cap cell hypothesis and suggested the existence of a yet unidentified universal stem-like cell that gives rise to the various cells present in the arachnoid layer. They hypothesized this stem-like cell as the cell of origin for all different meningioma subtypes. Additionally, they suggested that different meningioma subtypes originate from different tumour-initiating cells derived from the various cell types in the arachnoid layer (24). However, both these hypotheses remain unsolved.

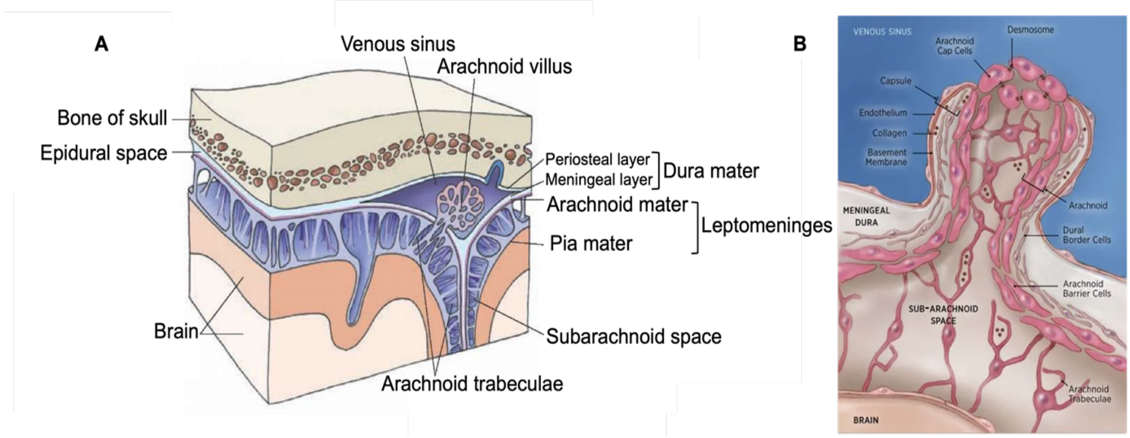

Figure 1.1 Schematic overview of the meninges

A) The meninges cover the brain and spinal cord with three layers: the dura mater, separated into the periosteal and meningeal layer at the venous sinus, the arachnoid mater, and the pia mater. *Adapted from what-when-how.com* (27) B) Arachnoid villi protrude into the dural sinuses and are structured from several components: including an endothelial layer, fibrous capsule, arachnoid layer, and arachnoid cap cells, which are thought to be the meningioma cell of origin. *Adapted from DeMonte et al.* (23)

1.2.2 Meningioma history and classification

The term meningioma was first introduced by Harvey Cushing, who used it to describe a set of tumours of meningeal origin occurring in the brain and spinal cord in the early 1900s (28). Soon after Cushing first described meningiomas, attempts were made to divide this heterogenous group of tumours into subtypes based on histological differences. The first classification included three subgroups, which further developed into the classification that is now used by the WHO to stratify meningiomas using both histological and molecular features (fig. 1.2) (28). The 2021 WHO classification defines three grades: WHO grade 1, typically benign and representing approximately 80% of meningiomas, WHO grade 2, atypical meningiomas representing ~18% of meningiomas and, the anaplastic WHO grade 3 meningiomas representing about 1-3% of tumours. This is further divided into 15 defined meningioma subtypes based on histological appearance (meningothelial, fibrous, transitional, psammomatous, angiomatous, microcystic, secretory, lymphoplasmacyte-rich, metaplastic, chordoid, clear cell, atypical, papillary, rhabdoid and anaplastic). Before 2021, meningioma subtypes were linked to grade, with 9 subtypes associated with grade 1 tumours, and 3 subtypes for grades 2 and 3. This was changed in the 2021 WHO classification in which criteria to define tumours grade are now considered independent from histologic subtype (29). Criteria for atypical WHO grade 2 tumours are a mitotic activity index of 4-19 mitoses per 10 high power fields (HPF) and/or the presence of several histo- and cytomorphological features such as increased cellularity, small cells with a high nucleus to cytoplasmic ratio, prominent nucleoli, sheeting, and foci of spontaneous necrosis. A tumour with at least 3-5 of these criteria should be considered WHO grade 2. In addition, brain invasion is a stand-alone criterion to classify a tumour directly as a WHO grade 2. For grade 3 grading, these criteria are 20 or more mitoses per 10 HPF, or loss of meningothelial differentiation (30). The classification system is under continuous revision and updates are released periodically. Recent papers have used mutations, methylation profiles, RNA sequencing signatures and proteomics to describe specific profiles to stratify meningiomas into prognostic groups. The latest version of the WHO grading included novel molecular signatures as independent criteria for grade 3 grading (TERT promoter mutation, or homozygous deletion of CDKN2A/B) and mentions methylation profiling of meningiomas as a superior tool compared to histopathology alone for the identification of patients at high risk of recurrence. The latter, however, is not yet included in the official grading criteria but, along with molecular classification based on copy number variation, point mutations and transcriptomic and proteomic data, is expected to be included in the next version (2,31).

1.2.3 Location

Meningiomas predominantly occur in the cranial meninges; most commonly in the parasagittal, convexity and sphenoid regions. Approximately 4.2% occur from the spinal meninges. Very rarely, meningiomas occur as primary tumours in the ventricles of the CNS and extracranial organs including the lungs, probably originating from aberrant arachnoid cells (<1%) (32,33). Interestingly, there is an association between certain meningioma histological subtypes and location. For instance, meningothelial meningiomas are often located at the skull base and spine, while fibroblastic meningiomas tend to occur in the brain convexity. In addition, higher-grade meningiomas are frequently found at the convexity and parasagittal locations, and are less common at the skull base (34). Intriguingly, arachnoid cap cells arise from two distinct origins during embryogenesis based on their anatomic location. The skull-based layer has a mesodermal origin while arachnoid cells in the cerebral convexity originate from the neural crest (21,35). As such, this could be an underlying factor predisposing certain regions to certain histological subtypes.

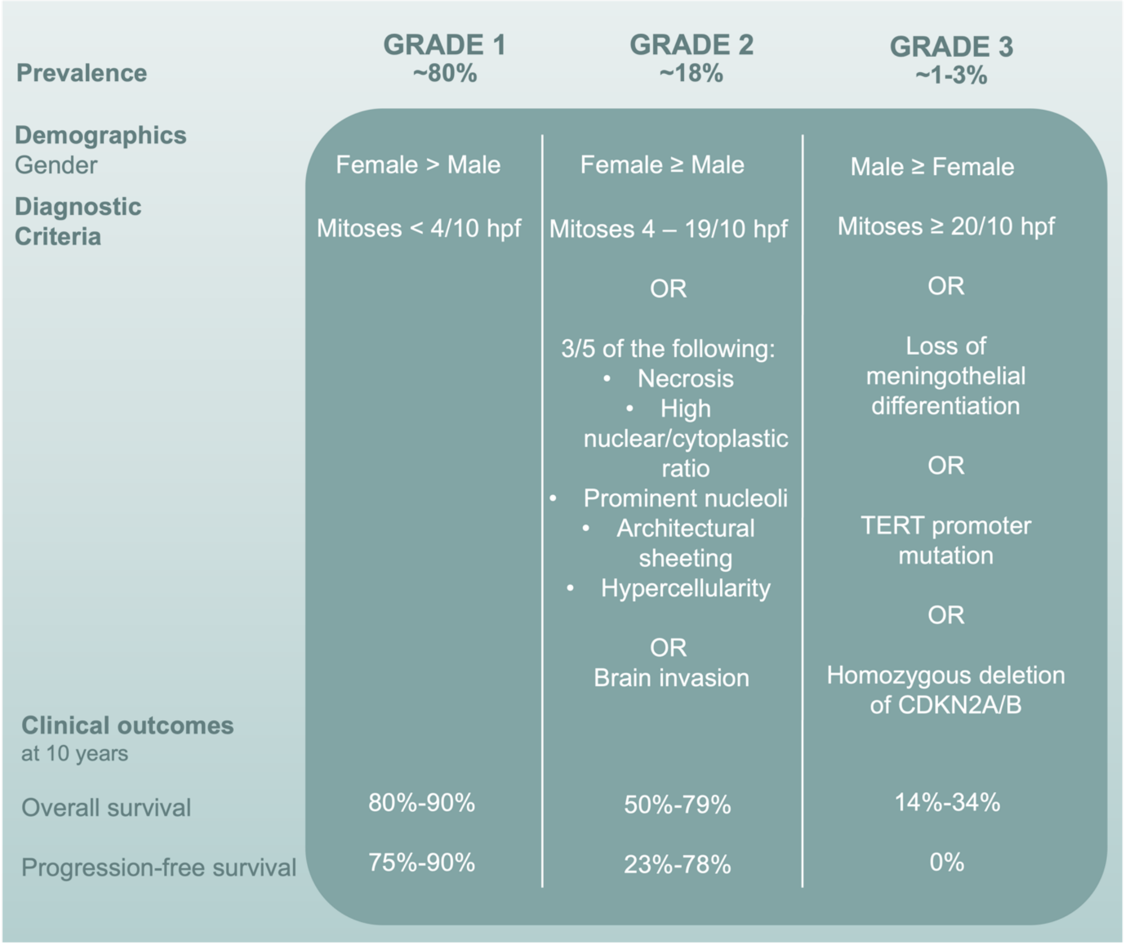

	GRADE 1	GRADE 2	GRADE 3
Prevalence	~80%	~18%	~1-3%
Demographics Gender	Female > Male	Female ≥ Male	Male ≥ Female
Diagnostic Criteria	Mitoses < 4/10 hpf	Mitoses 4 – 19/10 hpf OR 3/5 of the following: • Necrosis • High nuclear/cytoplastic ratio • Prominent nucleoli • Architectural sheeting • Hypercellularity OR Brain invasion	Mitoses ≥ 20/10 hpf OR Loss of meningothelial differentiation OR TERT promoter mutation OR Homozygous deletion of CDKN2A/B
Clinical outcomes at 10 years			
Overall survival	80%-90%	50%-79%	14%-34%
Progression-free survival	75%-90%	23%-78%	0%

Figure 1.2 WHO classification, diagnostic criteria, and clinical outcomes

Characteristics of meningioma CNS WHO grade I (benign), WHO grade II (atypical), and WHO grade III (malignant), including prevalence, demographics, diagnostic criteria and clinical outcomes: overall survival (OS) and progression-free survival (PFS). (2,3) Adapted from Bi *et al.* (36).

1.2.4 Incidence and risk factors

Approximately 36% of all primary CNS tumour cases, and 53% of benign CNS tumour cases, are meningiomas (21). They mainly present in elderly patients with the peak of cases at a median age of 66. Incidence increases with age and unlike other CNS tumours, incidence rates remain high post-85 years (33). Despite lower incidence rates at a younger age, in children, meningiomas are usually malignant and have a higher risk of recurrence (21). In adults, there is a clear bias towards females with an incidence rate of 2.32 times higher for non-malignant and 1.12 times higher for malignant meningiomas compared to males, suggesting a potential role of sex hormones in meningioma development (33). Although there is no clear evidence reinforcing this hypothesis, a high percentage of meningiomas were shown to express progesterone receptors (~88%), oestrogen receptors (~40%), and androgen receptors (~40%) (37). However, hormone therapy has failed to provide any clinical benefit (21,38). Nevertheless, meta-analyses have revealed an increased risk of meningiomas following hormone replacement therapy (21,37).

Ionising radiation (IR) is an environmental risk factor for meningioma. Individuals exposed to ionising radiation have a 6-10 fold higher risk to develop meningioma, for both low and high-dose IR (21). In addition, patients with radiation-induced meningiomas have an increased risk of developing high-grade meningiomas as well as high recurrence rates.

1.2.5 Clinical presentation

Many meningiomas have a slow growth rate and are rarely invasive, causing them to frequently remain asymptomatic. Consequently, these tumours are often incidentally discovered during medical investigations (computed tomography (CT) and magnetic resonance imaging (MRI)) of unrelated symptoms (39,40). Asymptomatic patients are closely monitored by frequent clinical and radiological follow-ups to detect tumour growth and the development of symptoms (41). Symptomatic meningiomas present with a wide range of symptoms, typically similar to symptoms associated with gradually increasing cranial pressure, including headaches, seizures, neurological deficits (38). Symptoms are dependent on the tumour's location, size, and invasive nature towards adjacent neurological tissues.

1.2.6 Recurrence and survival

The WHO grading system correlates grade with the risk for recurrence and overall survival (21). WHO grade I meningiomas have an overall survival (OS) of 80-90% and progression-free survival (PFS) of 75%-90%, WHO grade II have an OS of approximately 50-79% and PFS of 23%-78%, and WHO grade III meningiomas have an OS of approximately 14-34% and PFS of 0% (3,42). High grade meningiomas are more aggressive and have a higher recurrence risk. However, despite their benign nature, approximately 20% of benign meningiomas tend to recur (30). Atypical grade 2 meningiomas have an approximately 8-fold increased risk of recurrence and a slight, but significantly increased risk of mortality, over WHO grade 1 meningiomas (42,43). Anaplastic WHO grade 3 meningiomas demonstrate the highest risk for recurrence with approximately 50-94% (42,44). Variable recurrence rates are found between high-grade meningiomas based on location. High grade meningiomas at the skull base were found to have lower recurrence rates and better overall prognosis compared to similar tumours at the convexity (45).

The risk of recurrence is strongly associated with the degree of surgical resection. This resection is described by the Simpson grade. Simpson grading ranges from grade 1 to 5, whereby grade 1 indicates total resection and a higher number indicates the degree of incomplete resection and higher grade is associated with an increasing risk of recurrence. For example, WHO grade 1 tumours with any atypical features are at increased risk of recurrence when Simpson grade 1 resection is not reached (30,43). A study comparing 5-year survival of non-malignant brain tumours found meningioma as the third lowest, with a 5-year survival of 88.0%. Survival rates are also influenced by the site of occurrence. For malignant as well as non-malignant meningioma, the 10-year survival rate was higher for tumours in the spinal meninges compared to cerebral meninges (33).

1.3 Meningioma genetic landscape and molecular alterations

Over the last decade, the emergence of high-throughput sequencing techniques, such as next-generation sequencing (NGS), have elucidated the genetic landscape and molecular alterations of meningiomas. Genomic analysis has identified that, compared to other solid tumours, the meningioma genetic landscape is relatively simple with several common alterations (6,29) (Fig. 1.3).

The most common and well-known genetic alteration associated with meningioma is the loss of the tumour suppressor gene *Neurofibromatosis 2* (NF2; 22q12) (5,29,46). NF2 mutations are found in approximately 60% of meningiomas and occur across all grades (29,47). NF2-mutated meningiomas typically occur at the brain convexity and are often associated with a transitional or fibroblastic subtype (6,29). Furthermore, NF2 mutations are largely mutually exclusive with other frequent mutations, broadly dividing the mutational landscape into NF2 or non-NF2 mutated meningiomas (5). NF2 encodes for the membrane-cytoskeleton scaffolding protein, *Merlin*, which is involved in the regulation of several important pathways including the mammalian Hippo, PI3K/mTORC1/Akt, and mitogenic signalling pathways (5). Germline mutations of NF2 are strongly associated with the dominantly inherited genetic disorder NF2-related schwannomatosis (previously termed Neurofibromatosis 2). This disease is characterised by the presence of multiple tumours of the CNS, including meningiomas (48). Additionally, an aberration in the NF2 gene is the most frequent mutation detected in sporadically occurring meningiomas (11).

Other genes that are frequently mutated and associated with meningiomas include TRAF7 (tumour necrosis factor (TNF) receptor associated factor 7) (7,49), AKT1 (AKT serine/threonine kinase 1) (7,49), KLF4 (Krüppel-like factor 4) (7,49), SMO (smoothened) (7,49), POLR2A (RNA polymerase II) (8), PIK3CA (phosphatidylinositol-4,5-biphosphate 3-kinase catalytic subunit α) (7,9,49), BAP1 (BRCA1 associated protein 1) (50,51), SMARCB1 (switch/sucrose nonfermentable-related matrix-associated actin-dependent regulator of chromatin subfamily B member 1) and SMARCE1 (switch/sucrose nonfermentable-related matrix-associated actin-dependent regulator of chromatin subfamily E member 1) (10,29,46). TRAF7 is mutated in approximately a fifth of non-NF2 mutated sporadic meningiomas. TRAF7 mutations are mutually exclusive from NF2 mutations but are frequently mutated together with AKT1 or KLF4 (5). AKT1 mutations are found in approximately 10% of non-NF2 mutated meningiomas and cause AKT1 to be constitutively active independent of its activation through PI3K signalling. Likewise, mutations in KLF4, which is an important regulator of proliferation, also result in activation of the protein, increasing proliferation rates and thus, tumour growth. Even though both AKT1 and KLF4 are frequently co-occurring with TRAF7, they are mutually exclusive of each other (5). TRAF7, KLF4 and AKT1 mutations are typically found in WHO grade 1 tumours. Moreover, TRAF7 and KLF4 mutations are associated with secretory meningiomas, while AKT1 mutations are frequently found in meningothelial and transitional meningiomas (6,29). Mutations of SMO, a member of the sonic hedgehog (SHH) signalling pathway, are exclusively found in grade 1 meningiomas and typically occur in anterior skull base meningiomas (5). SMO mutations are commonly found in meningiomas of the meningothelial subtype (29). Although SMO mutations are relatively rare, 3-6% of non-NF2 mutants, this mutation is one of the few targetable mutations in meningiomas (5). Another potentially targetable molecular alteration in meningioma is the PIK3CA mutation, which is found in 4-7% of meningiomas (5). Most PIK3CA mutated meningiomas occur at the skull base and are associated with meningothelial or transitional histology (29). Mutations in POLR2A have been identified in approximately 6% of grade 1 meningiomas and are typically found in anterior skull based meningiomas of meningothelial subtype (5). BAP1 mutations are frequently occurring in WHO grade 3 rhabdoid meningiomas, and BAP1 mutation status has been shown to stratify rhabdoid tumours into aggressive and less aggressive forms (29). Several mutations in components of the Switch/sucrose non-fermentable (SWI/SNF) chromatin remodelling complex have been associated with meningioma formation, particularly high grade meningiomas (5). For instance, germline SMARCB1 mutations are found in several families with multiple meningiomas, but also in a small subset of sporadic meningiomas, usually co-occurring with NF2 mutations. In addition, SMARCE1 mutations, another member of the SWI/SNF complex, are associated with atypical meningiomas, particularly clear cell meningiomas (5,29). Furthermore, mutations in telomerase reverse transcriptase (TERT) gene promoter and CDKN2A are very rare in meningiomas and are associated with aggressiveness and high-grade meningiomas. In the definition of the 2021 WHO classification of CNS tumours, TERT promoter mutations and CDKN2A homozygous deletion have been included as stand-alone criterium for WHO grade 3 (11). Interestingly, TERT promoter mutations have only been detected in secondary atypical meningiomas that progressed from WHO grade 1 primary tumours and have thus been suggested as a marker to predict recurrence and tumour progression (11,52). Moreover, in 2002, Perry *et al.* identified the association between loss of chromosome 9p21 and malignant progression from grade 2 to grade 3 meningiomas (53). In addition, meningiomas carrying these mutations are associated with increased recurrence risk and shorter progression time (54). Furthermore, CDKN2A status, as well as CDKN2B status, was confirmed as highly prognostic for meningioma grading in a dataset of 528 meningioma patients with follow-up data (54).

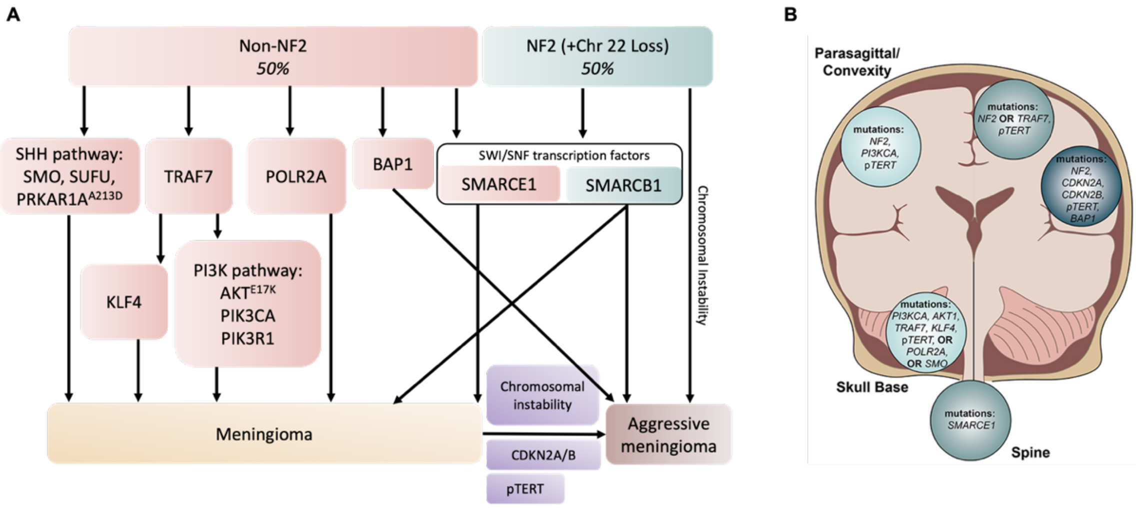

Figure 1.3 Mutational landscape of meningioma and their associated anatomical location

A) Schematic overview of mutations underlying meningioma: Mutations mutually exclusive with NF2 are shown in red, mutations associated with NF2 in green and pTERT mutations and CDKN2A/B homozygous deletion underlying progression to aggressive meningiomas in purple. Adapted from Robert *et al*. (55). B) Molecular aberrations and their associated brain regions. Adapted from Al-Rashed *et al.* (4).

1.4 Methylation profiling

The most recent addition to the characterisation of the meningioma genetic landscape is the identification of six clinically relevant DNA methylation classes (MC) (11,56). Analysis of DNA methylation data segregated meningiomas in two epigenetic groups: A and B, which were further divided into MC benign-1, MC benign-2, MC benign-3, MC intermediate-A, for group A, and into MC intermediate-B, MC malignant, for group B, resulting in 6 DNA methylation classes (fig. 1.4) (56). Classification based on methylation classes was found to more accurately predict WHO grade 1 patients at high risk of disease progression, and WHO grade 2 patients at lower risk of recurrence and to more accurately predict PFS compared to the WHO grading system (11,56). For example, WHO grade 1 patients that were characterised as MC-intermediate had a worse prognosis compared to patients that had a WHO grade 2 meningioma but were characterised as MC benign, while grade 1 MC intermediate patients seemed to have a similar prognosis as WHO grade 2 patients (11).

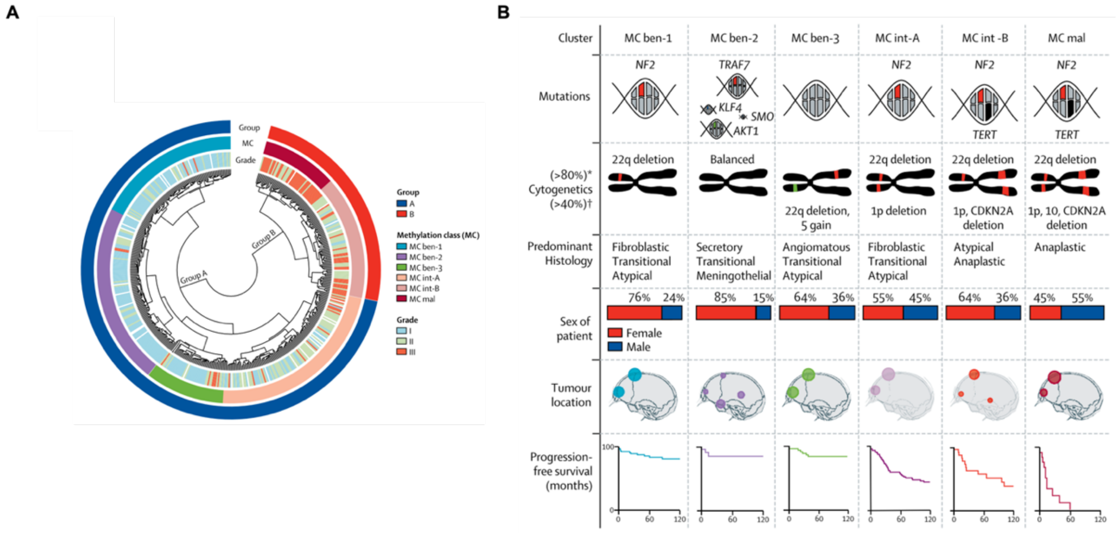

Figure 1.4 Methylation classes of meningiomas A) Sahm's unsupervised hierarchical clustering of 497 meningioma samples identified two distinct groups of meningiomas: group A and group B, which were further divided into 4 methylation classes (MC ben-1, MC ben-2, MC ben-3 and MC int-A) in group A and 2 methylation classes (MC int-B, MC mal) in group B. abbreviations: MC = methylation class, ben = benign, int = intermediate, mal = malignant. B) Overview of the six clinically relevant methylation classes and their molecular and clinical characteristics. Adapted from Sahm et al. (56)

1.5 Meningioma Intra-tumour heterogeneity

Within meningiomas, particularly high-grade 3 meningiomas, distinct genomic and histological features can be identified within one tumour (57). This is called intra-tumour heterogeneity. This feature complicates grading based on genomic characteristics because regional sampling could influence tumour grading. Furthermore, intra-tumour heterogeneity has been demonstrated to significantly impact the efficacy of cancer treatments by causing resistance, as therapies only affect sensitive clones conferring an advantage to insensitive subclones that can escape therapy (58). A paper studying intra-tumour heterogeneity in meningiomas compared RNA sequencing data of spatially distinct samples within meningiomas and characterized gene expression variance in principal component space (17). Interestingly, they found that most samples from each meningioma clustered together but that heterogeneity was evident for high grade meningiomas. Similar results were obtained when comparing DNA methylation profiles. Additionally, they assessed heterogeneity within the copy number variant (CNV) profile of meningiomas and found an increased number of CNVs as well as increased variance of CNVs per sample in high-grade meningiomas. Using the data on distribution of CNVs, the authors were able to generate phylogenetic trees and demonstrate that chromosome alterations are an early event in meningioma development and underlie transcriptomic and epigenetic signatures in high-grade meningiomas (17). This feature of high grade meningiomas has consequences for prognostic models of meningiomas which have been developed to identify samples at risk for recurrence. Particularly, since most of these prognostic models have been derived from clinical data taking one sample per tumour. Furthermore, it suggests that particularly high-grade meningiomas would benefit from multi-faceted therapy's such as combination therapy, to target several subclones within a spatially distinct tumour.

1.6 The immune microenvironment of meningiomas

The tumour immune microenvironment (TIME) comprises all immune components of a tumour, including immune cells and cytokines. The interaction between these immune components and the tumour cells significantly impacts tumour behaviour and has been associated with tumour progression, aggressivity and therapy resistance (59,60). Unlike other brain tumours, meningiomas are located outside the blood-brain barrier, making these tumours easily accessible for infiltrating immune cells (61). Recently, Nassiri et al. suggested a new molecular classification of meningiomas based on a unified analysis of multiple datatypes including genomic, transcriptomic and proteomic datasets and identified a specific molecular subtype of meningiomas associated with high immunogenicity, indicating a role for the immune system in meningioma pathology (62). The TIME of meningiomas is diverse and consists of myeloid cells, lymphocytes including T-cells (predominantly CD8$^+$), natural killer (NK) cells and to a lesser extent B-cells and T regulatory (T-reg) cells (61,63). Of these, macrophages comprise the largest population of infiltrating cells (approximately 18% of all cells in meningioma tissues), and this infiltration has been shown to increase with tumour grade (64). A study by Proctor *et al.* showed that ~80% of these tumour-associated (TA)-macrophages were of the immunosuppressive pro-tumour M2 subtype (64). Besides macrophages, CD8+ T cells were shown to represent the largest population of infiltrating lymphocytes in meningiomas (63). Interestingly, the mutational profile of meningiomas has been correlated to influence specific immune microenvironmental signatures (61). For example, WHO grade I meningiomas that harboured NF2 mutations were found to have higher levels of infiltrating CD163-positive M2 macrophages compared to meningiomas that were mutated for AKT1 (65). Additionally, meningiomas with TRAF7 mutations were shown to have increased expression of immune checkpoint molecules, including programmed death ligand 1 (PD-L1) compared to non-TRAF7 mutated tumours (66). PD-L1 and its receptor PD-1 are involved in immune regulation and its upregulation has been associated with evasion of the immune system in several malignancies. These findings demonstrate the importance of the immune microenvironment in meningioma pathology and form the basis of evidence supporting immunotherapy in meningiomas. Indeed, clinical trials of checkpoint inhibitors are currently under investigation.

1.7 Treatment strategies

Current treatment strategies for meningiomas are limited to surgical resection and radiotherapy. However, the expanding knowledge on the molecular landscape of meningiomas holds promise for the discovery of novel, effective therapeutic targets. Furthermore, improved classification and stratification could provide more reliable results on effectiveness in clinical trials on treatments targeting specific molecular backgrounds (41).

1.7.1 Active surveillance

Small (tumour diameter ≤3 cm), asymptomatic meningiomas are actively monitored for tumour growth and symptom development. Patients are evaluated by MRI 12-monthly intervals after the tumour is first discovered. The European Association of Neuro-Oncology (EANO) advises that this interval can increase to annual check-ups if the patient remains asymptomatic. After 5 years, this interval can be increased. However, if patients develop symptoms or substantial tumour growth is detected, active therapy is advised (41).

1.7.2 Surgical resection

For symptomatic patients, the primary treatment option is surgical resection (41). However, surgery is an invasive high-risk intervention. Post-operative complications such as cerebral haemorrhage, infections, neurological deficits, and brain oedema can leave patients with life-impacting morbidities (41,47). Risk factors include patient age and overall fitness, tumour size, location, and accessibility. In addition to risk factors, clinical symptoms are assessed prior to surgery (25,41). Although surgical resection is curative for most, particularly benign, meningiomas, risk of recurrence is high (25). Risk of recurrence is lowest when gross total resection (GTR) can be achieved (Simpson grade 1). In the case of subtotal resection (STR), adjuvant radiotherapy may be given to treat the residual tumour mass especially in higher grades (41).

1.7.3 Radiotherapy

Radiotherapy is offered as primary therapy to patients that can’t have surgery due to inaccessibility and/or their proximity to vital structures, or as adjuvant therapy after surgical resection (6). The purpose of adjuvant radiotherapy is to lower the risk of recurrence and improve local control of the tumour (6). Adjuvant radiotherapy is the standard of care therapy for WHO grade 3 meningiomas and is shown to improve the 5-year progression-free survival (PFS) rates from 28% to 57% (67). Since radiotherapy has been associated with many side effects, including alopecia, double vision, headaches, seizures, brain oedema, epilepsy, neurological deficits and even radio-induced meningiomas, the effectiveness of adjuvant radiotherapy in WHO grade 2 meningiomas remains controversial. Especially, in cases of gross total resection (GTR), it remains unclear whether the benefit of radiotherapy outweighs these side effects (6,67). However, adjuvant radiotherapy has been shown to improve overall PFS rates of WHO grade 2 meningiomas after subtotal resection (STR). In WHO grade 1 tumours, adjuvant radiotherapy is exclusively recommended after STR at low dose (6,41,67). Different radiotherapy approaches can be offered including conventional radiotherapy, stereotactic radiosurgery (SRS) and external beam radiotherapy (EBRT).

1.7.4 Systemic therapy: traditional chemotherapy and targeted therapy

Systemic therapy for meningiomas is largely experimental and has shown limited effectiveness in the clinic (6). It is used rarely and on a case-to-case basis, primarily in patients who can’t be treated with surgery and radiotherapy, often recurrent or progressive meningiomas (41,67). There is a variety of drugs approved for the treatment of aggressive meningiomas, including alkylating agents, tyrosine kinase inhibitors and endocrine drugs, however, the clinical effectiveness of their use remains disappointing (41). The RNA reductase inhibitor hydroxyurea (HU) has shown some modest benefits (40). HU is sometimes used as adjuvant therapy in recurrent or incompletely resected tumours and although it was found to prevent some patients’ tumours from progressing, it did not result in decreased tumour size (41,68,69).

The advances that were made in the understanding of the molecular landscape of meningiomas has identified some promising targets for treatment (40,41). Currently, there are several targeted compounds being investigated in clinical trials. For NF2-related meningiomas, a promising trail platform, which was launched in 2020, is the INTUITT-NF2 (Innovative Trial for Understanding the Impact of Targeted Therapies in NF2) trial (NCT04374305). This multi-arm phase 2 platform is currently investigating the effectiveness of two tyrosine kinase inhibitors called Brigatinib and Neratinib.

Another prospective therapy currently in clinical trials is the use of vascular endothelial growth factor (VEGF) receptor (VEGFR) inhibitors. VEGF is important for the formation of new blood vessels and is highly expressed in vascularised meningiomas (11). Furthermore, upregulated mTOR signalling was associated with meningiomas, which led to several ongoing clinical trials investigating mTOR inhibition and inhibition of related downstream signalling components e.g. PI3K/AKT and MEK signalling (11). In addition, the increasing understanding of the importance of the TIME, has highlighted the use of immunotherapies for the treatment of meningiomas. As such, immune checkpoint inhibitors are currently under investigation (6,40,70).

1.7.4.1 TAM receptor family of tyrosine kinases inhibitors

A novel treatment strategy for meningiomas still in the preclinical stage is targeting the Tyro3, Axl, MERTK (TAM) receptor family of tyrosine kinases inhibitors. TAM receptors are aberrantly expressed in several cancers (71), including breast cancer (72), ovarian cancer (73), glioblastoma (74), colorectal cancer (75), and schwannomas (76) and receptor activation has been associated with promoting survival, chemoresistance and cell motility (71). Signalling is activated by ligand binding (e.g. Gas6 and vitamin K-dependent protein S), which leads to receptor dimerization and autophosphorylation of the receptor. Cancer cells typically co-express high levels of TAM receptors and their ligands, which results in auto-signalling (71,77). The downstream cascade that follows is cell-dependent and can go through the oncogenic MEK/ERK, PI3K/AKT, JAK/STAT or NFkB signalling pathways, as well as anti-apoptotic signalling (77) (fig. 1.5). Moreover, TAM receptors have been associated with promoting migration and invasion through the activation of Snail and Slug, which are known to induce epithelial-to-mesenchymal transition (EMT) (77). Preclinical studies targeting TAM receptors have shown promising results for several cancers (71,73–75,78). Apart from targeting cancer cells directly, TAM receptor inhibition also has been shown to affect the TIME (77,79). Therefore, it is suggested that TAM inhibition can concomitantly target the tumour directly, as well as target the TIME (71,79). Unpublished work by our research group has identified aberrant expression and activation of all three TAM receptors in meningiomas and investigations into the role of TAM receptors in meningioma pathology are ongoing.

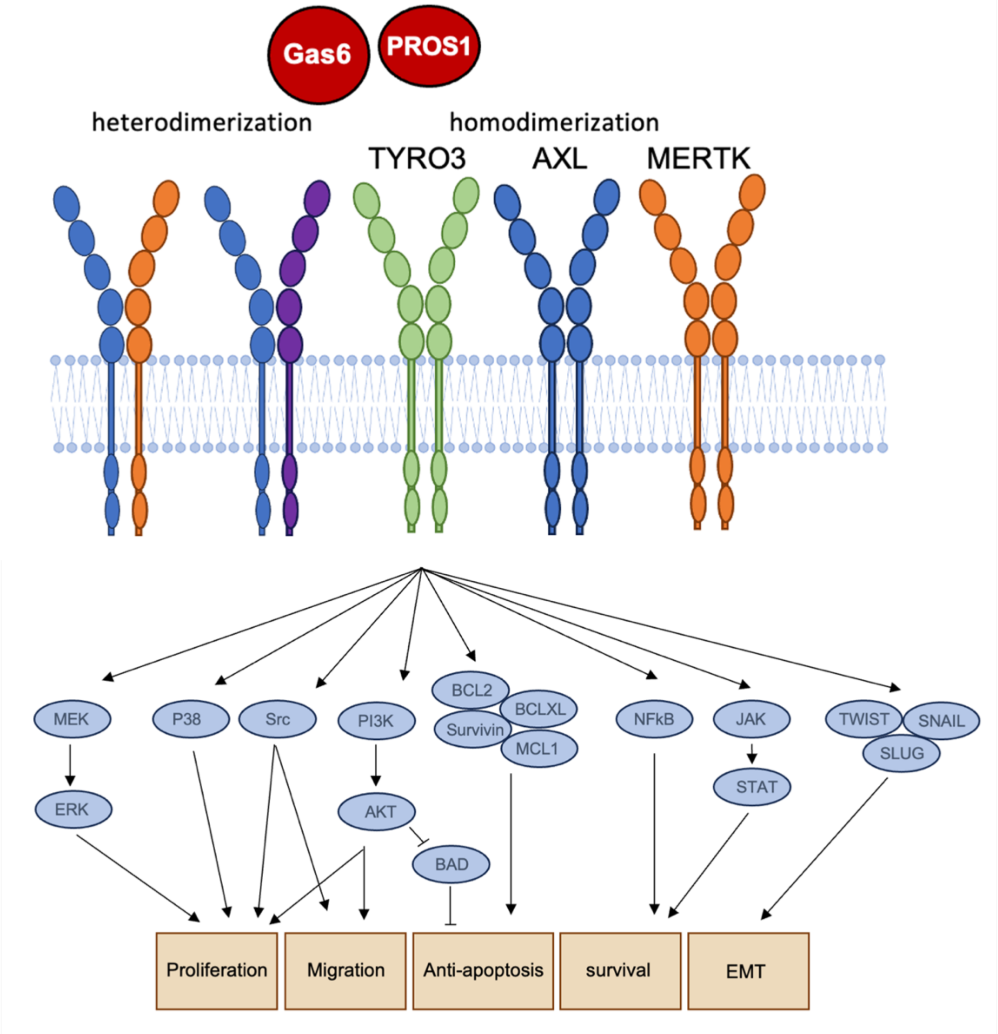

Figure 1.5 Schematic diagram of TAM receptor family of tyrosine kinase activation and downstream signalling pathways TYRO3, AXL and MERTK are activated by ligand binding (Gas6 and PROS1), and homophilic and/or heterophilic receptor dimerization of two TAM receptors or with another tyrosine kinase receptor (purple). Receptor activation activates downstream signalling of oncogenic MEK/ERK, P38, Src, PI3K/AKT, JAK/STAT or NFkB, as well as anti-apoptotic signalling (BCL2, BCLXL, MCL1, Survivin, BAD) and activation of EMT transcription factors (Twist, Slug, Snail), leading to proliferation, migration, anti-apoptosis and survival (60).

1.7.4.2 HDAC inhibitors

Another novel anti-meningioma therapy still in the preclinical phase, is histone deacetylase (HDAC) inhibition. HDACs are a group of chromatin remodelers, that regulate the accessibility of chromatin by modifying histone proteins, as a way of controlling gene expression. This group of epigenomic modulating enzymes has been shown to be upregulated in neoplastic cells (80,81). Specifically, HDACs control gene expression by catalysing the deacetylation of lysine residues from histones or non-histone proteins (fig. 1.6). Lysine residues carry a positive charge which is neutralized when it gets acetylated. Removal of the acetyl group counteracts this neutralisation, which then results in the tight conformation of the negatively charged DNA to the positively charged lysine residues. This causes a closed chromatin structure and repression of gene expression (80). These molecules function together with a group of enzymes called histone acetyltransferases (HATs), which are responsible for the opposite process. HDAC inhibitors have been shown to activate the transcription of several genes through chromatin remodelling, which partly caused their anti-cancer effects (82). Nevertheless, besides this direct effect on chromatin remodelling, HDAC inhibition can also directly mediate growth inhibition and apoptosis in cancer cells by removing acetylation of non-histone proteins (80,82,83). Their potential for the treatment of meningiomas became apparent from the results of Tatman *et al.* (84) that performed a high-throughput screening of epigenetic drug compounds. This screen revealed that compounds targeting HDACs were most potent to significantly inhibit meningioma growth, highlighting HDAC inhibitors as promising therapeutics. In addition, an earlier study using the HDAC inhibitor AR-42 showed suppression of proliferation and induction in cell-cycle arrest at G2 and apoptosis after AR-42 treatment in primary meningioma cells, which they could link to a dose-dependent decrease of phospho-AKT (85). AR-42 is currently in clinical trials and the moderately positive results of two early-phase clinical studies in NF2-associated meningiomas were published in 2021. These studies showed mixed results but with the majority of tumours decreasing in volume (86). Even though the efficacy of AR-42 was specifically studied in the context of NF2-mutated meningiomas, the results of Kawamura et al. (81) demonstrated the sensitivity of the NF2-intact high-grade meningioma cell line IOMM-Lee to HDAC inhibition. Currently, there are 4 HDAC inhibitors approved by the FDA for treatment of cutaneous T-cell lymphoma and multiple myeloma. These include Vorinostat, Romidepsin, Belinostat and Panobinostat and several others are in ongoing clinical trials, including the pan-HDAC inhibitor Trichostatin-A (NCT03838926) (87,88).

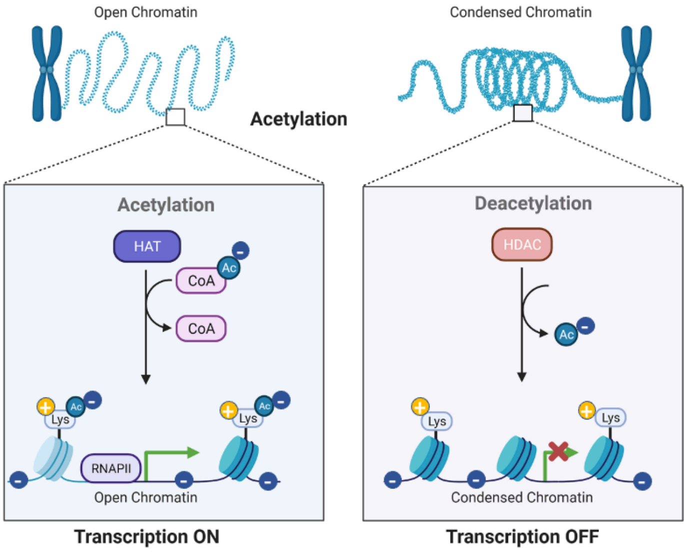

Figure 1.6 The mechanism of histone acetylation and histone deacetylation

The chromatin remodelling enzymes HAT and HDAC control gene expression by catalysing the acetylation (HAT) or deacetylation (HDAC) of lysine residues from histones, resulting in a change in the lysine charge. This leads to an open or condensed state of the chromatin turning transcription ON (gene expression) or OFF (gene repression). Adapted from Hai et. al (89).

1.7.4.3 Combination therapy

Targeted therapy using a combination of two or more drugs has the potential to substantially improve the efficacy of treatment (90,91). Indeed, this approach has proven successful for several cancers and a variety of combinations have been approved by the FDA (92). The basic principle of combination therapy is that drug combinations address tumour heterogeneity, by targeting different pathways and/or proteins while concomitantly interacting in a synergistic or additive manner (90). In addition, combination therapy can counteract crosstalk and feedback loops that occur between different pathways (93). A combination of drugs is synergistic when the total effect of the combination is greater than the sum of the individual effects of each drug. When the total effect of the combination is equal to the effect of the sum of the individual effects of each drug they function in an additive manner. When the total effect of a combination of drugs less than the sum of the individual effects of each drug, the interaction of the two drugs function in an antagonistic manner (94). The interaction of the mutual effect of two drugs can be represented in an isobole graph, in which the doses of the two drugs are represented on both axes whereby the curve depicts the dose-pairs that, when combined, achieve the desired effect (e.g. IC_{50} or EC_{50}) (Fig. 1.7) (94). When two drugs interact synergistically, their therapeutic dose can be lowered to achieve the same effect as what was needed for monotherapy, or drugs can be administered in the same as the monotherapy but reach a greater effect. In the former, the risk of severe toxicity and side effects is reduced, especially when different pathways are targeted (90). In addition, using combination therapy reduces the chance of developing resistance since combination therapy is more effective and already targets multiple signalling pathways, complicating therapy evasion by recruitment of alternative signalling pathways (90). A newer approach in combination therapy also considers the timing of drug administration using one drug to sensitize cancer cells to another drug. This approach benefits from the differences between non-cancerous and cancerous cells. For example, treating cells with a low dose of a DNA-damaging agent will result in G1/G2 cell cycle arrest in non-cancerous cells. In cancer cells with deregulated cell cycle control, cell cycle arrest is not induced. This difference can then be exploited by administering a second drug which only targets cells in mitosis, and thus only targets cancer cells (90,95).

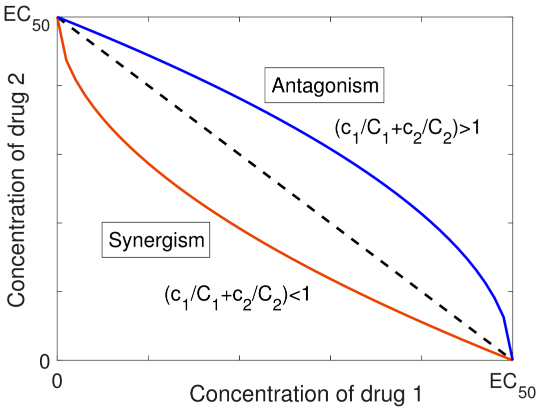

Figure 1.7 Isobole graph for drug combination synergism, antagonism and additivism The interaction of the mutual effect of two drugs can be represented in an isobole graph, in which the doses of the two drugs are represented on both axes and the curve depicts the dose pairs that, when combined, achieve the desired effect. The interaction is synergistic (red line), additive (dashed line), antagonistic (blue), when the total effect of the combination is greater (synergy), equal (additivism), less (antagonism), than the sum of the individual effect of each drug. Adapted from Vakil & Trappe (94).

For the treatment of meningiomas, few combination therapies have been tested in clinical trials. A phase II clinical trial tested the combination of the VEGF inhibitor bevacizumab with the mTOR inhibitor everolimus for the treatment of recurrent and progressive meningiomas of all grades after first-line treatment of surgical resection or radiotherapy. Although combination therapy did not result in any tumour shrinkage, the combination therapy resulted in a prolonged progression-free survival of 22 months, with a slight advantage for high-grade tumours compared to WHO grade I tumours (96). However, treatment was discontinued for four patients due to toxicity, which demonstrated the unsuitability of this combination strategy for long-term treatment. Another phase II study using everolimus in combination with the somatostatin agonist octreotide for the treatment of progressive meningiomas of all grades revealed effective antitumour activity in aggressive meningiomas (10 grade II and 8 grade III of a total of 20 patients). The median progression-free survival was 6.6 months and long-term tumour growth control (>2 years) was observed in 3/20 patients (97).

HDAC inhibitors have been shown to synergistically interact with a range of compounds, which makes them very suitable for use in combination strategies. Hence, combination therapy of HDAC inhibitors with various anti-cancer agents has demonstrated promising results in preclinical and clinical anti-cancer studies (81,98). Indeed, Kawamura *et al.* (81) demonstrated the potency of HDAC inhibition in combination with oncolytic herpes simplex virus (oHSV) therapy for the treatment of malignant meningioma by showing an increased intratumoral oHSV replication which controlled the growth of human meningioma xenografts. Moreover, one of the targeted therapies that have been shown to benefit from combination with HDAC inhibition in other cancers is the inhibition of receptor tyrosine kinases (98–101). For meningioma, this combination is not yet studied although monotherapy of both HDAC inhibition and receptor tyrosine kinases show promising results, as described in section 1.4.4.1 and 1.4.4.2. Hence, the avenue of studying a similar combination is discussed in this thesis.

1.8 Preclinical models for translational meningioma research

Translational cancer research heavily relies on the use of accurate pre-clinical tumour models to understand the role of genetic alterations and to investigate their influence on tumour biology, as well as evaluating the toxicity and efficacy of promising therapeutics. These models, varying from *in vivo* animal models to *in vitro* cell culture models, aim to resemble the function and processes of the tissue of interest and ultimately lead to experimental discoveries that can be translated into practical clinical applications (102,103). The lack of sufficient predictive power of these models remains a large obstacle in the development of therapies (104). This section will summarise the most common pre-clinical models and give an overview of their availability for meningioma research.

1.8.1 *in vivo* animal models

In vivo animal models are widely used in biological research. They have anatomical and physiological characteristics similar, but not identical, to humans which allows scientists to assess the effect of novel therapies in the context of a highly complex microenvironment (16). Genome editing allows these models to be modulated specifically for the researcher's requirements, making them useful for disease modelling. In addition, animal genomes share high similarity with the human genome and they generally have similar ageing patterns which enable researchers to study disease progression over the typically shorter lifetime of the animal (105). Examples of animal models that are commonly used in cancer research are the nematode *Caenorhabditis elegans (C.elegans)*, the fly *Drosophila melanogaster*, the frog *Xenopus*, Zebrafish, rabbits, mice, rats, dogs and rhesus macaque. Of these, mice and rats are the most commonly used (105).

Animal models can model tumour formation by *de novo* generation of cancer by using genetically engineered animals that have been bred to have germline mutations linked to tumour formation. These models are based on spontaneous tumour formation and have the advantage that they model all steps of tumour formation and maintain a functional immune system (16). Additionally, xenograft models, in which immunodeficient-mice are subcutaneously or orthotopically injected with cell lines or patient-derived tumour material to generate a tumour, are particularly suitable for modelling tumour development. However, these models are accompanied by several complicating factors such as limited presence of the immune microenvironment, limited availability and accessibility, high costs, requirement of high expertise levels and strict ethical control (102). Moreover, establishment of both these models can take up to many months, especially for genetic models, and do not account for differences between animal and human biology (106). These characteristics limit their therapeutic value and explain that successful pre-clinical testing in animals rarely translates into successful therapies (102,103,107).

Over the years, a limited number of animal models for meningioma have been successfully established. The first model using animals in meningioma research was a heterotopic transplantation of human meningioma cells using guinea pigs. However, only 1 out of 5 of the injected guinea pigs developed a tumour (108). Later in 1977, benign human meningioma cells were successfully implanted into mice and the xenograft that was developed showed morphology similar to the original human tumour (108,109). This heterotopic model has been further refined and showed success when injected into the subrenal capsule of nude mice (110). The first orthotopic xenograft model of meningioma was established using the meningioma cell line IOMM-Lee and first-passage primary cell cultures from human meningiomas. However, the tumours established from this model displayed several growth characteristics that are unusual in human tumours (111). Later, this model was adapted using human tumour cells that were immortalized, which generated tumours that retained the growth patterns and morphological features of grade 1 meningiomas (108). For xenograft models to be successful, the mice must be immunocompromised to allow the cells to establish and form a tumour (15). Therefore, they can't be used to model the influence of the immune microenvironment. Genetically modified mouse models overcome this problem and for meningioma several genetically modified models have been generated to model meningioma initiation (108). Conditional NF2 inactivation by direct injection of the recombinant Cre adenovirus system into the CSF of $NF2^{loxP/loxP}$ mice allowed for tissue-specific inactivation in leptomeningeal cells, which resulted in the development of meningiomas of various benign subtypes in 30% of these mice (108,112). Later, the Kalamarides group further optimized this Cre-loxP system by using the prostaglandin D synthase promoter to drive Cre expression exclusively in arachnoidal cells (26). However, the time to tumour formation is long and mice have to grow old to show tumours, which complicates their use in drug testing studies (26).

1.8.2 *In vitro* cell culture models

In vitro cell-based models have been used for a long time and have contributed tremendously to our general knowledge of cell biology and cancer (16). The most widely used technique is two-dimensional (2D) culture of immortalised cell lines. Traditionally, cell lines are grown as homogeneous cell populations in flat monolayers attached to plastic (treated to accommodate cell adhesion) or glass culture dishes (113). Cells are propagated in controlled conditions with optimal growth medium which typically allows for a large population of proliferating cells that can grow indefinitely (114). To allow for space and prevent competition for nutrition, cells are sub-cultured or passaged to continue their propagation. This model benefits from its simplicity, accessibility and reproducibility and constitutes a useful resource for identifying molecular mechanisms due to the large amount of cell lines available, their mostly well-defined molecular background and easy-to-manipulate nature (115). Nevertheless, cell lines are over-simplified models that are losing attraction since they do not resemble tissue organization and the tumour microenvironment (TME). The composition and proportion of the TME have been shown to contribute massively to cell behaviour in the tumour and should thus be considered when studying cancer *in vitro* (16,102,116). Moreover, immortalized cell lines typically consist of a clonal homogenous cell population that has been modified by introducing an immortalising gene such as hTERT (115). These cells have been cultured for generations which may introduce bias in their genetic, epigenetic and physiological characteristics (117). Hence, they do not adequately represent the original tumour nor the multicellular nature of tissues. This can be overcome by using primary patient-derived cells. These models offer more clinical relevance compared to immortalized cell lines. However, this approach has its own limitations, since primary cells have a limited availability, life span, possess less flexibility and display more heterogeneity (115,117). In 2D cell culture, cells are attached to rigid plastic or glass surfaces, which, unlike most *in vivo* substrates, deforms the cells into flat and elongated shapes as a result of high tensile strength and mechanical resistance (117). Consequently, the mechanosensory machinery in the cells senses these high mechanical forces of the stiff substrates, which leads to cytoskeleton remodelling and changes in signalling pathways (16). In addition, these substrates only allow the cells to expand in a bilateral way, resulting in a cell monolayer (116,118). Consequently, cells are exclusively in contact with the treated plastic, directly neighbouring cells, and the cell culture medium, whereas cells are normally surrounded by other cells and/or extracellular matrix (ECM) in tissues. It has been shown that the composition of the ECM produced by cancer cells *in vitro* is highly dependent on the culture method and that the ECM composition strongly influences cell signalling by exposing cells to ligands that can bind cell surface receptors (16). Altogether, these limitations of 2D cell culture are reflected by low success rates for the development and approval of new drug therapies of compounds validated in 2D cell models (117,119). This demonstrates a translational gap between *in vitro* and *in vivo* results. Recently, despite the immense contribution 2D cell culture has made in unravelling the complexity of cell biology, a shift towards the use of three-dimensional (3D) cell culture models has been taking place (Fig. 1.6) (120).

1.8.3 Advantages of 3D cell culture models over 2D cell culture models

Many types of *in vitro* 3D cell culture models have been developed and are rapidly gaining interest due to several advantages these models provide over 2D monolayer models (Fig. 1.8) (96). Firstly, 3D cell culture allows cells to retain their natural shapes and grow in multiple cell layers which preserves cell-cell and cell-matrix interactions (118). These interactions influence important cellular processes including morphology, adhesion, differentiation, proliferation, viability, gene expression (113,118,121). In addition, the multi-layered shape of a 3D model introduces a nutrient gradient, whereas cells in 2D cultures can uniformly access factors in the growth medium. The layered structure of 3D models causes the formation of three distinct layers as a result of the decreasing access to nutrients and oxygen: a proliferating peripheral cell layer, an intermediate quiescent cell layer and a necrotic inactive core (118). These layers resemble those found in tumour tissues, where cells situated further away from blood vessels are less actively proliferating (122). Inherently, cells in the outer core are also differently exposed to drugs and other external compounds, in comparison to cells in the inner core. This provides a more accurate representation of drug kinetics (113,123). Overall, 3D models, in contrast to 2D models, better resemble *in vivo* physiological conditions with respect to: cellular architecture, hierarchy and heterogeneity, cell-cell and cell-matrix interactions, protein and gene expression levels, drug exposure and metabolic gradients (124–126). The implementation of 3D cell culture technology has beneficially impacted the adequacy of drug developmental studies and has served to bridge the gap between *in vitro* and *in vivo* results. However, 2D cell culture is cheaper than using 3D cultures, especially in large-scale studies (118). Moreover, 3D cell culture often takes more time and analysis can be complicated and thus requires expertise (117). Although costs are reducing, for now 3D models are not fully replacing traditional 2D cell culture models. Instead, they can serve as additional step to smoothen the transition from *in vitro* cell culture to *in vivo* studies, by generating a more refined list of potential drug compounds before transitioning to *in vivo* testing and thereby decreasing the number of compounds that fail in further pre-clinical studies.

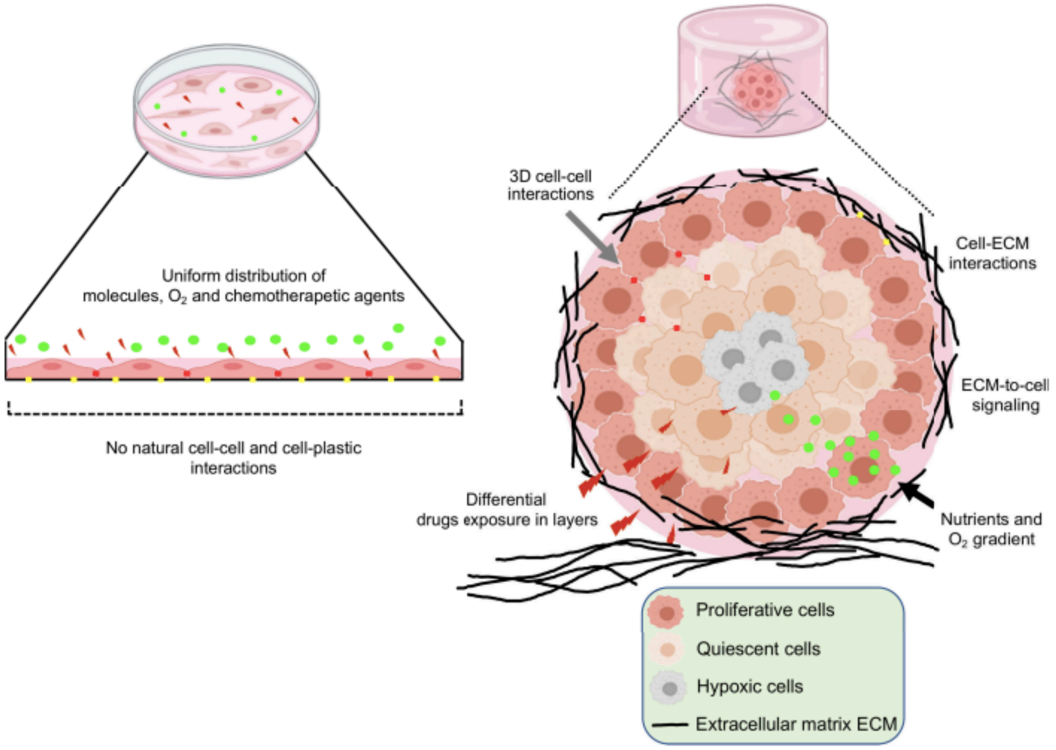

Figure 1.8 Comparison of 2D and 3D cell cultures

3D cultures (right) resemble *in vivo* physiological conditions with respect to: 3D cell-cell and cell-matrix interactions, cellular architecture, proliferation gradients, drug exposure and metabolic gradients, while 2D cultures (left) display no natural cell-cell and cell-plastic interactions as well as having uniform access to molecules, nutrients and chemotherapeutic agents. Adapted from (120).

1.8.4 Types of 3D culture models and their applications

A wide variety of 3D models have been developed. Jubelin *et al.* (16) described the categorization of 3D models based on the method used to produce the cultures and their final organization as follows: organ-slice cultures, multi-layered cell cultures and spherical cultures. Spherical models, which include spheroids and organoids, have gained the most attraction. However, precise agreement on the nomenclature of the different spherical models has not been reached and terms are sometimes incorrectly used interchangeably in literature (16). Spherical models can be generally categorized into scaffold-based and scaffold-free systems (16,119,127). Scaffold-based systems are grown and maintained in the presence of a scaffold such as a hydrogel or a polymeric hard material, while scaffold-free systems are free-floating and rely on cells to self-aggregate (119). The appropriate type of 3D model depends on the researcher's requirements. For instance, scaffold-based systems are suitable for the modelling of cell-ECM interactions, whereas scaffold-free systems are more widely used in studies where cellular and physiological gradients are modelled (119,128,129). Common scaffold-free 3D culture methods are the hanging drop method, the use of microplates coated with ultra-low adhesion coating and magnetic levitation (Fig. 1.9A-C) (118,119,130,131). In these methods, cells are prevented to attach to any substrate either by using cell-repellent coatings, gravity or fluid movement preventing cells from settling down and attaching to the culture vessel. The conditions promote cell-cell interactions resulting in the formation of cell aggregates or spheroids (16). In scaffold-based models, the scaffold provides physical support for cell attachment and proliferation, thus acting as the ECM (Fig. 1.9D). Scaffolds can be of biological or synthetic origin and their physical and chemical properties can influence cell characteristics and behaviour. Scaffolds of biological origin include hydrogels made from naturally occurring sources like collagen, fibrin, hyaluronic acid, Matrigel™ or natural material derivatives such as chitosan, alginate and silk fibres (117). Of these, Matrigel™ is the most extensively used in cancer research (16). These biological scaffolds are biocompatible and possess ECM-like features which can sustain cell function, induce controlled proliferation or differentiation and maintain cell viability (119,128). They can contain soluble factors, such as cytokines and growth factors, which can freely migrate through the gel (118,119). However, biological scaffolds are subject to batch-to-batch variability and their exact composition is undefined. Synthetic scaffolds include polyvinyl alcohol (PVA), polylactide-co-glycolide (PLG), polycaprolactore (PLA) and polyethylene glycol (PEG) hydrogels. Unlike scaffolds of natural origin, the biochemical and mechanical properties of synthetic scaffolds are fully defined, highly reproducible and can be modified to suit desired properties (e.g. matrix rigidity, porosity and biodegradability). Nevertheless, the lack of organic ECM materials limits their physiological relevance (117,119). A method to compensate loss of physiological relevance is 3D bioprinting of biocompatible materials (16,132). Although very complex, recent advances have allowed for the manufacturing of complex 3D functional tissue structures by positioning biological materials such as cells and supporting biochemicals with layer-by-layer precise positioning, similar to 3D printing (Fig. 1.9F) (132).

Another type of scaffold-based model are 3D microfluidic based cultures (Fig. 1.9E). In this technique, 3D cultures are generated in a microscopic chamber that contains microchannels in which the flow of microfluidics can be controlled, also known as organ-on-a-chip (133,134). This fluid system allows soluble factors to form concentration gradients similar to that generated by blood flow *in vivo* and better resembling nutrient and gas exchange (134).

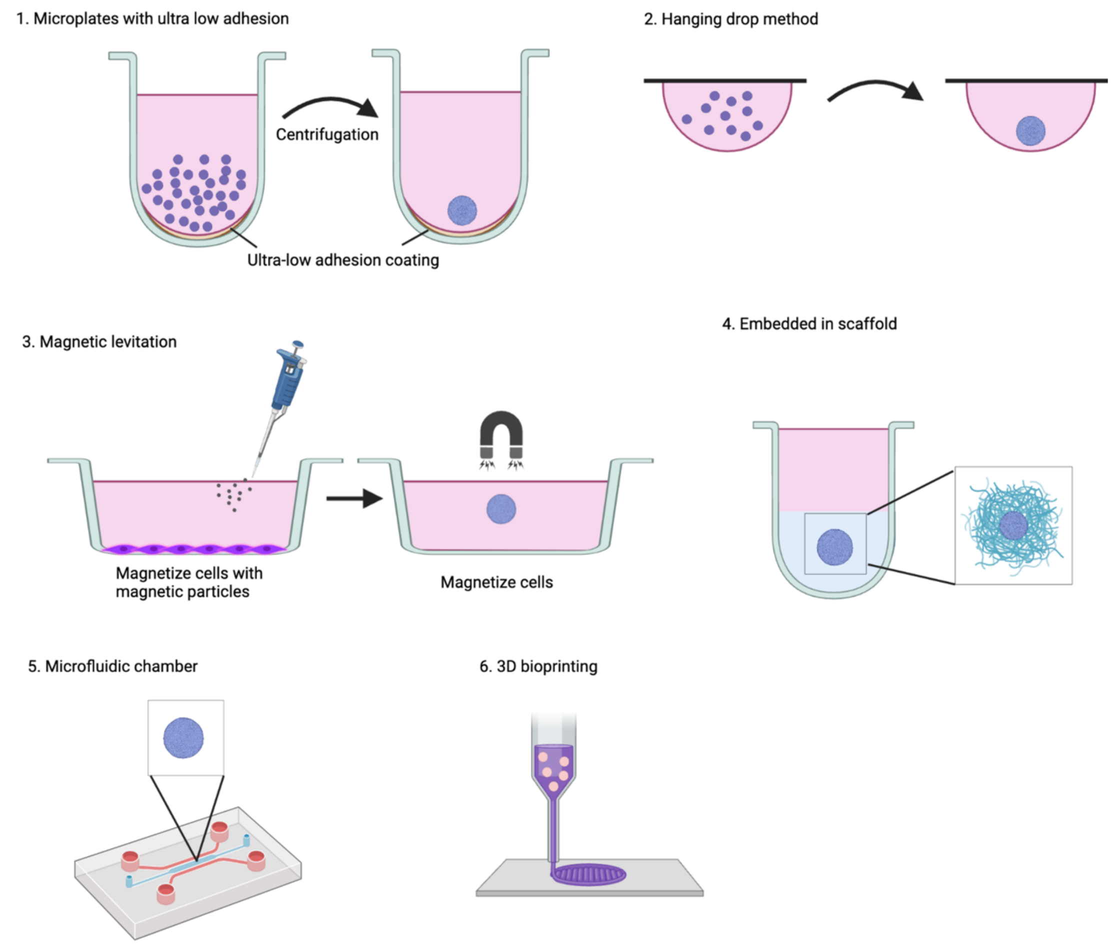

Figure 1.9 Overview of 3D cell culture techniques Spherical models can be generally categorized into (A-C) scaffold-free and (D-F) scaffold-based systems. Scaffold-free systems rely on cells to self-aggregate and common methods are (A) microplates coated with ultra-low adhesion coating, (B) the hanging drop method and (C) magnetic levitation. Scaffold-based systems rely on the presence of a biological or synthetic scaffold such as (D) ECM hydrogel, (E) microfluidic device or (F) 3D bioprinting. Figure adapted from Breslin *et al.* (135) and Mu *et al.* (134).

1.8.4.1 Spheroids

Spheroids are commonly used 3D culture systems in drug development. They are made from cancer cell lines, as monocultures or co-cultures, or patient-derived primary cells (Fig. 10A). Spheroids are characterised by the formation of a peripheral proliferating cell layer and a quiescent layer surrounding a necrotic centre core. These layers are formed due to the diffusion limit of growth factors, oxygen and other nutrients further to the spheroid core and the accumulation of metabolic waste products in the core. This morphology inherently reproduces the physical and chemical gradients of solid tumours which influences cell phenotypes and cellular responses. Thus, creating a heterogeneous population of cells. In addition, cell phenotype and function are influenced by their interactions with neighbouring cells and ECM, which differ within the distinct cell layers. These features allow for a physiologically relevant spheroid that can partially represent the tissue of interest (16).

Spheroid formation is dependent on cell type and the ability of cells to aggregate in culture (113,136). The process of spheroid formation is not completely understood. However, it is likely that it involves initial integrin interactions driving cell aggregation followed by homophilic cadherin interactions facilitating spheroid compaction (137–139). It has been suggested that cadherin interactions, particularly E-cadherin, are responsible for establishing strong cohesion and are required for the compaction stage of spheroid formation (138–140). Spheroid models have been created for a variety of cancers. Moreover, they have been generated from cell lines by mixing single cell suspensions of one or more cell lines under non-adherent conditions or by embedding in hydrogels such as agarose or Matrigel, to aid in spheroid formation (123,136,141). These spheroids represent the most basic version of the model and serve as extensions of the typical 2D cell line model by adding metabolic and proliferative gradients. Their relevance can be increased by co-culturing with other cell types (e.g. immune cells, fibroblasts or vascular cells), allowing the modelling of heterogeneous cell-cell interaction with the environment (16). For example, a study from Long *et al.* (142) describes how the interaction of tumour-associated macrophages and ovarian cancer cells was stronger in their spheroid co-cultures compared to 2D transwell co-cultures using the same cells. In a similar model, Shoval et al. (143) shows the formation of capillary-like structures in mixed spheroids of tumour cells with endothelial cells, evidencing the importance of using spheroid model systems for modelling environmental interactions. Besides cell lines, spheroids can be generated from primary cells directly isolated from tissues. These patient-derived spheroids contain a heterogenous cell population isolated from tissues including tumour cells and stroma cells. In addition, they have been shown to mimic tissue histology (144). A topic of interest in cancer research are cancer stem-like cells (CSCs). Spheroid culture (sphere-forming assay) was shown to be useful for the expansion CSCs by maintaining spheroids under serum-free conditions (144). This model was first developed for the expansion of neural stem cells, the so-called neurospheres, in which a single neural stem cell generates a spheroid with its self-renewal capacity (145). Later, this model was applied to various tumours, isolating CSCs and generating tumourspheres (146–152).

1.8.4.2. Organoids

Organoids are one of the most popular 3D cell culture models. Unlike spheroids, they are complex self-organizing organotypic structures that are generated from pluripotent or adult stem cells (Fig. 1.10B) (16). The discovery of induced pluripotent stem cell (iPSC) technology, in which differentiated cells can be reprogrammed into iPSCs, has made it possible to model organ development in culture. To generate organoids from iPSCs, the iPSCs are exposed to a variety of differentiation signals and cues, mimicking the developmental processes. This process generates organoids that closely represent the developing organ in terms of what cell types and cell interactions are present. An alternative method for organoid generation is using adult stem cells (ASC) directly from patient materials (Fig. 1.10B). Unlike iPSCs, these cells already have stem cell properties and do not have to undergo the complicated dedifferentiation process (153). However, this method is limited by the number of stem cells that can be extracted from the tissue (153). Generating organoids from adult stem cells is particularly interesting for studying disease. Using organoid technology, stem cells extracted from a variety of cancers, including colon, brain, prostate, pancreas, liver, breast, bladder, stomach, oesophageal, endometrial and lung, have been cultured as cancer organoids *in vitro* (153). Another method for organoid generation that relies on the presence of ASC, is the tissue strategy (20,154) (Fig.1.10C). In this method, tumour tissues are dissected into fragments of approximately 0.5-1 mm in a defined growth medium. The power of this strategy is that it maintains tissue architecture and important cell-cell interactions. However, this strategy is limited by slow growth compared to other organoid cultures (20,154). Most organoid models are scaffold-based and rely on the presence of ECM. Like spheroids, they can be co-cultured with stroma cells to enhance their biological relevance. Remarkably, several studies have shown that patient-derived cancer organoids can accurately predict patient therapy response. This shows great promise for the adoption of organoids as *in vitro* avatars for patient tumours to optimize personalised medicine in the clinic (16,155–158).

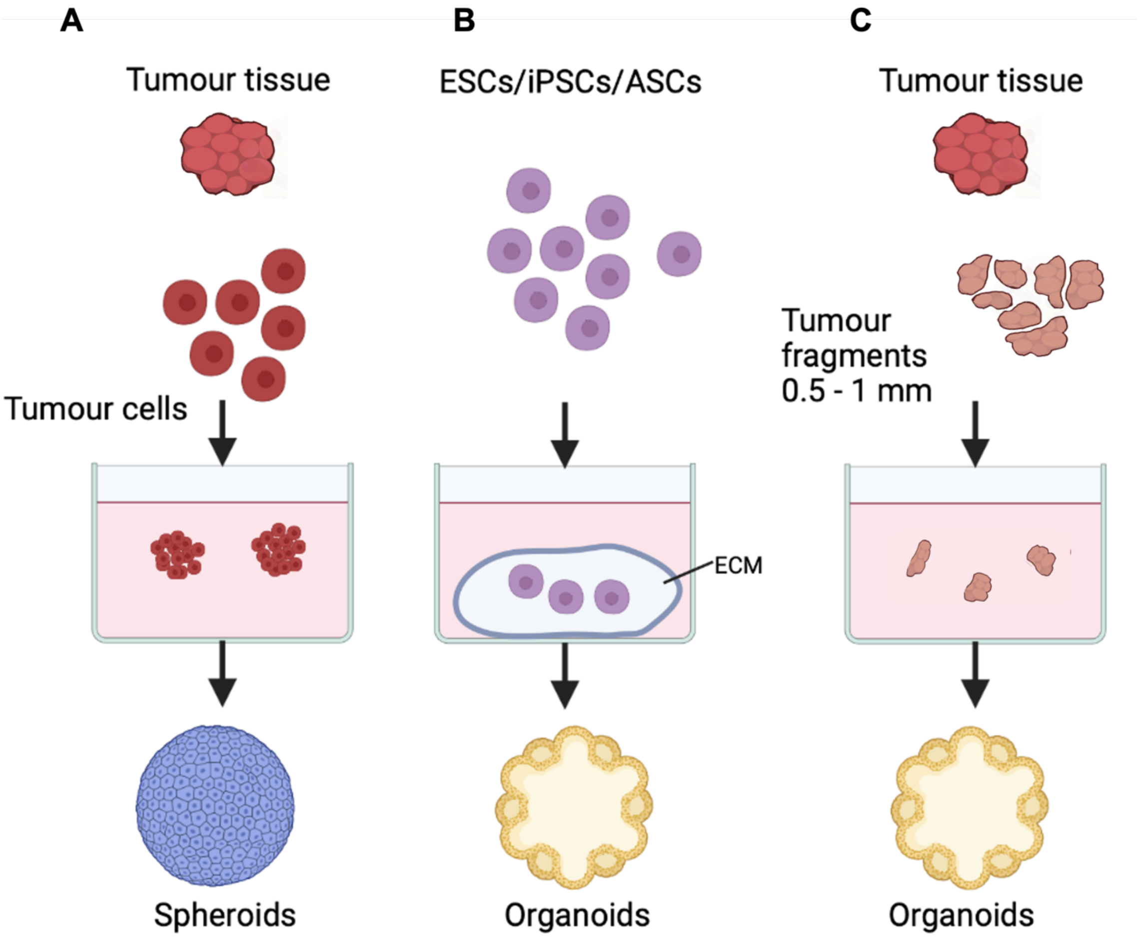

Figure 1.10 Diagram of spheroid and organoid formation (A) Spheroids can be formed from cancer cell lines, as monocultures or co-cultures, or patient-derived primary cells extracted from tissue that are placed in culture under spheroid culture conditions. (B) Organoids are generated from embryonic, pluripotent, or adult stem cells and self-organize into organotypic structures after embedding in ECM. (C) Organoids are formed from fresh tumour fragments of approximately 0.5-1mm. Tumour fragments start rounding in 1-2 weeks. Adapted from Velasco et al. (159).

1.8.5 Current *in vitro* models for meningiomas

For meningiomas, few immortalized cell lines have been established. Meningioma primary cultures are relatively easy to establish. However, this model is restricted to early passages due to low telomerase activity, causing the cells to go into senescence. Therefore, a common method to establish an immortalized meningioma cell line is by introducing expression of the telomerase catalytic subunit hTERT (13). Examples of low-grade meningioma cell lines immortalized by hTERT introduction are BenMen1 (160), SF-4433 (161) and Me3TSC (162). However, in addition to hTERT, human papilloma genes E6/E7 and SV40 large T antigen were induced in SF-4433 and Me3TSC respectively, to immortalize these cells. Despite the extensive characterisation of these cell lines, the introduction of oncogenes can alter the behaviour of these cells, which restricts their credibility as models (13). Additionally, some cell lines have been established from aggressive WHO grade 3 meningiomas. The IOMM-lee cell line is derived from an anaplastic intraosseous meningioma (163). While this cell line is very popular, it shows a complex karyotype which is likely influenced by long-term culture effects. In addition, it does not have a mutation in the NF2 gene, the most common driver mutation in meningiomas (13). Another high-grade cell line of meningioma is KT21, which unlike IOMM-lee has the monosomy of chromosome 22, harbouring the NF2 gene (164).

Over the last 20 years, various research groups have focused on the development of 3D culture models for meningioma research, and several research groups have published data acquired by 3D systems (17–19,149,165–169). One of the first studies working with 3D cell culture in meningiomas was published by Tonn *et al*. in 1997 (165). Spheroids were generated from tumour fragments (<0.5 mm) by placing them on agar-coated culture dishes overlaid with culture medium. Using this model, they were able to show that progesterone receptor (PgR) expression was preserved in tumour fragment spheroid cultures of meningiomas with a low proliferation index while PgR expression in matched monolayer cultures, displaying a high proliferation index could not be detected. Interestingly, PgR expression was re-expressed in spheroids generated from their monolayer cultures after a few passages. A few years later, a study investigating adenovirus replication in brain tumours successfully prepared meningioma spheroids from primary tumour materials, in which they showed adenovirus penetration could be more faithfully modelled in their 3D cultures compared to their monolayer cultures (166). Despite these results showing significant differences between monolayer and spheroid cultures, apart from a few studies using agar-coated plates for spheroid formation (167–169), the use of 3D models for meningioma research did not progress much or become widely adopted in the years that followed. In 2011, Hueng and colleagues (149) isolated and characterised a tumour stem-like cell population from meningiomas using the neurosphere model, previously described for gliomas (170–172). This spheroid model differs from the others by selecting a population of cells with stem-like characteristics and is particularly useful to study this cell type. Recently, several novel organoid models of meningioma have been developed (17–20). Magill *et al.* developed a system in which iPSC-derived human cerebral organoids are co-cultured with patient-derived primary meningioma cells generating a 3D organoid system for meningioma (17). Yamazaki *et al*. developed a patient-derived organoid system that uses meningioma tumour tissues from benign and malignant meningiomas (18). This model is a scaffold-based system and relies on the presence of Matrigel. A similar model was developed by Siu *et al.* (19). The most recently established organoid model was established in 2023 and was based on the tissue strategy described in section 1.6.4.2. This protocol dissected fresh tissue in small fragments which formed meningioma organoids within 1-2 weeks (20).

1.9 Epithelial to mesenchymal transition

Epithelial-to-mesenchymal transition (EMT) describes the cellular process in which epithelial cells undergo several molecular and cellular changes that allow cells to acquire a reversible mesenchymal phenotype. During this process, stationary epithelial cells lose their apical-basal polarity and intracellular adhesion molecules, while gaining enhanced motility and invasiveness. Furthermore, the mesenchymal phenotype is associated with enhanced resistance to apoptosis and an increase in ECM production (173–175). The reversible process of EMT is called mesenchymal-to-epithelial transition (MET), in which mesenchymal cells lose their mesenchymal phenotype and change back into epithelial cells (fig. 1.11).

In normal human biology, EMT is a major embryonic process that is crucial for specific steps during gastrulation and organ development. This is typically referred to as type 1 EMT. In addition, EMT occurs in adulthood during wound healing and tissue repair, referred to as type 2 EMT. Besides normal biology, EMT also plays a role in diseases and is related to cancer progression, metastasis, induction of pluripotency and stem cell behaviour (174,176). Cancer-associated EMT is referred to as type 3 EMT. While there are functional differences between the subtypes, their distinction on a molecular level remains unclear (173,174).

Type 1 EMT is associated with embryonic gastrulation and gives rise to the embryonic germ layers ectoderm, mesoderm, and endoderm, that generate all tissue types of the body (176).

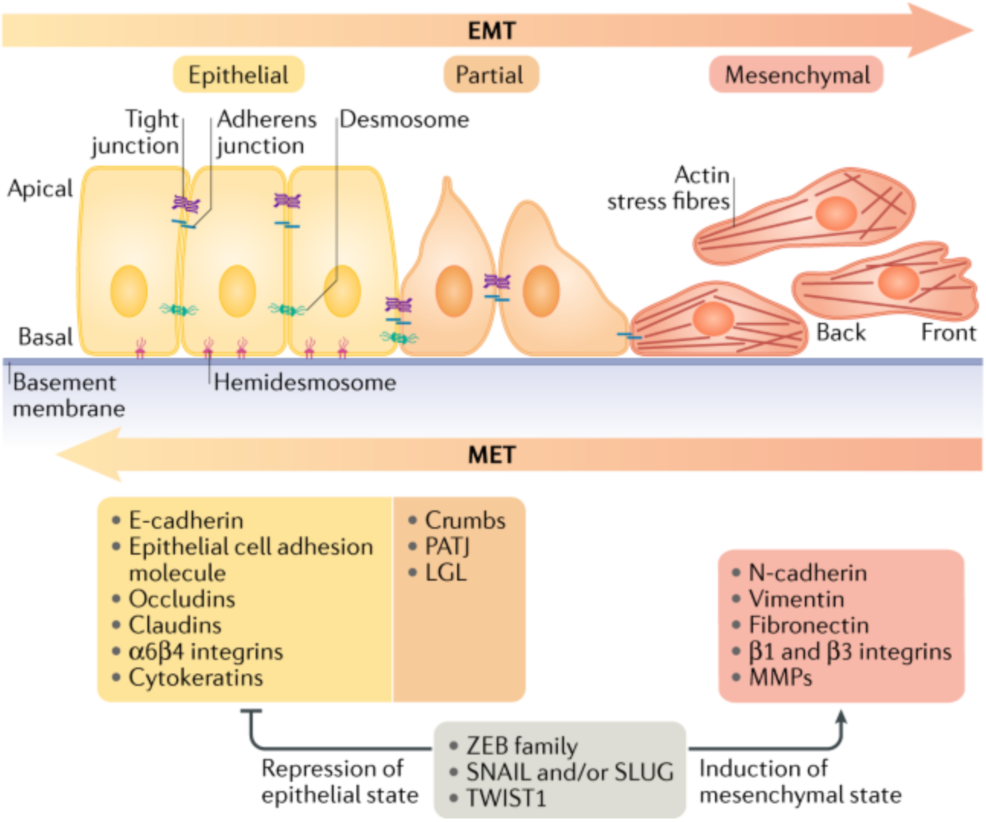

Figure 1.11 Epithelial-to-Mesenchymal transition (EMT)

During EMT, epithelial cells lose their apical-basal polarity and expression of adhesion molecules associated with the epithelial state (listed in the yellow box) that tightly tether cells to the underlying basement membrane, while gaining front-to-back polarity and expression of molecules associated with the mesenchymal state (listed in the red box). This process is induced by the expression of EMT inducing transcription factors ZEB, SNAIL, Slug and TWIST, and subsequent inhibition of epithelial genes and induction of mesenchymal genes. This dynamic process can be reverted by undergoing mesenchymal–epithelial transition (MET) and can occur in an intermediate form called partial EMT. Adapted from Dongre & Weinberg (173).

Type 2 EMT occurs as part of the tissue repair process, where epithelial cells, in response to inflammatory signals, differentiate into fibroblast-like cells that can rebuild tissue (177). Type 2 EMTs are terminated when the inflammatory signals are resolved, and the repair process is finished. In cases of chronic inflammation, EMT is not terminated which can result in tissue fibrosis (177).

Type 3 EMT is a highly deregulated form of EMT implicated with tumour growth and cancer progression (178). It typically involves tumour cells that acquire mesenchymal features facilitated by genomic or epigenetic alterations. This results in cells with increased invasive capacity, which enables them to migrate and metastasize (174). In addition, type 3 EMT has been linked to stemness and resistance to therapy (178).

1.9.1 Molecular mechanisms of EMT

EMT is orchestrated by a series of molecular events that include activation of transcription factors, expression of specific cell adhesion molecules, reorganization of the cytoskeleton, degradation of ECM and changes in the expression of specific miRNAs (174,177,178). Epithelial cells typically display apical-basal polarity and are attached to the basement membrane by strong hemidesmosomes. They attach to neighbouring cells by strong tight junctions and adherens junctions. These interactions ensure that cells are tightly held together, mitigating their ability to migrate (173). The main cell surface molecule involved in these strong interactions of epithelial cells is epithelial cadherin (E-cadherin) (173,179). E-cadherin forms mature adherens junctions by binding to β-catenin via its distal cytoplasmic domain, which in turn links to the actin cytoskeleton via α-catenin (179). During EMT, expression of E-cadherin is repressed and replaced by weaker cell surface markers associated with the mesenchymal state, including neural-cadherin (N-cadherin), vimentin and/or fibronectin. This so-called cadherin switch is a major hallmark of EMT and results in the disruption of epithelial cell-cell interactions and subsequent loss of the typical cobble-like epithelial cell morphology, resulting in a spindle-like mesenchymal morphology with front-to-back polarity (178). Consequently, this switch to weaker mesenchymal junctions, allows cells to detach from their neighbouring cells and migrate through the extracellular matrix (173). EMT is regulated by various EMT transcription factors such as zinc-finger E-box-binding homeobox (ZEB)-1 and ZEB2, Snail family transcriptional repressors Snail1 and Snail2 (also known as Slug), and TWIST, that repress the expression of epithelial genes, such as CDH1, and induce mesenchymal gene expression (177). In turn, EMT transcription factors are induced through several signalling pathways, e.g. TGFβ/SMAD, Notch, MAPK, PI3K/Akt and, Wnt signalling. These pathways are activated by microenvironmental signals, such as cell-cell (receptor-ligand) interaction, soluble factors released from (stroma) cells (e.g. cytokines, integrins, growth factors), extracellular matrix rigidity, cytoskeletal cues and oxygen conditions in the environment (176,177).

1.9.2 EMT in Meningioma

About 20% of meningiomas that have otherwise benign histology can be invasive and recurrent (180). EMT has been suggested to play a role in this phenomenon, as well as in meningioma progression and recurrence (181–190). Literature on the role of EMT in meningioma is limited, which may be related to the lack of suitable models that allow for studying this process of EMTs in meningiomas. The next section is an overview of the current understanding of the role of EMT and the molecules associated with EMT in meningiomas.

E-cadherin expression has been a focal point of meningioma research for many years, not just for its involvement in EMT but also for its suggested other tumour suppressor functions, including its role in preventing activation of WNT signalling through the sequestering of β-catenin to the cell membrane (191,192). This prevents the release of β-catenin into the cytoplasm and its subsequent translocation to the nucleus. Hence, precluding activation of target genes associated with activation of the WNT signalling pathway (141). Several papers report decreased expression of E-cadherin in meningiomas, which is a hallmark of EMT and associated with loss of tumour differentiation, high tumour grade and poor prognosis (186,193–195). However, the role of E-cadherin in meningioma and the association between reduced expression and tumour grade remains controversial. Over the years, contradictory findings have been reported. Several papers have demonstrated an inverse correlation between E-cadherin expression and the grade of malignancy in meningiomas (193,196,197). Contrastingly, other papers demonstrated low expression levels of E-cadherin in meningiomas independent of their WHO grade (194,198,199). In addition, several studies investigated the correlation between E-cadherin expression and brain invasion in meningiomas. Again, contradictory results were found whereby some papers detected an inverse correlation between E-cadherin expression levels and brain invasion (195,200) and others did not observe any significant differences of E-cadherin expression in invasive and non-invasive meningiomas (183).

Despite contrasting results on the relation of E-cadherin loss, invasiveness and tumour grade, the numerous reports on E-cadherin indicate that the molecule plays a role in meningioma biology, and thereby suggests the involvement of EMT (182,186). Indeed, the EMT-associated gene and protein expression levels have been investigated across meningiomas of all grades (185,186). One of the key research papers showing evidence for EMT in meningiomas was the paper of Wallesch *et al.* (188). This paper demonstrated a significant decrease in mRNA expression levels for E-cadherin and ZO-1, two common epithelial markers, and a significant increase in the mRNA levels of the EMT-associated transcription factors Zeb1 and Slug in high grade meningiomas (188).Interestingly, the authors observed a significant negative correlation between E-cadherin and Slug and between ZO-1 and Slug, which indicated that in meningioma, Slug is one of the transcription factors responsible for the downregulation of E-cadherin and ZO-1. Another interesting finding was that a significant loss of E-cadherin and a significant increase in Slug was found in recurrent benign meningiomas in comparison to non-recurrent benign meningiomas, which agrees with the hypothesis that EMT and subsequent E-cadherin loss underlie progression and recurrence in meningiomas. Furthermore, the authors observed high gene expression levels of EMT-associated genes in NF2 negative meningioma cells compared to NF2 expressing cells, indicating that NF2 negative cells are more mesenchymal than NF2 positive cells. This is in line with the hypothesis of EMT underlying progression since NF2-mutated meningiomas have a higher association with progression to higher grades compared to other mutations associated with benign meningiomas. Furthermore, a study that looked at posttranscriptional deregulation of signalling pathways of meningioma by miRNA expression identified 13 deregulated miRNAs between different subtypes of benign WHO grade 1 meningiomas, whose target genes were involved with EMT (201). More evidence supporting the hypothesis of a role for EMT and E-cadherin loss in meningiomas was the case study by Bukovac (187) that described a patient with two bilateral meningiomas of different grades, in which the WHO grade 2 lesion showed higher expression of the mesenchymal proteins Snail and Slug while E-cadherin was partially lost compared to the WHO grade 1 lesion, suggestive of a role for EMT in tumour progression. Another interesting case study described a patient with atypical meningioma that recurred twice (189). The first recurrency was graded as atypical WHO grade 2 meningioma while the second recurrency was diagnosed as an anaplastic WHO grade 3 meningioma. Both recurrent tumours lacked E-cadherin expression that was diffusely present in the primary tumour. Mesenchymal proteins N-cadherin, Twist, Snail and Slug showed increased expression in the primary recurrency, which increased to strong expression in the secondary recurrence. While these cases are describing individual patient events, they suggest a role for EMT in the pathogenesis of meningioma and therefore, support an avenue for more research on this biological process in meningioma biology.

1.9.3 Notch1 signalling and EMT

The involvement of Notch1 with EMT has been shown in many cancers, such as breast cancer (202,203), pancreatic cancer (204), lung cancer (205), colon cancer (206) and glioblastoma (207) and stimulates EMT by directly upregulating the EMT transcription factors Snail and Slug (203,207,208). For example, Li *et al.* (207) demonstrated the association between Notch1 and aggressive behaviour of metastasis, invasion and EMT, which were suppressed after Notch1 inhibition.

Furthermore, Timmerman *et al*. (209) demonstrated that over-expression of Notch1 in immortalized endothelial cells resulted in increased snail expression and decreased E-cadherin expression. Similarly, Shao *et al.* (203) showed that Notch1 regulates EMT and invasion in breast cancer cells in a slug-dependent manner. Under normal circumstances, Notch1 signalling is important for embryogenesis and determines cell fate by regulating apoptosis, differentiation, and proliferation. Notch1 is part of the highly conserved Notch family of transmembrane receptors, consisting of four family members in total (210). The Notch1 receptor consists of an extracellular ligand binding domain, a transmembrane region, and an intracellular activating domain. Canonical Notch1 signalling is activated upon binding of the canonical ligands Delta-like molecules (DLLs) and Jagged (Fig. 1.12) (211). Upon ligand binding, the extracellular domain is cleaved off by metalloproteinase cleavage (ADAM10 and ADAM17), followed by a Gamma (γ) -secretase enzyme-mediated cleavage whereby the intracellular domain (NICD) is cleaved off the transmembrane fragment. The NICD is then translocated to the nucleus where it activates transcription of Notch target genes: basic helix-loop-helix family transcription factors (bHLH TFs) Hes1 (hairy and enhancer of split -1) and Hey1 (hes related family bHLH TFs with YRPW motif 1), as well as EMT-inducing transcription factors Slug and Snail (210,211). Besides activation of target genes, the NICD also interacts with other non-canonical pathways, including NFκB, AKT, PTEN, Hippo, TGF-β and Wnt, which in turn can activate EMT-signalling (212). Moreover, Notch signalling has been shown to play a role in several other oncogenic processes including stemness maintenance, angiogenesis, and intervening with the immune system (212).

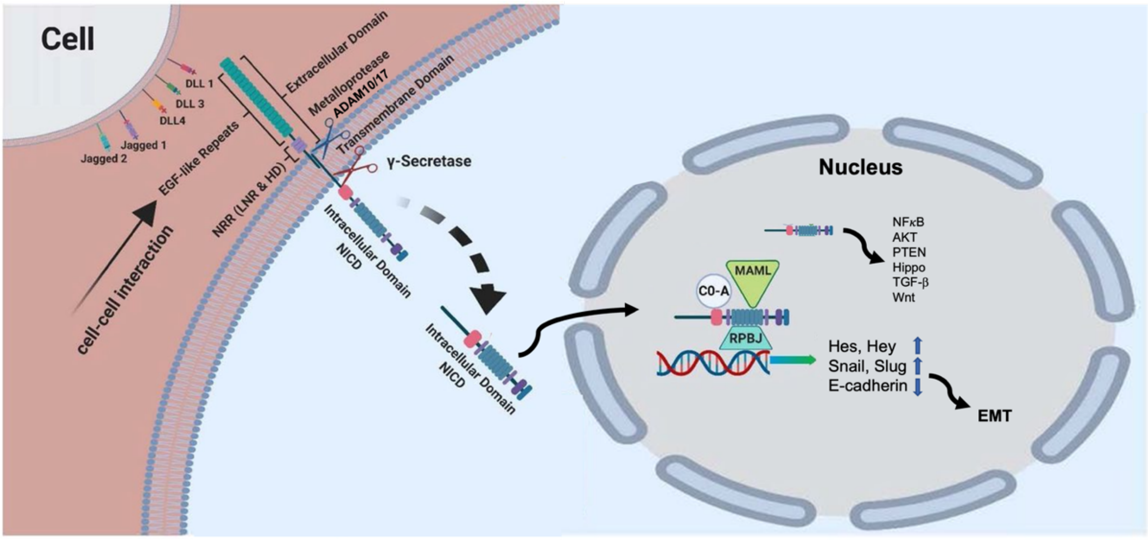

Figure 1.12 Notch1 signalling pathway

Canonical Notch1 signalling is activated upon binding of the canonical ligands Delta-like molecules (DLLs) and Jagged. Upon ligand binding, the Notch1 extracellular domain is cleaved off by metalloproteinase cleavage (ADAM10 and ADAM17), followed by cleavage of the Notch1 intracellular domain (NICD) by the γ-secretase enzyme. The NICD translocates to the nucleus and activates transcription of Notch target genes: basic helix-loop-helix family transcription factors Hes1 and Hey1, as well as EMT-inducing transcription factors Slug and Snail, which in turn repress E-cadherin leading to EMT. Besides activation of target genes, the NICD also interacts with other non-canonical pathways, including NFκB, AKT, PTEN, Hippo, TGF-β and Wnt. Adapted from Gharaibeh et al. (210) & Espinoza *et al.* (213)

1.9.4 Notch1 in meningioma

Few studies investigated the role of Notch signalling in meningiomas. Cuevas et al. (214) analyzed gene expression levels of Notch signalling pathway components in meningiomas of all grades and non-neoplastic meningeal tissue. In this screen, upregulation of both transcript and protein levels of Notch1, Notch2, Hes1 and the Notch ligand jagged1 were observed in meningiomas of all grades. Moreover, they observed induction in the expression of TLE2 and TLE3, members of the Groucho/transducin-like enhancer of split family corepressors that interact with and modulate Hes1. This increase was only observed in higher-grade meningiomas. The link between Notch1 and EMT in meningiomas has not yet been studied.

1.9.5 Targeting of Notch1: γ-secretase inhibitors

Considering the role of Notch1 signalling in EMT, inhibition is an interesting anti-cancer strategy (202–204,210). There are several strategies for the inhibition of Notch1 signalling. As the proteolytic cleavage of the Notch1 receptor is vital for effective signal transduction, interfering with this proteolytic processing has been a focus point in Notch signalling inhibition research (215,216). Particularly, deactivation of the γ-secretase enzyme, which mediates the release of the NICD, has been studied (210). All 4 Notch receptors are cleaved by γ-secretase, however, γ-secretase inhibitors are pharmacologically distinct and inhibit cleavage of the Notch receptors with different efficiency (215). Several γ-secretase inhibitors are currently under investigation for use as anti-cancer therapy in clinical trials for lung cancer, pancreatic cancer, breast cancer, colorectal cancer, ovarian cancer, glioma, melanoma and desmoid tumours (215). Several studies have showed an acceptable safety profile after γ-secretase inhibition (210). Besides monotherapy, γ-secretase inhibitors are also studied for their use as combination therapies (210).

1.10 Hypothesis and project aims

With low success rates in clinical trials, drug discovery for meningiomas is lagging (3). Hence, there is an urgent need for new technologies that improve precision in drug testing, such as the development of 3D cell culture models.

This thesis hypothesizes that it is feasible to establish a novel culture method for the generation of 3D patient-derived meningioma cultures that can be used in experimental *in vitro* studies and that these cultures resemble essential features of in vivo meningioma tissues.

To address this, this PhD thesis comprises the following aims:

1. Establish an easy-to-use *in vitro* patient-derived 3D meningioma culture method that can generate 3D cultures that resemble *in vivo* features of the parental tumour, including tissue histology, the immune microenvironment and the mutational profile.

2. Characterise the transcriptome of the novel 3D model and compare it with the transcriptome of matched parental tumours and our traditional monolayer model

3. Validate the use of the novel 3D meningioma model as a tool to explore key elements of meningioma biology and its use as a drug testing tool by assessing the response to several targeted therapies

2 Materials and Methods

2.1 Clinical material

Meningioma specimens were obtained with written informed consent of all participating patients after the national ethical approvals (Plymouth Brain Tumour Biobank, South Central – Hampshire B Research Ethics Committee, REC No: 19/SC/0267, IRAS project ID: 246667). All samples were de-identified prior to processing and given a unique identification number (‘MN’). Study methods were carried out in accordance with the approved guidelines. Clinical information on meningiomas presented in this project can be found in Table 2.1. All meningioma tumours were graded by a neuropathologist.

Table 2.1: Clinical and histopathological data for patient samples

Patient	Histopathological subtype	Grade	Age	Gender (F=female, M=male, T=transgender)
MN412	Fibrous	1	61	M
MN410	Secretory	1	78	M
MN406	Meningothelial	1	72	M
MN504	Unknown	1	44	F
MN490	Mixed meningothelial & microcystic	1	Unknown	M
MN523	Meningothelial	1	79	M
MN525	Fibrocollagenous	1	75	M
MN595	Fibroblastic	1	56	F
MN609	Transitional	1	62	F
MN611	Parasaggital	1	78	F
MN613	Transitional	1	64	F
MN614	Transitional	1	46	T
MN656	Parasaggital	1	78	F
MN655	Secretory	1	65	F
MN658	Transitional	1	58	F
MN485	Meningothelial	1	Unknown	Unknown
MN486	Meningothelial	1	Unknown	Unknown
MN487	Fibrous	1	Unknown	Unknown
MN493	Fibrous	1	Unknown	Unknown

MN554	Transitional	1	Unknown	Unknown
MN577	Psammomatous	1	75	Unknown
MN557	Unknown	1	43	F
MN567	Meningothelial	1	61	F
MN592	Meningothelial	1	Unknown	Unknown
MN602	Transitional	1	58	M
MN630	Atypical	2	58	M
MN566	Psammomatous	1	62	F
MN635	Meningothelial	1	66	F
MN610	Secretory	1	30	F
MN588	Meningothelial	1	Unknown	Unknown
MN429	Meningothelial	1	70	F
MN496	Unknown	1	57	M
MN573	Fibrous	1	70	F
MN518	Unknown	1	54	F
MN468	Unknown	1	41	F
MN460	Meningiothelial	1		F
MN461	Meningiothelial	1		M
MN472	Transitional	1		F
MN474	Psammomatous	1		F
MN467	Unknown	1	45	F
MN408	Transitional	1	25	F
MN414	Psammomatous	1	45	F
MN411	Fibrous	1	74	F
MN437	Meningothelial	1		F
MN481	Fibrous	1		F
MN553	Transitional	1		M
MN581	Meningothelial	1	34	F
MN516	Mixed fibrous & microcystic	1	Unknown	Unknown
MN524	Unknown	Unknown	Unknown	Unknown
MN601	Secretory	1	42	F
MN652	Unknown	1	62	M
MN491	Fibrous	1	Unknown	Unknown
MN233	Transitional	1	37	F
MN231	Transitional	1	58	F
MN329	Fibrous	1	Unknown	Unknown
MN313	Meningothelial	1	Unknown	Unknown
MN498	Angiomatous/microcystic	1	48	M
MN465	Transitional	1	75	M
MN418	Atypical	2	54	M
MN440	Atypical	2	Unknown	Unknown
MN521	Atypical	2	62	F
MN409	Atypical	2	Unknown	Unknown
MN428	Atypical	2	42	F
MN603	Atypical	2	67	M

MN605	Atypical	2	64	F
MN660	Atypical	2	Unknown	Unknown
MN582	Atypical	2	64	F

2.2 Cell culture

A range of culture media were used in this project. Culture medium recipes can be found in Table 2.2.

Table 2.2: medium components

Medium	**Components**
Meningioma grade 1 growth medium (MN1)	Dulbecco's Modified Eagle Medium (DMEM) (Thermo Fisher Scientific, #31966-021), 10% (v/v) FBS (Merck, F7524), 100 U/mL penicillin/streptomycin (Thermo Fisher Scientific, #15140-122), 1% (v/v) GlutaMAX (Thermo Fisher Scientific, #35050-038)
Meningioma grade 2 growth medium (MN2)	DMEM F-12 Ham's Nutrient Mixture (DMEM/F12) (1:1), 20% (v/v) FBS (Merck, F7524), 100 U/mL penicillin/streptomycin (Thermo Fisher Scientific, #15140-122) 1% (v/v) GlutaMAX (Thermo Fisher Scientific, #35050-038)
Growth Factor Supplemented Spheroid growth medium (GFS)	DMEM/Nutrient Mixture F12 (Thermo Fisher Scientific, #10565-018) and Neurobasal (Thermo Fisher Scientific, #21103049) at a 1:1 ratio, 5% (v/v) FBS (Merck, F7524), 1% (v/v) B27-supplement (Thermo Fisher Scientific, #17504044), 1% (v/v) N2-supplement (Thermo Fisher Scientific, #17502048), 20 ng/ml recombinant human epidermal growth factor (EGF) protein (Bio-Techne, 236-EG), 20 ng/ml recombinant human basic fibroblast growth

	factor (bFGF) protein (Bio-Techne, 233-FB), 100 U/ml penicillin/streptomycin (Thermo Fisher Scientific, #15140-122), 1% (v/v) GlutaMAX (Thermo Fisher Scientific, #35050-038), 1% (v/v) non-essential amino acids (NEAA) (Thermo Fisher Scientific, #11140-050)
Specimen transport medium	Hibernate™ A medium (Thermo Fisher Scientific, A1247501), 1% (v/v) Amphothericin B (Merck, A2942), 100 U/mL penicillin/streptomycin (Thermo Fisher Scientific, #15140-122)
Glioblastoma organoid medium (GBOM)	DMEM/Nutrient Mixture F12 (Thermo Fisher Scientific, #10565-018) and Neurobasal (Thermo Fisher Scientific, #21103049) at a 1:1 ratio, 1% (v/v) B27-supplement w/o vitamin A sup (Thermo Fisher Scientific, #12587010), 1% (v/v) N2-supplement (Thermo Fisher Scientific, #17502048), 1% GlutaMAX (Thermo Fisher Scientific, #35050-038), 100 U/ml Pen/Strep (Thermo Fisher Scientific, #15140-122), 1% (v/v) non-essential amino acids (Thermo Fisher Scientific, #11140-050), 2.5 µg/ml insulin (Thermo Fisher Scientific, 12585014).

2.2.1 Tissue digestion

Tumour samples from human meningiomas were freshly removed by craniotomy and promptly taken to the Department of Pathology to confirm meningioma diagnosis. Surplus tissue was transferred into a sterile tube containing specimen transport medium and brought to the laboratory for sample processing. This occurred within 1-3 hours after tumour resection for samples from the Derriford Hospital Plymouth and between 24-36 hours if the sample was from the

Southmead Hospital in Bristol. Specimens were washed twice in sterile 1X Phosphate Buffered Saline (PBS) (Thermo Fisher Scientific, #14190-144) and transferred to a 100mm culture dish containing meningioma medium (MN1) in a laminar flow cabinet. Tissue was dissected using a sterile scalpel (VWR International Ltd, 0507 n.21). Areas with substantial necrosis were removed and several tumour pieces were snap frozen and saved for extraction of DNA, RNA (2 mm^2) and protein (5 mm^2). Resected tumours were further dissected into single cells using sterile curved dissection scissors (VWR International Ltd, Z265977) and by pipetting up and down several times using a 10 ml sterile plastic pipette. The cell suspension was collected in a canonical 50 ml tube and incubated in 1X Red Blood Cell (RBC) lysis buffer (Thermo Fisher Scientific, eBioscience™, 00-4333-57) for 10 minutes under gentle rotation. Cells were pelleted, washed in 1X PBS, and resuspended in MN-1 medium. Cell suspensions were strained using a cell strainer with a 100mm nylon mesh to remove cellular debris and seeded into several 25-cm^2 cell culture flasks (Greiner Bio-One) according to tumour size or cryopreserved. Strained pieces were retrieved and put back in the 100mm digestion dish. Cell culture flasks were placed into an incubator at 37°C in a humidified atmosphere (5% CO_2). Cell medium was replaced every 3 days.

2.2.2 Maintaining and passaging monolayer cultures

WHO grade I meningioma primary cells were routinely grown in MN1 medium at 37°C in humidified atmosphere (5% CO_2) (see table 2.2). WHO grade II meningioma primary cells were routinely grown in MN2 medium (see table 2.2). Cells were grown until 90% confluency before passaging. For passaging, growth medium was removed, cells were washed in 1X PBS (Thermo Fisher Scientific, #14190-144) and incubated in 0.25% (v/v) Trypsin/EDTA (Thermo Fisher Scientific, #25200-056) for 2 minutes at 37°C in humidified atmosphere (5% CO_2). After cell detachment, trypsin was inactivated using MN1 medium and cells were collected in a canonical 50 mL tube. Cells were centrifuged at 1200rpm for 5 minutes and cell pellets were resuspended in MN-1 medium and seeded in the appropriate culture flask (T25, T75 or 96-well plates).

2.2.3 Spheroid culture

For spheroid culture, meningioma primary cells at passage 0 were detached using 0.25% Trypsin/EDTA, washed in PBS 1X and resuspended in complete spheroid growth medium (GFS). Cells were counted and seeded at 3000 cells/well in U-shaped ultra-low adherend (ULA) 96-well microplates (Greiner Bio-One, 650979). Culture plates were centrifuged at 1200 rpm for 15 minutes and placed in a humidified incubator with 5% CO_2 under constant rotation (65 rpm). Spheroids were left in the incubator for 3 days to allow spheroid formation. Spheroids were exclusively formed from cells attached at passage P0, forming passage P1 spheroids. Spheroids were also generated from cells frozen at P0 , and subsequently grown to confluence on p0 prior to forming P1 spheroids.

2.2.4 Meningioma organoid culture

For meningioma organoid experiments, during tissue digestion several pieces were carefully cut in approximately 0.5-1 mm^2 fragments. Fragments were distributed in ULA 96-well microplates (Greiner Bio-One, 650979), one fragment/well and overlaid with 200 µL of GBOM or GFS medium and placed on an orbital shaker within a 37°C humidified atmosphere (5% CO2). The medium was replaced every 2-3 days by carefully aspirating the medium without disturbing the fragments. Fragments generally developed into MgOs with spherical morphology within 2 weeks. After 2 weeks, spherical pieces were carefully selected by using a microscope and other pieces were discarded.

2.2.5 Cell counting

Cells were counted using a Neubauer-improved bright line counting chamber according to manufacturers' instructions. Briefly, cells were pelleted and resuspended in 1 ml of appropriate growth media. 10 µL of cell suspension was loaded onto the counting chamber and cells were counted under a phase-contrast light microscope (Leica) with a 10X objective. Cells bordering square edges and odd-shaped cells were excluded from the count. Cell concentration was determined per mL.

2.2.6 Cryopreservation and cell recovery

To cryopreserve cells for later use, cells were resuspended at a cell density of approximately ($3 *10^5 – 1 * 10^6$ cells) in 1 mL freezing medium (45% complete culture media, 45% FBS and 10% dimethyl sulphoxide (DMSO) (Merck, d2650)) and transferred to a cryovial. Cryovials were placed in a cryofreezing container (Nalgene®, Mr. Frosty Cryo 1°C freezing container) and kept at -80°C overnight to ensure rapid freezing at a rate of -1°C/minute. Cells were transferred to liquid nitrogen tanks for long-term storage. For cell recovery, vials were quickly thawed in a 37°C water bath. Cells were transferred to a 50 mL canonical tube containing 4 mL of pre-warmed complete medium. Cells were centrifuged at 1200 rpm for 5 minutes to remove freezing medium and seeded at desired concentrations in appropriate culture flasks.

To cryopreserve MgOs, they were cut into approximately 300 μm^2 fragments using a sterile scalpel under a microscope and incubated in their appropriate culture medium (GBOM or GFS) supplemented with 10 µM Y-27632 (Rock inhibitor, StemCell Technologies) for 1 hour. Subsequently, fragments were resuspended in freezing medium containing the appropriate culture medium, 10 µM Y-27632, and 10% DMSO (Merck, d2650) and placed in cryovials (approximately 20-30 pieces per cryovial). MgOs were incubated in freezing medium for 15 minutes at room temperature to allow the DMSO to penetrate into the core, followed by rapid freezing at a rate of -1°C/minute in a cryofreezing container (Nalgene®, Mr. Frosty Cryo 1°C freezing container) in a -80°C freezer. After a minimum of 24 hours, samples were transferred to liquid nitrogen tanks for long-term storage. For recovery, vials were quickly thawed in a 37°C water bath. Vials were added to 5 ml culture medium (GBOM or GFS) supplemented with 10 µM Y-27632 in a dropwise manner to dilute the DMSO. MgOs were allowed to settle and medium was aspirated and MgOs were resuspended in medium (GBOM or GFS) supplemented with 10 µM Y- 27632 and plated in ULA 96 well plates at 1 MgO/well. After 24 hours, medium was replaced with fresh GBOM or GFS to remove rock inhibitor Y-27632. MgOs were observed and successful recovery was determined by rounding of MgOs and histology.

2.2.7 Spheroid and MgO growth analysis

To measure the growth of spheroids and MgOs images of individual spheroids or MgOs were routinely obtained using a brightfield microscope (Leica IM8) at 10X objective. The maximal (max.) diameter was measured by using the measuring tool on imageJ. For spheroids, the max. diameter at day 3 and for MgOs the max. diameter when the MgO first became spherical was (between 3-14 days) taken to calculate the growth ratio for each following time point. The ratios were plotted on a growth curve visualising the growth. The ratios were plotted on a growth curve visualising the growth. Volume was calculated using the formula $V = \pi \cdot ø^3/6$, with V=spheroid volume, ø = diameter.

2.3 Drug Treatments

2.3.1 Spheroid and monolayer drug treatments

Spheroids and monolayer cultures were treated with the following inhibitors: gamma-secretase inhibitor PF-3084014 Nirogacestat (CAS 1290543-63-3) (Insight biotechnology, HY-15185) (217). Dual MERTK/Flt3 inhibitor (CAS 2070015-17-5) (218) (Cambridge Bioscience, CAY166130), HDAC inhibitor Trichostatin A (TSA) (CAS 58880-19-6) (Stratech, S1045-SEL) (219).

For monolayer treatments, cells were seeded at 3000 cells/well in a volume of 100 µL in opaque-walled flat-bottom 96-well plates (Corning™, #3917) 24 hours prior to treatment to allow cells to attach. Growth medium was replaced with fresh complete medium containing the drug at desired concentrations. Control wells were treated with empty vehicle (DMSO or ethanol) at a maximum concentration of 0.001%.

Spheroids were seeded at 3000 cells/100 µL per well in U-shaped ULA 96-well microplates (Greiner Bio-One, 650979) 3 days prior to treatment. Following spheroid formation, 50 µL of media was carefully aspirated from each well without disturbing the spheroid and replaced with 50 µL of fresh GFS containing 2X the desired concentration of the drug.

2.3.2 Spheroid and monolayer viability assays

ATP-based cell viability was assessed using Promega's CellTiter-Glo® Luminescent Cell viability assay (Promega, G7570) for monolayers and Promega's CellTiter-Glo® 3D Cell viability (Promega, G9681) for spheroids. Viability was measured in triplicate for monolayers and in 8 multiples for spheroids. All reagents were thawed at room temperature and culture plates were equilibrated at room temperature for 30 minutes. For monolayer assessment, CellTiter-Glo® Buffer was completely added to the CellTiter-Glo® substrate provided and briefly vortexed to obtain a homogeneous solution forming the CellTiter-Glo® working reagent. 100 µL of CellTiter-Glo® working reagent was added to each well, resulting in a mixture of equal volumes of reagent and media. Contents were mixed for 2 minutes on an orbital shaker to start cell lysis, followed by a 10-minute incubation at room temperature in the dark. Luminescence was measured using the BMG Labtech FLUOstar Omega microplate reader. To control for background luminescence generated by the media, wells exclusively containing media without cells were included in the analysis.

For spheroid assessment, CellTiter-Glo® 3D reagent was gently mixed by inverting to obtain a homogenous solution. 100µL of CellTiter-Glo® 3D reagent was added to each well resulting in a mixture of equal volumes of reagent and media. Contents were mixed vigorously for 5 minutes on an orbital shaker to start spheroid lysis, followed by a 25-minute incubation at room temperature in the dark. Luminescence was measured using the BMG Labtech FLUOstar Omega microplate reader. To control for background luminescence generated by the media, wells exclusively containing media without cells were included in the analysis. Luminescence values were represented as a percentage of control.

2.4 shRNA lentivirus infection

Meningioma primary cells were seeded in 6-well plates at 70% confluence one day prior to lentiviral infection. Cells were infected with GIPZ lentiviral particles targeting Notch1 (Horizon discovery, VGH5526-EG4851). For infections, GIPZ lentiviral particles were diluted in pre-warmed media containing 8 µg/ml protamine sulphate (Sigma, P4020) at an MOI of 10. Control cells were infected with GIPZ lentiviral non-silencing shRNA control (scrambled shRNA) in the same manner. Infection efficiency was assessed by assessing GFP signal using fluorescent microscopy. After 72-96 hours, medium was replaced with fresh culture media. 24 hours later, infected cells were selected using 4 µg/ml puromycin (Thermo Fisher Scientific, A11138-03). A non-infected control well was included to control for puromycin selection. Cells were kept under puromycin selection medium for a minimum of 3 days and a maximum of 2 weeks. Knockdown efficiency was assessed by western blot analysis of the Notch1 NICD. Three shRNA constructs targeting Notch1 were used: VGH5518-200223927, clone id V3LHS_637132, VGH5518-200227270, clone id V3LHS_637131, VGH5518-200226034, clone id V3LHS_637134.

2.5 DNA extraction and next-generation sequencing

Total genomic DNA was extracted from frozen meningioma tissues and spheroids seeded at P1 (3 days post spheroid formation), using the Dneasy® Blood and Tissue kit (QIAgen, 69504) following manufacturers' instructions. Tissues were snap-frozen using liquid nitrogen at tissue processing (section 2.2.1). DNA concentrations and quality was estimated using the NanoDrop Spectrophotometer. DNA was sequenced using the Illumina TruSight Oncology 500 panel and the raw sequence data was analysed using the TruSight Oncology 500 v2.2 Local App externally at the Southwest Genomic Laboratory Hub (SWGLH) North Bristol. Next, variant calling data was processed using the online servers CGI (Cancer genome interpreter) (22,23) and wANNOVAR (24–26) to identify and annotate the driver mutations. All driver mutations were filtered based on variant sample coverage (≥90% at 50X according to the set threshold by the TSU500 local app), allele frequency (VF, ≥ 0.05) (27), read depth (DP ≥100) (28,29), ExAC (≤ 0.05) (30) and fathmm_MKL score prediction (D= damaging) (31,32). All filtered drivers between spheroids and parent tumours were compared to identify the common variants. Variant calling and annotating of driver mutations were kindly performed by Miss Maryam Shah.

2.6 RNA extraction

Total RNA was extracted from primary meningioma cell monolayers and spheroids and meningioma tissues using the Direct-zol™ RNA MiniPrep kit (Zymo Research, R2050) following manufacturers' instructions. Tissues were snap-frozen using liquid nitrogen in 500 µL of QIAzol™ Lysis Reagent (Qiagen, #79306) during tissue processing (section 2.2.1) and stored at -20°C. Cell monolayers were harvested using 0.25% Trypsin-EDTA (Thermo Fisher Scientific, #25200-056). Spheroids were collected in 1.5 ml microcentrifuge tubes. Cells were washed in 1X PBS, and resuspended in 500 µL of QIAzol™ Lysis Reagent. QIAzol™-resuspended samples were kept at -20°C overnight or until RNA extraction. Samples were retrieved from storage and thawed at room temperature for 10 minutes. Tissue and spheroid samples were homogenized using a glass pestle tissue grinder and sonicated in a Grant Ultrasonic bath XUBA1 sonicator for 2 cycles (2 minutes on, 1 minute off). Tubes were centrifuged at 1200 rpm for 5 minutes to remove cell debris prior to proceeding to the kit's instructions. RNA was eluted in 25 µL nuclease-free water (Life Technologies, Ambion™ Nuclease-free Water, AM9937) and stored at -80 °C. Quantification was carried out using the NanoDrop Spectrophotometer.

2.7 Messenger RNA (mRNA) sequencing and data analysis

For transcriptomic analysis, isolated RNA was sent to Novogene where RNA integrity was assessed and assigned an RNA Integrity Number (RIN). Samples with RIN > 5 were processed for sequencing. Details of RNA integrity for each sample can be found in table 2.3. At Novogene, mRNA was purified from total RNA using poly-T oligo-attached magnetic beads and cDNA libraries were generated. Libraries were quantified using Qubit. Libraries were sequenced using an Illumina platform and paired-end reads were generated. Raw data (raw reads) of fastq format were processed to generate clean data (clean reads). Reads containing adapters, reads containing poly-N and low-quality reads were removed from raw data. Q20, Q30 and GC content of clean data were calculated. All downstream analyses were based on clean data with high quality. Paired-end clean reads were aligned to the reference genome using Hisat2 v2.0.5. The tool 'featureCounts v1.5.0-p3' was used to count the reads numbers mapped to each gene. FPKM of each gene was calculated based on the length of the gene and the reads count mapped to this gene. Differential expression analysis was performed using the DESeq2Rpackage (1.20.0). Resulting P-values were adjusted using the Benjamini and Hochberg's approach for controlling the false discovery rate (FDR). Genes with an adjusted P-value < 0.05 were assigned as differentially expressed. For Gene Set Enrichment Analysis (GSEA), genes were ranked according to the degree of differential expression and the predefined gene sets (GO or KEGG) were tested for enrichment. The local version of the GSEA analysis tool https://www.gsea-msigdb.org/gsea/index.jsp was used. All steps described above were performed by Novogene. ClueGO Gene ontology analysis was performed by uploading defined gene lists to the Cytoscape plug-in ClueGO (220). The kappa score threshold was set to 0.4.

Table 2.3 RNA samples and quality

Sample	Total amount (µg)	RIN	Status (E = excluded, I = included)	Reason for exclusion
MN487_3D	0.23745	3.4	E	unqualified integrity
MN490_3D	0.56716	9.6	I	N/A
MN491_3D	0.24394	10	E	Insufficient total amount
MN493_3D	0.25934	10	E	Insufficient total amount
MN504_3D	0.92383	10	I	N/A
MN516_3D	1.68522	10	E	Matched sample excluded
MN518_3D	1.68385	10	E	Matched sample excluded
MN521_3D	2.23078	10	I	N/A
MN523_3D	0.54431	10	I	N/A
MN524_3D	0.55131	8.2	E	Matched sample excluded
MN525_3D	1.70765	9.8	I	N/A
MN581_3D	0.45500	7.9	E	Matched sample excluded
MN588_3D	2.90000	9.3	E	Matched sample excluded

MN591_3D	0.83200	6.0	E	Matched sample excluded
MN592_3D	1.12000	9.3	E	Matched sample excluded
MN593_3D	0.76700	8.9	E	Matched sample excluded
MN595_3D	3.91000	9.7	I	N/A
MN609_3D	4.00000	9.4	I	N/A
MN610_3D	0.94000	9.4	E	Matched sample excluded
MN611_3D	2.36000	5.8	I	N/A
MN613_3D	1.71600	9.2	I	N/A
MN614_3D	2.66000	9.6	I	N/A
MN646_3D	1.16000	4.8	E	Matched sample excluded
MN655_3D	1.63900	8.0	I	N/A
MN656_3D	1.83680	8.5	I	N/A
MN658_3D	1.84800	6.9	I	N/A
MN487_2D	0.31022	10	E	Insufficient total amount
MN490_2D	5.78288	10	I	N/A
MN491_2D	2.34074	10	E	Matched sample excluded
MN493_2D	2.83375	1.6	E	unqualified integrity
MN504_2D	3.84083	10	I	N/A
MN516_2D	4.72784	10	E	Matched sample excluded
MN518_2D	3.95891	10	E	Matched sample excluded
MN521_2D	3.85913	10	I	N/A
MN523_2D	1.39556	10	I	N/A
MN524_2D	0.79353	9.9	E	Matched sample excluded
MN525_2D	1.45491	10	I	N/A
MN581_2D	4.56980	5.1	E	Matched sample excluded
MN588_2D	1.59000	9.4	E	Matched sample excluded
MN591_2D	1.43000	7.6	E	Matched sample excluded
MN592_2D	4.84000	9.6	E	Matched sample excluded

MN593_2D	2.27760	6.1	E	Matched sample excluded
MN595_2D	0.42000	8.0	I	N/A
MN609_2D	4.64880	9.1	I	N/A
MN610_2D	1.56000	9.7	E	Matched sample excluded
MN611_2D	3.08000	9.3	I	N/A
MN613_2D	2.89000	9.8	I	N/A
MN614_2D	0.65000	7.8	I	N/A
MN646_2D	3.99000	7.9	E	Matched sample excluded
MN655_2D	2.60650	6.2	I	N/A
MN656_2D	5.66640	8.7	I	N/A
MN658_2D	3.10980	6.0	I	N/A
MN487_T	1.75963	3.5	E	unqualified integrity
MN490_T	2.00875	9.3	I	N/A
MN491_T	1.07692	3.4	E	unqualified integrity
MN493_T	1.56077	3.5	E	unqualified integrity
MN504_T	0.71339	9.7	I	N/A
MN516_T	1.05832	3.6	E	unqualified integrity
MN518_T	1.71956	3.3	E	unqualified integrity
MN521_T	6.11099	8.1	I	N/A
MN523_T	28.12946	7.1	I	N/A
MN524_T	5.12562	3.4	E	unqualified integrity
MN525_T	2.18625	7.8	I	N/A
MN581_T	0.09800	7.8	E	Insufficient total amount
MN588_T	N/A	N/A	E	no sample obtained
MN591_T	0.14000	1.2	E	unqualified integrity
MN592_T	0.16000	3.5	E	unqualified integrity
MN593_T	0.09800	1	E	unqualified integrity
MN595_T	0.43000	6.6	I	N/A

MN609_T	2.18000	7.7	I	N/A
MN610_T	0.16000	2.4	E	unqualified integrity
MN611_T	0.83200	4.2	I	N/A
MN613_T	2.03000	5.5	I	N/A
MN614_T	6.55000	6.0	I	N/A
MN646_T	0.03000	6.0	E	Insufficient total amount
MN655_T	0.75400	5.9	I	N/A
MN656_T	1.63200	5.3	I	N/A
MN658_T	2.33730	7.6	I	N/A

2.8 qPCR expression analysis

Reverse Transcriptase PCR was performed starting from 1 µg of total RNA using the High-Capacity cDNA Reverse Transcription Kit (Thermo Fisher Scientific, #4368814) according to the manufacturer’s instructions. Reverse Transcription was performed using the following thermal cycler conditions (Labtech, G-storm GS4 Thermal Cycler System): 1: 25 °C for 10 minutes, 2: 37 °C for 120 minutes, 3: 85 °C for 5 minutes, 4: 4 °C until retrieval from the machine.

Samples were stored at -20 °C or used for qPCR immediately. qPCR was performed in triplicates using Taqman™ probes (Thermo Fisher Scientific, Applied Biosystems, #4331182) (table 2.4). cDNA was diluted using nuclease-free water and plated in a white 96-well microplate (Axygen, PCR-96-LC480-W-NF) at a volume of 10 µL. A mother mixture containing all other components of the reaction mixture was prepared containing Taqman™ 20X probe, Taqman™ Fast Advanced Master Mix (Thermo Fisher Scientific, Applied Biosystems, #4444557) and nuclease-free water. qPCR was run using the following program: 1: Hotstart 95 °C for 2 minutes; 2: Amplification (45 cycles of 15 seconds at 95 °C, 1 minute at 60 °C, 30 seconds at 40 °C). Gene expression was normalized to expression levels of two housekeeping genes GAPDH and RPL37A. Gene expression was quantified using the delta-delta Ct method (221).

Table 2.4: List of Taqman primers

Gene	**Taqman probe**
CDH1	Hs01023895_m1
GAPDH	Hs02786624_g1
Hes1	Hs00172878_m1
Hey1	Hs01114113_m1
Notch1	Hs01062014_m1
RPL37A	Hs01102345_m1
Snai1	Hs00195591_m1
Snai2	Hs00161904_m1
Zeb1	Hs00232783_m1
ZO-1	Hs01551861_m1

2.9 3D Matrigel™ invasion assay

To assess spheroid invasion capacity, spheroids were formed from passage 0 primary meningioma cells, forming P1 spheroids. 3 days post-seeding, compact spheroids were formed, and media was carefully aspirated without disturbing the spheroid. Matrigel (Thermo Fisher Scientific, 356234) was thawed on ice and 80 µL was carefully added to each well to embed spheroids in Matrigel™ drops avoiding air bubbles. Spheroids were gently positioned in the centre of the well using a pipet tip. Microplates were placed in the incubator for 30 minutes to allow Matrigel™ to set. When Matrigel was solidified, 100 µL of GFS was added to each well. In drug experiments, the drug was added to the media at desired concentrations. Spheroids were assessed for cell invasion 24 and 48 hours post-embedding using bright-field microscopy at 10x magnification (Leica, IM8). Invasion was measured as max. diameter of invaded area using ImageJ. Images were exported as TIFF and opened in ImageJ. A circle was drawn around the outer layer of invading cells and the maximal diameter was measured using the line measuring tool. The data was plotted as relative increase of invasion compared to controls.

For fluorescent staining of embedded spheroids, embedded spheroids were fixed by adding 4% PFA in each well until complete Matrigel droplet was covered for 30-minutes. PFA was removed and washed using 1X PBS. Spheroids were permeabilized with 0.5% Triton-X-100 (Sigma, T9284) for 1 hour at room temperature followed by three 5-minute washes in 1X PBS. Spheroids were incubated with DAPI (1:500) (Merck, D9542) and Alexa Fluor 488 Phalloidin (Thermo Fisher Scientific, A12379) at a concentration of 1:500 for 1 hour at room temperature followed by three 5-minute washes in 1X PBS. Spheroids (still embedded in Matrigel) were retrieved from the wells by using cut pipette tip and mounted on a slide for imaging. Fluorescence images were taken using fluorescence confocal microscopy.

2.10 Western blotting

2.10.1 Protein extraction

Monolayer cultures

For protein extraction of monolayer cultures, growth medium was aspirated and cells were washed in ice-cold PBS (1X). Lysis buffer (radioimmunoprecipitation assay buffer (RIPA) buffer (Thermo Fisher Scientific, Pierce™, #89900) supplemented with 1% phosphatase and protease inhibitor cocktail (Thermo Fisher Scientific, Halt™, #1861281)) was added and cells were detached using a sterile cell scraper (Thermo Fisher Scientific, #08-100-241) on ice. Lysates were collected in 1.5mL microcentrifuge tubes (Alpha laboratories, LW2375) and incubated on ice for 15 minutes. Lysates were centrifuged at maximum speed for 15 minutes to remove cellular debris and supernatant was transferred to a clean 1.5mL microcentrifuge tube. Lysates were stored at -80°C.

Spheroid cultures

Spheroids were collected in 1.5mL microcentrifuge tubes and let to settle down by gravity. Media was carefully aspirated, and spheroids were washed in 1X ice-cold PBS. PBS was removed and spheroids were resuspended in lysis buffer (approximately 50 µL per 96 spheroids). Spheroids were subjected to 3 cycles of freezing in liquid nitrogen and thawing in a heat block at 37°C. Next, spheroids were sonicated for 2 cycles of 2 minutes sonication and 1 minute rest on ice, using a water bath sonicator (Grant Ultrasonic bath XUBA1) to ensure complete spheroid lysis. Lysates were centrifuged at maximum speed for 15 minutes at 4°C to remove cellular debris and supernatant was transferred to a clean 1.5mL microcentrifuge tube. Lysates were stored at -80°C. On average, 96 spheroids were used per lysate.

Tissue samples

Tissue samples were homogenised manually in lysis buffer. The volume of lysis buffer used was estimated as 0.1mL per 100 mg weight. Homogenised tissues were placed at -80°C for at least 24 hours. Next, they were thawed on ice and centrifuged at maximum speed for 15 minutes at 4°C. Supernatant was collected and stored in a clean 1.5 mL microcentrifuge tube. Lysates were stored at -80°C.

2.10.2 Total protein quantification

For total protein quantification, the Pierce™ BCA Protein Assay kit (Thermo Fisher Scientific, 23225) was used. A standard curve was generated using 2 mg/ml Bovine Serum Albumin (BSA) (Thermo Fisher Scientific, BP1600) provided with the kit by diluting with ddH_2O into stock concentrations of 0, 25, 125, 250, 500, 750, 1000, 1500, and 2000 µg/ml BSA. Lysates were diluted 10 times to limit sample waste. To control for background absorbance produced by the lysis buffer, a blank sample of 10 times diluted lysis buffer in ddH_2O was included in the analysis. 25 µL of the blank, each standard, and each diluted lysate was pipetted into a 96-well microplate in duplicate. Working reagent was prepared by mixing reagent A with reagent B provided in the kit at a ratio of 50:1, and 200 µL was added to each well. The plate was incubated for 30 minutes at 37°C and absorbance was measured at 562 nm in the BMG Labtech FLUOstar Omega microplate reader. The absorbance values of the standards were used to plot a standard curve and sample concentrations were calculated using the linear equation formula of the standard curve using Microsoft Excel. The concentration of the blank was subtracted from that of the samples and concentration values were corrected for the dilution factor.

2.10.3 Sodium dodecyl sulphate polyacrylamide gel electrophoresis (SDS-PAGE)

Samples were prepared by mixing 20 µg of protein with 6X Laemmli buffer (Thermo Fisher Scientific, #15493939) to a final concentration of 1X. Proteins were denatured by boiling the samples in a heat block at 95°C for 5 minutes. Samples were allowed to cool down to room temperature. Proteins were separated according to size by gel electrophoresis using 4-15% gradient polyacrylamide gels (Bio-Rad, mini-PROTEAN TGX gels, 4561084). Gels were placed in a gel holder cassette which was placed in an electrophoresis chamber filled with 1X running buffer (4.55 g Trizma base, 21.6 g glycine, 1% SDS up to 1L of ddH_2O). Samples and 8 µL of precision plus pre-stained dual color protein ladder (Bio-Rad, #1610374) were loaded into the gel and run at 110V for 90 minutes.

2.10.4 Immunoblotting

After protein separation, proteins were transferred onto an activated polyvinylidene fluoride (PVDF) membrane using the Bio-Rad Trans-blot® Turbo™ transfer system at 2.5A constant, up to 25V, for 10 minutes. The PVDF membrane was activated in 100% methanol (VWR International Ltd, 20847.307) for 2 minutes. Blotting paper was soaked in 1X Turbo buffer (200 mL 5X Turbo buffer (Bio-Rad, 10026938), 200 mL 100% ethanol (VWR International Ltd, 20821.330), 600 mL ddH_2O) prior to transfer.

After transfer, membranes were blocked using 5% BSA (Thermo Fisher Scientific, BP1600) in 1X Tris Buffered Saline (100 ml 10X TBS (Thermo Fisher Scientific, J62938.K7) + 900 ml ddH_2O) with 0.05% Tween-20 (Sigma-Aldrich, P7949) (TBS-T) for one hour and incubated with primary antibodies overnight at 4°C under constant rotation. Primary antibody details are listed in table 2.5. To detect several proteins at the same time, membranes were cut at the desired size. The following day, primary antibodies were removed, and membranes were washed in 1X TBS-T 3 times for 15 minutes at room temperature on the shaker. Membranes were incubated with the appropriate HRP-conjugated secondary antibody (table 2.6) for 1 hour at room temperature followed by 3 15-minute washes in 1X TBS-T. Proteins were developed using the Pierce™ ECL western blotting substrate (Thermo Fisher Scientific, #32106) or the SuperSignal™ West Femto maximum sensitivity substrate (Thermo Fisher Scientific, #34095) depending on signal strength. Chemiluminescence signal was detected with the Syngene Pxi system. Membrane stripping was performed by washing the blot twice with 1X TBS-T for 5 minutes, followed by 5 minutes incubation in Restore™ PLUS Western Blot Stripping Buffer (Thermo Fisher Scientific, #46430). Stripping buffer was rinsed off with 1X TBS-T and membranes were re-blocked and re-probed accordingly.

Table 2.5: List of primary antibodies for Western blotting

Antibody	**Company**	**Catalogue number**	**Species**	**Dilution**
E-cadherin	Cell Signaling Technology	3195	Rabbit	1:500
N-cadherin	Cell Signaling Technology	13116	Rabbit	1:1000
Notch-1 NICD	Cell Signaling Technology	3608	Rabbit	1:1000
Slug	Cell Signaling Technology	9585	Rabbit	1:1000
GAPDH	Millipore	MAB374	Mouse	1:50000

Hes1	Cell Signaling Technology	11988	Rabbit	1:1000
Hey1	Abcam	Ab154077	Rabbit	1:1000
Vimentin	Cell Signaling Technology	3932	Rabbit	1:1000

Table 2.6: List of secondary antibodies for Western blotting

Antibody	**Company**	**Catalogue number**	**Dilution**
Goat anti-Rabbit IgG (H+L)-HRP conjugate	Bio-Rad	1706516	1:5000
Goat anti-Mouse IgG (H+L)-HRP conjugate	Bio-Rad	1706516	1:5000

2.10.5 Densitometry

Western blot results were quantified following a densitometry approach using ImageJ software. Bands were measured at the molecular weight specified by the antibody datasheet; all other non-specific bands were not included in the measurements. To take the measurements, the “rectangular selections” tool was selected and a rectangle was drawn around the first band. The rectangle was analyzed by imageJ using the “Gel analysis” tool (analyze > gels > select first lane). Next, the box was dragged over the second band and analyzed by clicking analyze > gels > select next lane. This step was repeated until all bands were selected. Finally, to plot the results, analyze > gels > plot lanes was selected, and the signal profile of each band was plotted in a separate window. The area under the curve of each peak was measured by drawing a straight line under the peak and using the “wand tracing” tool to measure the peak area. All values were normalized to the signal of the loading control protein GAPDH generating relative density of the protein of interest by dividing the value of target protein to the value of the loading control of that same lane. For drug treatments, after normalization to loading control, results were normalized to the untreated control to show the relative increase or decrease compared to the control. This was calculated by dividing all values by the value of the control sample.

2.11 Immunocytochemistry (ICC)

Meningioma primary spheroids were collected in 1.5 mL microcentrifuge tubes and washed in 1X PBS before fixing with 4% paraformaldehyde (PFA) (Fisher Scientific, Pierce™, #28908) for 30 min at room temperature. Spheroids were left to settle to the bottom of the tube by gravity and PFA was carefully aspirated, followed by three 5-minute washes in 1X PBS. Spheroids were permeabilized with 0.5% Triton-X-100 (Sigma, T9284) for 1 hour at room temperature followed by three 5-minute washes in 1X PBS. Non-specific binding of antibodies was blocked by incubating spheroids in blocking buffer containing 1% BSA and 10% normal goat serum (Abcam, ab7481) in 1X PBS for 2 hours at room temperature or overnight at 4 °C. Spheroids were incubated with anti-ki67 primary antibody diluted in 1% BSA in 1X PBS at a dilution of 1:100 overnight at 4 °C (Agilent Technologies Ltd, Dako, mouse anti-Ki67 (MIB-1), M7240). The next day, primary antibody was removed by three 15-minute washes in 1X PBS which was followed by incubation with secondary antibody goat anti-mouse IgG Alexa Fluor 594 (Thermo Fisher Scientific, #A1100) diluted (1:250) in 1% BSA in 1X PBS overnight at 4 °C while protected from light. The following day, secondary antibody was removed by three 15-minute washes in 1X PBS followed by incubation with nuclear stain DAPI (Merck, D9542) at a dilution of 1:500 for 1 hour in the dark at room temperature. DAPI was removed by three 15-minute washes in 1X PBS prior to mounting the spheroids on SuperFrost® Plus microscope slides (VWR International Ltd, #631-0448). Spheroids were mounted by resuspending spheroids in a small volume of 1X PBS and transferred onto the slide in a dropwise manner. The excess PBS was carefully removed without disturbing the spheroids. Vectashield® antifade mounting media (Vector Laboratories, H-1000) was pipetted onto the slide and spheroids were covered with a coverslip. Slides were sealed using nail varnish. Slides were imaged using 20X or 40X magnification using the Leica Confocal SP8 microscope.

2.12 Immunohistochemistry (IHC)

Immunohistochemistry staining of SSTR2, KI67, CD68, CD163, E-cadherin, Vimentin, and H&E staining, were kindly carried out by the Neuropathology department based within the department of Cellular and Anatomical Pathology of the Derriford Hospital in Plymouth. Spheroids were formalin-fixed 3 days post spheroid formation and brought to Neuropathology for paraffin embedding. Meningioma tissues were embedded as part of standard procedure post-surgery at Derriford hospital and Southmead hospital Bristol. Formalin Fixed Paraffin Embedded (FFPE) tissue and spheroid sections were cut at 4µm. Antibody optimisation was performed on sections of the BRAIN UK archives- UHP multi-tissue block, which contained sections of several tumours including meningioma sections. Positive control tissues were included in each antibody run. For immunodetection, sections were stained using the primary antibodies: CD68 (1:50) (Agilent Cat# M0876), CD163 (1:50) (Roche Cat# 05973929001), E-cadherin (1:50) (Agilent Cat# M3612), SSTR2 (1:400) (Abcam Cat# ab134152), Vimentin (1:2000) (Agilent Cat# M0725), Ki67 (1:100) (Agilent Cat# M7240) using the Ventanna automated machine. Nuclei were counterstained with haematoxylin (Merck). Images were acquired using a Leica DMRB microscope with the help of consultant neuropathologist, Dr David Hilton (Department of Cellular and Anatomical Pathology at Derriford hospital Plymouth).

2.13 Statistical analysis

GraphPad Prism data analysis software was used throughout the project to calculate the statistical significance of each experiment. The test used for each experiment is mentioned in the figure legend of each experiment. Significance levels are indicated as follows: ns = not significant ($p>0.05$), * = $p<0.05$, ** = $p<0.01$, *** = $p<0.001$.

3 Establishment and characterisation of a patient-derived meningioma spheroid model

3.1 Introduction

Current treatment strategies for meningiomas, surgery and radiotherapy, have a risk of post-operative morbidities, radiation neurotoxicity and tumour recurrence (3,67). Despite the comprehensive understanding of the genetic background of meningiomas and the mutations (NF2, TRAF7, AKT1, KLF4, SMO, POLR2A, PIK3CA, SMARCE1, SMARCB1, hTERT, CDKN2A/2B) underlying tumour development and progression (7–10), progress in the development of therapeutic approaches targeting genetically stratified tumours remains limited and all current pharmacotherapeutic approaches remain experimental (6,67). Hence, the development of effective drug-based therapeutics is imperative.

The diverse immune microenvironment of meningiomas has been demonstrated to influence meningioma pathogenesis (222,223). For example, a high degree of macrophage infiltration (CD68+ macrophages and CD163+ M2 macrophages) has been associated with tumour aggressiveness and therapy resistance of meningiomas and immunotherapy for treatment of meningiomas, including immune checkpoint inhibitors, are currently under investigation (40,64,70). Therefore, to investigate effective molecular therapies for meningiomas, the use of experimental models that can closely resemble patient tumours, including the immune microenvironment, and thus predict therapy response to bridge the translational gap between *in vitro* and *in vivo* results, is crucial (119,224).

A well-established method that is often used to test the therapeutic response to novel drug compounds is the use of patient-derived cells. These cells are typically propagated as two-dimensional (2D) monolayers (225). However, 2D monolayer cultures have limited predictive value due to the highly artificial culture conditions of being attached to the flat surface of culture dishes (118,225). Therefore, three-dimensional (3D) cell culture methods have been developed and demonstrated as more physiologically relevant *in vitro* experimental tools for tumour modelling compared to conventional 2D monolayer culture (118). Specifically, 3D cultures harbour the power to resemble *in vivo* tumours with respect to tissue-specific architecture, cell-cell and cell-microenvironment interactions, growth patterns and penetration gradients of oxygen and drugs (118). Therefore, development of accurate 3D model systems for meningiomas can improve the accuracy of drug developmental studies by modelling patient-specific characteristics and the TME (16).

For meningiomas, several patient-derived 3D models have been described (17,19,20), although to my knowledge no previous work has focused specifically on the preparation of patient-derived multicellular spheroids from WHO grade 1 and 2 meningiomas. This chapter addresses the first part of this thesis' hypothesis: is it feasible to establish a novel culture method for the generation of 3D patient-derived meningioma cultures. This is answered by a set of experiments that led to the establishment of an easy-to-use method for the generation of novel easy-to-use patient-derived multicellular meningioma spheroids. Additionally, the hypothesis that these cultures resemble essential features of *in* vivo meningioma tissues is also addressed. Several parameters, including cell seeding density, spheroid morphology, growth medium composition, spheroid histology, and mutational profile were evaluated to provide a detailed characterisation of this model. Furthermore, I investigated how the global transcriptomes of these newly established meningioma spheroids compared to those of traditional 2D cultures and how these related to the transcriptomes of matched patient tissues. Together, these results demonstrated that this novel 3D culture method is feasible for WHO grade 1 and WHO grade 2 meningiomas and that this novel spheroid model recapitulates histological and molecular features of patient tissues such as the maintenance of diverse cell populations, including tumour cells and macrophage populations and the maintenance of driver mutations. Comprehensive characterisation of the transcriptomes of 3D cultures, 2D cultures and parental tumour tissues revealed the biological processes that are affected by the different culture methods, which highlighted how the model can be best exploited to approach meningioma research.

3.2 Optimization of tissue digestion for primary meningioma cell extraction

To ensure optimal extraction of all cell populations from meningioma tissues, the protocol for cell isolation was optimized. In our original protocol, tumour specimens were enzymatically digested using collagenase 3A. Prolonged exposure to enzymes has been associated with reduced cell viability (226). Therefore, I tested whether it was possible to digest meningioma specimens without enzyme incubation (Fig. 3.1). I observed that in the absence of enzymatic digestion, instead of digestion of the tumour specimen into a single-cell suspension, fragments of approximately 0.1 – 1 mm^2 remained intact. Nevertheless, these fragments would attach to the culture dishes and cells in the fragments would proliferate (Fig. 3.1C, D). Thus, removing enzymatic digestion did not limit primary cell extraction. Therefore, the addition of collagenase 3A seemed unnecessary, whilst it could potentially be harmful. Therefore, I chose to remove this step from the protocol.

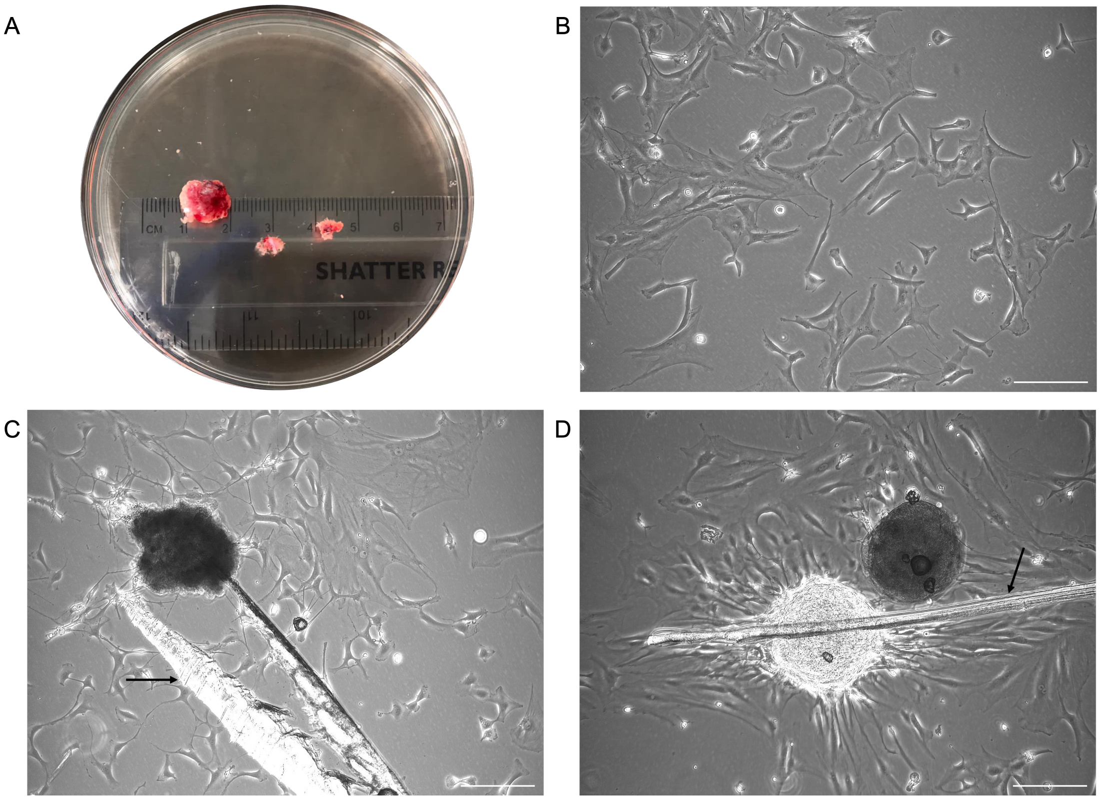

Figure 3.1 Primary meningioma cell extraction from specimen post-surgery

Representative images of meningioma specimen post-surgery (A) before and (B-D) after cell extraction. (B) Extracted single-cell suspension after enzymatic digestion attached to cell culture dishes. (C-D) Tumour fragments after mechanical digestion attach and release cells. Mechanical digestion can result in harmless cuts in the plastic (indicated with arrows). Representative: (A) MN428, (B-D) MN652. Leica IM8 microscope at 10X objective. Scale bar: 200 µm.

3.3 Optimization of patient-derived meningioma spheroid protocol

For spheroid generation, meningioma cells were isolated from intracranial meningioma specimens at the earliest opportunity after surgical intervention. To establish a reproducible spheroid model, several parameters important for spheroid generation were assessed. The first parameter to define was when to seed primary cells for spheroid generation. For this purpose, cells were seeded in T25 flat bottom ultra-low adherent (ULA) cell culture flasks directly after primary cell extraction (passage 0, P0) (Fig. 3.2A) and after initial attachment to cell culture dishes (passage 1) (Fig. 3.2B). For cells seeded from P0, seeding density could not be determined, for cells seeded from P1, approximately 100.000 cells were seeded in T25 flat-bottom ULA cell culture flasks. Spheroid generation was observed in both conditions. However, in P0 conditions, debris from the tumour digestion remained surrounding the spheroids (Fig. 3.2A). In contrast, for the P1 spheroids, initial cell attachment allowed for the selection of viable cells, eliminating cellular debris. In both conditions, the generation of multiple spheroids of various sizes were observed. In addition, both conditions contained single cells that were not included in any spheroid. Similar patterns in spheroid formation were observed when generating cells from P1+n following the same method. From these results, P1 was chosen as the method for spheroid generation.

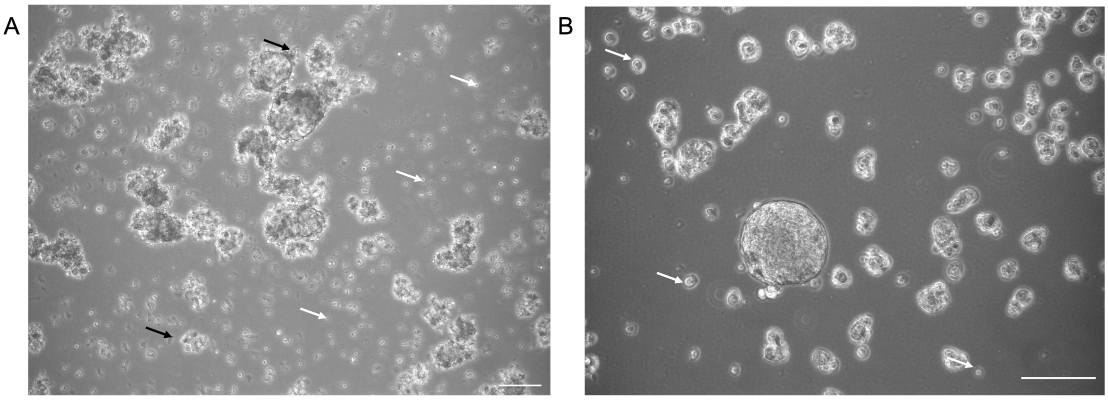

Figure 3.2 Assessment of optimal method for seeding primary cells for spheroid generation Brightfield microscopy images of primary meningioma cells seeded at (A) P0 and (B) P1 in ultra-low adherence (ULA) T25 cell culture flasks for spheroid formation after 72 hours. Spheroids were surrounded by debris (black arrows) and single cells (white arrows). Leica IM8 microscope, 10X objective. Scale bar: 200 µm. Representatives: (A) MN370, (B) MN377.

Next, it was assessed whether the use of u-bottom ultra-low adherence 96-well plates could promote the formation of a single spheroid per well, in order to control the number and size of spheroids generated. To do this, cells were seeded at varying cell densities in u-bottom ultra-low adherence 96-well plates, centrifuged and assessed for spheroid formation (Fig. 3.3A). The formation of a single spheroid was observed in each well. The spheroid formation process was analysed using two distinct medium formulations; the optimal medium for the propagation of meningioma monolayer cultures (MN1, *meningioma grade 1 medium*) and reduced-serum medium supplemented by growth factors previously described by Magill *et al.* (GFS, *growth factor supplemented medium*). GFS was included since this medium contained factors, e.g. EGF/bFGF and B27/N2, typically used in spheroid culture medium for other cell types, including brain, liver and breast cancer spheroids (101,227–229). Formation of compact spheroids was observed within 2 ± 1 days. The progress of spheroid formation is depicted in figure 3.3B. Spheroid formation was initiated after centrifugation in response to cell-cell contact. Within 24 hours, non-compact cellular aggregates were observed. The characteristic 3D structure was established 2-3 days post-seeding, confirmed by compact round-shaped spheroid structures with smooth edges. No differences were observed for spheroid formation between medium formulations.

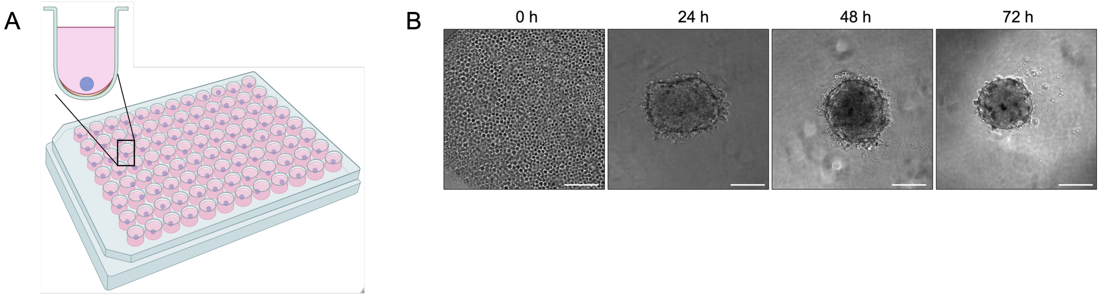

Figure 3.3 ULA 96 well plates allow for controlling the number of spheroids generated

(A) Schematic figure of a single spheroid/well generated using ULA 96 well plate. (B) Brightfield microscopy images showing the process of spheroid formation using GFS medium. Spheroid formation was initiated post-centrifugation in response to cell-cell contact (0h). Within 24 hours non-compact cellular aggregates were observed. The characteristic 3D structure was established

2-3 days post-seeding, confirmed by compact round-shaped spheroid structures with smooth edges. Representative: MN437.

3.4 Uniform-sized spheroids can be generated when controlling seeding conditions

Next, spheroid spatial features were assessed using brightfield microscopy. Spheroids with seeding densities of 1000, 3000 and 5000 cells/well were generated using MN1 or GFS medium using matched patient cells. Round spheroids with smooth edges were formed from all cell densities indicating the minimum number for spheroid formation as <1000 (Fig. 3.4A). The mean diameter for spheroids seeded at a density of 1000, 3000 and 5000 cells after 72 hours was respectively 196.7 ± 47.4, 331.3 ± 58.8, and 418.0 ± 66.2 μm for spheroids seeded in GFS and 180.5 ± 30.6, 307.7 ± 48.8, and 385.2 ± 75.5 μm for spheroids seeded in MN1 (Fig. 3.4B). Spheroid diameter was significantly increased with seeding density for spheroids in GFS, demonstrating spheroid diameter is controlled by seeding density. A similar trend was observed in spheroids in MN1, although this was not significant between seeding densities of 3000 and 5000 cells (Fig. 3.4B). Mean volume for spheroids seeded at a density of 1000, 3000 and 5000 cells/spheroids after 72 hours was respectively 4.43 ± 2.6, 20.2 ± 9.6, and 40.1 ± 17.2 μm^3 for spheroids seeded in GFS and 3.25 ± 1.4, 16.0 ± 6.7, and 32.2 ± 16.3 μm^3 for spheroids seeded in MN1 (Fig. 3.4C). Although a numerical difference was observed in diameter and volume between spheroids cultivated in GFS compared to MN1, with spheroids in GFS being consistently larger, this did not translate into a significant difference between GFS and MN1 for volume and diameter of spheroids with seeding density 1000 and 3000 and for diameter of spheroids with seeding density 5000 ($1000_{diameter}$: p=0.651, $3000_{diameter}$: p=0.305, $5000_{diameter}$: p=0.09; 1000_{volume}: p=0.230,

3000_{volume}: p=0.166, 5000_{volume}: p<0.05) (Fig. 3.4B, C). Additionally, the average standard deviation of the diameter in µm of spheroids generated from the same sample was 17.1 µm, 17.8 µm and 18.6 µm for spheroids seeded at a density of 1000, 3000 and 5000 respectively, indicating the generation of uniform spheroids per sample (seeding density and medium composition) (Fig. 3.4D).

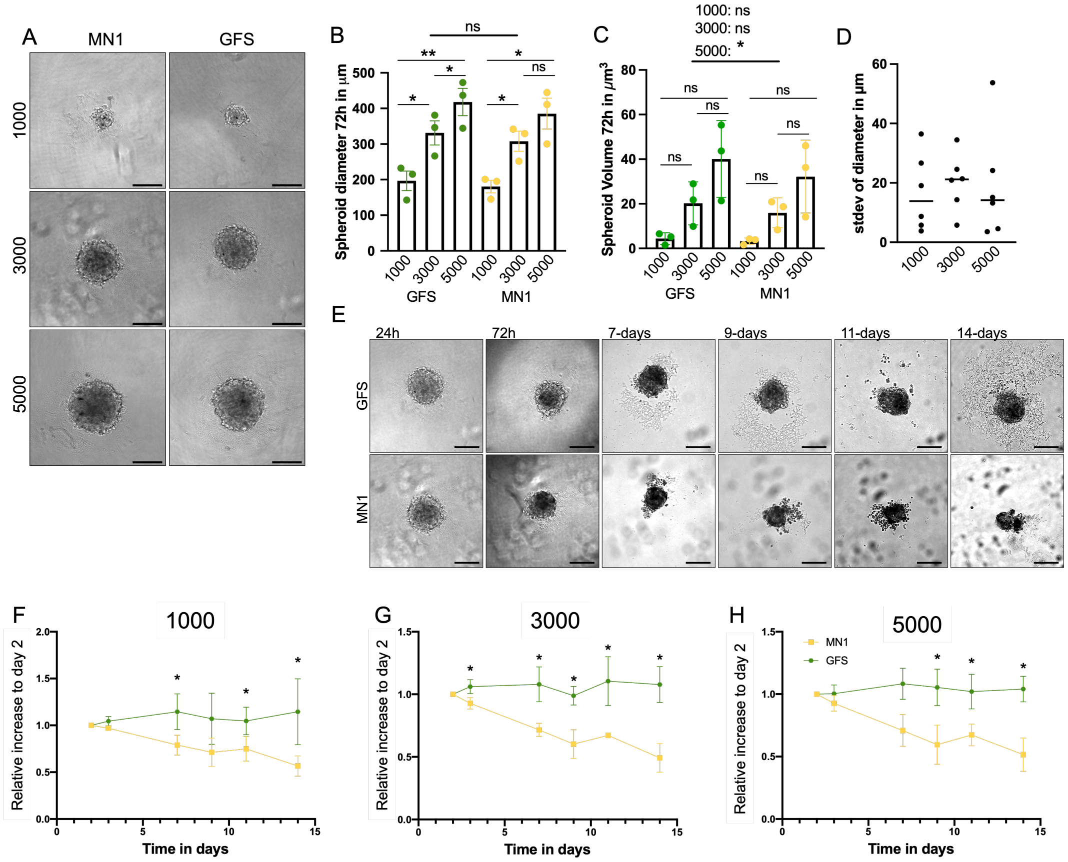

Figure 3.4 Spheroid size and growth are controlled by seeding density and medium composition (A) Representative brightfield microscopy images of spheroids formed from seeding densities of 1000, 3000 and 5000 cells/well in MN1 (yellow) and GFS (green) medium at 72h post seeding. (B-C) Bar graphs representing spheroid (B) diameter in µm and (C) volume in µm^3 at 72h of spheroids generated in GFS and MN1 for all analysed seeding densities (n=3). (D) Scatter plot of the average standard deviation of spheroid diameter in µm for spheroids derived from an individual patient sample in GFS (n=6). (E) Representative brightfield microscopy images of spheroid growth over a 14-day period with a seeding density of 3000 using MN1 and GFS (n=3). (F -H) Graphs of spheroid diameter over 14 days of spheroids of seeding density of (F) 1000, (G) 3000 and (H) 5000 cellls in MN1 (yellow) and GFS (green) medium (n=3). Data are represented

as the relative increase in diameter compared to size at day 2. Asterix indicates significant differences between the relative spheroid diameter in MN1 and GFS. One-way ANOVA: *$p<0.05$, **$p<0.01$. Images were taken with 10x objective, scale bar in each panel: 200µm. Representative MN437.

3.5 Spheroid growth and viability are dependent on growth medium

The effect of the two growth media MN1 and GFS on spheroid integrity, growth and viability was evaluated using 3 biological repeats of patient samples. Spheroids were seeded at 1000, 3000 and 5000 cells/spheroid and imaged by brightfield microscopy for a period of 14 days. Figure 3.4E shows the spheroid shape and integrity for spheroids with an initial seeding density of 3000 cells at various time points. Interestingly, while spheroid volume and diameter were not significantly different between GFS and MN1 on day 3 (Fig. 3.4B, C), spheroid volume and diameter did significantly differ between GFS and MN1 after 7 days ($p<0.05$) (Fig. 3.4E-H). Spheroids cultured in GFS and MN1 start to shed cell debris after 7 days, however, unlike spheroids growing in GFS, those growing in MN1 decreased in size (Fig. 3.4 E-H). This trend was continuously observed for the full 14-day period in spheroids of all three densities with no significant differences observed between the growth patterns of spheroids seeded at different densities. Generally, small spheroids are difficult to handle, while larger spheroids display less viable cells in their cores and have lower penetration efficiency (230). Thus, for the purpose of this thesis, an optimal seeding density of 3000 was chosen based on the following properties: visible by the naked eye, easy to handle while still allowing sufficient penetration and limited cell requirements.

3.6 Preparation of size-controlled patient-derived meningioma spheroids

After protocol optimization, patient-derived meningioma spheroids were successfully established from 96% (48/50) of the first 50 intracranial meningioma specimens that were assessed using u-bottom ULA 96-well plates under constant rotation (Table S3.1). Spheroids were formed from cells at P1 to separate cells from cellular debris. Uniform spheroids were generated by seeding primary meningioma cells in u-bottom ultra-low adherence 96-well plates at a seeding density of 3000 cells, forming one spheroid per well. Spheroids were seeded using GFS culture medium. Spheroids were successfully established from cells straight after digestion and cryopreserved cells. Figure 3.5 shows a schematic diagram of the spheroid protocol.

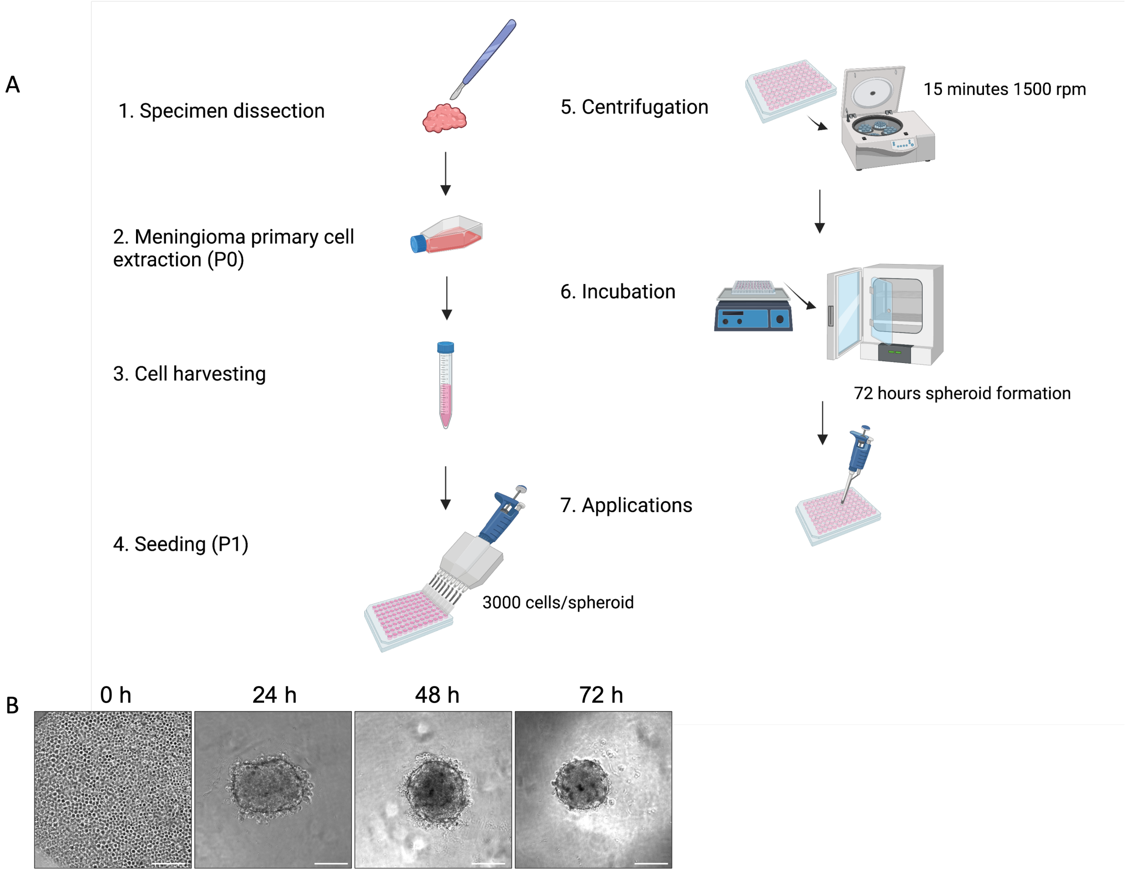

Figure 3.5 Establishment of 3D patient-derived meningioma spheroid model

(A) Schematic diagram of the protocol for the generation of patient-derived meningioma spheroids. (B) Representative brightfield microscopy images of spheroid formation: 0 hours- after centrifugation, 24 hours- cell aggregation, 48h-72 hours- compact spheroids, ready for use in downstream applications. Representative: MN437. Scale bar = 200μm. Figure was made using Biorender.

3.7 Meningioma spheroids exhibit histological and molecular features of parental tumours and models aspects of the tumour microenvironment

To investigate whether patient-derived spheroids could resemble the *in vivo* tumour characteristics of matched parent tissues or if certain characteristics are lost, immunohistochemical analysis was performed. The similarity of histological features was confirmed by pathologist Dr. David Hilton (Fig. 3.6). Haematoxylin & Eosin (H&E) staining revealed that the spheroids were solid structures, resembling the anatomy of meningioma *in vivo* (Fig. 3.6A, B). Spheroids were observed to retain histological characteristics such as prominent nucleoli and showed comparable levels of cellularity. There was no notable difference in cell density observed within the spheroids, although for some spheroids the outer rim of cells, that were directly in contact with the environment, showed a flattened morphology. Next, to obtain a more detailed picture of the cellular compositions of spheroids generated from WHO grade 1 and 2 tumours, immunostaining analysis was performed for several protein markers and stainings were given an immuno score by pathologist David Hilton ranging from 0 (no staining) to 4 (very strong staining). Spheroids generated from WHO grade 1 and 2 tumours showed similar levels of the proliferation marker Ki67 as compared to matched patient tissues (average immuno score of 1.29 for tissue and 1.57 for spheroids) (Fig. 3.6C) and retained expression of somatostatin receptor 2 (SSTR2), a marker commonly expressed by meningioma cells, although this staining was weaker in spheroids compared to tissue (average immuno score of 1.6 in spheroids compared to average score of 3.3 in tissue) (Fig. 3.6C). Additionally, spheroids lost expression of the epithelial meningioma marker EMA (epithelial membrane antigen) (Fig 3.6C).

To confirm the presence of infiltrating macrophages in our spheroid model, immunostaining analysis for the pan-macrophage marker CD68 and the M2 macrophage marker CD163 (Fig. 3.6) was performed. I could clearly identify the presence of CD68+ and CD163+ macrophages in all spheroids, indicating that important microenvironmental interactions are maintained in WHO grade 1 (Fig. 3.6A) and WHO grade 2 (Fig. 3.6B) derived spheroids. Together, these results validated that the model could represent important histological and immunohistochemical features of parental tumours.

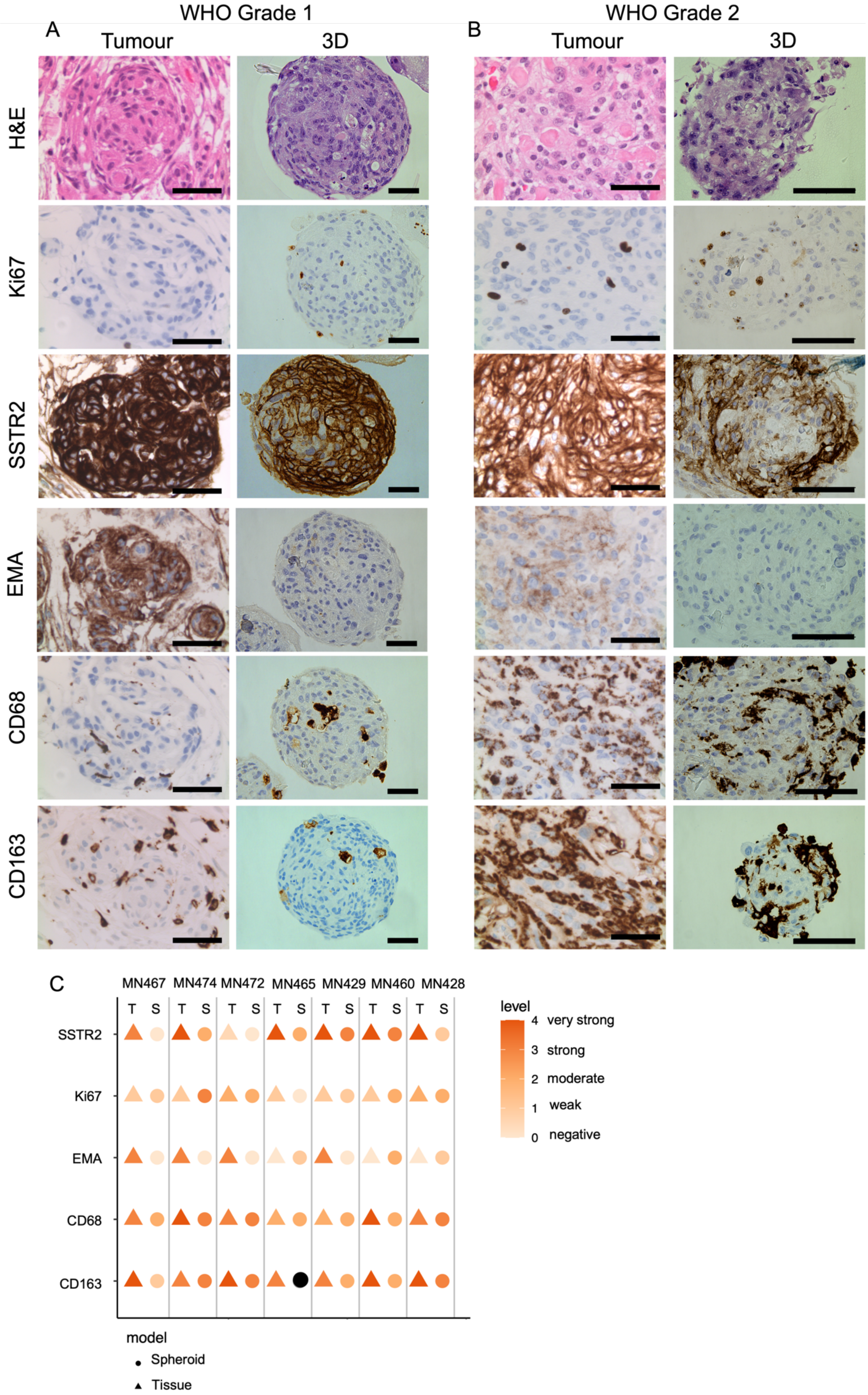
WHO Grade 1
A
Tumour
3D
WHO Grade 2
B
Tumour
3D
H&E
Ki67
SSTR2
EMA
CD68
CD163
C
MN467
MN474
MN472
MN465
MN429
MN460
MN428
T
S
SSTR2
Ki67
EMA
CD68
CD163
level
4 very strong
3 strong
2 moderate
1 weak
0 negative
model
Spheroid
Tissue

Figure 3.6 Patient-derived spheroids preserve histology, protein expression and immune components of matched tumour tissues Representative immunostaining images of (a) WHO grade 1 (n=6) and (b) WHO grade 2 (n=1) of patient tumour tissues (Tumour) and matched patient-derived meningioma spheroids (3D) in GFS at 72 hours post spheroid formation. Stainings are shown in order: H&E, anti-Ki67 (proliferation), anti-SSTR2 (meningioma marker), anti-EMA (meningioma marker), anti-CD68 (pan-macrophages) and anti-CD163 (M2-macrophages). Scale bars: 200μm. (c) Plot of immuno scores of stainings displayed in a and b in tissues, T, (triangle) and spheroids, S, (circle) (n=7). Colour represents immuno scores of 0-4 (0=negative, 1= weak, 2= moderate, 3= strong, 4= very strong) in orange. Black dot indicates no scoring.

3.8 Meningioma spheroids recapitulate genetic driver mutations

Meningioma spheroids were further characterised to see whether they maintained the genomic alterations of their matched parent tissues at 3 days post (P1) spheroid generation. Genomic analysis revealed that, on average 84.4% of all the identified driver mutations could also be detected in the patient-derived spheroids, with 100% preservation in 4 out of 6 cases (Fig. 3.7). Furthermore, the spheroids did not acquire any novel driver mutations that could not be detected in the matched patient tissues. Important driver mutations specifically associated with meningioma pathology (including NF2, TRAF7, SMO, PIK3C2B and AKT1) were consistently found in spheroids, except for a mutation in SMO in one of the samples (MN504). Details of all driver mutations identified in spheroids and tumour tissues can be found in appendix 1. Additionally, comparing the variant allele frequency (VAF) of detected driver mutations between spheroids and matched patient tumours revealed comparable VAF between both conditions for most cases (Fig 3.7, appendix 1). These results indicated that spheroid generation does not introduce genomic changes. Overall, these results showed that patient-derived meningioma spheroids conserved the genomic landscape present in matched parental tumours at the timepoint of use (shortterm fidelity at Passsage 1).

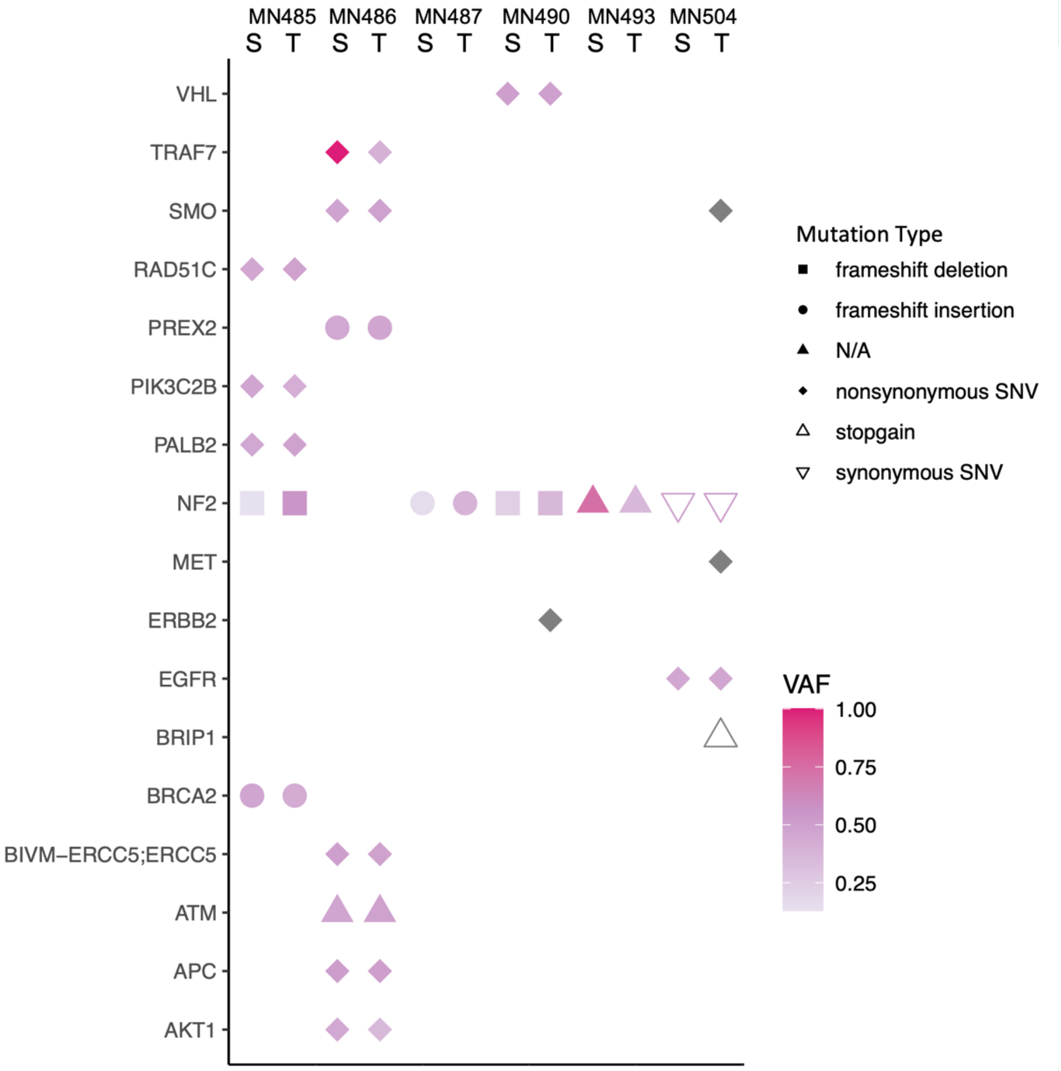

Figure 3.7 Patient-derived meningioma spheroids reflect the mutational profile of matched tumour tissues Comparison of driver mutations detected in spheroids (S) and matched tumour tissues (T) (n=6). Shapes indicate mutation type. Colour represents variant allele frequency (VAF) as indicated on the right of the graph. Pink shapes are detected in spheroids and tissues, while grey shapes are only detected in tissues. Details of driver mutations can be found in appendix 1.

3.9 Transcriptomes of 2D and 3D cell culture models and matched parental tissues show the highest correlation when compared to samples within their respective groups

Culture conditions have been described to influence the global transcriptome (228,231,232). To explore the similarities between the transcriptomes of the newly established 3D patient-derived spheroid cultures (n=13) and *in vivo* tumours (n=13), the transcriptomes of spheroid cultures were compared to those of matched patient tumour tissues. To understand how these similarities related to the *in vitro* monolayer model (2D), RNA extracted from monolayer cultures (n=13), derived according to the previously established protocol using normal cell culture medium (MN1), was also included in the analysis.

First, the correlation and variance of gene expression levels between groups and of samples within their respective groups, '2D', '3D' and 'Tissue' were assessed. Average correlation coefficients within groups were 0.887, 0.880, and 0.875 for '2D', '3D', and 'Tissue', respectively. The average correlation coefficient between groups was above 0.80 (R^2 = 0.84) when comparing '2D' with '3D', whilst comparing both '2D' and '3D' cell culture models to 'Tissue' individually the R^2 was below 0.80 (R^2 = 0.757 for 2D, R^2 =0.744 for 3D) (appendix 2 figure A1). Consistently, principal component analysis (PCA) of all sequenced samples revealed that samples from each condition (2D, 3D, Tissue) predominantly grouped together in principal component space, indicating that transcriptome signatures are more influenced by experimental conditions than by patient-specific characteristics. In addition, the clusters representing '2D' and '3D' showed low variance between each other as indicated by their proximity in principal component space, but showed higher variance compared to tissue, as indicated by the distance between both cell culture-derived groups and the tissue group (Fig. 3.8A). These findings were confirmed by hierarchical clustering analysis which showed the same pattern: two distinct clusters were identified, separating tissue samples (T) from cell culture models (2D and 3D). The cell culture cluster was further divided into two clusters mainly containing either '2D' or '3D' samples, although not all samples followed this pattern (Fig. 3.8B). For 3/13 patient samples, the 2D culture-derived samples clustered together with their respective matched 3D culture sample in the 3D cluster, while for 1/13, the 3D sample clustered together with its respective 2D culture sample in the 2D cluster. Furthermore, for 1/13 samples a different cluster pattern was observed in which the 2D sample clustered in the '3D cluster' but away from its matched 3D sample.

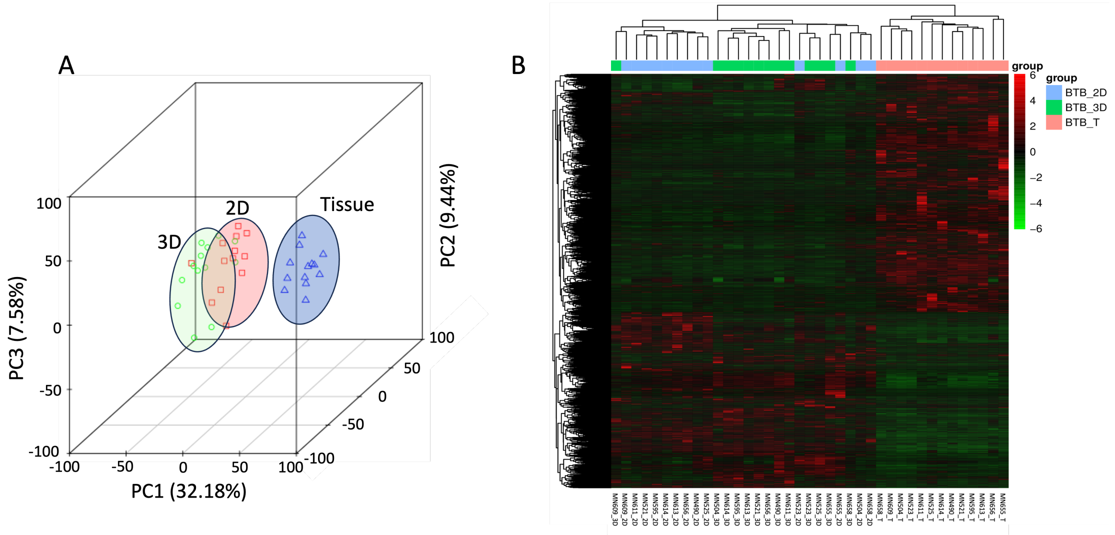

Figure 3.8 Transcriptomes of 2D and 3D cell culture models and matched parental tissues show the highest correlation when compared to samples within their respective groups

(A) Principal Component Analysis (PCA) plot explaining 49.3% of the variance based on three principal components (PC) (32.30%, 9.45% and 7.58% between the transcriptomes of samples derived from spheroids ('3D' green), ('2D' red) and Tissue ('T' blue). (B) Heatmap representing the hierarchical clustering analysis of the logarithmic transformation of gene expression values. Samples are divided split into two clusters, (1) tissue (2) cell culture, with the latter further split into a 3D and 2D cluster.

3.10 Co-expression analysis identified genes and associated biological processes uniquely represented by both cell culture models.

The correlation between groups was further investigated by performing a co-expression analysis. This analysis was used to identify which genes that are expressed in parent tissues were retained in both cell culture models (co-expressed) and which genes were unique to each group. 1370 genes were found uniquely expressed in tissues, whilst both cell culture models showed much lower numbers of uniquely expressed genes (299 for 2D and 353 for 3D) (Fig. 3.9). In addition, both cell culture conditions showed a similar number of genes co-expressed with tissue (11382 for 2D, 11375 for 3D) (Fig. 3.9). 331 out of 11382 transcripts that were co-expressed in 2D and Tissue, were not expressed in 3D cultures. Of these 331 transcripts, 234 were protein-coding transcripts (Fig. 3.10A).

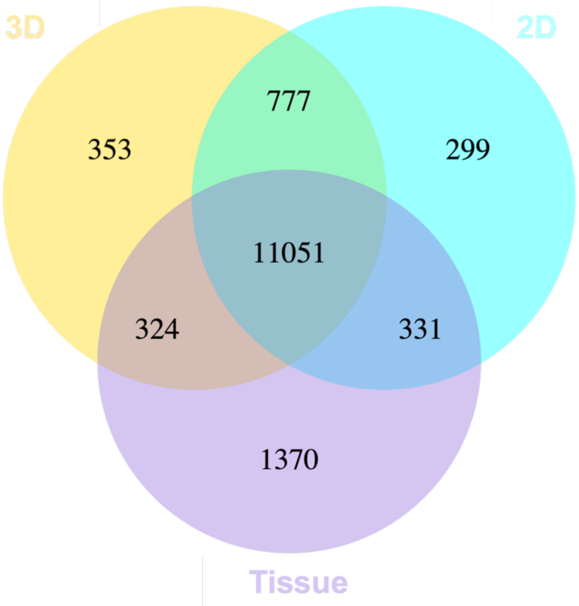

Figure 3.9 Co-expression of transcripts between 3D, 2D and Tumour tissues

Venn diagram depicting the distribution of 14505 transcripts identified across meningioma samples derived from three conditions 3D, 2D and Tissues. The Venn diagram was created by Novogene. 353, 299 and 1370 transcripts were uniquely identified in the transcriptomes of meningiomas derived from 3D, 2D or Tissue conditions.

To identify the biological processes these transcripts were associated with, they were submitted to the online gene ontology tool ClueGO (220), which is available as plug-in on the open-source platform Cytoscape. This tool annotates the biological function of genes by mapping the genes of interest to associated gene ontology (GO) terms. Gene ontology analysis on these 234 protein-coding transcripts only identified 1 group of biological processes significantly associated with these transcripts: ‘regulation of muscle contraction’ (Fig. 3.10B). A detailed table of this analysis can be found in appendix 3. The same analysis was performed on the 111375 transcripts co-expressed in 3D and Tissue. Of these, 324 transcripts were not expressed in 2D cultures, of which 221 transcripts were identified as protein-coding transcripts. Gene ontology analysis on these 221 transcripts revealed 6 clusters of biological processes associated with these transcripts (Fig. 3.10C, D). The 6 clusters were: “negative regulation of hh target transcription factor activity”, “lymphocyte apoptotic process”, “regulation of odontogenesis of dentin-containing tooth”, “long-chain fatty acid transport”, “regulation of macrophage activation” and “anterior/posterior pattern specification”. A full list of all GO terms identified can be found in appendix 3. This difference in the number of identified clusters suggested that, although 2D cultures had a slightly higher number of transcripts co-expressed with tissues compared to 3D cultures, these transcripts were involved in the same process. Contrastingly, the transcripts that were exclusively co-expressed in 3D and tissues, were associated with a larger number of processes.

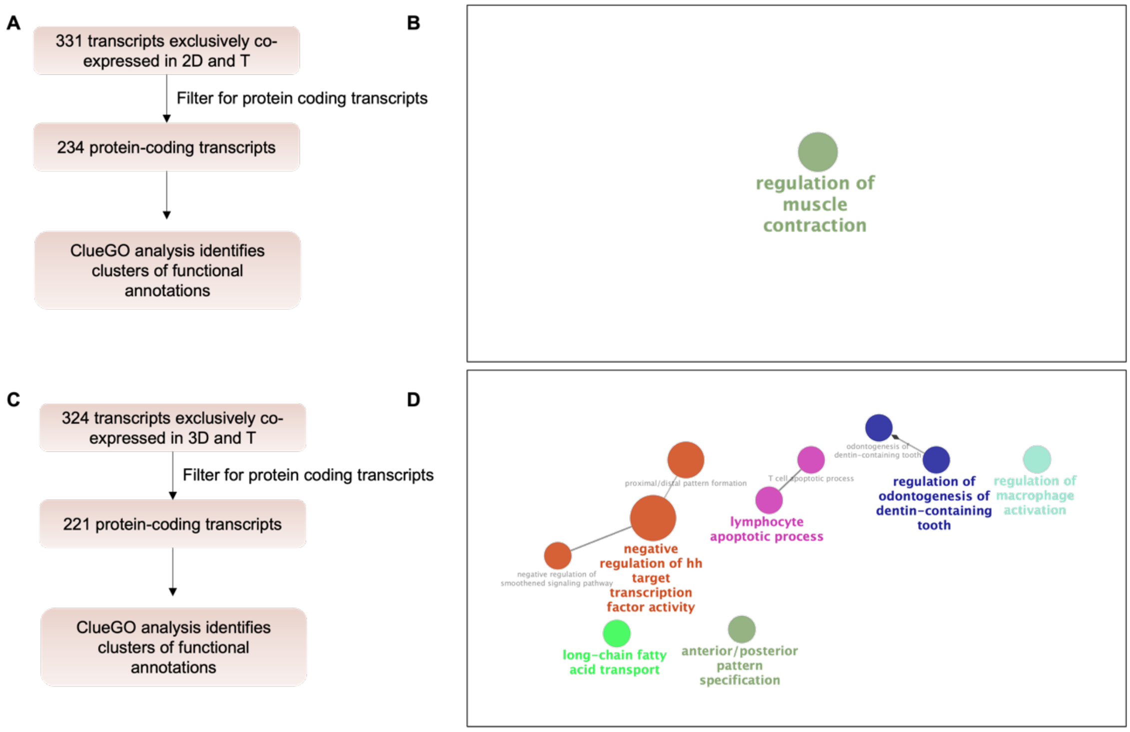

Figure 3.10 Functional annotation of genes exclusively co-expressed in either 2D or 3D and Tissue derived transcriptomes (A) flow chart of steps leading up to creating the network-based functional annotation shown in B. (B) Network depicting the biological function clusters identified using the ClueGO plug-in (v2.5.9) (220) in Cytoscape for functional annotation of 234 protein-coding transcripts exclusively co-expressed in 2D and tissue-derived transcriptomes. (C) flow chart of steps leading up to creating the network-based functional annotation shown in D. (D) Network depicting the biological function clusters identified using the ClueGO plug-in (v2.5.9) (220) in Cytoscape for functional annotation of 221 protein-coding transcripts exclusively co-expressed in 3D and tissue-derived transcriptomes. Created networks represent the terms as nodes which are linked (edge) based on their kappa score level (Kappa score treshhold: 0.4). Leading group term (printed in colour and bolded) was based on highest enrichment significance value. Node colours represent groups, node size represents enrichment significance. Statistical evaluation was generated through ClueGO using the Enrichment/Depletion two-sided hypergeometric test with Bonferroni step down correction. A full list of all GO terms identified can be found in appendix 3.

3.11 Matched monolayer and spheroid cultures undergo distinct global transcriptomic changes compared to parental tissues

To understand how the global gene expression profiles change when translated to cell culture and to understand differences in expression profiles between 2D and 3D, differential expression analysis between the three groups was performed. A total of 8770 genes (3402 up, 5368 down) in monolayers and 8863 genes (3511 up and 5352 down) in spheroids were significantly differentially expressed compared to matched parental tissues (log2FoldChange >1, adjusted p-value (padj) <0.05) (Fig 3.11A, B). Both comparisons showed equal distribution of up and down-regulated genes, with a slight bias towards downregulation compared to tissues. The 10 most significantly down-regulated genes were *TSC22D3, FAM107A, CYP2T1P, SLC47A1, HIF3A, CA14, THSD4, NECAB1, NET1, ZBTB16* for monolayers compared to tissue and CYP2T1P, *FOLR1, CLCNKB, CA14, P2RY12, EGFL6, ENPP6, SLC15A2, KLF15, TSC22D3,* for spheroids compared to tissue (Fig 3.11A, B). The 10 most significantly up-regulated genes were *RGS4, TNFRSF12A, EVA1A, PLK2, ALPK2, PVR, DIAPH3, CHAC1, LINC02154, ANKRD1* for monolayers compared to tissue and *SLC20A1, RGS4, TNFRSF12A, MMP9, LOXL2, APCDD1L, SPRED3, ADAMTS14, KCNG1, DCBLD2* for spheroids compared to tissue (Fig 3.11A, B). There is an overlap of genes down-regulated and up-regulated in both 2D and 3D compared to the tissue (*TSC22D3, CA14, RGS4, FAM83G).* A full list of significantly differentially expressed genes identified can be found in appendix 4 (supporting file 1).

Despite the similarities between the monolayer and spheroid transcriptomes when compared to the tissue, there were clear differences when compared directly. A total of 1879 deregulated genes were found to be significantly differentially expressed, with 869 genes up-regulated and 1010 genes down-regulated in 3D compared to 2D (log2FoldChange >1, padj<0.05). The 10 most significantly down-regulated genes were *SLC2A12, ELN, CITED2, MID1, EDN1, RGS5, AJUBA, KRT87P, PLCE1-AS1, SBSPON.* The 10 most significantly up-regulated genes were *LINC01050, MMP14, AC024909.1, BHLHE40, SLC20A1, HEY1, NPPC, MMP28, EGR3, TTYH2* (Fig 3.11C). A full list of significantly differentially expressed genes identified can be found in appendix 4 (supporting file 1).

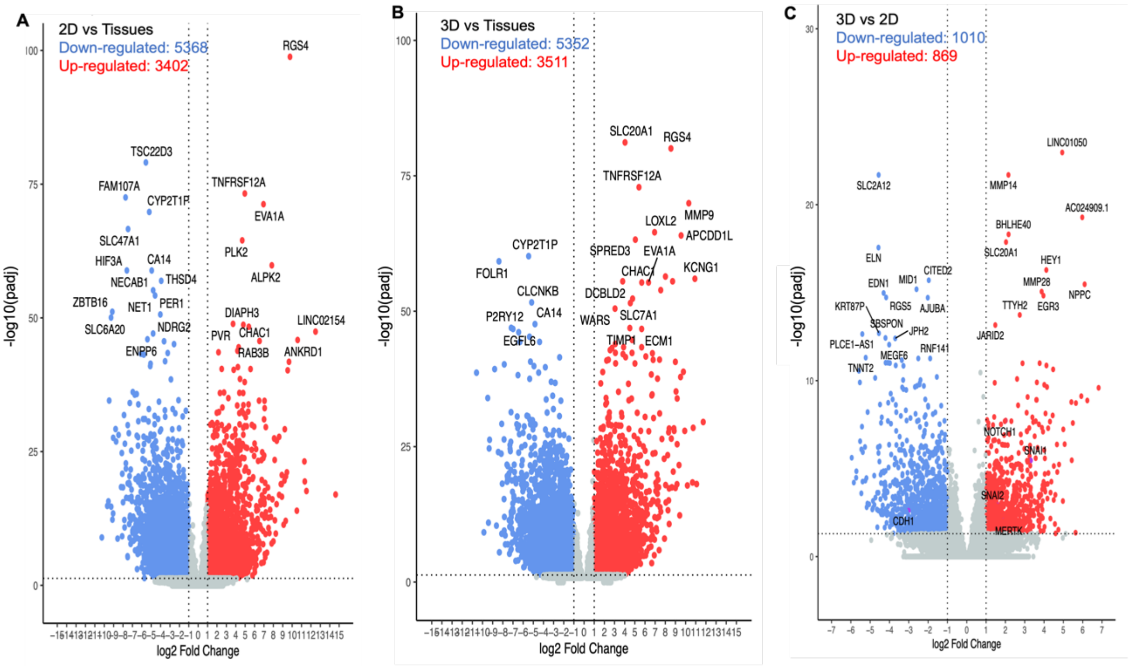

Figure 3.11: Transcriptome profiling of global gene expression changes in spheroids, monolayers and parental tissues. Volcano plots comparing fold change (Log2FoldChange) to adjusted p-value (-Log10padj) of differentially expressed genes between (A) 2D vs T, (B) 3D vs T, and (C) 3D vs 2D. Significance cut-offs were set as log2FoldChange >1 and padj<0.05. Significantly up-regulated genes are shown in red and significantly down-regulated genes are shown in blue. The top 25 most significantly deregulated genes are labelled with text. Genes labelled in purple represent significantly deregulated genes outside of the top 25 that are of particular interest in EMT. Full lists of significantly differentially expressed genes identified can be found in appendix 4 (supporting file 1).

3.12 Gene Set Enrichment Analysis (GSEA) highlights enriched biological processes between spheroids, monolayer cultures and matched patient tissues

To interpret the differences in transcriptomes between both models and matched patient tissues and to elucidate the overrepresented biological processes in each condition, Gene Set Enrichment Analysis (GSEA) was performed for each comparison (3D vs T, 2D vs T, 3D vs 2D). GSEA provides information on whether a particular biological process (a priori-defined set of genes) is significantly differentially expressed between two conditions (233). GSEA using gene ontology lists identified 1160, 1358 and 73 biological processes significantly enriched for “2D vs T”, “3D vs T” and “3D vs 2D” respectively (nom p-value<0.01) (appendix 5, supporting file 2). While only 110, 77 and 50 gene lists were enriched in “T vs 2D”, “T vs 3D” and “2D vs 3D” (appendix 5, supporting file 2). Detailed lists of all enriched gene ontology lists for all three comparisons can be found in appendix 5, supporting file 2. The biological processes with the highest enrichment scores in both cell culture models compared to the tissues are associated with the regulation of cellular processes including the cell cycle, cell adhesion, cell structure and morphogenesis (Fig 3.12A). Moreover, the tissues were mainly enriched in processes associated with glucose import and the catabolism of biomolecules compared to both cell culture models, although these findings had higher FDR q values (Fig. 3.12B).

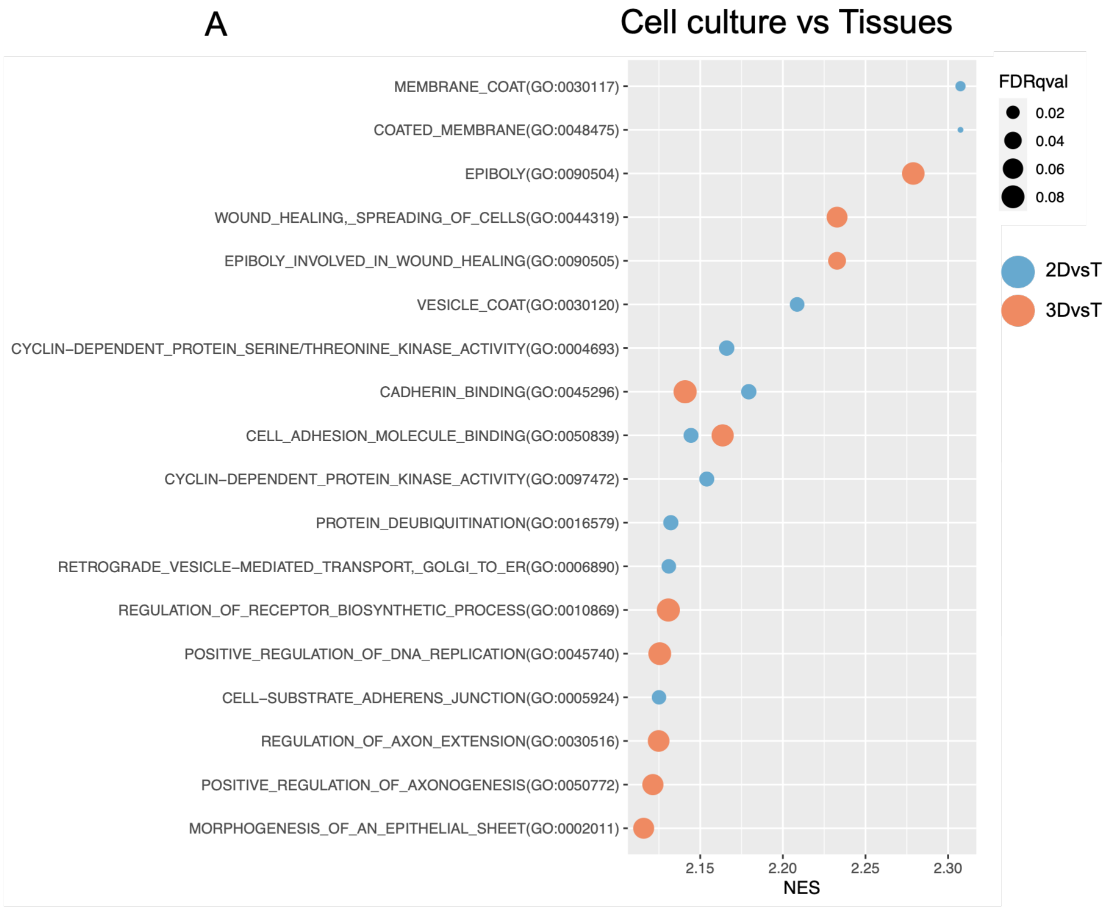
A
Cell culture vs Tissues
MEMBRANE_COAT(GO:0030117)
COATED_MEMBRANE(GO:0048475)
EPIBOLY(GO:0090504)
WOUND_HEALING,_SPREADING_OF_CELLS(GO:0044319)
EPIBOLY_INVOLVED_IN_WOUND_HEALING(GO:0090505)
VESICLE_COAT(GO:0030120)
CYCLIN–DEPENDENT_PROTEIN_SERINE/THREONINE_KINASE_ACTIVITY(GO:0004693)
CADHERIN_BINDING(GO:0045296)
CELL_ADHESION_MOLECULE_BINDING(GO:0050839)
CYCLIN–DEPENDENT_PROTEIN_KINASE_ACTIVITY(GO:0097472)
PROTEIN_DEUBIQUITINATION(GO:0016579)
RETROGRADE_VESICLE–MEDIATED_TRANSPORT,_GOLGI_TO_ER(GO:0006890)
REGULATION_OF_RECEPTOR_BIOSYNTHETIC_PROCESS(GO:0010869)
POSITIVE_REGULATION_OF_DNA_REPLICATION(GO:0045740)
CELL–SUBSTRATE_ADHERENS_JUNCTION(GO:0005924)
REGULATION_OF_AXON_EXTENSION(GO:0030516)
POSITIVE_REGULATION_OF_AXONOGENESIS(GO:0050772)
MORPHOGENESIS_OF_AN_EPITHELIAL_SHEET(GO:0002011)
2.15
2.20
2.25
2.30
NES
FDRqval
0.02
0.04
0.06
0.08
2DvsT
3DvsT


B
Tissues vs Cell culture
GLUCOSE IMPORT IN RESPONSE TO INSULIN STIMULUS(GO:0044381)
POSITIVE REGULATION OF GLUCOSE IMPORT IN RESPONSE TO INSULIN STIMULUS(GO:2001275)
ENTRAINMENT OF CIRCADIAN CLOCK BY PHOTOPERIOD(GO:0043153)
NEUROTRANSMITTER CATABOLIC PROCESS(GO:0042135)
REGULATION OF GLUCOSE IMPORT IN RESPONSE TO INSULIN STIMULUS(GO:2001273)
RESPONSE TO COLD(GO:0009409)
MONOCARBOXYLIC ACID CATABOLIC PROCESS(GO:0072329)
ENTRAINMENT OF CIRCADIAN CLOCK(GO:0009649)
EYE PHOTORECEPTOR CELL DIFFERENTIATION(GO:0001754)
MOTILE CILIUM ASSEMBLY(GO:0044458)
BRANCHED–CHAIN AMINO ACID METABOLIC PROCESS(GO:0009081)
PHOTOPERIODISM(GO:0009648)
G–PROTEIN COUPLED PURINERGIC RECEPTOR SIGNALING PATHWAY(GO:0035588)
MEMBRANE DEPOLARIZATION DURING CARDIAC MUSCLE CELL ACTION POTENTIAL(GO:0086012)
NEGATIVE REGULATION OF TORC1 SIGNALING(GO:1904262)
ORGANIC ACID CATABOLIC PROCESS(GO:0016054)
CARBOXYLIC_ACID_CATABOLIC_PROCESS(GO:0046395)
1.9
2.0
2.1
NES
FDRqval
0.1
0.2
0.3
0.4
0.5
2DvsT
3DvsT

Figure 3.12: Enrichment plots of top 10 most enriched GO terms in cell culture models and matched patient tissues. (A) Enrichment plot showing the top 10 most enriched GO biological processes in 2D (blue) and 3D (red) compared to matched tumour tissues. Normalized enrichment score (NES) is presented on the x-axis. Dot size represents FDR q-value. (B) Enrichment plot showing the top 10 most enriched GO biological processes in tissues compared to 2D (blue) and 3D (red). Normalized enrichment score (NES) is presented on the x-axis. Dot size represents FDR q-value. Plots were made using R.

The top 15 enriched GO biological processes in 2D compared to 3D were associated with mitochondrial structures and branched-chain amino acid metabolism (Fig. 3.13A). The top 15 enriched terms in 3D cultures were associated with histone demethylation, regulation of extracellular matrix organization, regulation of epithelial-to-mesenchymal transition (EMT) and the Notch signalling pathway in 3D cultures (Fig. 3.13B). Overall, GO terms enriched in 3D cultures had higher enrichment scores compared to terms enriched in 2D cultures.

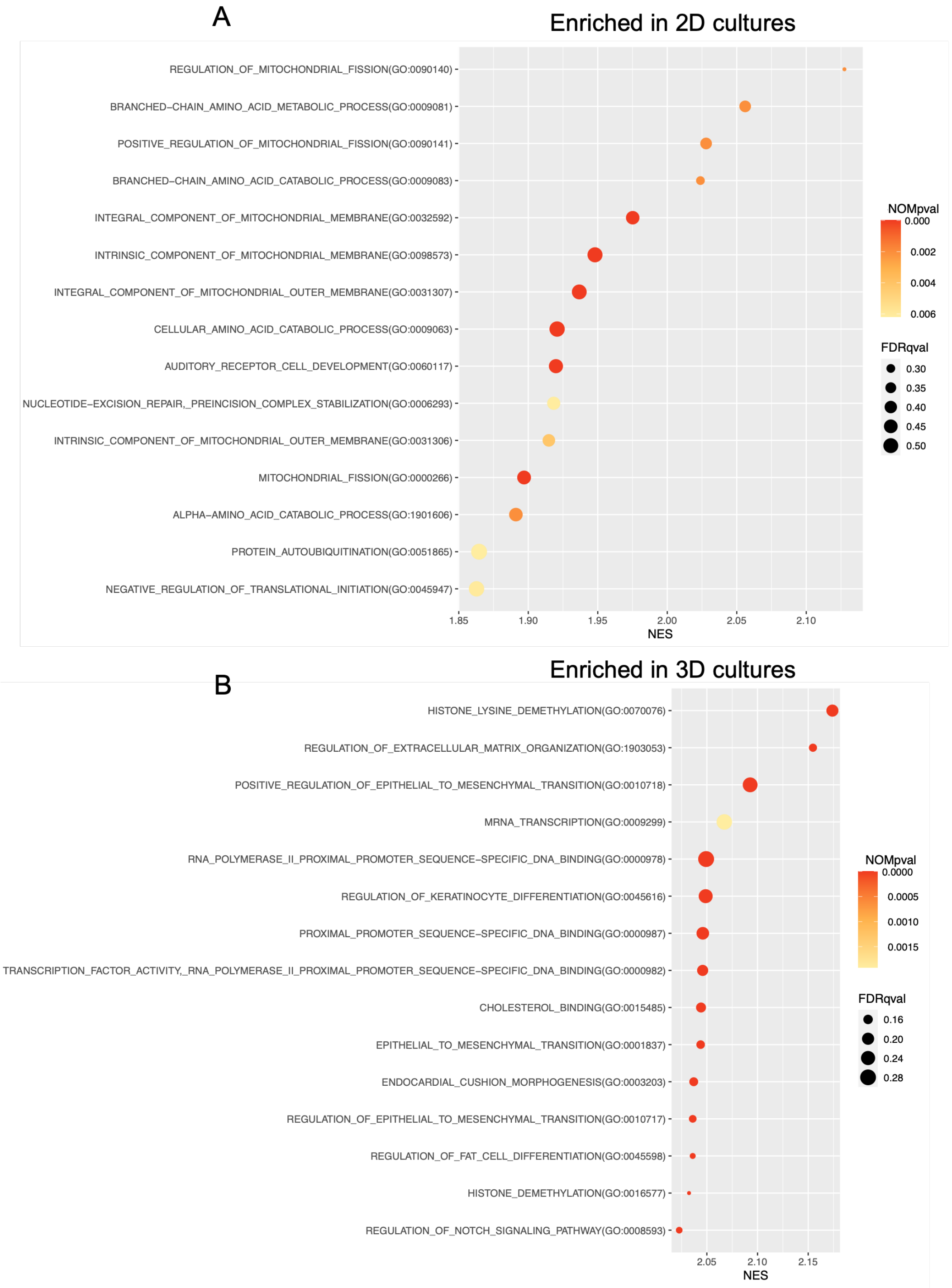

Figure 3.13: Enrichment plots of top 15 most enriched GO terms in spheroids (3D) and monolayers (2D) (A) Enrichment plot showing the top 15 most enriched GO biological processes in 2D monolayer cultures compared to 3D spheroid cultures. Normalized enrichment score (NES) is presented on the x-axis. Dot size represents FDR q-value. Colour represents nominal p-value (B) Enrichment plot showing the top 15 most enriched GO biological processes in 3D spheroid cultures compared to 2D monolayer cultures. Normalized enrichment score (NES) is presented on the x-axis. Dot size represents FDR q-value. Colour represents nominal p-value. Plots were made using R.

3.13 Spheroids express high levels of the mesenchymal meningioma marker vimentin and low levels of E-cadherin

GSEA identified EMT and Notch signalling as enriched in 3D vs 2D. In many cancers, including meningiomas, EMT is associated with tumour progression, treatment resistance, invasion capacity and poor prognosis (173,234,235). This process is characterised by the progressive loss of epithelial marker proteins (E-cadherin, ZO-1), and the concomitant increase of the expression of mesenchymal proteins such as N-cadherin and vimentin (188). Interestingly, expression of E-cadherin and vimentin have been demonstrated as characteristic markers for meningiomas and can be used to distinguish them from other neoplasms of meningeal origin (43,188). Therefore, immunostaining analysis for E-cadherin and vimentin was performed in spheroids and matched patient tissues (Fig. 3.14A). Spheroids were fixed and embedded in paraffin 3 days post spheroid formation and kindly stained for Vimentin and E-cadherin by the department of neuropathology in the Derriford hospital. Stainings were provided with an immuno score by pathologist David Hilton ranging from 0 (no staining) to 4 (very strong staining). All assessed patient tissues showed expression of both markers, although expression of vimentin was more prominent. Vimentin was strongly expressed in meningioma spheroids and tissues (average immuno scores of 4, and 3.75 for tissues and spheroids respectively) while expression of the epithelial marker E-cadherin was weak (average immuno scores of 1.75, and 0.25 for tissues and spheroids respectively) (Fig. 3.14B).

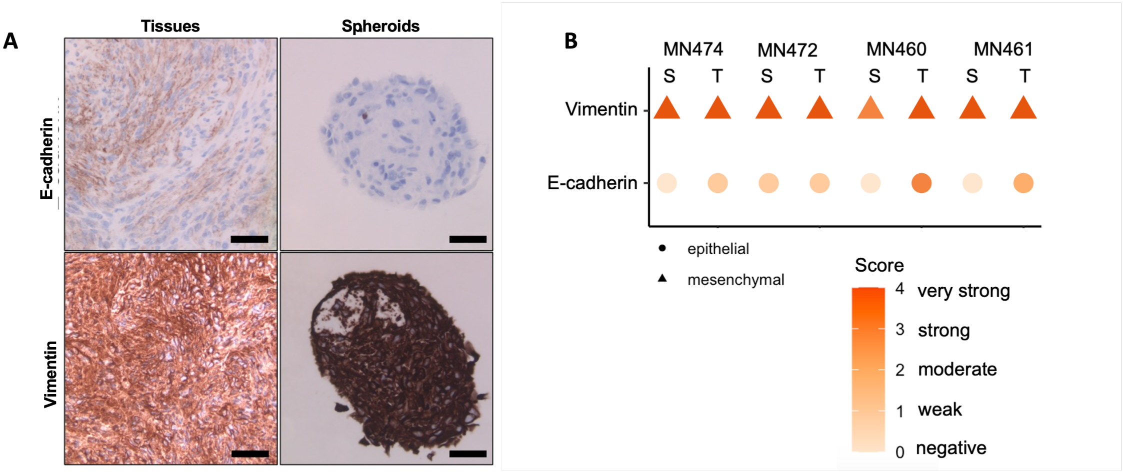

Figure 3.14: Patient-derived spheroids have high expression of vimentin and low expression of E-cadherin (A) Immunohistochemistry for anti-E-cadherin (epithelial), anti-Vimentin (mesenchymal) in matched grade 1 patient-derived spheroids and tumour tissue (n=4). Scale bars indicate 200μm. (B) Plot of immuno scores for immunostaining of E-cadherin (epithelial indicated as circle) and Vimentin (mesenchymal indicated as triangle) in spheroids (S) and matched tumour tissue (T) (n=4). Colour represents immunoscore of 0-4 (0=negative, 1= weak, 2= moderate, 3= strong, 4= very strong).

3.14 Increased expression of markers related to epithelial-to-mesenchymal transition (EMT) in the meningioma spheroid model

To further elucidate EMT changes, I interrogated the transcriptomic dataset for the expression of genes associated with meningiomas and EMT: VIM encoding for vimentin (mesenchymal) and CDH1 encoding for E-cadherin (epithelial) (186,236,237) and the expression of two EMT transcription factors snai1 (encoding for Snail) and snai2 (encoding for Slug). The gene encoding vimentin was not significantly deregulated. The CDH1 gene encoding for E-cadherin was significantly downregulated in 3D compared to 2D (log fold change: -3.01). Snai1 and Snai2 were significantly upregulated in 3D cultures compared to 2D cultures (snai1 log fold change: 3.32, snai2 log fold change: 1.58). Additionally, Notch signalling-associated genes were assessed including Notch1-4, and two downstream effectors Hey1 and Hes1. Of these, Notch1 was identified as the most deregulated Notch gene which was significantly upregulated in 3D cultures compared to 2D cultures (log fold change: 1.98). Hey1 was found to be significantly upregulated in 3D compared to 2D (log fold change: 4.12), and Hes1 was not significantly deregulated. Next, these results were validated through independent experiments. The changes in gene expression of a panel of markers associated with EMT and notch signaling in spheroids compared to monolayers were assessed by qPCR. The panel consisted of the epithelial markers E-cadherin (CDH1) and tight junction protein zona occludens-1 (TJP1/ZO-1), the EMT transcription factors Snail (snail1), Slug (snail2) and ZEB1 and the Notch signaling genes Notch1, Hes1 and Hey1. Consistent with the results of the RNAseq, an increase in the gene expression of EMT transcription factors was observed (Fig. 3.15C). For Snai1 (encodes the Snail protein) a significant average 6.3-fold increase ($p<0.05$) and for Snai2 (encodes the Slug protein) a significant average 8.5-fold increase was detected ($p<0.05$) in spheroid cultures compared to matched monolayer cultures. For Notch1, an average 7.7-fold increase ($p<0.01$) in RNA expression was observed with the downstream effectors Hes1 and Hey1 demonstrating a fold increase of 1.9 ($p=0.28$) and 28.8 ($p<0.05$) respectively (Fig. 3.15C). For the epithelial markers CDH1 (encoding for E-cadherin) and ZO-1 a change in gene expression was not observed (CDH1 $p=0.51$; ZO-1 $p=0.55$) (Fig. 3.15C). However, 4 out of 5 patient-derived spheroids showed an average decrease of 96% in E-cadherin expression, consistent with an increase of mesenchymal genes, while one sample showed a 16-fold increase. Next, it was assessed whether these changes in expression could also be detected on the protein level. A comparable trend of increased protein expression of mesenchymal and Notch signalling proteins: N-cadherin, Notch1 NICD, Hey1 and Slug was observed by western blotting although this increase was not significant due to the variability between patient samples (Fig. 3.15D, E). A decrease in E-cadherin expression was detected in some of the samples although the average change demonstrated an increase (Fig. 3.15D, E). These results suggest that predominantly mesenchymal markers are increased in spheroid cultures while epithelial markers remain similarly expressed.

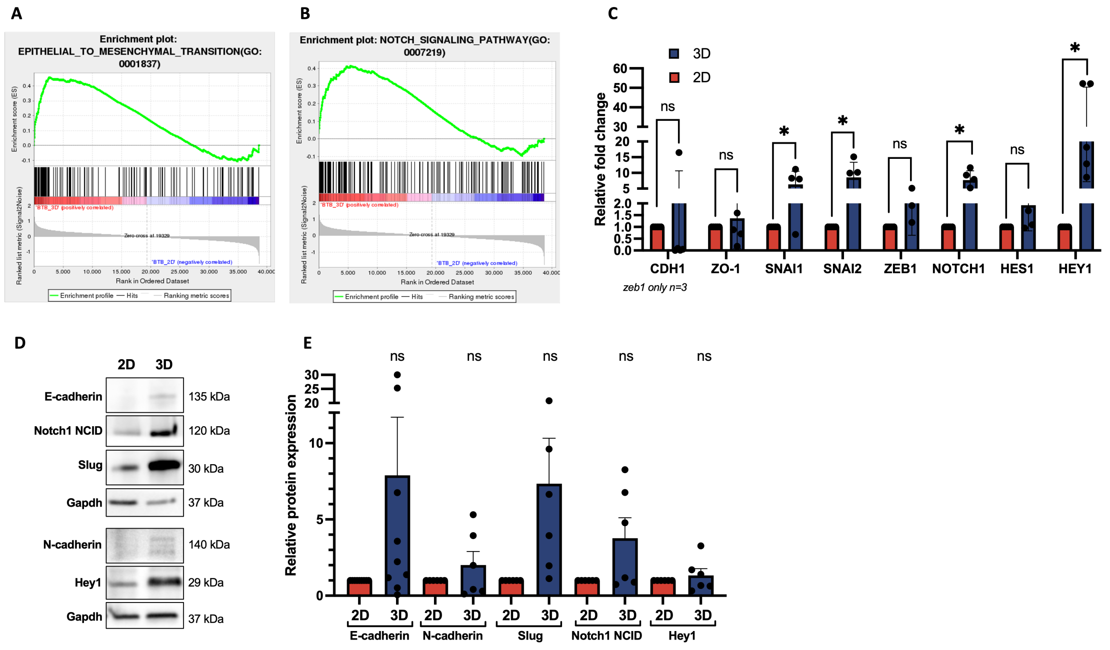

Figure 3.15: Patient-derived spheroids have increased expression of markers related to epithelial-to-mesenchymal transition (EMT) Enrichment plots showing the enrichment in (A) epithelial-to-mesenhcymal transition (GO:0001837) and (B) Notch signaling pathway (GO:0007219) in spheroids compared to monolayers. (C) Relative gene expression of a panel of EMT markers: CDH1 (E-cadherin), ZO-1 (TJP1), Notch1, Snai1, Snai2 (Slug), Zeb1, Notch1, Hes1, and Hey1 in monolayers compared to matched spheroids (n=5). (D) Representative western blot and I quantification showing the expression E-cadherin, Notch1 NICD, Slug, N-cadherin, Hey1 in spheroids (3D) compared to monolayers (2D). Expression is shown as the relative increase compared to monolayers. GAPDH was the loading control (n=5). Student's t test was used for statistical evaluation. ns = not significant, *p<0.05.

3.15 Meningioma spheroids exhibit dynamic invasion when embedded into the extracellular matrix mimicker Matrigel

The WHO classification includes brain invasion as a stand-alone criterium for grade 2 meningiomas (2). Moreover, an upregulated expression of the mesenchymal proteins Snail and Slug has been shown in atypical grade 2 meningioma tissues compared to grade 1 tissues (187,188). Considering the association between the mesenchymal phenotype and invasion, I assessed the functional invasiveness displayed by WHO grade 2 spheroids using a 3D Matrigel invasion assay. In agreement with the observation of an enhanced mesenchymal phenotype, embedded spheroids displayed observable protrusions in the Matrigel within 24 hours, which was observed to significantly increase after 48 hours ($p<0.001$) (Fig. 3.16A, B). Using F-actin and DAPI immunofluorescent staining, a disorganization of the compact spheroid characterized by invadopodia-like projections migrating into the ECM was observed in the embedded spheroids, while the spheroids that were not embedded in ECM retained their compact structure (Fig. 3.16C, D). While this invasion experiment was performed using WHO grade 2 spheroids, a similar dynamic invasion was observed following the embedding of WHO grade 1 spheroids (data not shown).

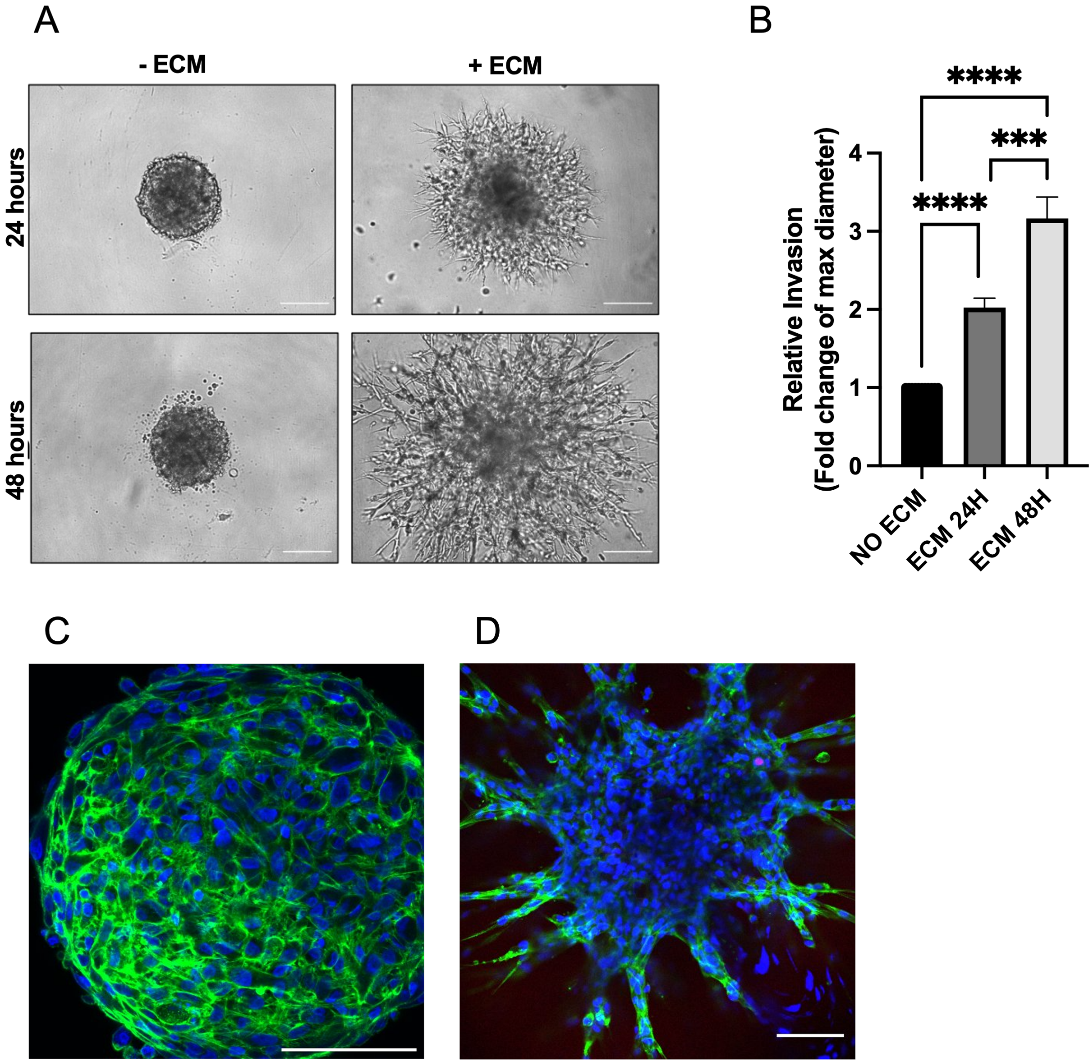

Figure 3.16: Patient-derived WHO grade 2 meningioma spheroids exhibit dynamic invasion upon Matrigel embedding (A) Representative phase-contrast microscopy images of WHO grade 2 spheroids with and without ECM (Matrigel) at 24h and 48h time points. Scale bars indicate 100µm. (B) Bar graph showing the relative invasion compared to not ECM embedded spheroid controls as fold change increase of the max. diameter. Max. diameter was measured using ImageJ. One-way ANOVA with Tukey's multiple comparisons test was used for statistical evaluation. ***$p<0.001$, ****$p<0.0001$. (C-D) Fluorescence microscopy image showing F-actin (phalloidin, green) and nuclei (DAPI, blue) in spheroids (C) without ECM and (D) with ECM showing invadopodia-like projections migrating into the ECM (Matrigel). Scale bars indicate 100 µm.

3.16 Establishing meningioma organoids following an adapted protocol of culturing GBM tumour organoids

In addition to the patient-derived meningioma spheroid model, preliminary experiments testing the feasibility of generating a meningioma organoid (MgO) model were performed. The protocol used to establish MgOs was adapted from the protocol for GBM organoids described by Jacob *et al*. (154). Briefly, meningioma specimens were dissected into 0.5-1 mm^2 fragments using curved dissection scissors at the earliest opportunity after surgical intervention. Following red blood cell lysis, fragments were cultured on an orbital shaker to facilitate organoid formation and increase access to nutrients and $O_{2.}$ MgOs were cultured in GBM organoid medium (154) and GFS medium (section 2.2.4) and morphology was monitored by microscopy. Formation of spherical morphology was observed for MgOs in both conditions in approximately 1-2 weeks (Fig. 3.17A). Next, MgO growth was assessed for MgOs generated from 3 individual patient samples. For MgOs cultured in GBOM, growth was not observed. For MgOs cultured in GFS, minimal growth was observed (Fig. 3.17A, B). To obtain a better understanding of MgO proliferation, WHO grade II derived MgOs were fixed and analysed for the proliferation marker ki67 by immunostaining (Fig. 3.17C). Staining was scored as intermediate positivity (++), low (+) and no staining (-). Using both culture conditions, GFS and GBOM, generated various MgOs with all three Ki67 levels (Fig. 3.17C). To assess whether MgOs retained the histological features of their corresponding parental tumours and to examine the effects of using different culture media, histological analyses were performed for two individual samples, one WHO grade I sample (assessed after 3 weeks in culture) and one WHO grade II sample (assessed after 2 weeks in culture). The WHO grade 1 derived MgOs did not show any viable tissue, while the WHO grade

2 derived MgOs showed viable tissue with similar histology to the parental tissue, as demonstrated by similar nucleus shapes and cellularity (Fig. 3.21D). No differences were observed between the two medium conditions. In addition, immunostaining analysis for the meningioma tumour cell marker SSTR2 showed expression in WHO grade 2 derived MgOs cultured using both media conditions. Next, I investigated whether viable MgOs could be cryopreserved and stored in liquid nitrogen for later use following the protocol previously described by Jacob *et al*. (154) for GBM organoids. Briefly, WHO grade 2 derived MgOs were cut into fragments of approximately 0.5 mm and frozen in culture medium (GBOM or GFS) supplemented with 10µM Y-27632 and 10% DMSO. After 1 month in liquid nitrogen, samples were thawed and cultured overnight in culture medium supplemented with 10µM Y-27632, as described in section 2.2.6. Morphology of recovered MgOs was observed to start rounding within three weeks for 80% of GFS-cultured MgOs and 50% of GBOM-cultured MgOs (Fig. 3.21E). H&E staining 3 weeks post-recovery did not show viable MgO tissue, indicating that this method for cryopreservation was unsuccessful (Fig. 3.21F). Overall, these results suggested that this method can generate viable WHO grade 2 derived MgOs. However, there is a large variability between individual pieces from a tumour including levels of proliferation. In addition, cryopreservation methods should be optimized.

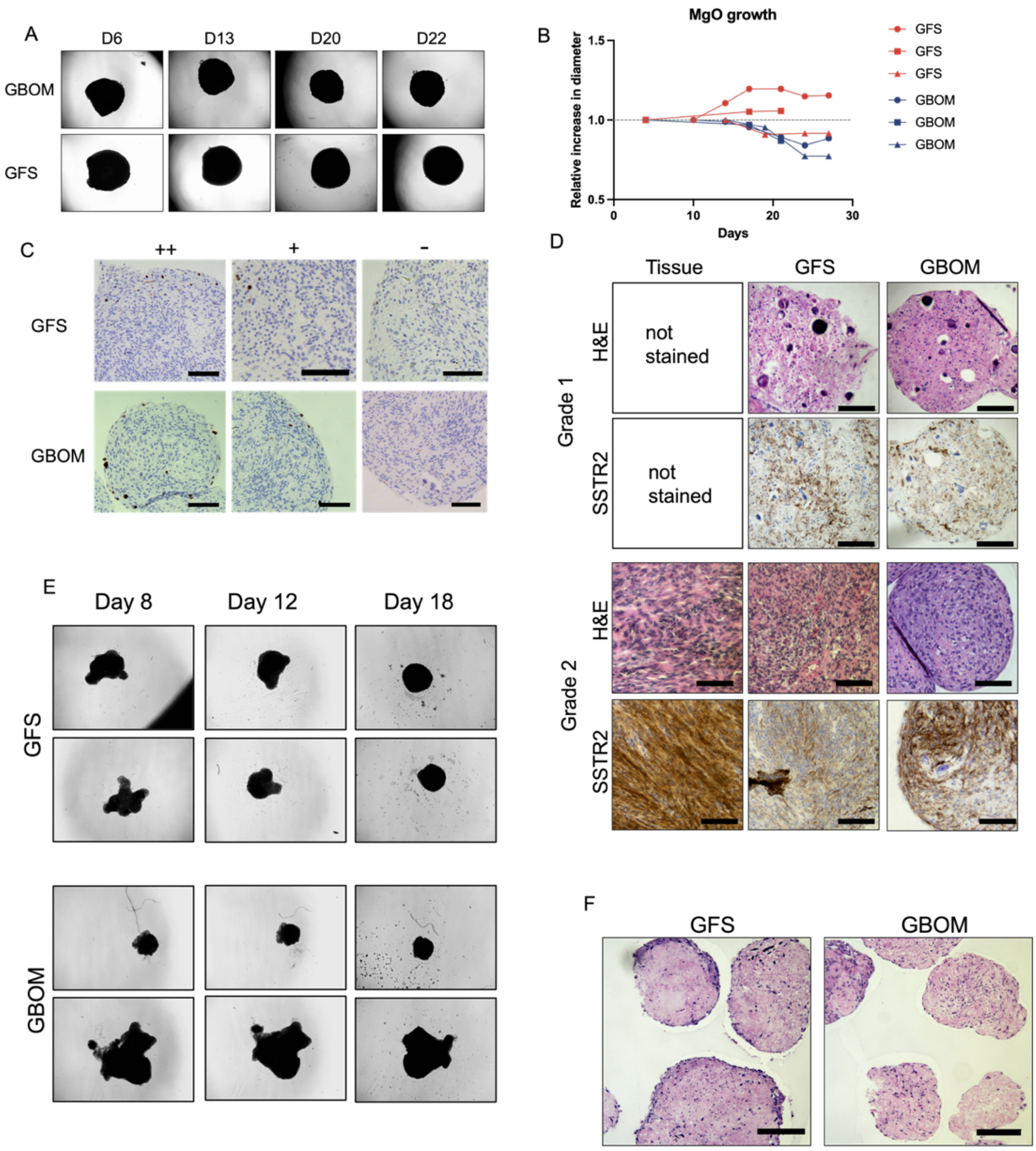

Figure 3.17: Characterisation of MgOs established following an adapted protocol of culturing GBM tumour organoids A) Representative light microscopy images and (B) quantification of the max diameter ratio change of MgOs in GBOM (blue) and GFS (red). Each line represents a tumour indicated by point shape (circle, triangle and square represent the individual tumour) (C) Representative microscopy images of proliferating cells (ki67+) in WHO grade 2 derived MgOs in GBOM and GFS, for each condition MgOs with variable levels of ki67 positivity was detected (++ = intermediate, + = low, - = no positivity; scale bar: 100 µm. (n=1) (D) Representative haematoxylin and eosin (H&E) (top) and SSTR2 (bottom) stained images of MgOs in GBOM and GFS and the corresponding parental tumours (Tissue); scale bar: 100 µm (n=1). (E) Representative light microscopy images of WHO grade 2 derived MgOs after cryopreservation in GFS and GBOM at day 8, day12 and day18 after thawing. (F) Representative H&E stained images of cryopreserved MgOs after 18 days in GBOM and GFS. MgOs do not show viable tissue.

3.17 Discussion

In the field of meningioma research, there is a need for accurate model systems to model the complexity and heterogeneity of meningioma pathology (13). Therefore, the aim of this study was to establish a patient-derived 3D cell culture model of meningioma that has the potential to bridge the translational gap between *in vitro* and *in vivo* experimental results. This chapter confirmed the hypothesis that it is feasible to establish a novel culture method for the generation of 3D patient-derived meningioma cultures and that they resemble essential features of *in vivo* meningioma tissues. I presented a method for the generation of patient-derived spheroids of WHO grade 1 and WHO grade 2 meningiomas with high establishment efficiency and reproducibility while maintaining morphological and molecular features of the parental tumours. Furthermore, initial experiments to establish meningioma organoid cultures are presented.

3.17.1 Optimization of a protocol for meningioma patient-derived spheroid cultures

3.17.1.1 Reducing the selection bias introduced by adapting the specimen processing protocol and culture conditions

To establish spheroid cultures that could closely mimic the parental tissue while additionally serving as an easy-to-use tool with a fast result turnaround, several parameters for protocol optimization were considered. It has been demonstrated that prolonged time between surgical removal and tissue processing reduces the number of viable cells extracted. Thus, introducing a selection bias by selecting cells that remain viable for longer (154). Hence, it is crucial to limit this time as much as possible. Unfortunately, due to the logistics of our collaboration with the

University Hospitals Plymouth and North Bristol, the period between tissue resection and processing for cell culture could not be decreased beyond approximately 2 hours for samples received from the Derriford hospital in Plymouth and 24 hours for samples received from the Southmead NHS hospital in Bristol. This is a disadvantage for optimal cell extraction (154). To limit the impact on sample viability, samples were transported in Hibernate™-A medium, a CO_2-independent nutrient medium formulated for the maintenance of neural tissue at ambient CO_2 levels. Another factor that can introduce selection bias is the use of digestion enzymes, such as dispase and collagenase, that serve to break down the interstitial meningioma matrix (238). Prior to this study, our research team was digesting meningioma specimens using an enzymatic digestion protocol which included an overnight incubation step with collagenase type 3A (65,239,240). Interestingly, I observed that despite incomplete digestion following mechanical digestion only, meningioma tissue fragments could attach and sprout cells. Therefore, the addition of collagenase type 3A seemed unnecessary and I chose to remove this step from the protocol. Furthermore, in 2D cultures, the passaging of cells has been shown to select dominant cell populations over time (241,242). For example, work published by our research group showed that the expression of macrophage markers decreased with each passage (65). Moreover, there is a consensus that the lower the passage of cells, the better the cell population resembles the *in vivo* situation (242). Therefore, this model was exclusively characterised using spheroids seeded at passage 1. For this same reason, I do not recommend the use of this spheroid model for the expansion of meningioma primary cells and subsequent dissociation for the formation of second or tertiary spheroids since it is impossible to prevent the selection of more resistant or more proliferating clones and cell types. The low proliferation levels displayed by spheroid cultures (Fig. 3.4 F-H) suggest that spheroid culture is not the method of choice if one wants to amplify cell numbers. However, I could successfully establish spheroids from cells that were cryopreserved at P0. Thus, demonstrating that spheroids can be used for the generation of a meningioma biobank.

3.17.1.2 Formulation of the spheroid growth medium

A clear difference was observed in spheroid growth rates between spheroids maintained in the two media conditions tested. The diameter of GFS-cultured spheroids remained stable, while the diameter of MN1-cultured spheroids decreased. This suggested that spheroids were dependent on the factors supplemented in the GFS media and that GFS is superior for the maintenance of primary meningioma spheroids over MN1. Interestingly, while most methods published on the culture of primary meningioma cells use medium formulations similar to MN1 (149), Magill *et al.* (17) was the first to successfully culture meningioma cells using GFS medium. Similar media formulations were later used for meningioma primary cells by other research teams (104,243). The base medium of GFS is a mixture of Neurobasal and DMEM with Ham's F12 nutrient mixture (DMEM/F12) at 1:1 ratio. Neurobasal media was tailored to resemble the biological properties of cerebral spinal fluid while DMEM/F12 resembles those of the blood (114). More importantly, the two media formulations differ in serum levels, which are low (5%) in GFS and high in MN-1 (10%). In addition, GFS is supplemented with the defined mitotic factors EGF and FGF2, which were shown to be superior in supporting the preservation of the phenotype and genotype of primary GBM cells compared to high serum cultured GBM cells (104,244). Other factors in GFS are B27 and N2, which contain basic molecules known to support cell growth such as vitamins and proteins such as insulin and transferrin (114). However, a recent paper on meningioma organoids (MgOs) described that serum free-conditions with the addition of B27 and N2 negatively impacted the MgO-establishing rates (20). Culturing cells under serum-free conditions has been associated with the selection of stem-like cells (149,245,246). Therefore, for the establishment of this spheroid model, the addition of low serum levels was preferred over serum-free conditions to ensure the maintenance of differentiated meningioma cells, and also preserving the preservation of the phenotype and genotype of the primary tumours.

3.17.1.3 Formation of uniform spheroids using 96-well ULA culture plates

Spheroid size, shape and compactness was shown to have a major influence on their anti-drug response (247,248). This is primarily due to the gradients of nutrients in the spheroids. For example, metabolic activity was shown to be altered in colorectal cancer spheroids compared to monolayer cultures due to perfusion-limited nutrient access (249). In addition, drug penetration has been shown to be decreased by spheroid compaction (118,230,250). Therefore, the generation of uniform-sized spheroids is crucial when using the spheroid model as a drug screening tool. For this reason, spheroids were generated using 96-well ULA culture plates, which allowed for controlled spheroid formation whilst the number of cells per spheroid could be kept consistent. This is supported by the low standard deviation of spheroid diameter, which indicated consistency between spheroids generated from the same patient sample and cell number. Additionally, for the purpose of consistency, I chose to use a standardized seeding density of 3000 cells/spheroid for all experiments. Spheroids generated from 3000 cells were visible to the naked eye, which was beneficial when handling them. In addition, this number was low enough to ensure the optimal use of cells when working with a finite cell number. Notably, the use of ULA culture plates for the generation of meningioma spheroids provides the advantage of a straightforward procedure which can be easily performed without the requirement of advanced cell culture skills. Furthermore, this method allowed for the generation of a high number of uniform spheroids in a short time frame. In addition, spheroids were maintained under constant rotation. This step was included in the spheroid protocol to limit the diffusional limitations of molecules and to allow for sufficient nutrient and gas exchange. This step was not tested for this model specifically but has been widely adopted in other published spheroid culture protocols (251,252).

3.17.1.4 Patient-derived meningioma spheroids resemble histology, immune microenvironment and mutational profile of parental tissues

Immunohistochemistry analysis showed that meningioma spheroids mimic the histopathology of matched parental tissues, suggesting that this model can provide an accurate platform for meningioma cell culture representing the *in vivo* tumours. Furthermore, this analysis revealed that the expression of SSTR2, which is commonly expressed by meningioma cells (253), is retained in the spheroid cultures. However, this expression was detected at lower levels compared to the original tissues. Additionally, spheroid cultures lost the expression of EMA, another differentiation marker for meningioma cells (149). This result suggests that while spheroids represent meningioma-derived structures, they are less differentiated compared to tumour tissues. Indeed, cells cultured under spheroid conditions have been described to maintain cells in a less differentiated state which is a feature that is inherent to spheroid culture (254).

Spheroids have been described to present with necrosis in the core due to hypoxic conditions as a consequence of reducing oxygen concentrations that penetrate the spheroid (118,251). Interestingly, H&E staining of meningioma spheroids did not reveal a difference in cellular density throughout the spheroid or the occurrence of necrosis in the spheroid cores. This can be explained by the maintenance of the spheroids under constant rotation which is suggested to allow for higher oxygen penetration. Moreover, the diameter of spheroids with an initial density of 3000 cells/spheroid does not exceed 510 µm, which might be small enough to achieve enough penetration. Furthermore, this parameter of spheroid morphology was assessed 3 days post-spheroid formation with might not be sufficient time to induce a necrotic core.

Besides meningioma cells, stromal cells have been described as crucial components of these tumours, contributing to cell organisation, biochemical signalling, and tumour behaviour (4,20,61,64,65,255,256). The most abundant infiltrating immune cell type in meningiomas are tumour-associated (TA)-macrophages (20,64). TA-macrophages have been associated with influencing drug responses and have even been shown to contribute to drug resistance in several cancers (257,258). Thus, it is fundamental to include this aspect of the meningioma microenvironment within the model when testing the efficiency of therapeutic agents. My results showed the expression of two macrophage markers: CD68 and CD163 in the spheroid cultures. This result demonstrated that these elements of the tumour microenvironment are recapitulated in this spheroid model. This finding was further supported by the results of the comparative expression analysis that identified genes associated with the biological process “regulation of macrophage activation” that were maintained in spheroids but not in monolayer cultures (Fig. 3.10D).

Furthermore, several disease-causing mutations, including NF2, TRAF7, KLF4, AKT1 and SMO, have been described in meningiomas and several compounds targeting these driver mutations are currently under investigation in clinical trials (259,260). This signifies the importance of maintaining the mutational landscape of meningiomas during *in vitro* experiments. Mutational analysis of the spheroids and their matched parental tissues revealed that culture conditions maintained the genomic alterations of parent tumour tissues upon generation and in short term. However, for some mutations the VAF in spheroids differed from the VAF detected in the tumour. This can be explained by the selection of a certain population of cells within the spheroid, that could be responsible for this change.

Since this spheroid model was optimized for short term use specifically, in order to preserve as much of the parent tumour signature as possible, the effect of long-term spheroid cultuivation on the genomic fidelity was not assessed. Other meningioma 3D culture models such as the model described by Yamazaki *et al.* (18) assessed the long-term genomic fidelity of their culture model and demonstrated that this was retained long-term. The culture medium used by Yamazaki et al. is similar to that used by us in this study, hence, suggesting that maintenance of genomic fidelity in our culture could be feasible. Nevertheless, since long-term culture is associated with the introduction of transcriptomic changes as well as changes in cell composition, the fidelity of this spheroid model is predicted to be the best in the short term (65,261).

These findings suggest that this newly developed method for spheroid culture represents the genomic background of meningiomas and is justified for use as drug development tool in studies assessing the efficiency of compounds targeting specific genomic alterations.

3.17.2 Spheroids, monolayers and patient tissues have unique transcriptome signatures

Comparing the transcriptomes of matched patient monolayers, spheroids and tissues revealed that each condition has its own transcriptomic signature demonstrated by the clustering of samples with samples of their respective group in the PCA and hierarchical cluster analysis. This finding is consistent with reports in literature demonstrating cell culture conditions significantly influence the global cell transcriptome (228,262–264). Although I used patient-derived materials, I observed significant differences between the transcriptome profiles of both cell culture models compared to matched patient tissues. These findings were not surprising as transcriptomic differences are to be expected due to the simplicity of *in vitro* modelling and loss of structures such as blood vessels and other cell types that are present *in vivo* (232). In this experimental set-up, the transcripts that are derived from structures in the tissue that are not present in the cell cultures (e.g. blood vessels), cannot be separated from the transcripts that are directly derived from the tumour cells, which presents a limitation of the experiment. To exclude the transcriptomic changes that are driven by the absence of these structures from the analysis, single-cell RNA sequencing should be carried out, which allows for comparing gene expression of exclusive populations, such as meningioma cells in tissues, to those in the *in vitro* cultures.

Alternatively, bulk RNA seq data could be deconvoluted using bioinformatic programs such as CIBERSORTx, although this heavily depends on the use of reliable reference software. Such analysis would give a broader overview of transcriptomic changes for different cell types in the tissues and in vitro models. However, the comparison between the two *in vitro* models is not limited by this feature. Additionally, co-expression analysis was performed to compute a list of transcripts exclusively expressed in tissues. This list indicates a group of genes that are underrepresented *in vitro*, and thus harder to study. For future use of these models, this list could be used as a reference to assess the suitability of this model to study a specific target. These gene lists were annotated using gene ontology analysis which allowed for the identification of biological processes associated with these genes. This highlighted some unexpected gene ontology (GO) terms which could not be directly linked to meningioma pathogenesis, including regulation of odontogenesis (tooth development). Interestingly, the process of tooth development and the process of bone development are closely related (265). For meningioma, osteogenesis has been described as feature in some tumours, where the spontaneous formation of pieces of bone occurs (266,267). It is therefore an interesting observation that genes specifically associated with this seemingly unassociated process are identified in the GO analysis.of co-expressed genes in 3D and Tissue. For the study of these type of meningiomas, it could thus be beneficial to use 3D cultures over 2D cultures.

3.17.3 Increased expression of markers related to EMT in spheroids compared to monolayers

Extensive analysis of the DEGs between the spheroids and monolayer cultures revealed how these models can be best exploited in meningioma research by highlighting the processes that are represented by each model. GSEA comparing the newly established spheroids and traditional monolayer cultures identified the enrichment of EMT (Fig. 3.13B, 3.15A). This finding is supported by several papers that reported similar findings in spheroids from other tissues (263,268–272). For instance, Wong and colleagues (263) comprehensively characterized the transcriptomes of placental extravillous trophoblast spheroids and found significant up-regulations in genes and proteins related to EMT, cell-cell contact, angiogenesis and invasion/migration as compared to monolayer cultures. Similarly, Kuo *et al.* (269) demonstrated that 3D spheroid culture of human epithelial ovarian cancer cells using microfluidic chips resulted in the acquisition of mesenchymal traits, as evidenced by an increased expression of the mesenchymal proteins N-cadherin, vimentin and fibronectin and a concomitant decrease in expression of CD326, an epithelial cell adhesion molecule, in comparison to traditional monolayer cultures. One of the suggested mechanisms behind this phenomenon is the microenvironment of the spheroids (270,273). For instance, oxygen gradients caused by limited oxygen diffusion result in hypoxic conditions in spheroid cores, which has been shown to result in hypoxia-induced EMT (270). Furthermore, the mitogenic growth factors EGF and FGF, commonly supplemented as components of spheroid culture media; including GFS, have been shown to trigger EMT (270). In addition, the presence of immune cells has been shown to induce EMT. For instance, exosomes secreted by M2-macrophage were shown to activate TGFβ-signalling mediated EMT in meningioma cells, which enhanced their migratory and invasive ability (273). In addition to EMT enrichment, an enrichment in the Notch signaling pathway was also identified in spheroid cultures. Interestingly, active Notch signalling has been shown to induce the EMT process. Again, the finding of enrichment in the Notch signalling pathway in spheroid cultures is supported by the literature. Previously, Mauretti et al. (256) demonstrated that Notch signalling was enhanced in cardiac progenitor cell spheroids and that this increase could be further enhanced when cultured under hypoxic conditions. However, this study did not assess the association with EMT.

Confirmation of the enrichment results by qPCR revealed that the EMT-transcription factor genes Snai1 (encoding Snail) and Snai2 (encoding Slug) were consistently upregulated in our spheroid cultures, while the EMT-transcription factor Zeb1 was only moderately increased. This suggests that in meningioma spheroids, EMT is mainly driven by the snail family of transcription factors. Interestingly, there are several reports in the literature that have correlated expression of the EMT transcription factors Snail and Slug, with high-grade meningiomas, while this correlation for other EMT transcription factors was less prominent (185,188). Furthermore, an increase in all tested mesenchymal proteins could be observed in spheroid cultures, although these findings did not reach significance. This is likely due to high patient variability, small sample size (n=5) and low expression levels of these proteins which makes them difficult to quantify reliably in Western blotting. Furthermore, a decrease in CDH1 (encoding E-cadherin) expression, corresponding with EMT, could be confirmed in 4 out of 5 patient samples, although western blotting showed variable results between patients. However, despite a relative increase in E-cadherin expression in some spheroids compared to monolayer cultures, overall E-cadherin expression in spheroids could only be detected at low levels compared to tissues (Fig. 3.14).

The increase in E-cadherin protein expression in spheroids compared to monolayer cultures is likely due to the role of E-cadherin in cell-cell adhesion, which is increased when cells are grown in 3D compared to 2D (138–140,271). Besides canonical EMT proteins, the increase in expression of Notch signalling proteins, Notch1 NICD, Hes1 and Hey1 was observed, confirming the GSEA enrichment analysis. Notch1 signalling and expression of its transcription factors has been associated with increased EMT (202–204,274). Together, these results suggest that meningioma spheroids are indeed progressing towards an increased mesenchymal state but have not yet fully completed EMT (173).

Besides molecular validation of the enrichment of EMT in spheroids compared to monolayers, functional properties associated with EMT, such as invasive capacity were also validated. In fact, WHO grade 1 and 2 derived spheroids displayed observable protrusions in the Matrigel that increased over time, suggestive of functional invasiveness. While the occurrence of invasion in benign WHO grade 1 meningiomas has been reported, this is not very common, and not entirely understood (181,182). Furthermore, since the 2021 version of the WHO grading system for CNS tumours, these tumours are no longer classified as WHO grade 1 and automatically become WHO grade 2 when invasion is observed (2,181). These results suggest, that under specific circumstances, that are enhanced in spheroid culture conditions, WHO grade 1 meningioma cells can undergo EMT and acquire invasive capacity. This model represents the first 3D meningioma that has this capacity and thus, could serve as a platform to study this phenomenon, demonstrating its relevance for meningioma research.

3.17.4 Spheroids display increased expression of markers associated with ECM organisation and histone demethylation

An obvious difference between monolayer and spheroid cultures is cell morphology, which has been shown to determine gene expression and cell behaviour (275). Indeed, GSEA between these models indicated the regulation of ECM organisation as enriched in meningioma spheroid cultures (Fig. 13A, SI6). In cancer cells, ECM has been shown to influence responsiveness to therapies. This suggests that this model is a valuable contribution to preclinical meningioma drug development since it can provide important insights into therapy response compared to monolayers. This will be further studied in the next chapter. In addition, GSEA showed enrichment of histone demethylation in spheroids compared to monolayers. Histone methylation is a type of histone modification and has been shown to have an important role in regulating gene expression. In cancer, enzymes that regulate this process, histone demethylases and histone methyltransferases, are often mutated, which leads to aberrant gene expression (276). Indeed, mutations in the lysine demethylases KDM5C and KDM6A have been identified in meningiomas (277). Furthermore, losses of trimethylation of lysine 27 on histone 3 (H3K27me3) has been shown to negatively impact meningioma patient prognosis (278). My finding suggests that this model could be of interest to studies involving demethylation in meningiomas. In 2D cultures, several processes linked with the mitochondrial structures and metabolic processes are enriched (Fig.13A, SI6). These findings can be explained by the enhanced proliferation rates of monolayer cultures compared to spheroid cultures, which marks a main difference between these two models (279).

3.17.5 Differences between patient-derived meningioma spheroids and MgOs

The spheroid model I presented here is the first 3D model to be established and used in our laboratory and represents the first model that has been extensively characterised. The model is different from other 3D meningioma models previously established and reported in the literature (17–20,149). Specifically, in contrast to the patient-derived organoid models developed by Yamazaki et al. (18) and Siu et al. (19), this spheroid model does not rely on having a structural component such as Matrigel. Therefore, it can serve as a less complex and easier-to-use model alternative to the complex organoid systems, while providing better control over reproducibility, which is particularly important in drug studies (280). The biggest difference between these models and the model I have presented here is the invasion capacity of the cells. In my hands, embedding spheroid cultures or a single cell suspension of primary patient-derived meningioma cells led to invasion into the matrix while in the models of Yamazaki and Siu this feature was not reported. This further highlighted the unique feature of this model to study this specific capacity of meningioma cells, although this observation has been previously reported for spheroid models of other cell types. Moreover, Matrigel is notorious for batch-to-batch variability which complicates reproducibility. Contrasting the organoid models of Yamazaki et al. and Siu et al., my novel spheroid model is a quick short-term model that in the short term maintains important features of the parental tumour. However, the model is not a long-term culture system. Therefore, in cases where long-term effects need to be respresented these organoid models could be a better option, while for studying the short-term effects, a spheroid models like represented here is a good solution to problems caused by the use of Matrigel.

The model presented by Hueng and colleagues (149) uses a serum-free growth factor medium that includes the stem cell niche factors EGF and FGF. Spheroid culture using serum-free medium with EGF and FGF such as used in the paper of Hueng et al. specifically selects for the growth of stem-like cells. Hence, these spheroids are useful to study this specific cell population but doesn't represent the full extend of diverse cell types within a tumour. To avoid the selective growth of meningioma stem-like cells, in my method, while including EGF and FGF, the medium was also supplemented with low serum levels, similar to the medium previously described by Magill et al. to allows for a more diverse cell population. In addition to this novel spheroid model, some experiments were performed to establish MgOs in our laboratory (section 3.15). This method was based on the paper published in 2020 to establish GBM organoids (154). In 2023, Huang *et al.* established meningioma organoids following a similar protocol (20). My experiments were only performed using 1 WHO grade 1 and 1 WHO grade 2 meningioma. However, my results demonstrated that it can be possible to establish viable MgOs following this method, although more optimization is needed for WHO grade 1 organoids. A downside of this model is the extensive hands-on time, which is required when cutting fragments. Furthermore, the slow growth rates limit the use of this model. The method published by Huang et al. (20) to establish MgOs used a different culture medium to establish organoids, which contained 10% FBS, in contrast to the 5% FBS in GFS. Additionally, they did not add any other supplements such as EGF and FGF or N2 and B27. Similar to the MgOs I generated, a limitation of this organoid model is the slow generation of these cultures and the high level of communication with surgeons that is required (20,154). Furthermore, since each MgO is generated from a different fragment of the tumour, it is hard to control for intra-tumour heterogeneity.

Nevertheless, it would be interesting to adopt this novel protocol in our laboratory to test whether the success rate of this model, including cryopreservation, can be increased.

3.17.6 Conclusions

In conclusion, I established a novel patient-derived meningioma spheroid model that resembled morphology, molecular features, and immune microenvironment of meningioma parental tissues. The recapitulation of these important features of the parental tissues suggests the potential to serve as a tool for diverse research purposes, including drug development. The enhanced expression of mesenchymal genes and proteins and enhanced mesenchymal traits, such as enhanced invasion capacity, demonstrate the relevance of this model to study the molecular mechanisms underlying EMT in meningiomas, which are not understood.

4 Application of a novel patient-derived meningioma spheroid model as drug development tool identified combination therapy of MERTK and HDAC inhibition as potential systemic therapy for meningiomas.

4.1 Introduction

Transcriptomic profiling analysis comparing our novel meningioma spheroid model to traditional monolayer cultures revealed the upregulation of genes associated with EMT and the Notch signalling pathway, demonstrating the suitability of this spheroid model to study EMT. EMT is a common oncogenic process associated with tumour progression, treatment resistance, invasion capacity and poor prognosis (185,188,190,234). It describes the process of epithelial cells that lose expression of their typical epithelial proteins (e.g. E-cadherin, Zonula Occludens (ZO)-1), while acquiring expression of mesenchymal proteins (e.g. N-cadherin, vimentin, fibronectin) (173,174,234). These changes are orchestrated by several EMT-associated transcription factors, including Slug, Snail, Zeb1, and Twist, that regulate E-cadherin expression (188). In meningiomas, low E-cadherin and high Slug expression have been correlated with recurrent tumours, suggesting the involvement of EMT in meningioma progression (188). Furthermore, in several tissues, but not in meningiomas, Notch signalling has been shown to induce EMT (203,281,282). Therefore, this oncogenic process is an interesting target for the treatment of meningiomas.

Several compounds have been described to target EMT, these include gamma-secretase inhibitors, HDAC inhibitors and TAM receptor family inhibitors (78,80,101,215,283). This chapter addressed the hypothesis that the novel meningioma patient-derived spheroid model can be as a tool for drug discovery for meningioma. I sought to demonstrate the use of my patient-derived spheroid model by investigating the association between Notch1 and EMT in meningiomas and studying the effect of several drug compounds on meningioma spheroid viability, proliferation and EMT. Firstly, I hypothesized that the enrichment of EMT in the spheroids compared to monolayers is driven by Notch1 signalling. Therefore, I assessed the basal expression levels of Notch1 in WHO grade 1, 2 and 3 meningiomas and normal meningeal tissues. Furthermore, I studied the influence of Notch1 on the expression of EMT-associated proteins and associated biological functions such as invasion and spheroid formation capacity. I proceeded to assess the potential of Notch1 as a therapeutic target in meningioma using the gamma-secretase inhibitor Nirogacestat.

Besides targeting EMT through inhibition of the Notch pathway, several other strategies to inhibit EMT were explored. HDAC inhibition has previously been studied as potential anti-meningioma therapy (84,86), and has been implicated in other cancers to effectively inhibit EMT (80,283). Another therapy that has been attracting interest as a potential anti-meningioma therapy, which has also been demonstrated to target the EMT pathway, is inhibition of the TAM receptor family of tyrosine kinases (78,101). Preliminary data of our group (unpublished) has shown potential for the TAM receptor family inhibitor UNC2025. More specifically, UNC2025 is a dual MERTK/Flt3 inhibitor. This data demonstrated that MERTK could effectively inhibit meningioma proliferation and induce apoptosis in primary meningioma monolayer cultures (284). Based on this data, I hypothesised that treatment with the MERTK/Flt3 inhibitor UNC2025 and the HDAC inhibitor Trichostatin-A (TSA) can inhibit meningioma spheroid viability, proliferation and EMT. Additionally, I hypothesised that these effects could be enhanced by combination therapy of these compounds.

The results presented here validated the application of this patient-derived meningioma spheroid model for use as *in vitro* drug development tool and for studying important oncogenic cellular processes such as EMT.

4.2 Notch1 NICD expression increases in meningioma tumours of all grades compared to normal meningeal tissues (NMT)

Transcriptomic analysis revealed Notch1 upregulation in meningioma spheroids compared to monolayers, which prompted me to investigate Notch1 expression in meningiomas. Previous work by Cuevas *et al.* (214) demonstrated an increase in Notch1 NICD protein expression in some, but not all meningiomas. To assess whether these findings could be replicated in our laboratory, I assessed the protein expression levels of the Notch1 NICD in normal meningeal tissues (NMT) and tissues of WHO grade 1, 2 and 3 meningiomas by western blot. Consistent with data by Cuevas et al. (214), western blot analysis showed low expression levels of the Notch1 NICD in NMT and a grade-independent increase in expression in meningioma tumours (Fig. 4.1A, B). This increase was significant for WHO grade 1 and 2 tumours ($p<0.05$), but not for WHO grade 3 meningiomas ($p=0.658$). The expression level of the Notch1 NICD was observed to vary considerably between patients. Since a grade-dependent increase could not be observed, Notch1 NICD expression levels were also assessed when combining all tumours and comparing them to the NMT control tissues (Fig. 4.1C). This data demonstrated a significant increase of Notch1 NICD expression in meningiomas compared to NMT ($p<0.001$)

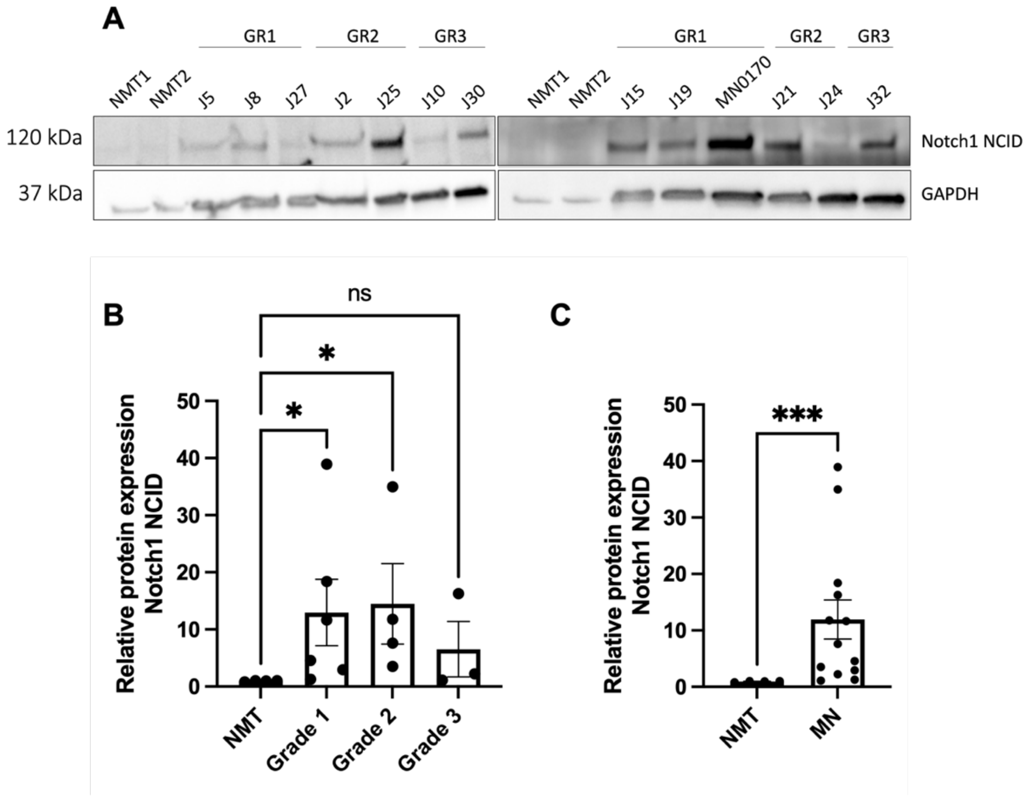

Figure 4.1: Notch1 NICD expression increases in meningioma tumours of all grades compared to NMT (A) Representative western blot showing Notch1 NICD expression in NMT and meningioma tissues of WHO grade 1, 2 and 3. GAPDH was the loading control. (B) Quantification of Notch1 NICD expression relative to NMT expression levels separated by WHO grade. NMT (n=4), Grade 1 (n=6), Grade 2 (n=4), Grade 3 (n=3). Non-parametric Kruskal-Wallis test was used for statistical evaluation; *p<0.05, ns=not significant. (C) Quantification of Notch1 NICD expression levels of all tumours independent of WHO grade (n=13). Non-parametric Mann-Whitney test was used for statistical evaluation; ***p<0.001, ns=not significant.

4.3 Knockdown of NOTCH1 decreases expression of the EMT-associated proteins Hes1 and Slug in monolayer cultures.

Notch1 expression has been associated with the induction of EMT. In the literature, there are only a few studies on Notch1 expression in meningiomas and none of these studied the association between Notch1 and EMT (214,285). First, I investigated whether shRNA-mediated knockdown of Notch1 influenced protein expression levels of EMT-associated proteins using primary meningioma monolayer cultures. To achieve this, primary meningioma cell lines were transfected using three shRNA constructs targeting Notch1 (section 2.4). First, to assess which construct was most effective to reduce Notch1 expression, the meningioma WHO grade 3 cell line KT21 was infected with three shRNA constructs and infection efficiency. Western blot analysis showed that constructs 132 and 134 effectively reduced the expression of the Notch1 NICD by approximately 20% and 23% respectively, in KT21 cells, confirming the efficiency of these constructs (Fig. 4.2A, B). However, a decrease in the expression of full-length Notch1 was not observed. Next, 4 out of 6 primary WHO grade 1 meningioma cell lines were successfully infected with lentiviral construct 132 and/or 134 (table 4.1). Western blot analysis revealed a significant decrease in the expression of the Notch1 NICD of 78% for construct 132 ($p<0.0001$) and 55% for construct 134 ($p<0.01$) (Fig. 4.2C, D). Expression of full-length Notch1 (Notch1 FL) was not assessed since expression was below the detectable threshold for western blot analysis in most experiments. The decrease in the expression of Notch1 NICD, resulted in a significant decrease of the Notch1 target protein Hes1 in all cases, with an average decrease of 63% for lentiviral construct 132 ($p<0.01$) and 62% for lentiviral construct 134 ($p<0.05$) (Fig. 4.2C, D). The expression of the EMT transcription factor Slug, was decreased with an average of 33% for construct 132 ($p<0.05$) and 13% for construct 134 ($p=0.882$) (Fig. 4.2C, D). The level of Slug reduction varied between samples and a correlation between the decreased expression of the Notch1 NICD and the decrease of Slug could not be observed. Furthermore, expression of the epithelial protein E-cadherin was not detected.

Next, I assessed whether the effects induced by the Notch1 knockdown were maintained in spheroid cultures. To achieve this, the sample in which the strongest Notch1 NICD silencing was observed (MN595), was selected for further assessment. Cells were subjected to spheroid formation and the expression of Notch1 NICD and its downstream targets Hes1 and Slug were assessed by western blot 3 days post-seeding. Unexpectedly, western blot analysis of spheroids generated from these cells with a confirmed Notch1 knockdown, showed that the effects on Notch1 NICD, Hes1 and Slug expression levels were rescued upon spheroid formation and a reduction in expression compared to the scrambled was not observed (Fig. 4.2E, F).

Table 4.1 Knock-down efficiency primary WHO grade 1 monolayer

Sample	**Knock-down efficiency** **Notch1 NICD**		
	Construct 131	Construct 132	Construct 134
MN577	~60%	~77%	~50%
MN595	N/A	~100%	N/A
MN605	N/A	N/A	N/A
MN611	N/A	~63%	~57%
MN613	N/A	N/A	N/A
MN630	N/A	~74%	N/A

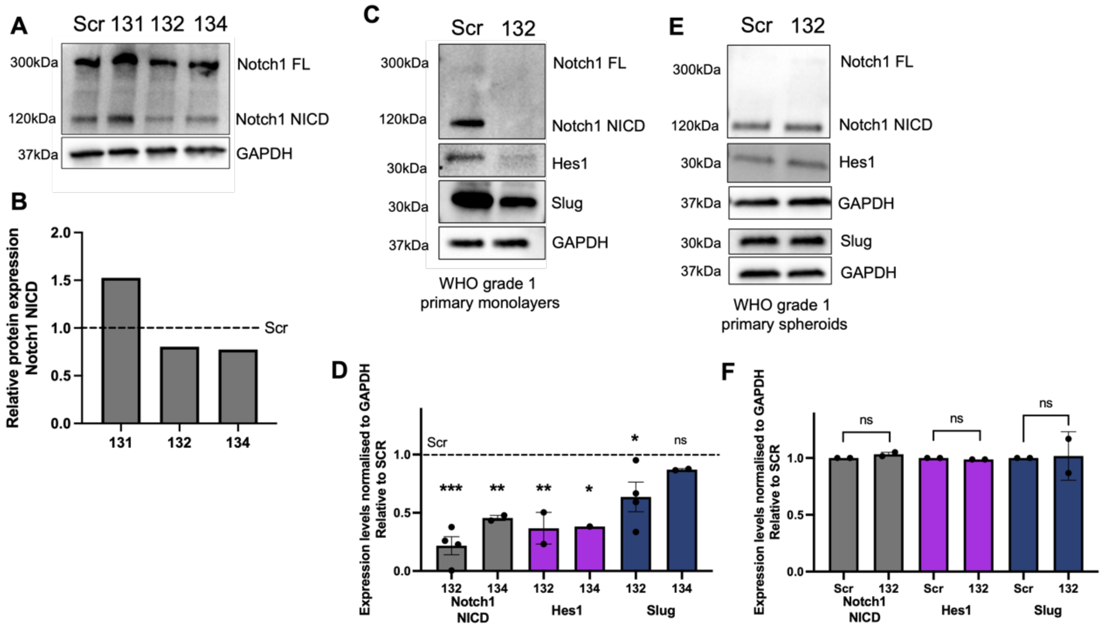

Figure 4.2: Knockdown of Notch1 NICD moderately decreases expression of the EMT-associated protein Hes1 and Slug in primary meningioma monolayer cultures

(A) Representative western blot and (B) quantifications of Notch1 NICD knockdown efficiency in monolayer cultures of KT21 cells using lentiviral constructs 131, 132, 134 compared to Notch1 NICD expression levels in scramble control (dashed line) (n=1). GAPDH was the loading control. (C) Representative western blot and (D) quantifications (E) showing the expression levels of Notch1 full length, Notch1 NICD, Hes1 and Slug compared to scramble controls in primary meningioma monolayers after transfection with lentiviral constructs 132 and 134 (n=4). Knockdown of Notch1 NICD significantly reduces Hes1 and Slug expression in primary monolayer cultures. One-way ANOVA, ***p<0.0001, **p<0.01, *p<0.05. (E) Representative western blot and (F) quantifications showing the expression levels of Notch1 full length, Notch1 NICD, Hes1 and Slug compared to scramble controls in primary meningioma spheroids after transfection with lentiviral construct 132 (n=2). ns= not significant. One-way ANOVA.

4.4 Inhibition of Notch1 signalling through the gamma-secretase inhibitor Nirogacestat reduces expression of Notch1 target protein Hes1 and the EMT-transcription factor Slug

An effective pharmacologic strategy to inhibit Notch signalling is by targeting gamma-secretase, the enzyme that cleaves the active Notch1 NICD, which can then translocate to the nucleus and activate transcription (215). Since shRNA-mediated Notch1-silencing induced a moderate decrease in the expression of the Notch target protein Hes1 and the EMT-transcription factor Slug, I assessed whether a similar effect could be achieved following gamma-secretase inhibition using Nirogacestat. Western blot analysis demonstrated that 72h-incubation with 5 µM and 10 µM Nirogacestat successfully inhibited Notch signalling, evidenced by the significant downregulation of the Notch target protein Hes1 in monolayers (5 µM; $p<0.01$, 10 µM; $p<0.05$) (Fig. 4.3A, B) and spheroids (5 µM; $p<0.01$, 10 µM; $p<0.01$) (Fig. 4.3C, D). Contrastingly, significant down-regulation of the Notch1 NICD was not observed (Fig. 4.3C, D). However, a trend towards significance was observed in spheroids (5 µM; $p=0.300$, 10 µM; $p=0.115$). Moreover, in 2 out of 4 patient-derived spheroids, treatment with a dose of 5 µM was sufficient to decrease Notch1 NICD expression levels. To further analyse this difference in effect between spheroids derived from different patient samples, the baseline expression levels of the Notch1 NICD and their absolute decrease were directly compared for 3 primary tumours (Fig. 4.3E). I observed that spheroids which showed a strong decrease in Notch1 NICD expression had a higher baseline expression compared to spheroids that did not show a significant decrease in Notch1 NICD expression (Fig. 4.3E). Furthermore, Nirogacestat treatment decreased the expression of the EMT transcription factor Slug at both concentrations in monolayers (5 µM; $p<0.05$, 10 µM; $p<0.01$) (Fig. 4.3A, B) and spheroids (5 µM; $p<0.0005$, 10 µM; $p<0.005$) (Fig. 4.3C, D). E-cadherin expression was only detected in 1 out of 3 samples in the monolayer experiment and in 1 out of 5 samples in the spheroid experiment (data not shown). However, an increase in expression was not observed.

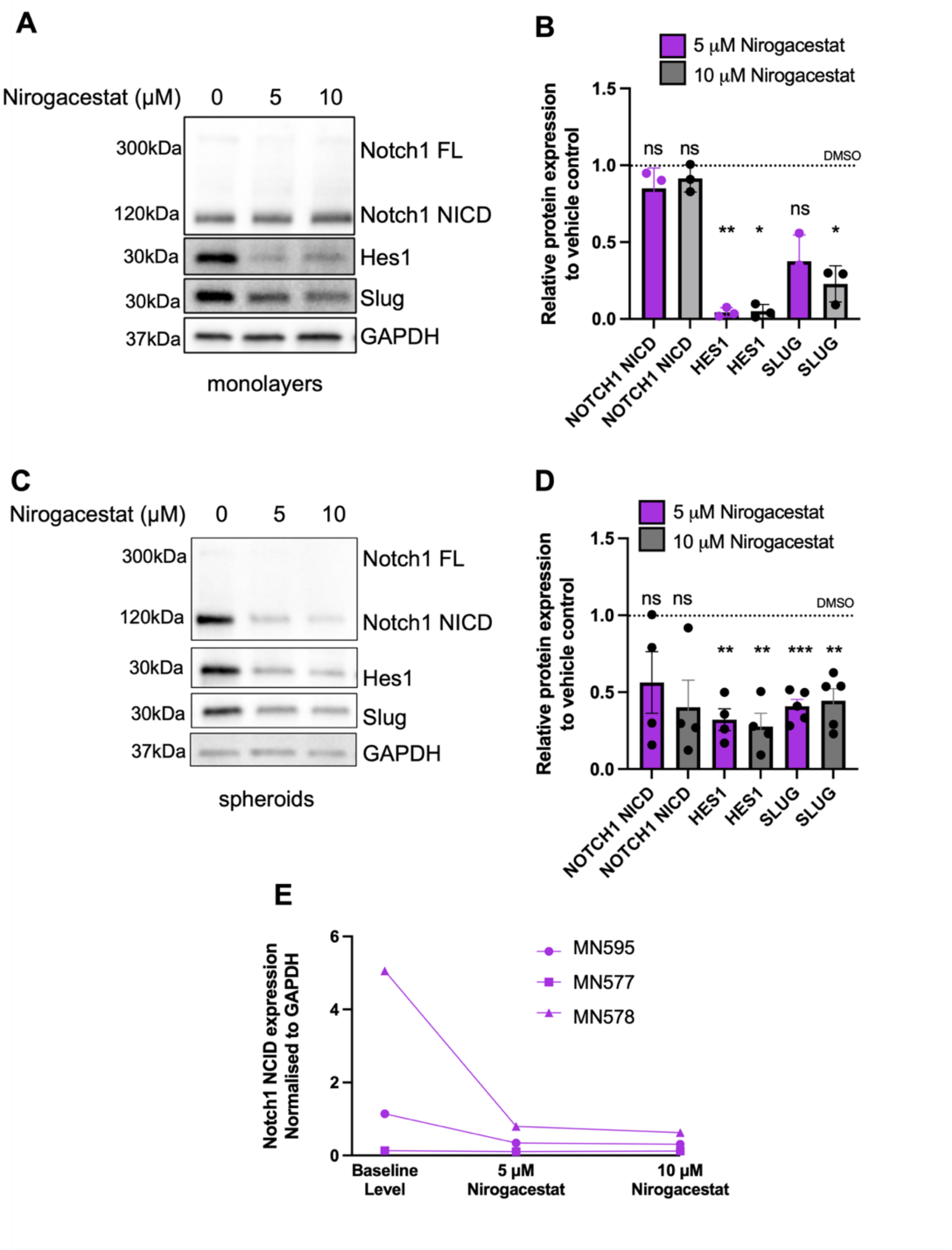

Figure 4.3: Nirogacestat treatment reduces expression of EMT-associated proteins Slug and Hes1 Representative western blot (A) and quantification (B) showing Notch1 full length (FL) and NICD, Hes1 and Slug expression in primary monolayer cultures incubated with vehicle, 5 μM or 10 μM Nirogacestat at 72h (n=3). Expression levels are relative to vehicle (DMSO 0.1%). Representative western blot (C) and quantification (D) showing Notch1 full length (FL) and NICD, Hes1 and Slug expression in spheroid cultures incubated with vehicle, 5 μM or 10 μM Nirogacestat at 72h (n=5). Expression levels are relative to vehicle (DMSO 0.1%). (E) Quantification of baseline expression levels normalised to GAPDH of the Notch1 NICD and their absolute decrease (n=3). Loading control was GAPDH. One-way ANOVA, *p<0.05, **p<0.01, ***p<0.001, ns=not significant.

4.5 Nirogacestat treatment does not impair spheroid formation and 3D Matrigel® invasion

Since Notch1 inhibition and a decrease in Slug expression have been implicated with a lowered spheroid formation capacity and reduced cell migration and invasion (282,286–288), I assessed these features in primary WHO grade 1 meningioma spheroids after Nirogacestat treatment. Cells were plated for spheroid formation in GFS media supplemented either with empty vehicle (DMSO), 1 µM, 5 µM or 10 µM Nirogacestat and spheroid formation capacity was assessed after 3 days by microscopy. Unexpectedly, while treatment with a concentration of 5 µM and 10 µM Nirogacestat significantly lowered Slug expression levels in spheroids, it did not show impaired spheroid formation capacity (Fig. 4.4A), suggesting Slug expression is not required for spheroid formation in meningiomas. Comparably, embedding spheroids in Matrigel, serving as ECM-mimicker and invasion matrix, a reduction in the invasion capacity of spheroids could not be observed after treatment with 5 µM Nirogacestat compared to the vehicle-treated controls (Fig 4.4B, C).

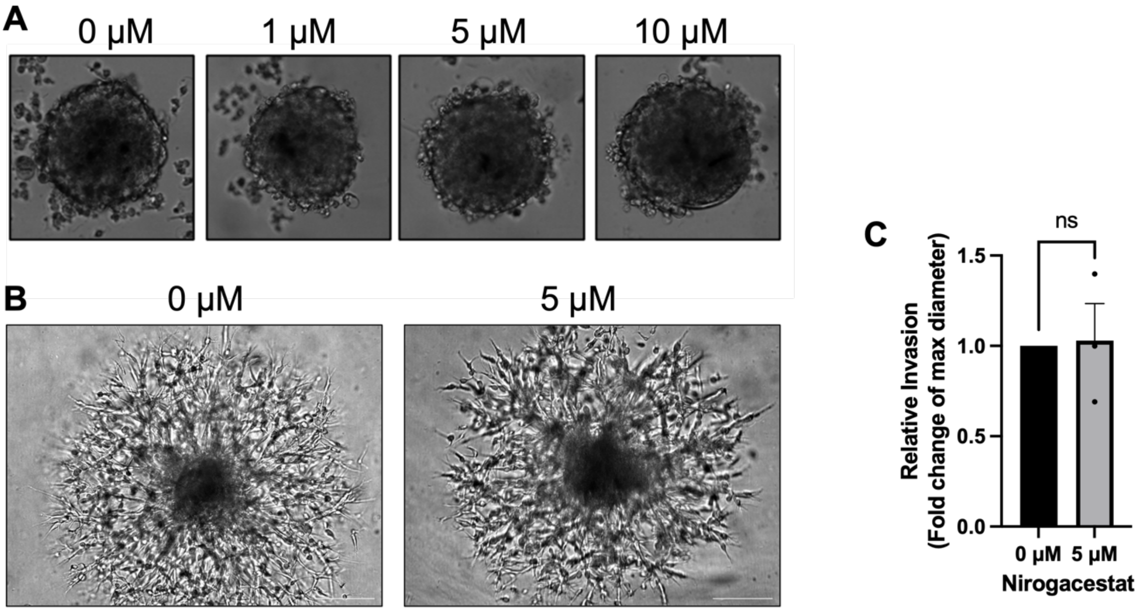

Figure 4.4: Nirogacestat has no effect on spheroid formation and invasion capacity

(A) Representative phase-contrast microscopy images of WHO grade 1 spheroids treated with 0, 1, 5 and 10 μM Nirogacestat upon cell seeding. Images were taken after 72 hours of spheroid formation. Nirogacestat treatment did not affect spheroid formation capacity. (B) Representative phase-contrast microscopy images of WHO grade 1 spheroids embedded in Matrigel at 48 hours of 5μM Nirogacestat treatment. Scale bar indicates 200μm. (C) Bar graph showing the relative increase of max. diameter of 5μM Nirogacestat treated spheroids at 48 hours compared to untreated (0 μM) control spheroids (n=3, biological repeats). T-test was used for statistical evaluation; ns=not significant.

4.6 Inhibition of Notch1 through the gamma-secretase inhibitor Nirogacestat does not affect meningioma cell viability and proliferation of monolayers and spheroids

I assessed the effect of Nirogacestat on proliferation and viability in primary monolayers and spheroid cultures. In contrast to the findings of Cuevas *et al.* (214), 72h-treatment of primary meningioma WHO grade 1 monolayers and spheroid cultures with Nirogacestat did not result in inhibition of meningioma cell viability up to a concentration of 10 μM (Fig. 4.5A-C). To exclude the influence of medium formulation, monolayers were treated using standard monolayer culture medium MN1 (Fig. 4.5B) and the spheroid culture medium GFS (Fig. 4.5A). Consistently, in both conditions, an effect on viability was not observed (n=4). Unexpectedly, for spheroids, a significant increase in viability was observed for 0.03 μM, 0.06 μM, 0.1 μM, 0.3 μM, 0.6 μM, 1 μM, and 3 μM compared to the untreated vehicle control (Fig. 4.5D). Furthermore, 72h treatment with Nirogacestat had a significantly different effect on spheroids compared to monolayers cultured using GFS medium when treated with a concentration between 0.03-3μM ($p<0.05$) (Fig. 4.5D). Immunostaining of the nuclear proliferation marker protein ki67 showed no change in the percentage of ki67-positive cells in spheroids treated with 5 μM and 10 μM Nirogacestat for 72h compared to the vehicle control (n=3) (Fig. 4.5E, F), suggesting Nirogacestat had no effect on spheroid proliferation. The effect on proliferation in monolayers was not assessed.

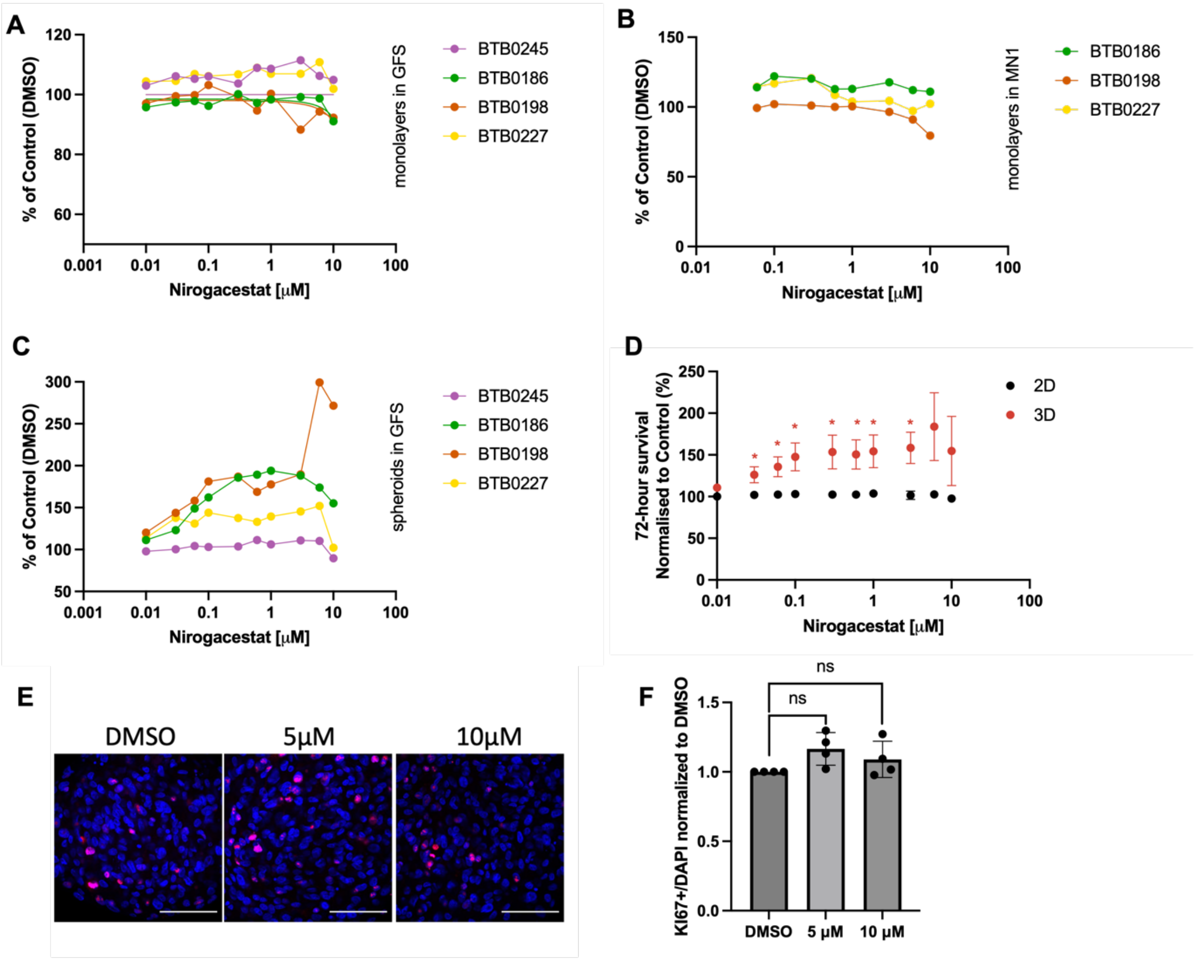

Figure 4.5: Nirogacestat treatment does not decrease meningioma cell viability in monolayers and spheroids Cell viability of meningioma primary monolayer cultures in GFS (n=4) (A) and MN1 (n=3) (B) and spheroid cultures in GFS (n=4) (C) at 72h after treatment with a single dose of Nirogacestat at concentrations 0.01, 0.03, 0.06, 0.1, 0.3, 0.6, 1, 3, 6, 10 µM relative to vehicle control (0.1% DMSO). Each line represents an individual sample. Cell viability was measured using the CellTiter Glo® assay. No decrease in viability was observed. (D) Cell viability of primary meningioma spheroids (3D, red) compared to primary meningioma monolayers (2D) at 72h treatment with Nirogacestat using GFS. One-way ANOVA, *$p<0.05$. Data represents n=4 experiments in 4 multiples for monolayers and 8 multiples for spheroids. Error bars indicate the standard error of mean. (E) Representative immunofluorescence image of KI67 (red) in spheroids following 48h of nirogacestat treatment at a single dose of 5 µM and 10 µM (n=3). Cell nuclei are stained with DAPI (blue). Scale bar = 100µm. Images were taken using the Leica confocal microscope SP8. (F) Quantification of KI67 positive cells relative to DAPI (nuclei) at concentrations of 5 µM and 10 µM, displayed as the ratio of KI67+/DAPI (n=3). ns=not significant, One-way ANOVA.

4.7 The dual MERTK/Flt3 inhibitor UNC2025 and the HDAC inhibitor Trichostatin A (TSA) decrease meningioma spheroid viability

Since Notch1 inhibition didn’t show satisfactory anti-tumour effects on meningioma spheroids, I wanted to further validate the functionality of the newly established 3D meningioma spheroid model testing other therapeutics that inhibit EMT and concomitantly inhibit spheroid proliferation and viability. Previous reports proposed TAM receptor inhibition and HDAC inhibition as potential therapeutic strategies for meningiomas (84,85,284). Unpublished work by our group has demonstrated the upregulation of MERTK expression in meningiomas. Furthermore, MERTK expression was significantly increased in spheroid cultures compared to monolayer cultures in the transcriptomics dataset (Fig. 4.6A). Therefore, I chose to investigate the effect of the dual MERTK/Flt3 inhibitor UNC2025 and the HDAC inhibitor TSA on primary meningioma monolayer and spheroid viability.

4.7.1 UNC2025

72h treatment of primary meningioma spheroids with increasing concentrations of UNC2025 effectively decreased spheroid viability at a µM range, with an average IC_{50} of 1.59 µM for meningioma WHO grade 1 and 3.82 µM for meningioma WHO grade 2 spheroids (Fig. 4.6B, C). Although WHO grade 2 spheroids showed a higher drug resistance compared to WHO grade 1 spheroids, this difference was not statistically significant ($p=0.263$) (Fig. 4.6D, E). Consistently, treatment of primary meningioma WHO grade 1 monolayers with increasing concentrations of UNC2025 effectively decreased cell viability in a dose-dependent manner (Fig. 4.6F). However, this decrease was exclusively significant when treated with a dose of 3 μM or higher. For WHO grade 2 meningioma, the monolayer assay was not performed. Strikingly, with an average IC_{50} of 3.79 μM and 1.59 μM in monolayers and spheroids respectively, UNC2025 more effectively inhibited meningioma cell viability in spheroid cultures compared to monolayer cultures derived from the same patient (Fig. 4.6G, H). Monolayers were cultured in the same medium as the spheroids (GFS) to be able to exclude any effect potentially induced by the culture medium.

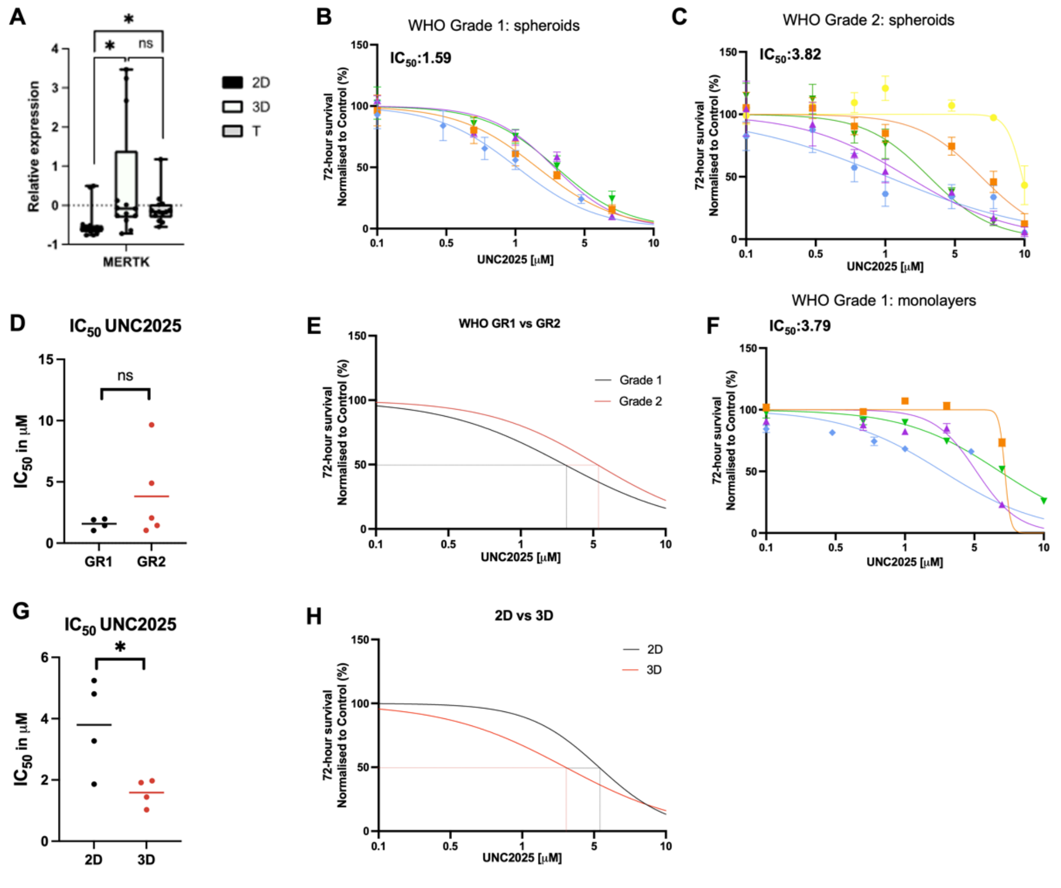

Figure 4.6: UNC2025 treatment has an inhibitory effect on meningioma cell viability in monolayers and spheroids (A) Relative MERTK expression (RNAseq) in 2D, 3D, and tissue. (B-C) Cell viability of meningioma (B) WHO grade 1 spheroid (n=4) and (C) WHO grade 2 spheroid (n=5) cultures decreased 72h after treatment with a single dose of UNC2025 at concentrations up to 10 µM relative to vehicle control (0.1% Ethanol). Cell viability was measured using the CellTiter Glo® assay. Error bars indicate standard error of mean for quadruplicates in monolayer experiments and 8 multiples in spheroid experiments. Each line represents an

individual sample. (D) Average IC_{50} does not significantly change in WHO grade 2 spheroids (red) (IC_{50}: 3.82 µM) compared to WHO grade 1 (black) (IC_{50}: 1.59 µM) spheroids (p=0.263). (E) Average viability curves comparing dose response in WHO grade 1 and WHO grade 2 spheroids. (F) Cell viability of meningioma primary WHO grade 1 monolayer cultures (n=4) decreased following 72h treatment with a single dose of UNC2025 at concentrations up to 10 µM relative to vehicle control (0.1% Ethanol). (G) Average IC_{50} concentration is significantly higher for monolayer cultures (2D, black) ((IC_{50}: 3.79 µM) compared to spheroid cultures (3D, red) (IC_{50}: 1.59 µM) (p<0.05) (n=4). (H) Average viability curves comparing dose response in matched 2D (black) and 3D (red) samples. IC_{50} was calculated using GraphPad Prism analysis software. Student’s t test was used for statistical evaluation; ns=not significant, *p<0.05.

4.7.2 TSA

Incubation of meningioma spheroid cultures with TSA for 72 hours significantly inhibited cell viability in a dose-dependent manner from 1 µM for WHO grade 1 and WHO grade 2 meningiomas, with an average IC_{50} of 1.33 µM and 1.6 µM respectively (Fig. 4.7A, B). Despite the small increase in IC_{50} concentration, the difference between grades was not statistically significant (p=0.371) (Fig. 4.7C, D). Additionally, 72 hours treatment of primary monolayer cultures with TSA significantly decreased viability from 0.50 µM, with an average IC_{50} of 0.70 µM (Fig. 4.7E). In contrast with the pattern observed following UNC2025 treatment, the IC_{50} of TSA treatment in spheroids was significantly increased compared to the IC_{50} in monolayers (p=0.002) (Fig. 4.7F, G). Penetration of TSA in the spheroid was confirmed by increased levels of acetylation of histone 3 (H3) after 1µM of 72h TSA treatment (Fig. 4.7H, I).

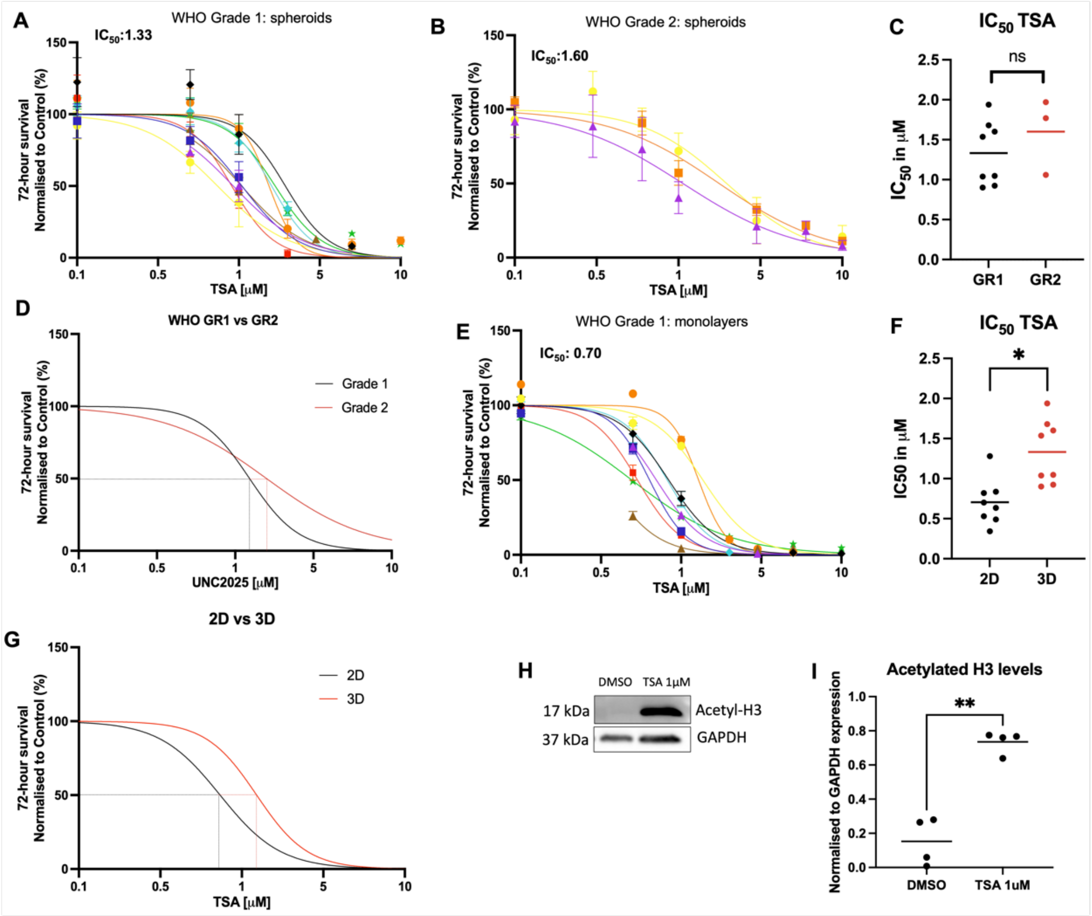

Figure 4.7: TSA treatment has an inhibitory effect on meningioma cell viability in monolayers and spheroids Cell viability of meningioma (A) WHO grade 1 spheroid (n=9) and (B) WHO grade 2 spheroid (n=3) cultures decreased 72h after treatment with a single dose of TSA at concentrations up to 10 μM relative to vehicle control (0.1% DMSO). Cell viability was measured using the CellTiter Glo® assay. Error bars indicate standard error of mean for quadruplicates in monolayer experiments and 8 multiples in spheroid experiments. Each line represents an individual sample. (C) The average IC_{50} concentration did not significantly change in WHO grade 2 (red) (IC_{50}: 1.60 μM) compared to WHO grade 1 (black) (IC_{50}: 1.33 μM) spheroids (p=0.371). (D) Average viability curves comparing dose response in WHO grade 1 and WHO grade 2 spheroids. (E) Cell viability of meningioma primary WHO grade 1 monolayer cultures (n=9) decreased following 72h treatment with a single dose of TSA at concentrations up to 10 μM relative to vehicle control (0.1% DMSO). (F) The average IC_{50} concentration is significantly decreased in monolayer cultures (IC_{50}: 0.70 μM) (2D, black) compared to spheroid cultures (3D, red) ($p<0.05$) (n=8). (G) Average viability curves comparing dose response in matched 2D (black) and 3D (red) samples. (H) Representative western blot and (I) quantification showing increased acetylation of Histon 3 (acetyl-H3) following 72h treatment with 1μM TSA compared to vehicle

control (0.1% DMSO) ($p<0.01$) in WHO grade 1 spheroids, demonstrating TSA penetration. GAPDH was the loading control. IC_{50} was calculated using GraphPad Prism analysis software. Student's t test was used for statistical evaluation; ns=not significant, *$p<0.05$, **$p<0.01$.

4.8 Combined therapy of the dual MERTK/Flt3 inhibitor UNC2025 and HDAC inhibitor TSA synergistically inhibit meningioma spheroid viability and decrease proliferation

Combination therapy has the potential to lower the required dose of drug administration and thereby potentially mitigate side effects, while simultaneously providing anti-cancer benefits (90). Therefore, I investigated the potential of combined therapy of UNC2025 and TSA to enhance their effectivity on decreasing meningioma spheroid viability and proliferation. To test the effect of combined therapy, spheroids were treated for 72 hours with both drugs as monotherapy and in combination using the dose of the average IC_{50} for monotherapy, 1.3 µM and 1.6 µM for TSA and UNC2025 respectively. Monotherapy with each drug and combination therapy using the same doses significantly decreased spheroid viability compared to the vehicle control (Fig. 4.8A). Interestingly, combination therapy significantly decreased spheroid viability compared to monotherapy with UNC2025 ($p<0.002$) but did not significantly decrease spheroid viability compared to monotherapy with TSA ($p=0.220$). Next, spheroids were treated with equal doses of both drugs of 1 µM, 0.5 µM, and 0.25 µM to test how much the doses could be lowered to reach a significant effect on spheroid viability (Fig. 4.8B, C, D). Combination therapy with 1 µM of both drugs significantly decreased spheroid viability compared to the untreated control ($p<0.0001$) and monotherapy using the same dose (UNC2025: $p<0.0001$; TSA: $p<0.01$) (Fig. 4.8B, E). Combination therapy with lower doses of 0.25 µM and 0.5 µM decreased spheroid viability to approximately 88% and 57%

for 0.25 µM and 0.5 µM respectively, although this did not reach the significance threshold (0.25 µM: p=0.772; 0.5 µM: p=0.144) (Fig. 4.8C, D). To investigate the interaction of the effect of this combination strategy, the combination index (CI) was calculated according to the formula described by Chou and Talalay; the sum of the ratio of the dose of each drug in the combination strategy to reach 50% efficacy to the IC_{50} dose used in monotherapy. Synergy is implied when the CI<1 (289). The CI for combining UNC2025 and TSA in meningioma WHO grade 1 spheroids was (0.6 µM/1.6 µM) + (0.6 µM/1.3 µM) = 0.837. Hence, UNC2025 and TSA in meningioma WHO grade 1 spheroids have a synergistic effect on decreasing spheroid viability. Furthermore, the effect of the combination strategy of UNC2025 and TSA was tested in WHO grade 2 spheroids (Fig. 4.8F, G, H). Consistent with the observation of decreased sensitivity to monotherapy (section 4.7), WHO grade 2 spheroids were less sensitive to combination therapy at the same dose compared to WHO grade 1 spheroids. A combined dose of 1 µM was required to reach 50% efficacy, which is approximately double the dose required in WHO grade 1 (4.8F). Interestingly, at this concentration, combination therapy significantly decreased spheroid viability compared to the untreated control (p<0.05) and monotherapy using the same dose (UNC2025: p<0.05; TSA: p<0.05).

To further test the potential of this combination strategy, the effect of combination therapy on spheroid proliferation was assessed. Meningioma WHO grade 1 and grade 2 spheroids were treated with a dual dose of 0.5 µM of UNC2025 and TSA for 72 hours (Fig. 4.8I). Spheroid proliferation was significantly decreased in spheroids of both grades (GR1: p<0.0001; GR2: p<0.01) following combination therapy at a dose of 0.5 µM compared to the untreated control (Fig. 4.8J, K).

Whilst a strong decrease in proliferation after combination therapy was observed compared to single dose therapy for both drugs, this difference did not reach significance. The combination index could not be calculated from this data.

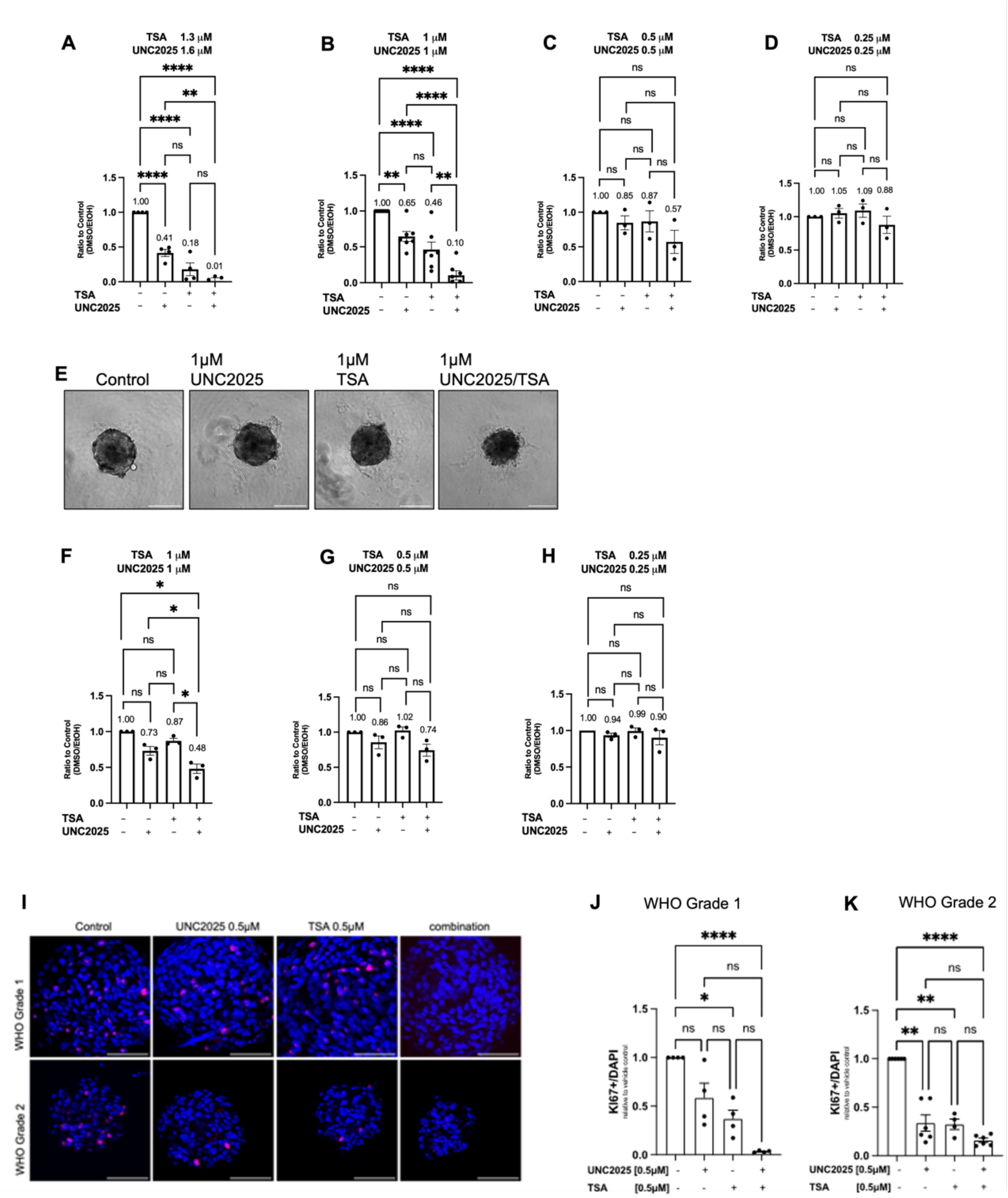

Figure 4.8: Combination therapy of UNC2025 and TSA synergistically inhibits spheroid viability and proliferation Cell viability of meningioma WHO grade 1 spheroids after treatment with monotherapy and combination therapy of UNC2025 and TSA at a concentration of (A) 1.3 µM TSA and 1.6 µM UNC2025 (n=4), (B) 1 µM TSA and 1 µM UNC2025 (n=7), (C) 0.5 µM TSA and 0.5 µM UNC2025 (n=3), (D) 0.25 µM TSA and 0.25 µM UNC2025 (n=3). Data is presented as ratio to vehicle control. Average ratio for each condition is represented above each bar. (E) Representative phase-contrast image showing spheroids after monotherapy and combination therapy of UNC2025 and TSA at a concentration of 1µM UNC2025 and 1µM TSA. Scale bar = 200µm. Image taken with the Leica IM8 fluorescence microscope at 20X objective. Cell viability of meningioma WHO grade 2 spheroids after treatment with monotherapy and combination therapy of UNC2025 and TSA at a concentration of (F) 1 µM TSA and 1 µM UNC2025 (n=3), (G) 0.5 µM TSA and 0.5 µM UNC2025 (n=3), (H) 0.25 µM TSA and 0.25 µM UNC2025 (n=3). Data is presented as ratio to vehicle control. Average ratio for each condition is represented above each bar. Viability was measured in 8 multiples per condition for each experiment using the CellTiter Glo® assay. Error bars indicate standard error of mean. (I) Representative immunofluorescence images of KI67 (red) in WHO grade 1 (top) (n=4) and WHO grade 2 (bottom) (n=5) spheroids of following 72h of mono or combination treatment with a dose of 0.5 µM TSA and 0.5 µM UNC2025. Cell nuclei are stained with DAPI (blue). Scale bar = 100µm. Images were taken using the Leica confocal microscope SP8. Quantification of KI67 positive cells relative to DAPI (nuclei) after combination treatment with 0.5 µM TSA and 0.5 µM UNC2025 in (J) WHO grade 1 (n=4) and (K) WHO grade 2 (n=3) spheroids displayed as the ratio of KI67+/DAPI. ns=not significant, *p<0.05, **p<0.01, ****p<0.0001. One-way ANOVA with Dunett’s test for multiple comparisons was used for statistical evaluation.

4.9 Combined therapy of the dual MERTK/Flt3 inhibitor UNC2025 and HDAC inhibitor Trichostatin-A reverses expression of EMT- associated protein expression in meningioma spheroids

Inhibition of MERTK and HDAC have been associated with inhibition of the EMT process in several cancers (71,78,290,291). To investigate the effects of UNC2025 and TSA on the EMT process in meningioma spheroids, the expression levels of EMT-associated genes and proteins were assessed after mono and combination therapy. Monotherapy of 1 µM UNC2025 increased expression of the epithelial protein E-cadherin and decreased expression of the EMT transcription factor Slug, suggesting an inhibitory effect on EMT in meningioma WHO grade 1 spheroids. A change in the expression of the mesenchymal protein N-cadherin could not be observed (Fig. 4.9A, B). However, these changes were not statistically significant (E-cadherin $p=0.1463$; Slug $p=0.5357$; N-cadherin $p=0.6547$).

Next, I investigated whether the combination therapy of UNC2025 and TSA had an effect on the expression of EMT-associated genes and proteins. qPCR analysis revealed a significant increase in the epithelial protein E-cadherin after 72 hours of treatment with 0.5µM UNC2025 and 0.5 µM TSA in WHO grade 1 meningiomas ($p<0.05$) and an increase approaching significance in WHO grade 2 meningiomas ($p=0.06$) (Fig. 4.9C, D). This difference between grades is consistent with the observation that WHO grade 2 meningiomas seem more resistant to this therapy in comparison to WHO grade 1 meningiomas (Fig. 4.8). However, I did not observe a decrease in gene expression levels of the EMT transcription factors SNAI1 (corresponding to the protein Snail) and SNAI2 (corresponding to the protein Slug) in spheroids of both grades (Fig. 4.9C, D).

Additionally, a significant decrease in gene expression of Notch1 could not be observed (Fig. 4.9C, D). At protein level, combination treatment of 72 hours with 0.5 µM UNC2025 and 0.5 µM TSA resulted in a significant 11-fold increase in E-cadherin expression in WHO grade 1 spheroids ($p<0.01$) (Fig. 4.9E, F). Moreover, I detected a modest but significant decrease in the EMT-associated proteins Slug (1.4-fold decrease, $p<0.05$) and the active intracellular domain of Notch1 (NICD) (2.6-fold decrease, $p<0.01$) (Fig. 4.9E, F). For the mesenchymal protein Snail (1.2-fold decrease, $p=0.55$), but not N-cadherin (1.26-fold increase, $p=0.65$), a decreasing trend was observed. Similarly, WHO grade 2 derived spheroids treated with a higher dose of 1 µM UNC2025 and 1 µM TSA showed a significant 339-fold increase in E-cadherin ($p<0.05$) and a significant 2.5-fold decrease in Slug ($p<0.001$) (Fig. 4.9G, H). These results suggest that the combination strategy of UNC2025 and TSA is potent to induce E- cadherin to a strong level but only moderately reduces the expression of mesenchymal proteins in meningioma spheroids.

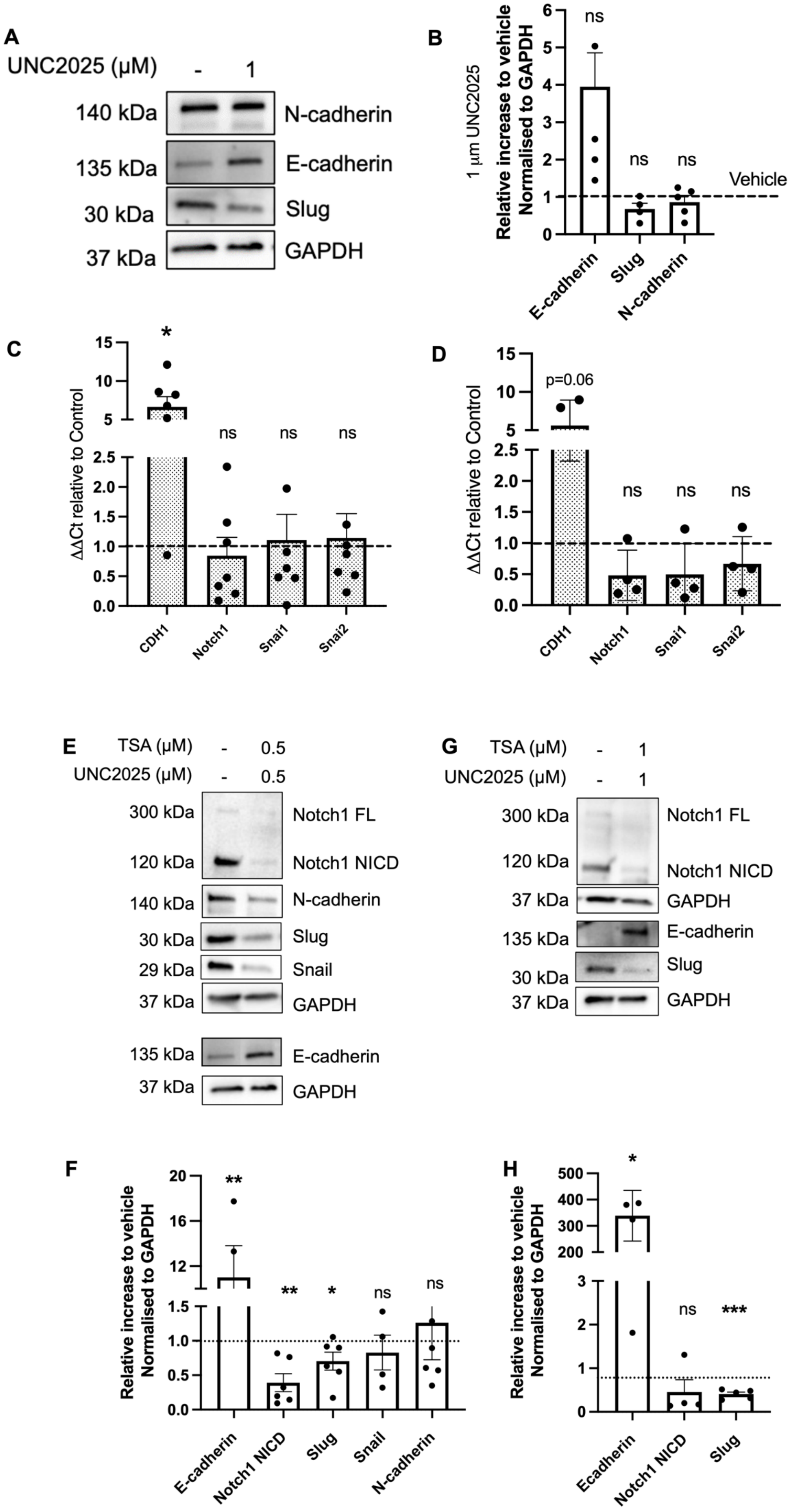
A
UNC2025 (μM) - 1
140 kDa N-cadherin
135 kDa E-cadherin
30 kDa Slug
37 kDa GAPDH
B
1 μm UNC2025
Relative increase to vehicle
Normalised to GAPDH
0 1 2 3 4 5 6
ns
ns
ns
Vehicle
E-cadherin
Slug
N-cadherin
C
ΔΔCt relative to Control
0.0 0.5 1.0 1.5 2.0 2.5 5 10 15
*
ns
ns
ns
CDH1
Notch1
Snai1
Snai2
D
ΔΔCt relative to Control
0.0 0.5 1.0 1.5 2.0 2.5 5 10 15
p=0.06
ns
ns
ns
CDH1
Notch1
Snai1
Snai2
E
TSA (μM) - 0.5
UNC2025 (μM) - 0.5
300 kDa Notch1 FL
120 kDa Notch1 NICD
140 kDa N-cadherin
30 kDa Slug
29 kDa Snail
37 kDa GAPDH
135 kDa E-cadherin
37 kDa GAPDH
G
TSA (μM) - 1
UNC2025 (μM) - 1
300 kDa Notch1 FL
120 kDa Notch1 NICD
37 kDa GAPDH
135 kDa E-cadherin
30 kDa Slug
37 kDa GAPDH
F
Relative increase to vehicle
Normalised to GAPDH
0.0 0.5 1.0 1.5 12 16 20
**
**
*
ns
ns
E-cadherin
Notch1 NICD
Slug
Snail
N-cadherin
H
Relative increase to vehicle
Normalised to GAPDH
0 1 2 3 200 300 400 500
*
ns
***
Ecadherin
Notch1 NICD
Slug

Figure 4.9: Combination therapy of UNC2025 and TSA reverses expression of EMT-related markers (A) Representative western blot and (B) quantification showing N-cadherin, E-cadherin and Slug expression in WHO grade 1 spheroids incubated with vehicle (0.1% ethanol) or 1 µM UNC2025 at 72h (n=4). Expression levels are displayed relative to the vehicle control. (C-D) Relative gene expression of CDH1 (E-cadherin), Notch1, Snai1 and Snai2 (Slug) compared to vehicle control (0.1% ethanol + 0.1% DMSO) following 72h combination therapy of 0.5 µM UNC2025 and 0.5 µM TSA in (C) WHO grade 1 (n=6) and (D) WHO grade 2 (n=4) spheroids. Representative western blots (E, G) and quantifications (F, H) showing Notch1 (FL and NICD), N-cadherin, Slug, Snail and E-cadherin expression in (E, F) WHO grade 1 and (G, H) WHO grade 2 spheroids after combination therapy at a concentration of 0.5 µM (grade 1) and 1 µM (grade 2). GAPDH was the loading control. Paired t-test was used for statistical evaluation: *p<0.05, **p<0.01, ***p<0.001, ns=not significant, FL = full length.

4.10 Combined therapy of the dual MERTK/Flt3 inhibitor UNC2025 and HDAC inhibitor Trichostatin-A reduces spheroid invasion capacity

Next, I assessed whether the changes in the expression of EMT-markers were sufficient to exert a functional effect on the invasive capacity of WHO grade 2 meningiomas. To do this, WHO grade 2 meningioma-derived spheroids were embedded in Matrigel and treated with a single dose and combination doses of UNC2025 and TSA. Invasion was assessed at two time points of 24 hours and 48 hours (Fig. 4.10). Indeed, combination therapy using a dose of 0.5 μM and 1 μM UNC2025 and TSA significantly decreased the spheroid invasion capacity after both timepoints compared to vehicle controls, but did not significantly enhance the effect compared to monotherapy (Fig. 4.10B, C). In addition, monotherapy of UNC2025 at both concentrations and monotherapy with TSA at 0.5 μM also significantly decreased invasion after 48 hours (Fig. 4.10C). Although approaching significance (p=0.058), TSA at the higher dose of 1 μM did not significantly decrease invasion. After 24 hours, 1 μM UNC2025 decreased the invasion capacity to a similar level as the combination strategy at that same dose. Altogether, the overall effect of treatment with both UNC2025 and TSA and the combination of the two compounds showed an inhibitory effect on spheroid invasion capacity which is indicative of a functional effect on EMT.

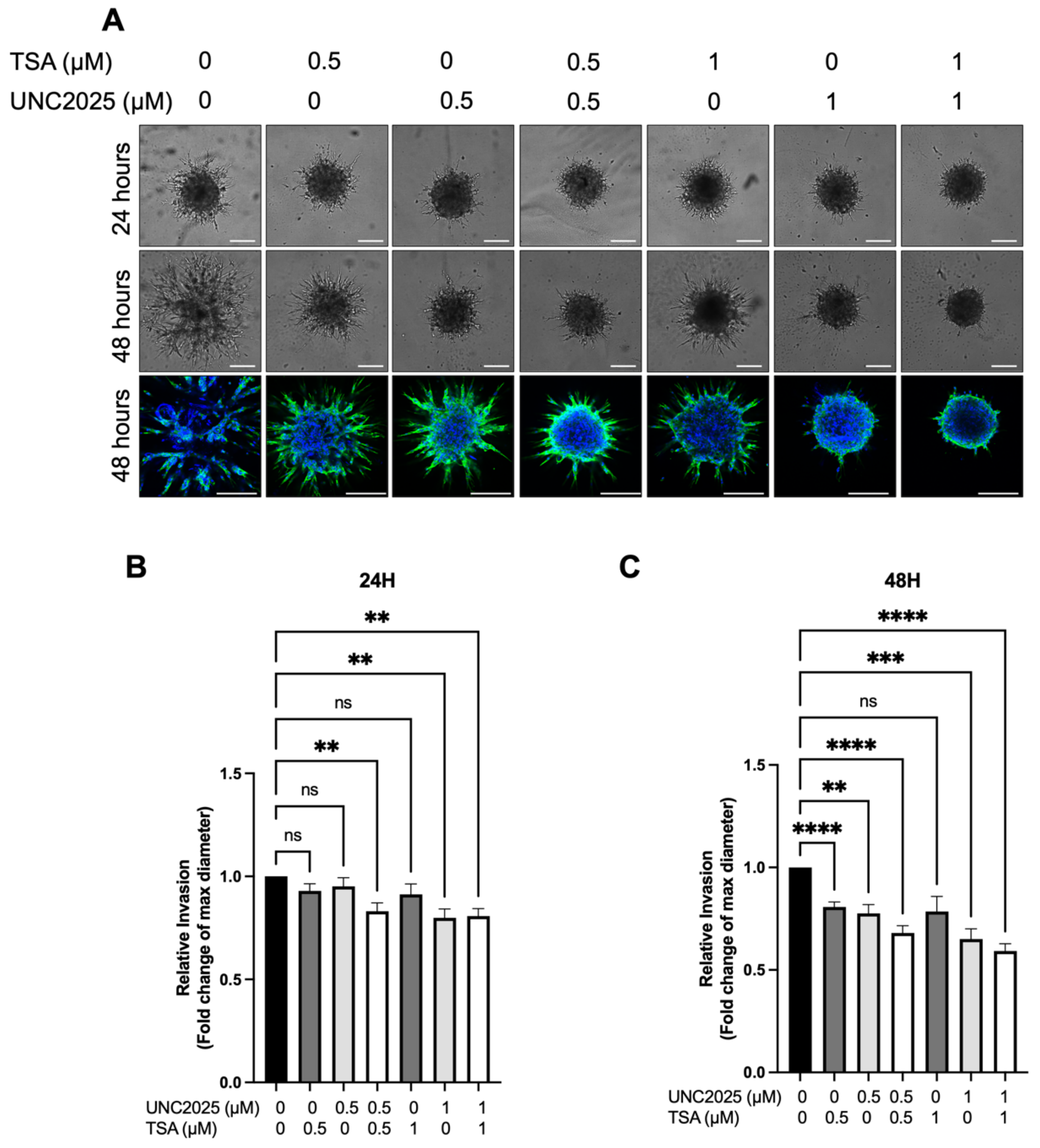

Figure 4.10: UNC2025 and TSA treatment abrogate invasion capacity of WHO grade 2 spheroids (A) 3D Matrigel invasion assay showing invasion capacity of WHO grade 2 spheroids at 24 (top panel) and 48 (middle, bottom) hours following monotherapy and combination therapy of UNC2025 and TSA at various concentrations (0.5 µM; 1 µM) compared to vehicle control (0.1% DMSO, 0.1% Ethanol) (n=3). Images were taken using bright field microscopy with 10x objective (top and middle panel), and confocal microscopy 20x objective (bottom panel). Scale bar in each panel: 200µm. Cell nuclei are stained with DAPI (blue) and Phalloidin (green). (B-C) Quantification of relative invasion at (B) 24 hours and (C) 48 hours presented as max. diameter of the total invasive zone in µm. Error bars indicate standard error of mean. One-way ANOVA with Dunett's test for multiple comparisons was used for statistical evaluation; ns=not significant, $^{**}p<0.01$, $^{***}p<0.001$, $^{****}p<0.001$.

4.11 Discussion

In meningiomas, loss of the epithelial adhesion molecule E-cadherin and increased Slug have been associated with aggressive tumours, which is suggestive of a link between EMT and meningioma progression (188). Furthermore, EMT has been associated with resistance to therapies which remains a big hurdle in the management of meningiomas (21). Hence, finding drug compounds that could target this oncogenic process in meningiomas is an attractive treatment strategy. Here, I validated the newly established patient-derived spheroids as *in vitro* drug-development tool by investigating the effect of several drug compounds on meningioma spheroid viability, proliferation and EMT.

4.11.1 The role of Notch1 in meningiomas and its involvement with EMT

EMT can be initiated by several pathways, including the Notch signalling pathway (202–204,274). Interestingly, GSEA analysis (chapter 3) comparing primary meningioma monolayers cultures with spheroid cultures revealed an enrichment of the notch signaling pathway as well as EMT in 3D cultures. Therefore, I hypothesised that the enrichment of EMT in spheroids was driven by Notch signaling. However, there are a limited number of studies on the role of Notch signalling in meningiomas and the association between Notch signalling and EMT in meningiomas remains unknown (214,285). My findings have demonstrated a grade-independent increase in the expression of the Notch1 NICD in meningiomas compared to normal meningeal tissues. This is consistent with previous studies that have suggested an oncogenic role for Notch signalling in meningiomas (214,285). Furthermore, both the results reported by Cuevas *et al.* and my findings revealed considerable variability of Notch1 NICD expression levels between patients, suggesting that Notch signalling might be particularly relevant in an (undefined) subgroup of meningiomas (214).

Slug has been demonstrated to function as an important target gene of Notch1 signalling in the regulation of the EMT process in a variety of solid tumours and this regulation is mainly achieved through the repression of E-cadherin (173,203). Unexpectedly, in primary meningioma monolayer cultures, shRNA silencing of Notch1 only moderately reduced Slug expression and an increase in E-cadherin expression could not be observed. Since protein silencing using an shRNA-mediated approach exclusively targeted Notch1 expression and did not directly silence the expression of other Notch receptors, it could be argued that silencing the Notch1 receptor exclusively, did not repress Slug expression to a sufficient level to overcome its inhibitory effect on E-cadherin. This could possibly be due to a compensatory effect of signalling of the other Notch receptors (292,293). However, pharmacological inhibition of Notch signalling using the gamma-secretase inhibitor Nirogacestat (PF-3084014), which recently showed significant benefits for the treatment of desmoid tumours in a phase 3 clinical trials (294), also did not result in an increase in E-cadherin expression, making it less likely that the compensatory mechanism is orchestrated through the Notch signalling pathway.

Furthermore, the shRNA silencing experiments were only successful when using the monolayer culture system. Comprehensive transcriptomic analysis revealed an increase in Notch1 expression in spheroids compared to monolayers, with monolayer cultures exhibiting relatively low expression levels of Notch1 (chapter 3). Therefore, in monolayer cultures, the effect of further down-regulation of these levels is likely not inducing a strong effect. Hence, the use of the spheroid model to induce Notch1 expression and subsequent Notch1-induced EMT, could be required to assess the effect of Notch1 repression in a high Notch1 state. Unfortunately, Notch1 silencing in spheroids was unsuccessful as spheroid formation using Notch1-silenced monolayers resulted in restored expression levels of Notch1 to the expression level of control cells. This is likely due to insufficient levels of shRNA production to target the strong increase in Notch1 expression induced by spheroid formation. Ultimately, this result demonstrated a limitation of this model for studying the role of Notch1 in patient-derived spheroids and whether a similar effect of re-expression of shRNA silenced proteins post-spheroid formation will occur in future experiments targeting different proteins should be assessed. The use of more precise techniques such as the CRISPR-Cas9 system could allow for a more effective method to investigate the role of Notch1, and other proteins in meningiomas (295).

Consistent with the effects observed following shRNA-mediated Notch1 repression, pharmacological repression of Notch1 signalling using the gamma-secretase inhibitor Nirogacestat (PF-3084014) (212,215,294) resulted in decreased expression of the Notch1 downstream target proteins Hes1 and Slug but did not lead to a decrease in Notch1 NICD expression in monolayer and spheroid cultures. However, Nirogacestat does not directly target the Notch1 NICD, but instead targets the gamma-secretase enzyme which cleaves off this domain and thereby prevents it from translocating to the nucleus. Hence the decreased effect observed on the downstream proteins is a more reliable readout. Interestingly, in spheroid cultures, at a dose of 10 μM Nirogacestat significantly decreased expression of Notch1 NICD for 3/4 tumours and similar repression levels could be observed for 2/4 tumours at a dose of 5 μM. This difference in repression of Notch1 NICD expression levels in monolayers and spheroids led me to hypothesize that a strong decrease in Notch1 NICD expression can only be observed if baseline expression is high. This hypothesis was further supported by the observation that spheroids derived from patient samples which showed a strong decrease in Notch1 NICD expression (at a dose of 5 μM) had higher Notch1 NICD baseline levels than the spheroids that didn't show Notch1 NICD repression (Fig. 4.3E).

Despite detecting changes in the protein levels of the Notch1 NICD, Hes1 and Slug after Nirogacestat treatment, any inhibitory effect on invasion capacity, spheroid formation capacity, cell viability or spheroid proliferation following Nirogacestat treatment was not observed. This is in contrast with previous literature that showed a clear decrease in the surviving fraction of the WHO grade 1 meningioma cell lines SF4433 and SF4068 treated with 0 to 5 μmol/L of the gamma-secretase inhibitor I (214). However, this study did not include any data on the effect of gamma-secretase inhibitor I treatment on expression levels of Notch signalling molecules. Moreover, in these experiments, cell survival was measured using the colony-forming efficiency assay. With the colony-formation assay, the main outcome is the ability of a single cell to grow into a colony, which essentially tests the ability of a cell to undergo unlimited division without the need for neighbouring cells (296). In contrast, I used the ATP viability assay which determines the surviving fraction by the amount of ATP present, which is used as a marker of the relative number of viable cells (297). Although both assays measure similar cell functions, they are different in nature which could explain the opposing results. Furthermore, the SF4433 and SF4068 cell lines were transformed with the human papillomavirus oncogenes E6 and E7 and hTERT, which induces capacity for unlimited divisions. This could potentially cause genetic drift in the cells, which can result in loss of the typical meningioma profile with passages (161). Moreover, gamma-secretase inhibitors are pharmacologically and functionally distinct. Hence, it could be that gamma-secretase inhibitor I is more potent for the treatment of meningiomas (298).

The grade-independent increase of Notch1 expression in meningiomas is suggestive of an oncogenic role, whilst the observed increase in spheroid viability following Nirogacestat treatment indicated a tumour suppressive function. Although the absence of an inhibitory effect on spheroid proliferation and viability following Nirogacestat treatment (Fig. 4.5) contradicts previous findings, there are several reports in the literature that observed similar contradictory results after Notch inhibition and the role of Notch signalling has been shown to be both oncogenic and tumour suppressive in different contexts (214,299). For instance, in medulloblastoma, Notch2 has been shown to promote tumour growth, whereas Notch1 has the opposite effect of inhibiting tumour growth (299). In addition, controversial data on the role of Notch in hepatocellular carcinoma have been published showing both pro-tumorigenic and tumour-suppressive functions (300). Thus, whether Notch signalling plays a tumour-suppressive or oncogenic role in meningiomas was not clarified with my results and remains doubtfull. Furthermore, various reports in the literature have demonstrated a positive correlation between Slug and proliferation (203,287,288,301). For example, Slug was demonstrated to control mammosphere growth, regulate cell proliferation in metastatic prostate cancer cells and promote tumour growth and invasion in human gliomas (301–303). Consistently, in meningiomas, an increased expression of Slug has been associated with higher grade tumours and tumour-promoting function (185,188). These findings are in contrast with my results following Nirogacestat treatment in meningioma spheroids, which showed a decrease in Slug expression without affecting proliferation. Interestingly, Guelfi *et al.* showed a strong upregulation of Slug following Notch1 activation in GSCs, which had an inhibitory effect on their proliferation and induced a pericyte-like cell differentiation, indicating the duality of this protein in different contexts (304,305).

4.11.2 Spheroids display altered drug sensitivity compared to monolayers

Traditionally, the effectiveness of anti-cancer therapeutics is evaluated using monolayer cell culture models, which do not accurately resemble *in vivo* conditions (230,306). For this reason, many drugs prove clinically ineffective, despite promising experimental *in vitro* results (307). Consistently, my results showed a significant difference in sensitivity towards Nirogacestat, UNC2025 and TSA of meningioma spheroids compared to monolayer cultures. Interestingly, the pattern of this difference was the opposite for UNC2025 compared to TSA and Nirogacestat. Comparing the IC_{50} values for UNC2025 showed a 2.3-fold increase in monolayers, while for TSA, the IC_{50} value was decreased by 1.9-fold in monolayers compared to spheroids. For Nirogacestat the IC_{50} values could not be calculated since the IC_{50} value was not reached. Interestingly, in other cancer models, spheroid cultures typically display higher drug resistance (307–309). For instance, Filipiak-Duliban *et al.* demonstrated decreased sensitivity of melanoma spheroids to the common anti-cancer drugs Everolimus and Cisplatin compared to monolayer cultures (307). Similarly, the formation of breast cancer spheroids (308) and head and neck cancer spheroids (309) has been associated with decreased drug sensitivity. These reports are consistent with my observations of a decreased sensitivity to TSA in the spheroid model. Increased drug resistance in spheroids has been suggested to be caused by several mechanisms including decreased drug penetration, decreased drug metabolism, upregulation of drug efflux molecules and acquisition of stem-like characteristics (230). The increased sensitivity of spheroids to UNC2025 contrasts these findings. However, similar findings of enhanced sensitivity were previously observed for spheroids derived from the colorectal cancer cell line DLD1 to Erlotinib treatment (280). These results suggest that drug sensitivity is culture system and cell type dependent (280). In the case of UNC2025, several hypotheses can be made to explain the enhanced drug sensitivity in spheroids. Firstly, the target proteins of UNC2025: MERTK and Flt3, are receptor tyrosine kinases. Activation of these receptors is dictated by receptor dimerization and subsequent phosphorylation (71,78). Due to enhanced cell-cell contact in spheroid cultures, MERTK and Flt3 have enhanced potential to dimerize, which leads to increased receptor signalling, making the spheroid more dependent on MERTK/Flt3. In that case, inhibiting these receptors using UNC2025 would have a stronger effect. Secondly, it has been previously demonstrated that 3D cell culture can induce changes in gene and protein expression (228,275,310). Interestingly, Fang & Imoukhuede (311) previously demonstrated a strong increase in the expression of two receptor tyrosine kinases VEGF2 and Axl in ovarian cancer spheroids compared to monolayers and suggested that low-RTK expressing monolayers are less responsive to the RTK targeted therapies. A similar mechanism could be occurring in meningioma spheroids, causing the enhanced sensitivity of spheroids to UNC2025. Indeed, expression of MERTK is increased in 3D cultures compared to monolayer cultures, as demonstrated by results of my transcriptomic analysis generated in chapter 3. Thirdly, in addition to meningioma cells, MERTK is expressed by tumour-associated macrophages (71,77). As previously demonstrated in chapter 3, macrophages are maintained in the patient-derived meningioma spheroid model. The altered macrophage-tumour cell interaction in spheroids could potentially affect their crosstalk, which in turn, could influence spheroid sensitivity to these drugs. However, the opposite could be true since the presence of macrophages and other stroma compounds have been suggested to enhance drug resistance (257,258).

4.11.3 Combination therapy using UNC2025 and TSA as novel systemic therapy for meningiomas.

My results demonstrated a synergistic effect of UNC2025 and TSA to inhibit meningioma spheroid viability. Combination therapy strategies using tyrosine kinase inhibitors with HDAC inhibitors are a commonly studied anti-cancer approach as tyrosine kinases play an important role in promoting the activation of HDACs (99). Whilst a comparable combination strategy was previously suggested for the treatment of diffuse intrinsic pontine glioma (DIPG), a similar strategy has not yet previously been suggested for the treatment of meningiomas (101). Furthermore, promising results demonstrating anti-meningioma effects have previously been reported following monotherapy of both TSA and UNC2025 (81,284). Although TSA has not been approved by the FDA for clinical use, it is currently in a phase 1 clinical trial (NCT0383926) investigating the safety and tolerability for patients with relapsed or refractory haematological malignancies (88). To date, five HDAC inhibitors have been FDA-approved (80). Likewise, UNC2025 is also not FDA-approved. However, a very similar inhibitor called MRX-2843 is in ongoing clinical trials (NCT04872478) (312). The synergy between UNC2025 and TSA might allow for the administration of lower drug concentrations in patients, which can reduce off-target effects and improve overall clinical outcomes.

Whilst there was a trend of reduced proliferation of meningioma spheroids treated with the combination therapy compared to treatment with each drug alone using the same dose, this decrease was not statistically significant. This is likely due to the low sample size, limiting the statistical power and inter-sample variability. For the analysis of protein and gene expression changes following combination therapy, a dose of 0.5μM and 1 μM for both compounds was used for WHO grade 1 and WHO grade 2 spheroids respectively. Whether the effect on EMT-associated gene and protein expression following combination treatment showed synergy compared to monotherapy was not assessed due to limited sample availability.

4.11.4 The effect of combination therapy using UNC2025 and TSA on EMT

UNC2025 and TSA have both been previously described to independently reverse EMT in several cancers (78,101,290,291). Interestingly, unlike Nirogacestat, treatment with 1 μM UNC2025 resulted in a moderate effect on the induction of the epithelial adhesion protein E-cadherin, while simultaneously moderately reducing the expression of the transcriptional regulator of mesenchymal transition Slug. The expression of N-cadherin, a common mesenchymal adhesion protein, was not affected by treatment with 1 µM UNC2025. Notably, these results displayed a high variability between spheroids derived from individual patients. In this experimental design, I chose to treat all patient-derived spheroids with the same dose. However, as indicated by the variability in the IC_{50}, UNC2025 sensitivity varies per patient sample. Hence, treating all patient-derived spheroids with their exact IC_{50} dose could potentially improve the significance values. However, contrasting reports on the effect of TSA on EMT in the literature exist. For example, Wang and colleagues (290) demonstrated that TSA reversed EMT and attenuated invasion and migration capacity in MCF-7 breast cancer cells, whilst Shen *et al.* (313) observed the induction of EMT in nasopharyngeal cells following TSA administration. Similar findings to those of Wang *et al*. were reported by Ganatra *et al.* (291) who showed the restoration of epithelial adherens and tight junction proteins following EMT in the human epithelial cell line FHL124. Despite this, I provided evidence for the potency of the combination therapy of UNC2025 and TSA to induce E-cadherin expression alongside the repression of the mesenchymal proteins Slug and Notch1 NICD. However, combination therapy did not decrease N-cadherin expression or Snail expression, which suggests that only a partial reversal of EMT is achieved (314–317). Although synergy could not be determined, treatment of a combination dose of 0.5 µM UNC2025 and 0.5 µM TSA significantly enhanced the effect observed for E-cadherin and Slug protein expression compared to single dose treatment of UNC2025. However, it must be noted that this experiment was performed using spheroids derived from different patients than those in the monotherapy experiment with 1 µM UNC2025. Moreover, single-dose experiments using TSA alone were not included in the analysis. Therefore, it cannot be excluded that the enhanced effect on these proteins is caused by TSA alone.

In contrast with results observed for protein expression, 0.5μM combination therapy did significantly increase expression of the gene encoding for E-cadherin: CDH1. All other genes tested were not significantly affected by the therapy. This suggests that the effect observed on protein levels mainly occurs post-translationally. Additionally, western blotting analysis revealed a strong decrease of the Notch1 NICD following combination therapy in WHO grade 1 spheroids, although no change in Notch1 expression was observed at the transcription level. Noteworthily, WHO grade 2-derived spheroids treated with 1 μM of UNC2025 and 1 μM TSA followed the same trend. However, in this study, I have only looked at a small portion of EMT-associated proteins/genes and for a more detailed overview of the influence of these inhibitors on this process, more research is necessary.

4.11.5 Invasion capacity and E-cadherin expression

It is commonly accepted that loss of E-cadherin can initiate cell migration and invasion, due to loss of E-cadherin mediated cell-cell adhesion (316). Indeed, my results showed that treatment with combination therapy of UNC2025 and TSA increased the expression of E-cadherin and decreased the invasion capacity of cells as demonstrated by the 3D Matrigel invasion assay using WHO grade 2 meningioma spheroids. While treatment with Nirogacestat did significantly decrease mesenchymal proteins such as Slug, it did not lead to an increase in E-cadherin expression or affect invasion capacity. This indicates that re-expression of E-cadherin in meningiomas is required to decrease the invasive capacity, despite levels of mesenchymal proteins such as N-cadherin and Slug, and thus that a partial reversal of EMT is enough to exert an effect on invasion capacity in WHO grade 2 meningioma spheroids. Therefore, treatment that leads to re-expression of E-cadherin could be an attractive strategy to decrease brain invasion.

4.11.6 Conclusions

In conclusion, despite the suggested role of Notch1 in regulating proliferation and EMT in meningiomas (chapter 3), targeted lentiviral shRNA silencing and pharmacological inhibition of Notch1 using Nirogacestat did not decrease meningioma viability and proliferation or affect functional assays associated with EMT. These data suggest that Notch1 is not critical for the maintenance of cell proliferation in these tumours and that Notch1 downregulation alone is not enough to exert strong inhibitory effects on EMT. Hence, the data presented in this chapter do not suggest that Notch signaling is the main driver of the enrichment of EMT in spheroids compared to monolayers.

Nevertheless, using meningioma spheroid cultures, I demonstrated that both the dual MERTK/Flt inhibitor UNC2025 and the HDAC inhibitor TSA could inhibit meningioma spheroid viability and proliferation and partially had an effect on EMT. Furthermore, I provided evidence for the combination therapy of UNC2025 and TSA as promising strategy for treatment of meningioma by exerting an inhibitory effect on viability, proliferation and EMT. Additionally, the data presented in this chapter clearly demonstrated that this newly established patient-derived spheroid model can serve as a powerful tool to investigate the EMT process in meningioma cells and how it can be exploited for drug testing in meningioma research.

5 Summarizing discussion and conclusions

This thesis has sought to establish a patient-derived 3D cell culture model for meningioma, which resembles important features of the parental tissue including spatial architecture and the tumour microenvironment. As such, this work has described the establishment of a novel easy-to-use patient-derived meningioma spheroid model. In the comprehensive characterisation that followed, I showed that this novel spheroid model recapitulates important features of the parental tissue, including molecular and morphological characteristics, and genetic alterations (chapter 3). Next, I demonstrated that patient-derived meningioma spheroids can serve as a platform for drug screening and can be used to study important oncogenic processes such as epithelial-to-mesenchymal transition (EMT) (chapter 4). Finally, using this model, I provided evidence for the therapeutic potential of the combination therapy of the MERTK inhibitor UNC2025 and the HDAC inhibitor Trichostatin A (TSA) to treat WHO grade 1 and grade 2 meningiomas.

The current clinical situation of meningioma management makes this model highly relevant. Currently, the only available treatment options for meningiomas are limited to surgery and/or radiotherapy and there are no effective drug-based therapies (5,6). Therefore, it is crucial that effective targeted therapies are developed. Restricted *in vitro* modelling used in drug development research for meningioma remains one of the biggest limitations in the development of novel therapies (13,18). In my opinion, this novel patient-derived spheroid model provides an additional *in vitro* research tool which allows for more accurate results. This will ultimately help to bridge the gap between *in vitro* and *in vivo* drug development research. As an example, the work published by Hofmann *et al.* (318) demonstrated a proof-of-concept that their patient-derived breast cancer spheroid cultures, which were generated following a similar method to the method established in this thesis, could be utilized as *in vitro* model for the prediction of drug response. In their study, the authors applied a small panel of commonly used chemotherapeutics onto their spheroids and showed that spheroids had a diverse response to the different therapies which was consistent with the *in vivo* response (318). Similarly, a study using patient-derived ovarian cancer spheroids, which were generated prior to the administration of any chemotherapeutics, compared the response of the spheroids with the clinical response following treatment with the same chemotherapeutic agent. This study revealed that the spheroids had an overall prediction accuracy of 89% (319). A similar setup could be feasible for meningiomas, especially in cases where GTR cannot be reached but enough material can be obtained for the formation of spheroid cultures. Patient-derived meningioma spheroids can be established from patient tissue within a week and these spheroids could be used to predict drug response of these patients. Such a pipeline, although still far from being realised, could allow for personalised therapy, and overcome the problem of heterogeneity in drug response.

Over the years, several meningioma 3D cell culture models have been established, although none of these have yet been widely adopted (17–19). Nevertheless, this novel spheroid model represents the first 3D meningioma culture method that can be routinely used in laboratories. Unlike organoid models that have been established for meningiomas (17–20), the method I have established uses a scaffold-free approach, is easy to handle, highly reproducible and has a fast result turnaround. This makes it simple, less time-consuming, and less expensive when compared to other 3D techniques. Furthermore, this model is the first 3D model for meningiomas that is capable of functional invasion. Therefore, it provides an essential tool to study the complex process of brain invasion in meningiomas.

Stromal cell populations contribute to tumorigenesis (320,321). Hence, maintenance of these populations and tumour cell-stromal cell interactions is crucial to ensure accurate disease modelling (258). However, time in culture and cell passaging have been inversely correlated with the presence of stromal cell populations in *in vitro* cultures (65). In chapter 3, I have shown the maintenance of a macrophage population in P1 spheroids. However, since the spheroid growth medium did not specifically contain factors for the growth of specific stromal cell populations, this spheroid model is intended for use as short-term model. Especially, since at these early time points, the highest cellular diversity is present. However, even though spheroids can model the 3D spatial organization of tissues in a more accurate manner compared to monolayers, spheroids remain artificially formed structures that did not rely on self-organisation. In addition, they lack the representation of blood vessels which represents a limitation of this model.

Whilst the presence of patient-specific tumour-stromal interactions are essential in drug development studies, this culture method can also be applied using high passage cells or immortalized cell lines, which consist of purer meningioma tumour cell populations. For example, to study specific interactions of one type of stromal cell with the tumour, spheroids could be generated from higher passages, and co-cultured with a cell type of interest. A similar method has previously been described for breast cancer spheroids and patient-derived immune cells (322). In this study, the authors used the patient’s own peripheral blood mononuclear cells (PBMCs) and co-cultured them with spheroids. Using this method, they demonstrated altered anti-tumour responses in co-cultures compared to monoculture spheroids. In fact, currently in our laboratory initial experiments using this technique are now being performed, which presents another way of how this model can be applied.

Chapter 4 of this thesis served as proof of principle for applying this novel model as *in vitro* tool. I described the application of patient-derived meningioma spheroids to study the association between Notch1 signalling and EMT. Although a role for Notch1 in meningioma was previously suggested, a link with the process of EMT in meningiomas had not been previously studied. Interestingly, even though the transcriptomic data suggested an increase in EMT through induction of Notch1 signalling, this association could not be confirmed by Notch1 silencing experiments in meningioma monolayer cells or spheroids. Although conclusive results on the role of Notch1 in EMT in meningioma biology could not be reached, these results validated the use of this model as in vitro tool.

Additionally, using patient-derived meningioma spheroids revealed the combination strategy of UNC2025 and TSA as potential therapeutic approach. The mechanism of action behind the synergy of these compounds has yet to be elucidated, although there is ample evidence for synergy between inhibiting HDACs and receptor tyrosine kinases in the literature, and several dual inhibitors targeting HDAC and a receptor tyrosine kinase have been developed (323–325).

However, the synergistic effect may be attributed to the ability of both compounds to target multiple oncogenic pathways. Hence, limiting the activation of compensatory survival pathways (324). Furthermore, a similar combination therapy which used an Axl inhibitor and another HDAC inhibitor in diffuse intrinsic pontine glioma (DIPG) revealed a downregulation of genes associated with radiation-induced DNA damage repair (101). This suggests that this combination in DIPG functioned as a radiosensitizer. Hence, a similar mechanism could be true for meningioma spheroids following combined therapy of UNC2025 and TSA. In the future, it could be interesting to explore the potential triple combination of UNC2025, TSA and irradiation as treatment strategy for meningiomas.

In conclusion, this work described the development of a novel patient-derived 3D model for meningiomas which resembles essential features of parental tumours. Implementation of this model can serve to decrease the translational gap between *in vitro* and *in vivo* and thereby improve drug development. Furthermore, this model creates the unique opportunity to study invasion and associated EMT in a 3D model for meningioma.

6 References

1. Nassiri F, Tabatabai G, Aldape K, Zadeh G. Challenges and opportunities in meningiomas: Recommendations from the International Consortium on Meningiomas. Vol. 21, Neuro-Oncology. Oxford University Press; 2019. p. I2–3.
2. Louis DN, Perry A, Wesseling P, Brat DJ, Cree IA, Figarella-Branger D, et al. The 2021 WHO Classification of Tumors of the Central Nervous System: a summary. Neuro Oncol. 2021 Aug 2;23(8):1231–51.
3. Preusser M, Brastianos PK, Mawrin C. Advances in meningioma genetics: Novel therapeutic opportunities. Vol. 14, Nature Reviews Neurology. Nature Publishing Group; 2018. p. 106–15.
4. Al-Rashed M, Foshay K, Abedalthagafi M. Recent Advances in Meningioma Immunogenetics. Front Oncol. 2020;9(January):1–11.
5. Suppiah S, Nassiri F, Bi WL, Dunn IF, Hanemann CO, Horbinski CM, et al. Molecular and translational advances in meningiomas. Neuro Oncol. 2019 Jan 14;21:I4–17.
6. Maggio I, Franceschi E, Tosoni A, Nunno V Di, Gatto L, Lodi R, et al. Meningioma: Not always a benign tumor. A review of advances in the treatment of meningiomas. CNS Oncol. 2021;10(2).
7. Clark VE, Erson-omay EZ, Serin A, Yin J, Cotney J, Avşar T, et al. Genomic analysis of non-NF2 meningiomas reveals mutations in TRAF7, KLF4, AKT1, and SMO. 2016;339(6123):1077–80.
8. Clark VE, Harmancl AS, Bai H, Youngblood MW, Lee TI, Baranoski JF, et al. Recurrent somatic mutations in POLR2A define a distinct subset of meningiomas. Nat Genet. 2016;48(10):1253–9.

9. Abedalthagafi M, Bi WL, Aizer AA, Merrill PH, Brewster R, Agarwalla PK, et al. Oncogenic PI3K mutations are as common as AKT1 and SMO mutations in meningioma. Neuro Oncol. 2016;18(5):649–55.
10. Smith MJ, O'Sullivan J, Bhaskar SS, Hadfield KD, Poke G, Caird J, et al. Loss-of-function mutations in SMARCE1 cause an inherited disorder of multiple spinal meningiomas. Nat Genet. 2013;45(3):295–8.
11. Maggio I, Franceschi E, Di Nunno V, Gatto L, Tosoni A, Angelini D, et al. Discovering the molecular landscape of meningioma: The struggle to find new therapeutic targets. Vol. 11, Diagnostics. MDPI; 2021.
12. Seyhan AA. Lost in translation: the valley of death across preclinical and clinical divide – identification of problems and overcoming obstacles. Transl Med Commun. 2019;4(1):1–19.
13. Boetto J, Peyre M, Kalamarides M. Mouse models in meningioma research: A systematic review. Cancers (Basel). 2021;13(15).
14. Kim M, Mun H, Sung CO, Cho EJ, Jeon HJ, Chun SM, et al. Patient-derived lung cancer organoids as in vitro cancer models for therapeutic screening. Nat Commun. 2019 Dec 1;10(1).
15. Richmond A, Su Y. Mouse xenograft models vs GEM models for human cancer therapeutics. Dis Model Mech [Internet]. 2008;1(2–3):78–82. Available from: https://pubmed.ncbi.nlm.nih.gov/19048064
16. Jubelin C, Muñoz-Garcia J, Griscom L, Cochonneau D, Ollivier E, Heymann MF, et al. Three-dimensional in vitro culture models in oncology research. Cell Biosci [Internet]. 2022;12(1):1–28. Available from: https://doi.org/10.1186/s13578-022-00887-3
17. Magill ST, Vasudevan HN, Seo K, Villanueva-Meyer JE, Choudhury A, John Liu S, et al. Multiplatform genomic profiling and magnetic resonance

imaging identify mechanisms underlying intratumor heterogeneity in meningioma. Nat Commun. 2020 Dec 1;11(1).

18. Yamazaki S, Ohka F, Hirano M, Shiraki Y, Motomura K, Tanahashi K, et al. Newly Established Patient-derived Organoid Model of Intracranial Meningioma. Neuro Oncol [Internet]. 2021; Available from: https://academic.oup.com/neuro-oncology/advance-article/doi/10.1093/neuonc/noab155/6313216

19. Siu H, Chan C, Keung H, Chan AK, Ha S, Chow C, et al. Establishment and characterization of meningioma patient-derived organoid. J Clin Neurosci [Internet]. 2021;94:192–9. Available from: https://doi.org/10.1016/j.jocn.2021.10.035

20. Huang M, Xu S, Li Y, Shang L, Zhan X, Qin C, et al. Novel Human Meningioma Organoids Recapitulate the Aggressiveness of the Initiating Cell Subpopulations Identified by ScRNA-Seq. Adv Sci. 2023;2205525:1–16.

21. Ogasawara C, Philbrick BD, Adamson DC. Meningioma: A review of epidemiology, pathology, diagnosis, treatment, and future directions. Biomedicines. 2021;9(3).

22. Central Nervous System Tumours WHO Classification of Tumours. 5th ed. 2021.

23. DeMonte F, McDermott MW, Al-Mefty O. 3 Anatomy and Biology of the Leptomeninges. In: Al-Mefty’s Meningiomas [Internet]. Second Edi. Georg Thieme Verlag KG; 2011. Available from: http://www.thieme-connect.de/products/ebooks/lookinside/10.1055/b-0034-81182

24. Baki Albayrak S, Black PM. Chapter 3 The origin of meningiomas. In: Meningiomas. 2010. p. 53–60.

25. Marosi C, Hassler M, Roessler K, Reni M, Sant M, Mazza E, et al. Meningioma. Vol. 67, Critical Reviews in Oncology/Hematology. 2008. p. 153–71.

26. Kalamarides M, Stemmer-Rachamimov AO, Niwa-Kawakita M, Chareyre F, Taranchon E, Han ZY, et al. Identification of a progenitor cell of origin capable of generating diverse meningioma histological subtypes. Oncogene. 2011 May 19;30(20):2333–44.

27. What-when-how.com. Meninges and Cerebrospinal Fluid (Gross Anatomy of the Brain) Part 1 [Internet]. [cited 2023 Jan 30]. Available from: http://what-when-how.com/neuroscience/meninges-and-cerebrospinal-fluid-gross-anatomy-of-the-brain-part-1/

28. Prayson RA. 5 Pathology of Meningiomas Historical Perspective. In: Meningiomas. 2009. p. 31–42.

29. Gritsch S, Batchelor TT, Gonzalez Castro LN. Diagnostic, therapeutic, and prognostic implications of the 2021 World Health Organization classification of tumors of the central nervous system. Cancer. 2021;47–58.

30. Harter PN, Braun Y, Plate KH. Classification of meningiomas-advances and controversies. Vol. 6, Chinese Clinical Oncology. AME Publishing Company; 2017.

31. Torp SH, Solheim O, Skjulsvik AJ. The WHO 2021 Classification of Central Nervous System tumours: a practical update on what neurosurgeons need to know—a minireview. Acta Neurochir (Wien) [Internet]. 2022 Jul 26; Available from: https://link.springer.com/10.1007/s00701-022-05301-y

32. Hallinan JTPD, Hegde AN, Lim WEH. Dilemmas and diagnostic difficulties

in meningioma. Vol. 68, Clinical Radiology. W.B. Saunders Ltd; 2013. p. 837–44.

33. Ostrom QT, Cioffi G, Gittleman H, Patil N, Waite K, Kruchko C, et al. CBTRUS Statistical Report: Primary Brain and Other Central Nervous System Tumors Diagnosed in the United States in 2012-2016. Neuro Oncol. 2019;21:V1–100.

34. Mawrin C, Chung C, Preusser M. Biology and Clinical Management Challenges in Meningioma. 2015.

35. Dasgupta K, Jeong J. Developmental biology of the meninges. Vol. 57, Genesis. John Wiley and Sons Inc.; 2019.

36. Bi WL, Zhang M, Wu WW, Mei Y, Dunn IF. Meningioma Genomics: Diagnostic, Prognostic, and Therapeutic Applications. Front Surg. 2016;3(July):1–7.

37. Qi ZY, Shao C, Huang YL, Hui GZ, Zhou YX, Wang Z. Reproductive and exogenous hormone factors in relation to risk of meningioma in women: A meta-analysis. PLoS One. 2013;8(12).

38. Riemenschneider MJ, Perry A, Reifenberger G. Histological classification and molecular genetics of meningiomas. Vol. 5, Lancet Neurology. Lancet Publishing Group; 2006. p. 1045–54.

39. Goldbrunner R, Stavrinou P, Jenkinson MD, Sahm F, Mawrin C, Weber DC, et al. EANO guideline on the diagnosis and management of meningiomas. Neuro Oncol. 2021 Jun 28;

40. Kim L. A narrative review of targeted therapies in meningioma. 2020;9(6):1–8.

41. Zhao L, Zhao W, Hou Y, Wen C, Wang J, Wu P, et al. An Overview of Managements in Meningiomas. Vol. 10, Frontiers in Oncology. Frontiers

Media S.A.; 2020.

42. Roehrkasse AM, Peterson JEG, Fung KM, Pelargos PE, Dunn IF. The Discrepancy Between Standard Histologic WHO Grading of Meningioma and Molecular Profile: A Single Institution Series. Front Oncol. 2022;12(March):1–9.

43. Mawrin C, Perry A. Pathological classification and molecular genetics of meningiomas. Vol. 99, Journal of Neuro-Oncology. 2010. p. 379–91.

44. Ye W, Ding-Zhong T, Xiao-Sheng Y, Ren-Ya Z, Yi L. Factors Related to the Post-operative Recurrence of Atypical Meningiomas. Front Oncol. 2020;10(April):1–7.

45. Wilson TA, Huang L, Ramanathan D, Lopez-Gonzalez M, Pillai P, De Los Reyes K, et al. Review of Atypical and Anaplastic Meningiomas: Classification, Molecular Biology, and Management. Front Oncol. 2020;10(November).

46. Domingues P, González-Tablas M, Otero Á, Pascual D, Ruiz L, Miranda D, et al. Genetic/molecular alterations of meningiomas and the signaling pathways targeted [Internet]. 2015. Available from: www.impactjournals.com/oncotarget/

47. Whittle IR, Smith C, Navoo P, Collie D. Meningiomas. Lancet [Internet]. 2004 May;363(9420):1535–43. Available from: https://linkinghub.elsevier.com/retrieve/pii/S0140673604161539

48. Lee S, Karas PJ, Hadley CC, Bayley V. JC, Basit Khan A, Jalali A, et al. The role of merlin/NF2 loss in meningioma biology. Vol. 11, Cancers. MDPI AG; 2019.

49. Yuzawa S, Nishihara H, Tanaka S. Genetic landscape of meningioma. Brain Tumor Pathol. 2016 Oct;33(4):237–47.

50. Shankar GM, Santagata S. BAP1 mutations in high-grade meningioma: implications for patient care. Neuro Oncol. 2017 Oct;19(11):1447–56.

51. Abdel-Rahman MH, Pilarski R, Cebulla CM, Massengill JB, Christopher BN, Boru G, et al. Germline BAP1 mutation predisposes to uveal melanoma, lung adenocarcinoma, meningioma, and other cancers. J Med Genet. 2011 Dec;48(12):856–9.

52. Spiegl-Kreinecker S, Lötsch D, Neumayer K, Kastler L, Gojo J, Pirker C, et al. TERT promoter mutations are associated with poor prognosis and cell immortalization in meningioma. Neuro Oncol. 2018;20(12):1584–93.

53. Perry A, Banerjee R, Lohse CM, Kleinschmidt-DeMasters BK, Scheithauer BW. A role for chromosome 9p21 deletions in the malignant progression of meningiomas and the prognosis of anaplastic meningiomas. Brain Pathol. 2002 Apr;12(2):183–90.

54. Sievers P, Hielscher T, Schrimpf D, Stichel D, Reuss DE, Berghoff AS, et al. CDKN2A/B homozygous deletion is associated with early recurrence in meningiomas. Acta Neuropathol [Internet]. 2020;140(3):409–13. Available from: https://doi.org/10.1007/s00401-020-02188-w

55. Robert SM, Vetsa S, Nadar A, Vasandani S, Youngblood MW, Gorelick E, et al. The integrated multiomic diagnosis of sporadic meningiomas: a review of its clinical implications. J Neurooncol [Internet]. 2022;156(2):205–14. Available from: https://doi.org/10.1007/s11060-021-03874-9

56. Sahm F, Schrimpf D, Stichel D, Jones DTW, Hielscher T, Schefzyk S, et al. DNA methylation-based classification and grading system for meningioma: a multicentre, retrospective analysis. Lancet Oncol. 2017;18(5):682–94.

57. Vasudevan HN, Choudhury A, Hilz S, Villanueva-meyer JE, Chen WC, Lucas CG, et al. Intratumor and informatic heterogeneity influence meningioma molecular classification. Acta Neuropathol. 2022;144(3):579–83.
58. Gerlinger M, Swanton C. How Darwinian models inform therapeutic failure initiated by clonal heterogeneity in cancer medicine. Br J Cancer [Internet]. 2010;103(8):1139–43. Available from: http://dx.doi.org/10.1038/sj.bjc.6605912
59. Sun Y. Tumor microenvironment and cancer therapy resistance. Cancer Lett [Internet]. 2016;380(1):205–15. Available from: http://dx.doi.org/10.1016/j.canlet.2015.07.044
60. LV B, Wang Y, Ma D, Cheng W, Liu J, Yong T, et al. Immunotherapy: Reshape the Tumor Immune Microenvironment. Front Immunol. 2022;13(July):1–15.
61. Garzon-Muvdi T, Bailey DD, Pernik MN, Pan E. Basis for Immunotherapy for Treatment of Meningiomas. Vol. 11, Frontiers in Neurology. Frontiers Media S.A.; 2020.
62. Nassiri F, Liu J, Patil V, Mamatjan Y, Wang JZ, Hugh-White R, et al. A clinically applicable integrative molecular classification of meningiomas. Nature [Internet]. 2021;597(7874):119–25. Available from: http://dx.doi.org/10.1038/s41586-021-03850-3
63. Fang L, Lowther DE, Meizlish ML, Anderson RCE, Bruce JN, Devine L, et al. The immune cell infiltrate populating meningiomas is composed of mature, antigen-experienced T and B cells. Neuro Oncol. 2013;15(11):1479–90.
64. Proctor DT, Huang J, Lama S, Albakr A, Van Marle G, Sutherland GR.

Tumor-associated macrophage infiltration in meningioma. Neuro-Oncology Adv. 2019;1(1):1–10.

65. Adams CL, Ercolano E, Ferluga S, Sofela A, Dave F, Negroni C, et al. A rapid robust method for subgrouping non-nf2 meningiomas according to genotype and detection of lower levels of M2 macrophages in AKT1 E17K mutated tumours. Int J Mol Sci. 2020;21(4):15–20.

66. Hao S, Huang G, Feng J, Li D, Wang K, Wang L, et al. Non-NF2 mutations have a key effect on inhibitory immune checkpoints and tumor pathogenesis in skull base meningiomas. J Neurooncol. 2019 Aug 15;144(1):11–20.

67. Apra C, Peyre M, Kalamarides M. Current treatment options for meningioma. Vol. 18, Expert Review of Neurotherapeutics. Taylor and Francis Ltd; 2018. p. 241–9.

68. Weston GJ, Martin AJ, Mufti GJ, Strong AJ, Gleeson MJ. Hydroxyurea Treatment of Meningiomas: A Pilot Study. Skull Base. 16.08.2006. 2006;16(03):157–60.

69. Chamberlain MC. Hydroxyurea for recurrent surgery and radiation refractory high-grade meningioma. J Neurooncol [Internet]. 2012;107(2):315–21. Available from: https://doi.org/10.1007/s11060-011-0741-z

70. Brastianos PK, Kim AE, Giobbie-Hurder A, Lee EQ, Wang N, Eichler AF, et al. Phase 2 study of pembrolizumab in patients with recurrent and residual high-grade meningiomas. Nat Commun. 2022;13(1).

71. Graham DK, Deryckere D, Davies KD, Earp HS. The TAM family: Phosphatidylserine-sensing receptor tyrosine kinases gone awry in cancer. Nat Rev Cancer. 2014;14(12):769–85.

72. Png KJ, Halberg N, Yoshida M, Tavazoie SF. A microRNA regulon that mediates endothelial recruitment and metastasis by cancer cells. Nature. 2012;481(7380):190–6.

73. Massad K, Guo L, Zhao P, Beck-noia H, Hagemann IS, Andrea R. Improves Sensitivity to Platinum and Taxane in Ovarian Cancer. 2020;18(2):389–98.

74. Onken J, Vajkoczy P, Torka R, Hempt C, Patsouris V, Heppner FL, et al. Phospho-AXL is widely expressed in glioblastoma and associated with significant shorter overall survival. Oncotarget. 2017;8(31):50403–14.

75. Bosurgi L, Bernink JH, Cuevas VD, Gagliani N, Joannas L, Schmid ET, et al. Paradoxical role of the proto-oncogene Axl and Mer receptor tyrosine kinases in colon cancer. Proc Natl Acad Sci U S A. 2013;110(32):13091–6.

76. Ammoun S, Provenzano L, Zhou L, Barczyk M, Evans K, Hilton DA, et al. Axl/Gas6/NFκB signalling in schwannoma pathological proliferation, adhesion and survival. Oncogene. 2014;33(3):336–46.

77. Aehnlich P, Powell RM, Peeters MJW, Rahbech A, Straten PT. Tam receptor inhibition–implications for cancer and the immune system. Vol. 13, Cancers. MDPI AG; 2021. p. 1–16.

78. Chen CJ, Liu YP. Mertk inhibition: Potential as a treatment strategy in egfr tyrosine kinase inhibitor-resistant non-small cell lung cancer. Vol. 14, Pharmaceuticals. MDPI AG; 2021. p. 1–25.

79. Zhou Y, Wang Y, Chen H, Xu Y, Luo Y, Deng Y, et al. Immuno-oncology: are TAM receptors in glioblastoma friends or foes? Cell Commun Signal [Internet]. 2021;19(1):1–13. Available from: https://doi.org/10.1186/s12964-020-00694-8

80. Li Y, Seto E. HDACs and HDAC inhibitors in cancer development and therapy. Cold Spring Harb Perspect Med. 2016 Oct 1;6(10).

81. Kawamura Y, Hua L, Gurtner A, Wong E, Kiyokawa J, Shah N, et al. Histone deacetylase inhibitors enhance oncolytic herpes simplex virus therapy for malignant meningioma. Biomed Pharmacother [Internet]. 2022;155(August):113843. Available from: https://doi.org/10.1016/j.biopha.2022.113843

82. Chen CS, Weng SC, Tseng PH, Lin HP, Chen CS. Histone acetylation-independent effect of histone deacetylase inhibitors on Akt through the reshuffling of protein phosphatase 1 complexes. J Biol Chem [Internet]. 2005;280(46):38879–87. Available from: http://dx.doi.org/10.1074/jbc.M505733200

83. Burns SS, Akhmametyeva EM, Oblinger JL, Bush ML, Huang J, Senner V, et al. Histone deacetylase inhibitor AR-42 differentially affects cell-cycle transit in meningeal and meningioma cells, potently inhibiting NF2-deficient meningioma growth. Cancer Res. 2013 Jan 15;73(2):792–803.

84. Tatman PD, Wroblewski TH, Fringuello AR, Scherer SR, Foreman WB, Damek DM, et al. High-throughput mechanistic screening of epigenetic compounds for the potential treatment of meningiomas. J Clin Med. 2021 Jul 2;10(14).

85. Bush ML, Oblinger J, Brendel V, Santarelli G, Huang J, Akhmametyeva EM, et al. AR42, a novel histone deacetylase inhibitor, as a potential therapy for vestibular schwannomas and meningiomas. Neuro Oncol. 2011 Sep;13(9):983–99.

86. Welling DB, Collier KA, Bs SSB, Oblinger JL, Shu E, Beth BS, et al. Early phase clinical studies of AR-42 , a histone deacetylase inhibitor , for

neurofibromatosis type 2-associated vestibular schwannomas and meningiomas. 2021;(November 2018):1008–19.

87. Kim JH, Ali KH, Oh YJ, Seo YH. Design, synthesis, and biological evaluation of histone deacetylase inhibitor with novel salicylamide zinc binding group. J Bone Jt Surg. 2022;101(17):E29049.

88. Moreira-silva F, Camilo V, Gaspar V, Mano JF, Henrique R, Jerónimo C. Repurposing old drugs into new epigenetic inhibitors: Promising candidates for cancer treatment? Pharmaceutics. 2020;12(5).

89. Hai R, He L, Shu G, Yin G. Characterization of Histone Deacetylase Mechanisms in Cancer Development. Front Oncol. 2021;11(July).

90. Mokhtari RB, Homayouni TS, Baluch N, Morgatskaya E, Kumar S, Das B, et al. Combination therapy in combating cancer. Oncotarget [Internet]. 2017;8(23):38022–43. Available from: www.impactjournals.com/oncotarget

91. Plana D, Palmer AC, Sorger PK. Independent Drug Action in Combination Therapy: Implications for Precision Oncology. Cancer Discov. 2022;12(3):606–24.

92. Fudio S, Sellers A, Pérez Ramos L, Gil-Alberdi B, Zeaiter A, Urroz M, et al. Anti-cancer drug combinations approved by US FDA from 2011 to 2021: main design features of clinical trials and role of pharmacokinetics. Cancer Chemother Pharmacol [Internet]. 2022;90(4):285–99. Available from: https://doi.org/10.1007/s00280-022-04467-7

93. Gu W, Shen HZ, Xie L, Zhang X, Yang J. The Role of Feedback Loops in Targeted Therapy for Pancreatic Cancer. Front Oncol. 2022;12(May):1–13.

94. Vakil V, Trappe W. Drug combinations: Mathematical modeling and

networking methods. Pharmaceutics. 2019;11(5):1–31.

95. Blagosklonny M V. “Targeting the absence” and therapeutic engineering for cancer therapy. Cell Cycle. 2008;7(10):1307–12.

96. Shih KC, Chowdhary S, Rosenblatt P, Weir AB, Shepard GC, Williams JT, et al. A phase II trial of bevacizumab and everolimus as treatment for patients with refractory, progressive intracranial meningioma. J Neurooncol [Internet]. 2016;129(2):281–8. Available from: http://dx.doi.org/10.1007/s11060-016-2172-3

97. Graillon T, Sanson M, Campello C, Idbaih A, Peyre M, Peyriere H, et al. Everolimus and octreotide for patients with recurrent meningioma: Results from the phase II CEVOREM trial. Clin Cancer Res. 2020;26(3):552–7.

98. Suraweera A, O’Byrne KJ, Richard DJ. Combination therapy with histone deacetylase inhibitors (HDACi) for the treatment of cancer: Achieving the full therapeutic potential of HDACi. Front Oncol. 2018;8(MAR):1–15.

99. Rausch M, Weiss A, Zoetemelk M, Piersma SR, Jimenez CR, van Beijnum JR, et al. Optimized combination of HDACI and TKI efficiently inhibits metabolic activity in renal cell carcinoma and overcomes sunitinib resistance. Cancers (Basel). 2020;12(11):1–22.

100. Gray JE, Haura E, Chiappori A, Tanvetyanon T, Williams CC, Pinder-Schenck M, et al. A phase i, pharmacokinetic, and pharmacodynamic study of panobinostat, an HDAC inhibitor, combined with erlotinib in patients with advanced aerodigestive tract tumors. Clin Cancer Res. 2014;20(6):1644–55.

101. Meel MH, de Gooijer MC, Metselaar DS, Sewing CPA, Zwaan K, Waranecki P, et al. Combined therapy of AXL and HDAC inhibition reverses mesenchymal transition in diffuse intrinsic pontine glioma. Clin

Cancer Res. 2020 Jul 1;26(13):3319–32.

102. Yin X, Mead BE, Safaee H, Langer R, Karp JM, Levy O. Engineering Stem Cell Organoids. Vol. 18, Cell Stem Cell. Cell Press; 2016. p. 25–38.

103. Mak IWY, Evaniew N, Ghert M. Lost in translation : animal models and clinical trials in cancer treatment. 2014;6(2):114–8.

104. Kim E, Kim M, So K, Park YS, Woo CG, Hyun SH. Characterization and comparison of genomic profiles between primary cancer cell lines and parent atypical meningioma tumors. Cancer Cell Int. 2020 Jul 28;20(1).

105. Patrick B, Gauvin S, Ferland K, Caneparo C, Pellerin È. Innovative Human Three-Dimensional Tissue-Engineered Models as an Alternative to Animal Testing. 2020;(Figure 1).

106. Siolas D, Hannon GJ. Patient-derived tumor xenografts: Transforming clinical samples into mouse models. Vol. 73, Cancer Research. 2013. p. 5315–9.

107. Sachs N, Clevers H. Organoid cultures for the analysis of cancer phenotypes. Vol. 24, Current Opinion in Genetics and Development. 2014. p. 68–73.

108. Kalamarides M, Peyre M, Giovannini M. Meningioma mouse models. 2010;325–31.

109. Rana MW, Pinkerton H, Thornton H, Nagy D. Heterotransplantation of human glioblastoma multiforme and meningioma to nude mice. Proc Soc Exp Biol Med Soc Exp Biol Med (New York, NY). 1977 May;155(1):85–8.

110. Medhkour A, Van Roey M, Sobel RA, Fingert HJ, Lee J, Martuza RL. Implantation of human meningiomas into the subrenal capsule of the nude mouse. A model for studies of tumor growth. J Neurosurg. 1989 Oct;71(4):545–50.

111. McCutcheon IE, Friend KE, Gerdes TM, Zhang BM, Wildrick DM, Fuller GN. Intracranial injection of human meningioma cells in athymic mice: an orthotopic model for meningioma growth. J Neurosurg. 2000 Feb;92(2):306–14.

112. Kalamarides M, Niwa-kawakita M, Leblois H, Abramowski V, Perricaudet M, Janin A, et al. Nf2 gene inactivation in arachnoidal cells is rate-limiting for meningioma development in the mouse. 2002;1060–5.

113. Kapałczyńska M, Kolenda T, Przybyła W, Zajączkowska M, Teresiak A, Filas V, et al. 2D and 3D cell cultures – a comparison of different types of cancer cell cultures. Arch Med Sci. 2018;14(4):910–9.

114. Ledur PF, Onzi GR, Zong H, Lenz G. Culture conditions defining glioblastoma cells behavior: what is the impact for novel discoveries? Oncotarget. 2017;8(40):69185–97.

115. Carter M, Shieh J. Cell Culture Techniques. Guid to Res Tech Neurosci [Internet]. 2015 Jan 1 [cited 2022 Apr 12];295–310. Available from: https://linkinghub.elsevier.com/retrieve/pii/B9780128005118000149

116. Gupta N, Liu JR, Patel B, Solomon DE, Vaidya B, Gupta V. Microfluidics-based 3D cell culture models: Utility in novel drug discovery and delivery research. Bioeng Transl Med. 2016 Mar;1(1):63–81.

117. Horvath P, Aulner N, Bickle M, Davies AM, Nery E Del, Ebner D, et al. Screening out irrelevant cell-based models of disease. Vol. 15, Nature Reviews Drug Discovery. Nature Publishing Group; 2016. p. 751–69.

118. Jensen C, Teng Y. Is It Time to Start Transitioning From 2D to 3D Cell Culture? Vol. 7, Frontiers in Molecular Biosciences. Frontiers Media S.A.; 2020.

119. Langhans SA. Three-dimensional in vitro cell culture models in drug

discovery and drug repositioning. Vol. 9, Frontiers in Pharmacology. Frontiers Media S.A.; 2018.

120. Salinas-Vera YM, Valdés J, Pérez-Navarro Y, Mandujano-Lazaro G, Marchat LA, Ramos-Payán R, et al. Three-Dimensional 3D Culture Models in Gynecological and Breast Cancer Research. Front Oncol. 2022;12(May):1–13.

121. Weiswald LB, Bellet D, Dangles-Marie V. Spherical Cancer Models in Tumor Biology. Vol. 17, Neoplasia (United States). Neoplasia Press, Inc.; 2015. p. 1–15.

122. Forster J, Harriss-Phillips W, Douglass M, Bezak E. A review of the development of tumor vasculature and its effects on the tumor microenvironment. Hypoxia. 2017 Apr;Volume 5:21–32.

123. Lagies S, Schlimpert M, Neumann S, Wäldin A, Kammerer B, Borner C, et al. Cells grown in three-dimensional spheroids mirror in vivo metabolic response of epithelial cells. Commun Biol. 2020 Dec 1;3(1).

124. Clevers H. Modeling Development and Disease with Organoids. Cell. 2016.

125. Jeppesen M, Hagel G, Glenthoj A, Vainer B, Ibsen P, Harling H, et al. Short-term spheroid culture of primary colorectal cancer cells as an in vitro model for personalizing cancer medicine. PLoS One. 2017 Sep 1;12(9).

126. Xu H, Lyu X, Yi M, Zhao W, Song Y, Wu K. Organoid technology and applications in cancer research 11 Medical and Health Sciences 1112 Oncology and Carcinogenesis. Vol. 11, Journal of Hematology and Oncology. BioMed Central Ltd.; 2018.

127. Zanoni M, Cortesi M, Zamagni A, Arienti C, Pignatta S, Tesei A. Modeling

neoplastic disease with spheroids and organoids. Vol. 13, Journal of Hematology and Oncology. BioMed Central; 2020.

128. Doyle AD, Carvajal N, Jin A, Matsumoto K, Yamada KM. Local 3D matrix microenvironment regulates cell migration through spatiotemporal dynamics of contractility-dependent adhesions. Nat Commun. 2015 Nov 9;6.

129. Ekert JE, Johnson K, Strake B, Pardinas J, Jarantow S, Perkinson R, et al. Three-dimensional lung tumor microenvironment modulates therapeutic compound responsiveness in vitro - Implication for drug development. PLoS One. 2014 Mar 17;9(3).

130. Ryu NE, Lee SH, Park H. Spheroid Culture System Methods and Applications for Mesenchymal Stem Cells. Vol. 8, Cells. NLM (Medline); 2019.

131. Mittler F, Obeïd P, Rulina A V., Haguet V, Gidrol X, Balakirev MY. High-content monitoring of drug effects in a 3D spheroid model. Front Oncol. 2017 Dec 11;7(DEC).

132. Murphy S V., Atala A. 3D bioprinting of tissues and organs. Nat Biotechnol. 2014;32(8):773–85.

133. Yu F, Hunziker W, Choudhury D. Engineering microfluidic organoid-on-a-chip platforms. Micromachines. 2019;10(3):1–12.

134. Mu P, Zhou S, Lv T, Xia F, Shen L, Wan J, et al. Newly developed 3D in vitro models to study tumor-immune interaction. J Exp Clin Cancer Res [Internet]. 2023;42(1):81. Available from: https://doi.org/10.1186/s13046-023-02653-w

135. Breslin S, O'Driscoll L. Three-dimensional cell culture: The missing link in drug discovery. Drug Discov Today [Internet]. 2013;18(5–6):240–9.

Available from: http://dx.doi.org/10.1016/j.drudis.2012.10.003

136. Vinci M, Gowan S, Boxall F, Patterson L, Zimmermann M, Court W, et al. Advances in establishment and analysis of three-dimensional tumor spheroid-based functional assays for target validation and drug evaluation. BMC Biol. 2012 Mar 22;10.

137. Lin RZ, Chang HY. Recent advances in three-dimensional multicellular spheroid culture for biomedical research. Vol. 3, Biotechnology Journal. Wiley-VCH Verlag; 2008. p. 1172–84.

138. Lin RZ, Chou LF, Chien CCM, Chang HY. Dynamic analysis of hepatoma spheroid formation: Roles of E-cadherin and β1-integrin. Cell Tissue Res. 2006 Jun;324(3):411–22.

139. Smyrek I, Mathew B, Fischer SC, Lissek SM, Becker S, Stelzer EHK. E-cadherin, actin, microtubules and FAK dominate different spheroid formation phases and important elements of tissue integrity. Biol Open. 2019;8(1).

140. Powan P, Luanpitpong S, He X, Rojanasakul Y, Chanvorachote P. Detachment-induced E-cadherin expression promotes 3D tumor spheroid formation but inhibits tumor formation and metastasis of lung cancer cells. Am J Physiol Cell Physiol. 2017 Nov;313(5):C556–66.

141. Yip D, Cho CH. A multicellular 3D heterospheroid model of liver tumor and stromal cells in collagen gel for anti-cancer drug testing. Biochem Biophys Res Commun. 2013 Apr 12;433(3):327–32.

142. Long L, Hu Y, Long T, Lu X, Tuo Y, Li Y, et al. Tumor-associated macrophages induced spheroid formation by CCL18-ZEB1-M-CSF feedback loop to promote transcoelomic metastasis of ovarian cancer. J Immunother Cancer. 2021 Dec 27;9(12).

143. Shoval H, Karsch-Bluman A, Brill-Karniely Y, Stern T, Zamir G, Hubert A, et al. Tumor cells and their crosstalk with endothelial cells in 3D spheroids. Sci Rep. 2017 Dec 1;7(1).

144. Ishiguro T, Ohata H, Sato A, Yamawaki K, Enomoto T, Okamoto K. Tumor-derived spheroids: Relevance to cancer stem cells and clinical applications. Vol. 108, Cancer Science. Blackwell Publishing Ltd; 2017. p. 283–9.

145. Weiss S, Dunne C, Hewson J, Wohl C, Wheatley M, Peterson AC, et al. Multipotent CNS Stem Cells Are Present in the Adult Mammalian Spinal Cord and Ventricular Neuroaxis. 1996.

146. Zhao H, Yan C, Hu Y, Mu L, Huang K, Li Q, et al. Sphere-forming assay vs. Organoid culture: Determining long-term stemness and the chemoresistant capacity of primary colorectal cancer cells. Int J Oncol. 2019 Mar 1;54(3):893–904.

147. Chen YH, McGowan LDA, Cimino PJ, Dahiya S, Leonard JR, Lee DY, et al. Mouse low-grade gliomas contain cancer stem cells with unique molecular and functional properties. Cell Rep. 2015 Mar 24;10(11):1899–912.

148. Guo X, Pan Y, Gutmann DH. Genetic and genomic alterations differentially dictate low-grade glioma growth through cancer stem cell-specific chemokine recruitment of T cells and microglia. Neuro Oncol. 2019;21(10):1250–62.

149. Hueng DY, Sytwu HK, Huang SM, Chang C, Ma HI. Isolation and characterization of tumor stem-like cells from human meningiomas. J Neurooncol. 2011 Aug;104(1):45–53.

150. Quereda V, Hou S, Madoux F, Scampavia L, Spicer TP, Duckett D. A

Cytotoxic Three-Dimensional-Spheroid, High-Throughput Assay Using Patient-Derived Glioma Stem Cells. SLAS Discov. 2018 Sep 1;23(8):842–9.

151. Wang R, Lv Q, Meng W, Tan Q, Zhang S, Mo X, et al. Comparison of mammosphere formation from breast cancer cell lines and primary breast tumors. J Thorac Dis. 2014;6(6):829–37.

152. Song Y, Kim JS, Kim SH, Park YK, Yu E, Kim KH, et al. Patient-derived multicellular tumor spheroids towards optimized treatment for patients with hepatocellular carcinoma. J Exp Clin Cancer Res. 2018 May 25;37(1).

153. Kim J, Koo BK, Knoblich JA. Human organoids: model systems for human biology and medicine. Vol. 21, Nature Reviews Molecular Cell Biology. Nature Research; 2020. p. 571–84.

154. Fadi Jacob, Ryan D. Salinas, Daniel Y. Zhang, Phuong T.T. Nguyen, Jordan G. Schnoll, Samuel Zheng Hao Wong, et al. A Patient-Derived Glioblastoma Organoid Model and Biobank Recapitulates Inter- and Intra-tumoral Heterogeneity. Cell. 2020 Jan 19;188–204.

155. Vlachogiannis G, Hedayat S, Vatsiou A, Jamin Y, Fernández-Mateos J, Khan K, et al. Patient-derived organoids model treatment response of metastatic gastrointestinal cancers [Internet]. Available from: https://www.science.org

156. Karakasheva TA, Gabre JT, Sachdeva UM, Cruz-Acuña R, Lin EW, DeMarshall M, et al. Patient-derived organoids as a platform for modeling a patient’s response to chemoradiotherapy in esophageal cancer. Sci Rep. 2021 Dec 1;11(1).

157. Yao Y, Xu X, Yang L, Zhu J, Wan J, Shen L, et al. Patient-Derived

Organoids Predict Chemoradiation Responses of Locally Advanced Rectal Cancer. Cell Stem Cell. 2020 Jan 2;26(1):17-26.e6.

158. Karkampouna S, La Manna F, Benjak A, Kiener M, De Menna M, Zoni E, et al. Patient-derived xenografts and organoids model therapy response in prostate cancer. Nat Commun. 2021 Dec 1;12(1).

159. Velasco V, Shariati SA, Esfandyarpour R. Microtechnology-based methods for organoid models. Microsystems Nanoeng [Internet]. 2020;6(1). Available from: http://dx.doi.org/10.1038/s41378-020-00185-3

160. Püttmann S, Senner V, Braune S, Hillmann B, Exeler R, Rickert CH, et al. Establishment of a benign meningioma cell line by hTERT-mediated immortalization. Lab Investig. 2005;85(9):1163–71.

161. Baia GS, Slocum AL, Hyer JD, Misra A, Sehati N, VandenBerg SR, et al. A genetic strategy to overcome the senescence of primary meningioma cell cultures. J Neurooncol [Internet]. 2006;78(2):113–21. Available from: https://doi.org/10.1007/s11060-005-9076-y

162. Cargioli TG, Ugur HC, Ramakrishna N, Chan J, Black PM, Carroll RS. Establishment of an in vivo meningioma model with human telomerase reverse transcriptase. Neurosurgery. 2007 Apr;60(4):750–9.

163. Lee W-H. Characterization of a Newly Established Malignant Meningioma Cell Line of the Human Brain: IOMM-Lee. Neurosurgery [Internet]. 1990;27(3). Available from: https://journals.lww.com/neurosurgery/Fulltext/1990/09000/Characterization_of_a_Newly_Established_Malignant.8.aspx

164. Tanaka K, Sato C, Maeda Y, Koike M, Matsutani M, Yamada K, et al. Establishment of a human malignant meningioma cell line with amplified c-myc oncogene. Cancer. 1989 Dec;64(11):2243–9.

165. Tonn J-C, Ichaela Ott MM, Bouterfa H, Kerkau S, Kapp M, Konrad Muller-Hermelink H, et al. EXPERIMENTAL STUDIES Inverse Correlation of Cell Proliferation and Expression of Progesterone Receptors in Tumor Spheroids and Monolayer Cultures of Human Meningiomas [Internet]. Vol. 41, Neurosurgery. 1997. Available from: https://academic.oup.com/neurosurgery/article/41/5/1152/2846203

166. Grill J, Lamfers MLM, van Beusechem VW, Dirven CM, Pherai DS, Kater M, et al. The Organotypic Multicellular Spheroid Is a Relevant Three-Dimensional Model to Study Adenovirus Replication and Penetration in Human Tumors in Vitro. Mol Ther. 2002 Nov;6(5):609–14.

167. Kondraganti S, Gondi CS, McCutcheon I, Dinh DH, Rao JS, Olivero WC. RNAi-mediated downregulation of urokinase plasminogen activator and its receptor in human meningioma cells inhibits tumor invasion and growth. Int J Oncol. 2006;28:1353–60.

168. Grill J, Lamfers MLM, Van Beusechem VW, Van Der Valk P, Huisman A, Sminia P, et al. Oncolytic virotherapy of meningiomas in vitro with replication-competent adenovirus. Neurosurgery. 2005 Jan;56(1):146–53.

169. Tichomirowa M, Theodoropoulou M, Daly A, Yassouridis A, Hansen S, Lu J, et al. Toll-like receptor-4 is expressed in meningiomas and mediates the antiproliferative action of paclitaxel. Int J Cancer. 2008;123:1956–63.

170. Zgheib R, Battaglia-Hsu SF, Hergalant S, Quéré M, Alberto JM, Chéry C, et al. Folate can promote the methionine-dependent reprogramming of glioblastoma cells towards pluripotency. Cell Death Dis. 2019 Aug 1;10(8).

171. Han Y, Wang H, Huang Y, Cheng Z, Sun T, Chen G, et al. Isolation and characteristics of CD133-/A2B5+ and CD133-/A2B5- cells from the

SHG139s cell line. Mol Med Rep. 2015 Dec 1;12(6):7949–56.

172. Bourkoula E, Mangoni D, Ius T, Pucer A, Isola M, Musiello D, et al. Glioma-associated stem cells: A novel class of tumor-supporting cells able to predict prognosis of human low-grade gliomas. Stem Cells. 2014;32(5):1239–53.

173. Dongre A, Weinberg RA. New insights into the mechanisms of epithelial–mesenchymal transition and implications for cancer. Vol. 20, Nature Reviews Molecular Cell Biology. Nature Publishing Group; 2019. p. 69–84.

174. Kalluri R, Weinberg RA. Review series The basics of epithelial-mesenchymal transition. J Clin Invest [Internet]. 2009;119. Available from: http://www.jci.org

175. Lachat C, Peixoto P, Hervouet E. Epithelial to mesenchymal transition history: From embryonic development to cancers. Biomolecules. 2021;11(6).

176. Hyung Kim D, Xing T, Yang Z, Dudek R, Lu Q, Chen Y-H. Clinical Medicine Epithelial Mesenchymal Transition in Embryonic Development, Tissue Repair and Cancer: A Comprehensive Overview. Available from: www.mdpi.com/journal/jcm

177. Marconi G, Fonticoli L, Rajan Soundara T, Pierdomenico S, Trubiani O, Pizzicannella J, et al. Epithelial-Mesenchymal Transition (EMT): The Type-2 EMT in Wound Healing, Tissue Regeneration and Organ Fibrosis. 2021;10(1587):1–14.

178. Ribatti D, Tamma R, Annese T. Translational Oncology Epithelial-Mesenchymal Transition in Cancer : A Historical Overview. Transl Oncol [Internet]. 2020;13(6):100773. Available from:

https://doi.org/10.1016/j.tranon.2020.100773

179. Wong SHM, Fang CM, Chuah LH, Leong CO, Ngai SC. E-cadherin: Its dysregulation in carcinogenesis and clinical implications. Crit Rev Oncol Hematol. 2018;121(November 2017):11–22.

180. Shao Z, Liu L, Zheng Y, Tu S, Pan Y, Yan S, et al. Molecular Mechanism and Approach in Progression of Meningioma. Vol. 10, Frontiers in Oncology. Frontiers Media S.A.; 2020.

181. Behling F, Hempel JM, Schittenhelm J. Brain invasion in meningioma—a prognostic potential worth exploring. Cancers (Basel). 2021 Jul 1;13(13).

182. von Spreckelsen N, Kesseler C, Brokinkel B, Goldbrunner R, Perry A, Mawrin C. Molecular neuropathology of brain-invasive meningiomas. Vol. 32, Brain Pathology. John Wiley and Sons Inc; 2022.

183. Backer-Grøndahl T, Moen BH, Arnli MB, Torseth K, Torp SH. Immunohistochemical characterization of brain-invasive meningiomas [Internet]. Vol. 7, Int J Clin Exp Pathol. 2014. Available from: www.ijcep.com/

184. Collord G, Tarpey P, Kurbatova N, Martincorena I, Moran S, Castro M, et al. An integrated genomic analysis of anaplastic meningioma identifies prognostic molecular signatures. Sci Rep. 2018 Dec 1;8(1).

185. Bukovac A, Kafka A, Raguž M, Brlek P, Dragičević K, Müller D, et al. Are we benign? What can wnt signaling pathway and epithelial to mesenchymal transition tell us about intracranial meningioma progression. Cancers (Basel). 2021 Apr 1;13(7).

186. Pecina-Slaus N, Cicvara-Pecina T, Kafka A. Epithelial-to-mesenchymal transition: possible role in meningiomas [Internet]. Vol. 4, Frontiers in Bioscience. 2012. Available from:

http://www.stanford.edu/group/nusselab/cgi-

187. Bukovac A, Panić H, Mrgan T, Šlaus N, Kafka A, Njirić N, et al. Bilateral Meningioma: A Case Report and Review of the Literature. Int J Mol Sci. 2022 Feb 1;23(3).

188. Wallesch M, Pachow D, Blücher C, Firsching R, Warnke JP, Braunsdorf WEK, et al. Altered expression of E-Cadherin-related transcription factors indicates partial epithelial-mesenchymal transition in aggressive meningiomas. J Neurol Sci. 2017 Sep 15;380:112–21.

189. Celebre A, Wu MY, Danielson B, Cohen S, Munoz D, Das S, et al. Anaplastic meningioma with extensive single-cell infiltration: A potential role for epithelial-mesenchymal transformation in the progression of a meningothelial tumour? Vol. 62, Histopathology. 2013. p. 1111–4.

190. Chen X, Tian F, Lun P, Feng Y. Curcumin Inhibits HGF-Induced EMT by Regulating c-MET-Dependent PI3K/Akt/mTOR Signaling Pathways in Meningioma. Evidence-based Complement Altern Med. 2021;2021.

191. Pecina-Slaus N, Kafka A, Vladuŝi T, Peina HI, Hraŝan R. Axin1 expression and localization in meningiomas and association to changes of apc and e-cadherin. Anticancer Res. 2016;36(9):4583–94.

192. Pecina-Slaus N, Nikuseva Martic T, Jakov Deak A, Zeljko M, Hrascan R, Tomas D, et al. Genetic and protein changes of E-cadherin in meningiomas. J Cancer Res Clin Oncol. 2010;695–702.

193. Schwechheimer K, Zhou L, Birchmeier W. E-Cadherin in human brain tumours : loss of immunoreactivity in malignant meningiomas. Virchows Arch. 1998;432:163–7.

194. Brunner EC, Romeike BFM, Jung M, Comtesse N, Meese E. Altered expression of b -catenin / E-cadherin in meningiomas. 2006;178–87.

195. Utsuki S, Oka H, Sato Y, Kawano N, Tsuchiya B. Invasive meningioma is associated with a low expression of E-cadherin and β -catenin. 2005;(April 2021).

196. Akat K, Bleck CKE, Lee YA, Haselmann-weiss U. Characterization of a novel type of adherens junction in meningiomas and the derived cell line HBL-52. Cell Tissue Res. 2008;331:401–12.

197. Panagopoulos AT, Penteado Lancellotti CL, Esteves Veiga JC, Pires de Aguiar PH, Colquhoun A. Expression of cell adhesion proteins and proteins related to angiogenesis and fatty acid metabolism in benign , atypical , and anaplastic meningiomas. J Neurooncol. 2008;89:73–87.

198. Figarella-Branger D, Pellissier JF, Bouillot P, Bianco N, Mayan M, Grisoli F, et al. Expression of neural cell-adhesion molecule isoforms and epithelial cadherin adhesion molecules in 47 human meningiomas: correlation with clinical and morphological data. Mod Pathol an Off J United States Can Acad Pathol Inc. 1994 Sep;7(7):752–61.

199. Shimada S, Ishizawa K, Hirose T. Expression of E-cadherin and catenins in meningioma : Ubiquitous expression and its irrelevance to malignancy. 2005;(September 2004):1–7.

200. Zhou K, Wang G, Wang Y, Jin H, Yang S, Liu C. The Potential Involvement of E-cadherin and b -catenins in Meningioma. 2010;5(6):2–7.

201. Ludwig N, Kim YJ, Mueller SC, Backes C, Werner T V., Galata V, et al. Posttranscriptional deregulation of signaling pathways in meningioma subtypes by differential expression of miRNAs. Neuro Oncol. 2015;17(9):1250–60.

202. Bolós V, Mira E, Martínez-Poveda B, Luxán G, Cañamero M, Martínez-A C, et al. Notch activation stimulates migration of breast cancer cells and

promotes tumor growth. Breast Cancer Res [Internet]. 2013;15(4):R54. Available from: http://breast-cancer-research.com/content/15/4/R54

203. Shao S, Zhao X, Zhang X, Luo M, Zuo X, Huang S, et al. Notch1 signaling regulates the epithelial-mesenchymal transition and invasion of breast cancer in a Slug-dependent manner. Mol Cancer. 2015 Feb 3;14(1).

204. Bao B, Wang Z, Ali S, Kong D, Li Y, Ahmad A, et al. Notch-1 induces epithelial-mesenchymal transition consistent with cancer stem cell phenotype in pancreatic cancer cells. Cancer Lett [Internet]. 2011/04/03. 2011 Aug 1;307(1):26–36. Available from: https://pubmed.ncbi.nlm.nih.gov/21463919

205. Yuan X, Wu H, Han N, Xu H, Chu Q, Yu S, et al. Notch signaling and EMT in non-small cell lung cancer: Biological significance and therapeutic application. J Hematol Oncol. 2014;7(1):1–10.

206. Pal D, Tyagi A, Chandrasekaran B, Alattasi H, Ankem MK, Sharma AK, et al. Suppression of Notch1 and AKT mediated epithelial to mesenchymal transition by Verrucarin J in metastatic colon cancer. Cell Death Dis [Internet]. 2018;9(8). Available from: http://dx.doi.org/10.1038/s41419-018-0810-8

207. Li J, Li Q, Lin L, Wang R, Chen L, Du W, et al. Targeting the Notch1 oncogene by miR-139-5p inhibits glioma metastasis and epithelial-mesenchymal transition (EMT). BMC Neurol. 2018 Aug 31;18(1).

208. Miao K, Lei JH, Valecha MV, Zhang A, Xu J, Wang L, et al. NOTCH1 activation compensates BRCA1 deficiency and promotes triple-negative breast cancer formation. Nat Commun [Internet]. (2020). Available from: http://dx.doi.org/10.1038/s41467-020-16936-9

209. Timmerman LA, Grego-Bessa J, Raya A, Bertrán E, Pérez-Pomares JM, Díez J, et al. Notch promotes epithelial-mesenchymal transition during cardiac development and oncogenic transformation. Genes Dev. 2004;18(1):99–115.

210. Gharaibeh L, Elmadany N, Alwosaibai K, Alshaer W. Notch1 in cancer therapy: Possible clinical implications and challenges. Vol. 98, Molecular Pharmacology. American Society for Pharmacology and Experimental Therapy; 2020. p. 559–76.

211. Zhang YU, Xie ZY, Guo XT, Xiao XH, Xiong LX. Notch and breast cancer metastasis: Current knowledge, new sights and targeted therapy (review). Oncol Lett. 2019;18(3):2743–55.

212. Zhou B, Lin W, Long Y, Yang Y, Zhang H, Wu K, et al. Notch signaling pathway: architecture, disease, and therapeutics. Signal Transduct Target Ther. 2022;7(1):1–33.

213. Espinoza I, Pochampally R, Xing F, Watabe K, Miele L. Notch signaling: Targeting cancer stem cells and epithelial-to-mesenchymal transition. Onco Targets Ther. 2013;6:1249–59.

214. Cuevas IC, Slocum AL, Jun P, Costello JF, Bollen AW, Riggins GJ, et al. Meningioma Transcript Profiles Reveal Deregulated Notch Signaling Pathway. Cancer Res [Internet]. 2005 Jul 15;65(12):5070–5. Available from: http://aacrjournals.org/cancerres/article-pdf/65/12/5070/2535085/5070-5075.pdf

215. McCaw T, Inga E, Chen H, Jaskula-Sztul R, Dudeja V, Bibb J, et al. Gamma Secretase Inhibitors in Cancer : A Current Perspective on Clinical Performance. Oncologist. 2021;26(4):e608–21.

216. Tyagi A, Sharma AK, Damodaran C. A Review on Notch Signaling and

Colorectal Cancer. Cells. 2020;9(6).

217. Brodney MA, Auperin DD, Becker SL, Bronk BS, Brown TM, Coffman KJ, et al. Design, synthesis, and in vivo characterization of a novel series of tetralin amino imidazoles as γ-secretase inhibitors: discovery of PF-3084014. Bioorg Med Chem Lett. 2011 May;21(9):2637–40.

218. Zhang W, Deryckere D, Hunter D, Liu J, Stashko MA, Minson KA, et al. UNC2025, a potent and orally bioavailable MER/FLT3 dual inhibitor. J Med Chem. 2014;57(16):7031–41.

219. Yoshida M, Kijima M, Akita M, Beppu T. Potent and specific inhibition of mammalian histone deacetylase both in vivo and in vitro by trichostatin A. J Biol Chem. 1990;265(28):17174–9.

220. Bindea G, Mlecnik B, Hackl H, Charoentong P, Tosolini M, Kirilovsky A, et al. ClueGO: A Cytoscape plug-in to decipher functionally grouped gene ontology and pathway annotation networks. Bioinformatics. 2009;25(8):1091–3.

221. Livak KJ, Schmittgen TD. Analysis of relative gene expression data using real-time quantitative PCR and the 2-ΔΔCT method. Methods. 2001;25(4):402–8.

222. Kalluri AL, Shah PP, Lim M. The Tumor Immune Microenvironment in Primary CNS Neoplasms: A Review of Current Knowledge and Therapeutic Approaches. Int J Mol Sci. 2023;24(3).

223. de Stricker Borch J, Haslund-Vinding J, Vilhardt F, Maier AD, Mathiesen T. Meningioma–brain crosstalk: A scoping review. Vol. 13, Cancers. MDPI AG; 2021.

224. Zhu L, Jiang M, Wang H, Sun H, Zhu J, Zhao W, et al. A narrative review of tumor heterogeneity and challenges to tumor drug therapy. Ann Transl

Med. 2021;9(16):1351–1351.

225. Richter M, Piwocka O, Musielak M, Piotrowski I, Suchorska WM, Trzeciak T. From Donor to the Lab: A Fascinating Journey of Primary Cell Lines. Front Cell Dev Biol. 2021;9(July):1–11.

226. Seaman SA, Tannan SC, Cao Y, Peirce SM, Lin KY. Differential effects of processing time and duration of collagenase digestion on human and murine fat grafts. Plast Reconstr Surg. 2015;136(2):189e-199e.

227. Cesselli D, Beltrami AP, Pucer A, Bourkoula E, Ius T, Vindigni M, et al. Human low-grade glioma cultures. In: Diffuse Low-Grade Gliomas in Adults: Natural History, Interaction with the Brain, and New Individualized Therapeutic Strategies. Springer-Verlag London Ltd; 2013. p. 137–63.

228. Muñoz-Galindo L, Melendez-Zajgla J, Pacheco-Fernández T, Rodriguez-Sosa M, Mandujano-Tinoco EA, Vazquez-Santillan K, et al. Changes in the transcriptome profile of breast cancer cells grown as spheroids. Biochem Biophys Res Commun. 2019 Sep 3;516(4):1258–64.

229. Afshari A, Shamdani S, Uzan G, Naserian S, Azarpira N. Different approaches for transformation of mesenchymal stem cells into hepatocyte-like cells. Stem Cell Res Ther. 2020;11(1):1–14.

230. Han SJ, Kwon S, Kim KS. Challenges of applying multicellular tumor spheroids in preclinical phase. Vol. 21, Cancer Cell International. BioMed Central Ltd; 2021.

231. Gallo A, Cuscino N, Contino F, Bulati M, Pampalone M, Amico G, et al. Changes in the Transcriptome Profiles of Human Amnion-Derived Mesenchymal Stromal/Stem Cells Induced by Three-Dimensional Culture: A Potential Priming Strategy to Improve Their Properties. Int J Mol Sci. 2022;23(2):1–15.

232. King D, Skehel PA, Dando O, Emelianova K, Barron R, Wishart TM. Microarray profiling emphasizes transcriptomic differences between hippocampal in vivo tissue and in vitro cultures. Brain Commun. 2021;3(3):1–11.

233. Subramanian A, Tamayo P, Mootha VK, Mukherjee S, Ebert BL, Gillette MA, et al. Gene set enrichment analysis: A knowledge-based approach for interpreting genome-wide expression profiles. Proc Natl Acad Sci U S A. 2005;102(43):15545–50.

234. Pastushenko I, Blanpain C. EMT Transition States during Tumor Progression and Metastasis. Vol. 29, Trends in Cell Biology. Elsevier Ltd; 2019. p. 212–26.

235. Krasnapolski MA, Todaro LB, Bal De Kier Joffé E. Is the Epithelial-to-Mesenchymal Transition Clinically Relevant for the Cancer Patient? Vol. 12, Current Pharmaceutical Biotechnology. 2011.

236. Satelli A, Li S. Vimentin as a potential molecular target in cancer therapy Or Vimentin, an overview and its potential as a molecular target for cancer therapy. Cell Mol Life Sci. 2011;68(18):3033–46.

237. Leggett SE, Hruska AM, Guo M, Wong IY. The epithelial-mesenchymal transition and the cytoskeleton in bioengineered systems. Cell Commun Signal [Internet]. 2021;19(1):1–24. Available from: https://doi.org/10.1186/s12964-021-00713-2

238. Sahab Negah S, Aligholi H, Khaksar Z, Kazemi H, Modarres Mousavi SM, Safahani M, et al. Survival, proliferation, and migration of human meningioma stem-like cells in a nanopeptide scaffold. Iran J Basic Med Sci. 2016 Dec 1;19(12):1271–8.

239. Rimmer JL, Ercolano E, Baiz D, Makhija M, Berger A, Sells T, et al. The

potential of mln3651 in combination with selumetinib as a treatment for merlin-deficient meningioma. Cancers (Basel). 2020;12(7).

240. Negroni C, Hilton DA, Ercolano E, Adams CL, Kurian KM, Baiz D, et al. GATA-4, a potential novel therapeutic target for high-grade meningioma, regulates miR-497, a potential novel circulating biomarker for high-grade meningioma. EBioMedicine. 2020 Sep;59:102941.

241. Kaur G, Dufour JM. Cell lines. Spermatogenesis. 2012;2(1):1–5.

242. Piccirillo SGM, Vescovi AL. Human brain tumor stem cells. Autologous And Cancer Stem Cell Gene Therapy. 2007. 299–316 p.

243. Uhlmann EJ, Rabinovsky R, Varma H, El Fatimy R, Kasper EM, Moore JM, et al. Tumor-Derived Cell Culture Model for the Investigation of Meningioma Biology. J Neuropathol Exp Neurol. 2021;80(12):1117–24.

244. Lee J, Kotliarova S, Kotliarov Y, Li A, Su Q, Donin NM, et al. Tumor stem cells derived from glioblastomas cultured in bFGF and EGF more closely mirror the phenotype and genotype of primary tumors than do serum-cultured cell lines. Cancer Cell. 2006;9(5):391–403.

245. Zheng X, Naiditch J, Czurylo M, Jie C, Lautz T, Clark S, et al. Differential effect of long-term drug selection with doxorubicin and vorinostat on neuroblastoma cells with cancer stem cell characteristics. Cell Death Dis. 2013 Jul;4(7).

246. Chiou H-YC, Lai W-K, Huang L-C, Huang S-M, Chueh S-H, Ma H-I, et al. Valproic acid promotes radiosensitization in meningioma stem-like cells [Internet]. Vol. 6. 2015. Available from: www.impactjournals.com/oncotarget

247. Azizipour N, Avazpour R, Weber MH, Sawan M, Ajji A, Rosenzweig DH. Uniform Tumor Spheroids on Surface-Optimized Microfluidic Biochips for

Reproducible Drug Screening and Personalized Medicine. Micromachines. 2022;13(4).

248. Friedrich J, Seidel C, Ebner R, Kunz-Schughart LA. Spheroid-based drug screen: Considerations and practical approach. Nat Protoc. 2009;4(3):309–24.

249. Tidwell TR, Røsland G V., Tronstad KJ, Søreide K, Hagland HR. Metabolic flux analysis of 3D spheroids reveals significant differences in glucose metabolism from matched 2D cultures of colorectal cancer and pancreatic ductal adenocarcinoma cell lines. Cancer Metab [Internet]. 2022;10(1):1–16. Available from: https://doi.org/10.1186/s40170-022-00285-w

250. Deisboeck TS, Berens ME, Kansal AR, Torquato S, Stemmer-Rachamimov AO, Chiocca EA. Pattern of self-organization in tumour systems: Complex growth dynamics in a novel brain tumour spheroid model. Cell Prolif. 2001;34(2):115–34.

251. Takahashi J, Mizutani T, Sugihara HY, Nagata S, Kato S, Hiraguri Y, et al. Suspension culture in a rotating bioreactor for efficient generation of human intestinal organoids. Cell Reports Methods [Internet]. 2022;2(11):100337. Available from: https://doi.org/10.1016/j.crmeth.2022.100337

252. Shen H, Cai S, Wu C, Yang W, Yu H, Liu L. Recent advances in three-dimensional multicellular spheroid culture and future development. Micromachines. 2021;12(1):1–21.

253. Wu W, Zhou Y, Wang Y, Liu L, Lou J, Deng Y, et al. Clinical Significance of Somatostatin Receptor (SSTR) 2 in Meningioma. Front Oncol. 2020;10(September).

254. Baillargeon M. Organoids Versus Spheroids: The 3D Difference Matters! [Internet]. Crown Bioscience. 2023. Available from: https://blog.crownbio.com/organoids-versus-spheroids-the-3d-difference-matters

255. Ding Y, Qiu L, Xu Q, Song L, Yang S, Yang T. Relationships between tumor microenvironment and clinicopathological parameters in meningioma [Internet]. Vol. 7, Int J Clin Exp Pathol. 2014. Available from: www.ijcep.com/

256. Kanno H, Nishihara H, Wang L, Yuzawa S, Kobayashi H, Tsuda M, et al. Expression of CD163 prevents apoptosis through the production of granulocyte colony-stimulating factor in meningioma. Neuro Oncol. 2013 Jul;15(7):853–64.

257. Xiao M, He J, Yin L, Chen X, Zu X, Shen Y. Tumor-Associated Macrophages: Critical Players in Drug Resistance of Breast Cancer. Front Immunol. 2021;12(December):1–16.

258. Ruffell B, Coussens LM. Cancer Cell Perspective Macrophages and Therapeutic Resistance in Cancer. Cancer Cell [Internet]. 2015;27(4):1–11. Available from: http://dx.doi.org/10.1016/j.ccell.2015.02.015

259. Pellerino A, Bruno F, Palmiero R, Pronello E, Bertero L, Soffietti R, et al. Clinical Significance of Molecular Alterations and Systemic Therapy for Meningiomas: Where Do We Stand? Cancers (Basel). 2022;14(9):1–14.

260. Brastianos PK, Twohy EL, Gerstner ER, Kaufmann TJ, Iafrate AJ, Lennerz J, et al. Alliance A071401: Phase II Trial of Focal Adhesion Kinase Inhibition in Meningiomas With Somatic NF2 Mutations. J Clin Oncol Off J Am Soc Clin Oncol. 2023 Jan;41(3):618–28.

261. Torres M, Betts Z, Scholey R, Elvin M, Place S, Hayes A, et al. Long term

culture promotes changes to growth, gene expression, and metabolism in CHO cells that are independent of production stability. Biotechnol Bioeng. 2023;120(9):2389–402.

262. Pacheco-Marin R, Melendez-Zajgla J, Castillo-Rojas G, Mandujano-Tinoco E, Garcia-Venzor A, Uribe-Carvajal S, et al. Transcriptome profile of the early stages of breast cancer tumoral spheroids. Sci Rep. 2016;6(March):1–15.

263. Wong MK, Wahed M, Shawky SA, Dvorkin-Gheva A, Raha S. Transcriptomic and functional analyses of 3D placental extravillous trophoblast spheroids. Sci Rep. 2019 Dec 1;9(1).

264. Zhou Y, Arai T, Horiguchi Y, Ino K, Matsue T, Shiku H. Multiparameter analyses of three-dimensionally cultured tumor spheroids based on respiratory activity and comprehensive gene expression profiles. Anal Biochem. 2013;439(2):187–93.

265. Svandova E, Peterkova R, Matalova E, Lesot H. Formation and Developmental Specification of the Odontogenic and Osteogenic Mesenchymes. Front Cell Dev Biol. 2020;8(July):1–16.

266. Barresi V, Caffo M, Ieni A, Alafaci C, Tuccari G. Osteoblastic meningiomas: Clinico-pathological and immunohistochemical features of an uncommon variant. J Neurooncol. 2011;105(2):225–32.

267. Huang J, Petersson F. Intracerebral metaplastic meningioma with prominent ossification and extensive calcification. Rare Tumors. 2011;3(2):59–61.

268. Jeon S, Lee HS, Lee GY, Park G, Kim TM, Shin J, et al. Shift of EMT gradient in 3D spheroid MSCs for activation of mesenchymal niche function. Sci Rep. 2017 Dec 1;7(1).

269. Kuo C Te, Chiang CL, Huang RYJ, Lee H, Wo AM. Configurable 2D and 3D spheroid tissue cultures on bioengineered surfaces with acquisition of epithelial-mesenchymal transition characteristics. NPG Asia Mater. 2012;4(9):1–8.

270. Essid N, Chambard JC, Elgaaïed AB. Induction of epithelial-mesenchymal transition (EMT) and Gli1 expression in head and neck squamous cell carcinoma (HNSCC) spheroid cultures. Bosn J Basic Med Sci. 2018;18(4):336–46.

271. Gheytanchi E, Naseri M, Karimi-Busheri F, Atyabi F, Mirsharif ES, Bozorgmehr M, et al. Morphological and molecular characteristics of spheroid formation in HT-29 and Caco-2 colorectal cancer cell lines. Cancer Cell Int [Internet]. 2021;21(1):1–16. Available from: https://doi.org/10.1186/s12935-021-01898-9

272. Mauretti A, Rossi F, Bax NAM, Miano C, Miraldi F, Goumans MJ, et al. Spheroid three-dimensional culture enhances Notch signaling in cardiac progenitor cells. MRS Commun. 2017 Sep 1;7(3):496–501.

273. Fu X, Li J, Li X, Tan Y, Zhao M, Zhang S, et al. M2-Macrophage-Derived Exosomes Promote Meningioma Progression through TGF- β Signaling Pathway. 2022;2022.

274. Qian X, Tang S, Shen Y, Chen L, Cheng X, Wan X. Notch1 Affects Chemo-resistance Through Regulating Epithelial-Mesenchymal Transition (EMT) in Epithelial Ovarian cancer cells. 2020;17.

275. Zschenker O, Streichert T, Hehlgans S, Cordes N. Genome-wide gene expression analysis in cancer cells reveals 3D growth to affect ECM and processes associated with cell adhesion but not DNA repair. PLoS One. 2012;7(4).

276. D’Oto A, Tian Q, Davidoff AM, Yang J. Histone demethylases and their roles in cancer epigenetics. J Med Oncol Ther. 2016;1(2):34–40.

277. Brastianos PK, Horowitz PM, Santagata S, Jones RT, Mckenna A, Getz G, et al. Genomic sequencing of meningiomas identifies oncogenic SMO and AKT1 mutations. Nat Genet. 2013;45(3):285–9.

278. Cello G, Patel R V., McMahon JT, Santagata S, Bi WL. Impact of H3K27 trimethylation loss in meningiomas: a meta-analysis. Acta Neuropathol Commun [Internet]. 2023;11(1):1–11. Available from: https://doi.org/10.1186/s40478-023-01615-9

279. Horbay R, Bilyy R. Mitochondrial dynamics during cell cycling. Apoptosis [Internet]. 2016;21(12):1327–35. Available from: http://dx.doi.org/10.1007/s10495-016-1295-5

280. Zoetemelk M, Rausch M, Colin DJ, Dormond O, Nowak-Sliwinska P. Short-term 3D culture systems of various complexity for treatment optimization of colorectal carcinoma. Sci Rep. 2019;9(1):1–14.

281. Xie J, Lin LS, Huang XY, Gan RH, Ding LC, Su BH, et al. The NOTCH1-HEY1 pathway regulates self-renewal and epithelial-mesenchymal transition of salivary adenoid cystic carcinoma cells. Int J Biol Sci. 2020;16(4):598–610.

282. Hassan WA, Yoshida R, Kudoh S, Hasegawa K, Niimori-Kita K, Ito T. Notch1 controls cell invasion and metastasis in small cell lung carcinoma cell lines. Lung Cancer [Internet]. 2014;86(3):304–10. Available from: http://dx.doi.org/10.1016/j.lungcan.2014.10.007

283. Ji M, Lee EJ, Kim KB, Kim Y, Sung R, Lee SJ, et al. HDAC inhibitors induce epithelial-mesenchymal transition in colon carcinoma cells. Oncol Rep. 2015;33(5):2299–308.

284. Dave F. Investigating the role of TAM (Tyro3, Axl, MerTK) family receptors in Merlin deficient tumours. University of Plymouth;

285. Baia GS, Stifani S, Kimura ET, McDermott MW, Pieper RO, Lal A. Notch activation is associated with tetraploidy and enhanced chromosomal instability in meningiomas. Neoplasia. 2008;10(6):604–12.

286. Grudzien P, Lo S, Albain KS, Robinson P, Rajan P, Strack PR, et al. Inhibition of notch signaling reduces the stem-like population of breast cancer cells and prevents mammosphere formation. Anticancer Res. 2010;30(10):3853–67.

287. Oh SJ, Ahn EJ, Kim O, Kim D, Jung TY, Jung S, et al. The Role Played by SLUG, an Epithelial–Mesenchymal Transition Factor, in Invasion and Therapeutic Resistance of Malignant Glioma. Cell Mol Neurobiol [Internet]. 2019;39(6):769–82. Available from: https://doi.org/10.1007/s10571-019-00677-5

288. Fenouille N, Tichet M, Dufies M, Pottier A, Mogha A, Soo JK, et al. The epithelial-mesenchymal transition (EMT) regulatory factor SLUG (SNAI2) is a downstream target of SPARC and AKT in promoting melanoma cell invasion. PLoS One. 2012;7(7).

289. Chou TC. Theoretical basis, experimental design, and computerized simulation of synergism and antagonism in drug combination studies. Pharmacol Rev. 2006;58(3):621–81.

290. Wang X, Chen S, Shen T, Lu H, Xiao D, Zhao M, et al. Trichostatin A reverses epithelial-mesenchymal transition and attenuates invasion and migration in MCF-7 breast cancer cells. Exp Ther Med. 2020 Jan 3;

291. Ganatra DA, Vasavada AR, Vidya NG, Gajjar DU, Rajkumar S. Trichostatin a restores expression of adherens and tight junction proteins

during transforming growth factor β-mediated epithelial-to-mesenchymal transition. J Ophthalmic Vis Res. 2018;13(3):274–83.

292. Fujimaki S, Seko D, Kitajima Y, Yoshioka K, Tsuchiya Y, Masuda S, et al. Notch1 and Notch2 Coordinately Regulate Stem Cell Function in the Quiescent and Activated States of Muscle Satellite Cells. Stem Cells. 2018;36(2):278–85.

293. Radtke F, Fasnacht N, MacDonald HR. Notch Signaling in the Immune System. Immunity [Internet]. 2010;32(1):14–27. Available from: http://dx.doi.org/10.1016/j.immuni.2010.01.004

294. Gounder M, Ratan R, Alcindor T, Schöffski P, van der Graaf WT, Wilky BA, et al. Nirogacestat, a γ-Secretase Inhibitor for Desmoid Tumors. N Engl J Med [Internet]. 2023 Mar 8;388(10):898–912. Available from: https://doi.org/10.1056/NEJMoa2210140

295. Nidhi S, Anand U, Oleksak P, Tripathi P, Lal JA, Thomas G, et al. Novel crispr–cas systems: An updated review of the current achievements, applications, and future research perspectives. Int J Mol Sci. 2021;22(7):1–42.

296. Franken NAP, Rodermond HM, Stap J, Haveman J, van Bree C. Clonogenic assay of cells in vitro. Nat Protoc. 2006;1(5):2315–9.

297. Riss TL, Moravec RA, Niles AL, Duellman S, Benink HA, Worzella TJ, et al. Cell Viability Assays. Assay Guid Man [Internet]. 2004;(Md):1–25. Available from: http://www.ncbi.nlm.nih.gov/pubmed/23805433

298. Ran Y, Hossain F, Pannuti A, Lessard CB, Ladd GZ, Jung JI, et al. γ-Secretase inhibitors in cancer clinical trials are pharmacologically and functionally distinct. EMBO Mol Med. 2017;9(7):950–66.

299. Fan X, Mikolaenko I, Elhassan I, Ni XZ, Wang Y, Ball D, et al. Notch1 and

Notch2 have opposite effects on embryonal brain tumor growth. Cancer Res. 2004;64(21):7787–93.

300. Huang Q, Li J, Zheng J, Wei A. The Carcinogenic Role of the Notch Signaling Pathway in the Development of Hepatocellular Carcinoma. J cancer. 2019;10.

301. Yang HW, Menon LG, Black PM, Carroll RS, Johnson MD. SNAI2 / Slug promotes growth and invasion in human gliomas. 2010;

302. Baygi ME, Soheili Z, Essmann F, Deezagi A, Engers R, Goering W, et al. Slug / SNAI2 regulates cell proliferation and invasiveness of metastatic prostate cancer cell lines. 2010;297–307.

303. Faraldo MM. Slug Controls Stem / Progenitor Cell Growth Dynamics during Mammary Gland Slug Controls Stem / Progenitor Cell Growth Dynamics during Mammary Gland Morphogenesis. 2012;(December).

304. Guelfi S, Orsetti B, Deleuze V, Bauchet L, Duffau H, Rothhut B, et al. SLUG and Truncated TAL1 Reduce Glioblastoma Stem Cell Subpopulations in Glioblastoma Multiforme. 2021;1–22.

305. Guichet P-O, Guelfi S, Teigell M, Hoppe L, Bakalara N, Bauchet L, et al. Notch1 stimulation induces a vascularization switch with pericyte-like cell differentiation of glioblastoma stem cells. Stem Cells. 2015 Jan;33(1):21–34.

306. Barbosa MAG, Xavier CPR, Pereira RF, Petrikaitė V, Vasconcelos MH. 3D Cell Culture Models as Recapitulators of the Tumor Microenvironment for the Screening of Anti-Cancer Drugs. Vol. 14, Cancers. MDPI; 2022.

307. Filipiak-Duliban A, Brodaczewska K, Kajdasz A, Kieda C. Spheroid Culture Differentially Affects Cancer Cell Sensitivity to Drugs in Melanoma and RCC Models. Int J Mol Sci. 2022;23(3).

308. Imamura Y, Mukohara T, Shimono Y, Funakoshi Y, Chayahara N, Toyoda M, et al. Comparison of 2D- and 3D-culture models as drug-testing platforms in breast cancer. Oncol Rep. 2015 Apr;33(4):1837–43.

309. Melissaridou S, Wiechec E, Magan M, Jain MV, Chung MK, Farnebo L, et al. The effect of 2D and 3D cell cultures on treatment response, EMT profile and stem cell features in head and neck cancer 11 Medical and Health Sciences 1112 Oncology and Carcinogenesis. Cancer Cell Int [Internet]. 2019;19(1):1–10. Available from: https://doi.org/10.1186/s12935-019-0733-1

310. Birgersdotter A, Sandberg R, Ernberg I. Gene expression perturbation in vitro - A growing case for three-dimensional (3D) culture systems. Vol. 15, Seminars in Cancer Biology. Academic Press; 2005. p. 405–12.

311. Fang Y, Imoukhuede PI. Axl and Vascular Endothelial Growth Factor Receptors Exhibit Variations in Membrane Localization and Heterogeneity Across Monolayer and Spheroid High-Grade Serous Ovarian Cancer Models. GEN Biotechnol. 2023;2(1):43–56.

312. Summers RJ, Jain J, Vasileiadi E, Smith B, Chimenti ML, Yeung TY, et al. Therapeutic Targeting of MERTK and BCL-2 in T-cell and Early T-Precursor Acute Lymphoblastic Leukemia. Cancers (Basel). 2022;14.

313. Shen Z, Liao X, Shao Z, Feng M, Yuan J, Wang S, et al. Short-term stimulation with histone deacetylase inhibitor trichostatin a induces epithelial-mesenchymal transition in nasopharyngeal carcinoma cells without increasing cell invasion ability. BMC Cancer. 2019;19(1):1–13.

314. Roche J. The Epithelial-to-Mesenchymal Transition in Cancer. Cancers (Basel) [Internet]. 2018;10:52. Available from: www.mdpi.com/journal/cancers

315. Aban CE, Lombardi A, Neiman G, Biani MC, La Greca A, Waisman A, et al. Downregulation of E-cadherin in pluripotent stem cells triggers partial EMT. Sci Rep. 2021 Dec 1;11(1).

316. Kariya Y, Oyama M, Suzuki T, Kariya Y. αvβ3 Integrin induces partial EMT independent of TGF-β signaling. Commun Biol [Internet]. 2021;4(1):1–11. Available from: http://dx.doi.org/10.1038/s42003-021-02003-6

317. Haerinck J, Berx G. Partial EMT takes the lead in cancer metastasis. Dev Cell [Internet]. 2021;56(23):3174–6. Available from: https://doi.org/10.1016/j.devcel.2021.11.012

318. Hofmann S, Cohen-Harazi R, Maizels Y, Koman I. Patient-derived tumor spheroid cultures as a promising tool to assist personalized therapeutic decisions in breast cancer. Transl Cancer Res. 2022;11(1):134–47.

319. Shuford S, Wilhelm C, Rayner M, Elrod A, Millard M, Mattingly C, et al. Prospective Validation of an Ex Vivo, Patient-Derived 3D Spheroid Model for Response Predictions in Newly Diagnosed Ovarian Cancer. Sci Rep. 2019 Dec 1;9(1).

320. Whiteside TL. The tumor microenvironment and its role in promoting tumor growth. Vol. 27, Oncogene. 2008. p. 5904–12.

321. Neophytou CM, Panagi M, Stylianopoulos T, Papageorgis P. The role of tumor microenvironment in cancer metastasis: Molecular mechanisms and therapeutic opportunities. Cancers (Basel). 2021;13(9).

322. Saraiva DP, Matias AT, Braga S, Jacinto A, Cabral MG. Establishment of a 3D Co-culture With MDA-MB-231 Breast Cancer Cell Line and Patient-Derived Immune Cells for Application in the Development of Immunotherapies. Front Oncol. 2020;10(August):1–13.

323. Zhou N, Xu W, Zhang Y. Histone deacetylase inhibitors merged with protein tyrosine kinase inhibitors. Drug Discov Ther. 2015;9(3):147–55.

324. Ranganna K, Selvam C, Shivachar A, Yousefipour Z. Histone deacetylase inhibitors as multitarget-directed epi-drugs in blocking pi3k oncogenic signaling: A polypharmacology approach. Int J Mol Sci. 2020;21(21):1–27.

325. Zhao N, Powell RT, Yuan X, Bae G, Roarty KP, Stossi F, et al. Morphological screening of mesenchymal mammary tumor organoids to identify drugs that reverse epithelial-mesenchymal transition. Nat Commun. 2021 Dec 1;12(1).

7 Appendix

Appendix 1

Table A1: Details of all driver mutations identified in spheroids and tumour tissues.

Patient	Category	Chr	Start	End	Ref	Alt	Func.refGene	Gene.refGene	ExonicFunc.refGene
MN 485	S	1	204399155	204399155	C	T	exonic	PIK3C2B	nonsynonymous SNV
MN 485	S	13	32913381	32913381	-	A	exonic	BRCA2	frameshift insertion
MN 485	S	16	23635370	23635370	C	T	exonic	PALB2	nonsynonymous SNV
MN 485	S	17	56798128	56798128	A	G	exonic	RAD51C	nonsynonymous SNV
MN 485	S	22	30035081	30035103	ACTGGATCATGATGTTTCAAAGG	-	exonic	NF2	frameshift deletion
MN 485	T	16	23635370	23635370	C	T	exonic	PALB2	nonsynonymous SNV
MN 485	T	17	56798128	56798128	A	G	exonic	RAD51C	nonsynonymous SNV
MN 485	T	1	204399155	204399155	C	T	exonic	PIK3C2B	nonsynonymous SNV
MN 485	T	13	32913381	32913381	-	A	exonic	BRCA2	frameshift insertion
MN 485	T	22	30035081	30035103	ACTGGATCATGATGTTTCAAAGG	-	exonic	NF2	frameshift deletion
MN 486	S	11	108198370	108198370	A	C	splicing	ATM	
MN 486	S	13	103520565	103520565	A	G	exonic	BIVM-ERCC5;ERCC5	nonsynonymous SNV
MN 486	S	14	105246551	105246551	C	T	exonic	AKT1	nonsynonymous SNV
MN 486	S	16	2225896	2225896	A	G	exonic	TRAF7	nonsynonymous SNV
MN 486	S	5	112178805	112178805	G	A	exonic	APC	nonsynonymous SNV
MN 486	S	7	128851867	128851867	C	T	exonic	SMO	nonsynonymous SNV
MN 486	S	8	68981282	68981282	-	A	exonic	PREX2	frameshift insertion

MN 486	T	13	103520565	103520565	A	G	exonic	BIVM-ERCC5;ERCC5	nonsynonymous SNV
MN 486	T	14	105246551	105246551	C	T	exonic	AKT1	nonsynonymous SNV
MN 486	T	5	112178805	112178805	G	A	exonic	APC	nonsynonymous SNV
MN 486	T	7	128851867	128851867	C	T	exonic	SMO	nonsynonymous SNV
MN 486	T	8	68981282	68981282	-	A	exonic	PREX2	frameshift insertion
MN 486	T	11	108198370	108198370	A	C	splicing	ATM	
MN 486	T	16	2225896	2225896	A	G	exonic	TRAF7	nonsynonymous SNV
MN 487	S	22	30051583	30051583	-	T	exonic	NF2	frameshift insertion
MN 487	T	22	30051583	30051583	-	T	exonic	NF2	frameshift insertion
MN 490	S	3	10191605	10191605	C	T	exonic	VHL	nonsynonymous SNV
MN 490	S	22	30038212	30038233	GAAAAGATCTACTGCCCTCCTG	-	exonic	NF2	frameshift deletion
MN 490	T	17	37879585	37879585	A	G	exonic	ERBB2	nonsynonymous SNV
MN 490	T	3	10191605	10191605	C	T	exonic	VHL	nonsynonymous SNV
MN 490	T	22	30038212	30038233	GAAAAGATCTACTGCCCTCCTG	-	exonic	NF2	frameshift deletion
MN 493	S	22	30054177	30054177	G	C	splicing	NF2	
MN 493	T	22	30054177	30054177	G	C	splicing	NF2	
MN 504	S	7	55233049	55233049	T	C	exonic	EGFR	nonsynonymous SNV
MN 504	S	22	30050663	30050663	C	T	exonic	NF2	synonymous SNV
MN 504	T	17	59857686	59857686	G	T	exonic	BRIP1	stopgain
MN 504	T	7	116411990	116411990	C	T	exonic	MET	nonsynonymous SNV
MN 504	T	7	55233049	55233049	T	C	exonic	EGFR	nonsynonymous SNV
MN 504	T	22	30050663	30050663	C	T	exonic	NF2	synonymous SNV
MN 504	T	7	128850341	128850341	G	T	exonic	SMO	nonsynonymous SNV

Table A1: Details of all driver mutations identified in spheroids and tumour tissues.

Appendix 2

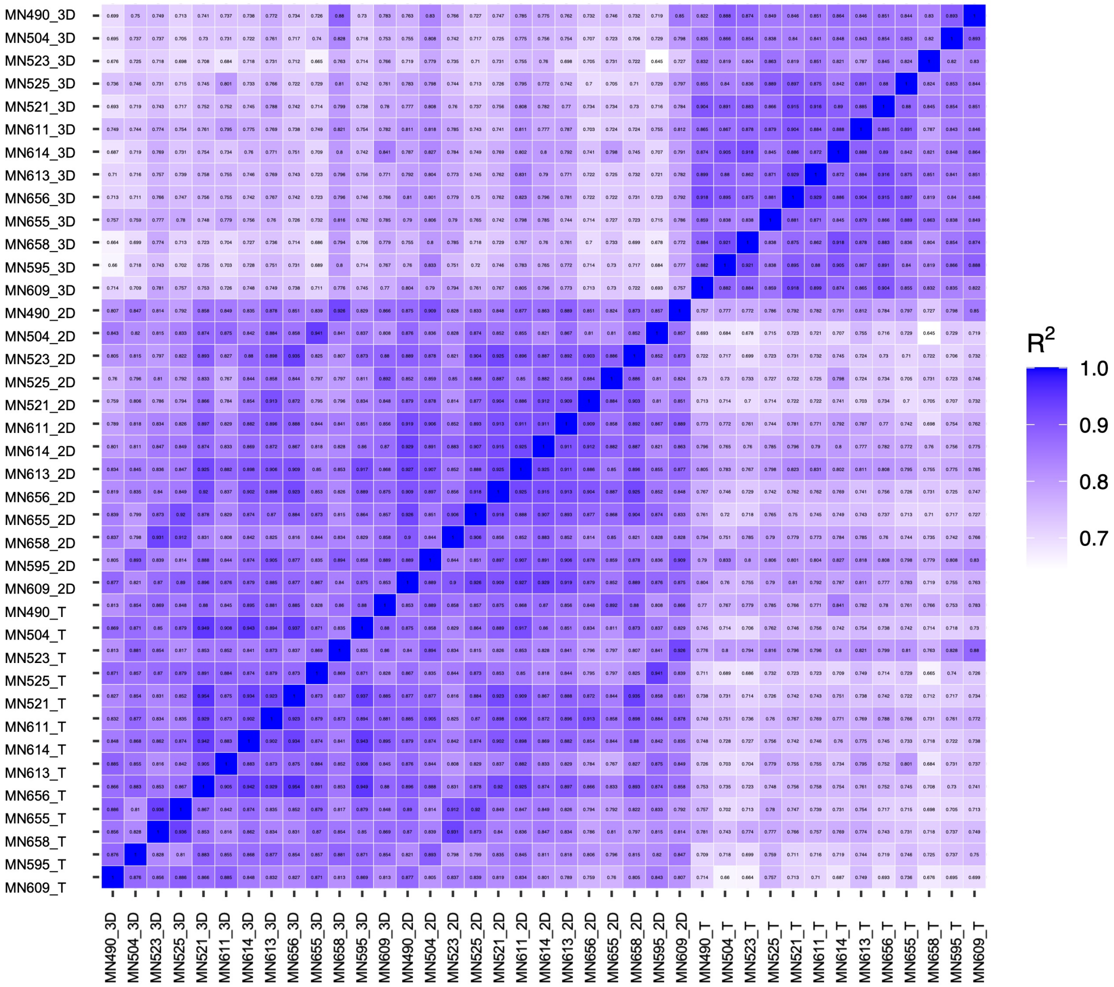

Figure A1: **Pearson's correlation between samples.**

Pearson's correlation (R^2) between samples transcriptomes is indicated in each square.

Colour coding indicates level of correlation with blue = 1.0.

Appendix 3

Table A2: Details of the functional annotation of genes identified in the co-expression analysis.

roups exclusively co expressed	GO ID	Term	Term PValue	Term PValue Corrected with Bonferroni step down	Group PValue	Group PValue Corrected with Bonferroni step down	% Associated Genes	Nr. Genes	Associated Genes Found
2D and T	GO:0006937	regulation of muscle contraction	0.00	0.05	0.00	0.00	4.55	8.00	[ADRB2, CALCRL, DMD, KCNJ2, KIT, PPP1R12B, TMEM38A, TNNT2]
3D and T	GO:0009952	anterior/posterior pattern specification	0.00	0.02	0.00	0.00	4.35	10.00	[ALDH1A2, DLL1, EMX2, GLI3, HEY1, HEYL, HHEX, HOXB6, HOXC9, LEF1]
3D and T	GO:0015909	long-chain fatty acid transport	0.05	0.05	0.05	0.05	4.05	3.00	[AMH, FABP4, PLA2G6]
3D and T	GO:0043030	regulation of macrophage activation	0.00	0.01	0.00	0.00	9.23	6.00	[AMH, CST7, FCGR2B, IL33, LRFN5, SNCA]
3D and T	GO:0042475	odontogenesis of dentin-containing tooth	0.00	0.05	0.00	0.00	6.19	6.00	[APCDD1, BCL2L11, GLI3, LEF1, NGFR, RUNX2]
3D and T	GO:0042487	regulation of odontogenesis of dentin-containing tooth	0.00	0.02	0.00	0.00	25.00	3.00	[APCDD1, NGFR, RUNX2]
3D and T	GO:0070227	lymphocyte apoptotic process	0.00	0.03	0.00	0.00	6.90	6.00	[AMH, BCL2L11, DOCK8, GIMAP8, GLI3, ZC3H8]
3D and T	GO:0070231	T cell apoptotic process	0.00	0.04	0.00	0.00	8.20	5.00	[BCL2L11, DOCK8, GIMAP8, GLI3, ZC3H8]
3D and T	GO:0009954	proximal/distal pattern formation	0.00	0.00	0.00	0.00	13.51	5.00	[ALDH1A2, DLL1, GLI1, GLI3, HOXC9]

3D and T	GO:0045879	negative regulation of smoothened signaling pathway	0.00	0.04	0.00	0.00	11.43	4.00	[ENPP1, GLI1, GLI3, RUNX2]
3D and T	GO:1990787	negative regulation of hh target transcription factor activity	0.00	0.00	0.00	0.00	75.00	3.00	[ENPP1, GLI1, GLI3]

Appendix 4

Supporting file 1: Lists of significant differentially expressed genes.

Sheet 1 shows the gene list of 2D compared to Tissue

Sheet 2 shows the gene list of 3D compared to Tissue

Sheet 3 shows the gene list of 3D compared to 2D

Appendix 5

Supporting file 2: List of all gene ontology lists identified by GSEA

Sheet 1 shows the gene ontology list of Tissue compared to 3D

Sheet 2 shows the gene ontology list of 3D compared to Tissue

Sheet 3 shows the gene ontology list of Tissue compared to 2D

Sheet 4 shows the gene ontology list of 2D compared to Tissue

Sheet 5 shows the gene ontology list of 3D compared to 2D

Sheet 6 shows the gene ontology list of 2D compared to 3D